Development of a light sheet microscopy system to analyse microtubule dynamics in Arabidopsis thaliana. Study of VIP3 gene function during floral development

Matthieu Cortes

Numéro National de Thèse : **2021LYSEN007**

THESE de DOCTORAT DE L'UNIVERSITE DE LYON

opérée par

l'Ecole Normale Supérieure de Lyon

Ecole Doctorale N° 340
Biologie Moléculaire, Intégrative et Cellulaire (BMIC)

Spécialité de doctorat : Biologie du Développement, Biologie des Plantes
Discipline : Sciences de la Vie

Soutenue publiquement le 26/05/2021, par :

Matthieu CORTES

Développement d'un système de microscopie à feuille de lumière pour analyser la dynamique des microtubules *chez Arabidopsis thaliana*. Etude de la fonction du gène *VIP3* au cours du développement floral

Devant le jury composé de :

Mme Chabouté Marie-Edith,	DR, IBMP - CNRS UPR2357	Rapporteure
Mme Peyriéras Nadine,	DR, BioEmergences	Rapporteure
Mme Monéger Françoise	DR, RDP – UMR5667	Examinateurice
M Coquelle Frédéric	MCU, Univ. Paris-Saclay	Examinateur
M Tréhin Christophe	MCU, Univ. Lyon 1	Directeur de thèse
M Lyuboshenko Igor	Gérant de PhaseView	Co-encadrant

Table des matières

Summary

In plants, the development of aerial organs is indeterminate: it takes place throughout their lifespan. In contrast, the development of floral organs is determinate in *Arabidopsis thaliana*, each flower has the same number of floral organs. This difference in development is due to the maintenance or not of the pool of stem cells present in the stem cell niches, the meristems. During my thesis I showed that the transcriptional regulator VIP3 contributes to the regulation of the switch from indeterminate to determinate in flowers. This also revealed that the control of flower termination is not as robust as classically thought. Because VIP3 is also involved in the regulation of epigenetic marks and response to external mechanical stimuli, this work opens new questions on the role of mechanical signals in indeterminacy. On a more technical standpoint, the analysis of shoot development suffers from a lack of imaging methods with high temporal resolution and in-depth optical sectioning. During the last decade, light sheet microscopy has emerged as a competitive imaging modality in developmental biology. However, in plants, the technique has mainly been used in roots because of limits in the microscope design. During my thesis, I developed protocols allowing the imaging of aerial organs in *A. thaliana* using a novel light sheet set-up (Phaseview Alpha3) where shoot samples can be observed while in water. I set up an imaging pipeline from sample mounting to quantitative analysis, with a focus on local dynamics of microtubules in cotyledon epidermis in relation to cell shape. Altogether, this work provides both conceptual and technical prospects for future quantitative projects in plant development.

List of abbreviations:

AG	AGAMOUS
AP1	APETALA 1
AP2	APETALA 2
AP2	APETALA2
AP3	APETALA 3
ARRs	ARABIDOPSIS RESPONSE REGULATORS
ATX1	ARABIDOPSIS TRITHORAX 1
CCD camera	Charged Coupled Device camera
CDK12	CYCLIN DEPENDENT KINASE 12
CESAs	CEllulose SynthAse
CLSM	Confocal Laser Scanning Microscopy
CLV1	CLAVATA 1
CLV2	CLAVATA 2
CLV3	CLAVATA 3
CNA	CORONA
CRC	CRABS CLAW
CRN	CORYNE
CSI1	Protein CELLULOSE SYNTHASE INTERACTIVE 1
CTD	C-Terminal Domain
CZ	Central Zone
DEF	DEFICIENS
DNA	Deoxyribonucleic acid
ELF	EARLY FLOWER
ER	ERECTA
ETT/ARF3	ETTIN/AUXIN RESPONSE FACTOR 3
FLC	FLOWERING LOCUS C
FM	Floral Meristem
FOV	Field Of View
HAM	HAIRY MERISTEM
HAN	HANABA TARANU
HUA	HUA ENHANCER
IM	Inflorescence Meristem
ISH	In Situ Hybridization
KNU	KNUCKLES
LFY	LEAFY
LRR	Leucine-Rich Repeat
LSFM	Light Sheet Fluorescence Microscopy
MAP	Mitogen-Activated Protein
MCM1	MINICHROMOSOME MAINTENANCE 1
mRNA	messenger RNA
OC	Organizing Center
Paf1C	RNA Polymerase II-associated factor 1 Complex
PALM	Photo-Activated Localization Microscopy
PAN	PERIANTHIA

PCG	Polycom Group
PDMS	Polydimethylsiloxane
PHB	PHABULOSA (PHB),
PHP	PARAFIBROMINE HOMOLOGICAL PLANT
PHV	PHAVOLUTA
PI	PISTILLATA
PI	Propidium Ioide
PIC	PreInitiation Complex
PMT	PhotoMultiplier Tube
Pol II	RNA polymerase II
PRC1	Polycomb Repressive Complex 1
PRC2	Polycomb Repressive Complex 2
PSF	Point Spread fonction
PZ	Peripheral Zone
RBL	REBELOTE
RLK	Receptor Like Kinase
RLP	Receptor Like Proteine
RNA	Ribonucleic acid
RPK 2	RECEPTOR-LIKE PROTEIN KINASE 2
RPK	RECEPTOR-LIKE PROTEIN KINASE
SAM	Shoot Apical Meristem
SEP (1 to 4)	SEPALLATA (1 to 4)
SIM	Structured Illumination Microscopy
smFISH	single molecule Fluorescence In Situ Hybridization
SRF	SERUM RESPONSE FACTOR
STED	STimulated Emission-Depletion
STIP	STIMPY/WOX9
STM	SHOOTMERISTEMLESS
STORM	Stochastic Optical Reconstruction Microscopy
SYD	SPLAYED
TBP	TATA-box Binding Protein
TFII	Transcription Factor for RNA Pol II
TFL2/LHP1	HETEROCHROMATIN PROTEIN 1
TOR	TARGET OF RAPAMYCIN
TrxG	Trithorax Group
ULT 1	ULTRAPETALA 1
ULT 2	ULTRAPETALA 2
VIP (1 to 6)	VERNALIZATION INDEPENDENCE (1 to 6)
WOX	Wus-HomeoboX
WUS	WUSHEL

A mon cousin Maxime

Remerciements

Je m’excuse d’avance pour ces remerciements. Ils sont à l’image de la difficulté que j’ai eue pour rédiger ce manuscrit. On va dire que la brièveté et la simplicité de de ceux-ci représentent le mieux ce que je ressens pour toutes les personnes qui ont été importantes lors de ma thèse.

Je commencerai par remercier PhaseView et le RDP qui m’ont permis de faire ces trois ans de thèse au sein de l’ENS de Lyon. Je remercie Olivier et Igor de m’avoir fait confiance et permis de créer et mener mon propre projet au sein du RDP.

Je remercie bien évidement Christophe et Olivier pour m’avoir encadré et soutenu pendant ma thèse.

Un merci tout particulier pour Christophe qui pendant trois ans m’a permis d’avancer dans mes réflexions scientifiques et extérieur à la science. Il m’a été rare de voir quelqu’un d’aussi prompt à discuter de tout sujet avec un intérêt et une vivacité aussi importants. De voir quelqu’un aussi impliqué à la fois dans son travail et sa famille ! Je pense que je resterais longtemps impressionné par quelqu’un qui arrive aussi bien à gérer famille, cours, recherche, encadrement de doctorant, etc. Je ne remercierai jamais assez Christophe pour sa patience et son aide pour la rédaction de ce manuscrit qui fut une période très difficile pour moi.

Je remercie énormément Claire pour son support technique sur la microscopie, sans qui je n’aurais jamais réussi à apprivoiser le light sheet. Claire a été un pilier à tout mon travail de thèse sur la microscopie, son expertise et sa disponibilité furent indispensables au bon déroulement de ma thèse.

Je remercie Anais Favre stagiaire de M2 qui a participée à tout le travail préparatoire sur l’imagerie des microtubules. Sans elle il n’est pa sûr que tout les travail présenté dans ma thèse sur les microtubule aurai été possible.

Je remercie de tout cœur l’équipe Mechanodevo dans laquelle il est fabuleux de pouvoir mener des projets de recherche.

Comme une thèse, c’est aussi beaucoup d’interaction sociale, je remercie le GN1 pour ces trois ans de bonne humeur, de soirées, de foyer etc. Sans ça, il aurait été difficile pour moi de finir ces trois années aussi sereinement.

Je remercie mes parents pour ces trois ans de soutien et de discussions sur bien des sujets qu'ils ne maitrisaient pas. Ils ont dû supporter des heures de discussions téléphoniques au sujet de microscopie, méristème et microtubule et je les remercie pour cela ! Sans ça, il m'aurait été difficile de garder de la motivation durant ces années.

Je remercie Audrey Garcia pour son amitié sans faille durant toute ces années à la fois dans les bon et les mauvais moments.

Je voudrais remercier Coline sans qui cette thèse n'aurait pas été possible. Elle a été d'un soutien sans faille durant ces trois dernières années. Elle m'a supporté et soutenu même durant les périodes difficiles de la thèse. Les ascenseurs émotionnels sont légions dans notre formation. Je ne lui serais jamais assez reconnaissant pour son soutien durant ma rédaction. Sans elle je n'aurais jamais fini ce manuscrit ! Sans motivation et avec une lettre de démission quasi écrite elle a su me remettre sur le chemin de la rédaction et me pousser à finir mon manuscrit.

En définitive, je remercie toutes les personnes qui m'ont aidées de près ou de loin lors de ma thèse.

General introduction

1. Microscopy and imaging history

1.1. A question of scale

Developmental biologists are driven by the desire to understand organism shape themselves. Observation is one of the fundamental components of their quest. Indeed, observation is often the very first step to describe an organism and to gather data regarding its shape, organization and developmental changes. Observations can be qualitative or quantitative but, in any case, it is an essential step to develop hypotheses and theories on living organisms.

Observation is not trivial and is a skill that must be acquired and exercised to improve its scope. In fact, all scientists exercise their ability to observe in a relevant way and to question their observations. As examples among so many others illustrating the importance of observation in science, we can cite Gregor Mendel for his work on pea phenotypes leading to the establishment of the founding laws of genetics (Gayon, 2016), or Goethe and his observation of monstrous plants, later to feed concepts such as homeosis, positional information and organ identity definition (Wolgan von Goethe, 1955).

In developmental biology, the scale at which observations are done is of a particular importance. Working hypotheses actually depend on the scale at which observations are done (Castiglione et al., 2014). Furthermore, observation at multiple spatial scales (e.g. whole organism *vs* tissue or cell scale) is also essential for most concepts. For instance, compensation is a process which maintains tissue homeostasis: modifications of cell number and size do not necessarily affect final size and shape of organs (De Veylder, 2001; Fankhauser, 1945; Neufeld et al., 1998). Temporal scales are also essential when dealing with growth. For instance, in Arabidopsis sepals, the spatiotemporal averaging of cell growth variability can buffer organ shape variability: spatial variability is compensated by temporal variability (Hong et al., 2016).

In the end, these concepts require the right observation techniques. The human naked eye is limited when it is about to distinguish very closely spaced points. It is estimated that the smallest distance between two points that humans can distinguish with a naked eye is 0.2 mm for an object located 25 cm away. Technological helps (lenses) are thus needed to increase this spatial resolution and allow observation of smaller structures or zoom in into samples, (Fig.1)

Zacharias Janssen invented the first microscope in 1590, and from then on a large community of scientists worked on the development and improvement of microscopy techniques (Fig 1-A). In 1665, Robert Hooke published Micrographia (Fig 2-C), a seminal book that collected patterns of different microorganisms such as lice and fleas (Hooke, 1665). Thanks to his microscope, albeit rudimentary (Fig 2-A-B), he was the first to show alveolar structures in cork, which he named “cells” because they resembled walled cells in a monastery (Fig 2-D).

1.2. Optical microscope - Transmitted light microscopy

1.2.1. Principle

The optical microscope has several roles. The first is to produce an enlarged image of objects to be observed. This is called magnification. The second is to increase the ability to separate two objects of a same image to preserve as much detail as possible. This is called resolution or resolving power. The third is to distinguish the structures from each other according to their emission properties. This is called contrast.

The first microscopes were single-lens microscopes. This is what we would call magnifying glasses today (Fig 1-A). Later, microscopes consisted of two lenses, the objective and the eyepieces. One can highlight two important microscopes in the history of modern microscopy: the microscope developed by Powell and Lealand in 1850, and the Zeiss microscope (Fig 1-B), produced in 1930. Modern microscopes are composed of several main components: a light source which can be a lamp or a laser, an objective which is responsible for the magnification and that determines the resolution of the microscope, eyepieces which serve as additional magnifying glasses for viewing the sample, and finally a detection system, for images to be recorded (Fig 1-C).

The objective is the most important element of the optical microscope. It determines the magnification, the numerical aperture, which is the efficiency of light collection, the resolution, and the working distance, which is the distance between the objective and the sample. It is therefore the key element that makes possible the observations and that determines the optical properties of the microscope.

The second most important element is the illumination. In addition to the light source itself, there is a so-called condenser placed between the light source and the sample. The condenser

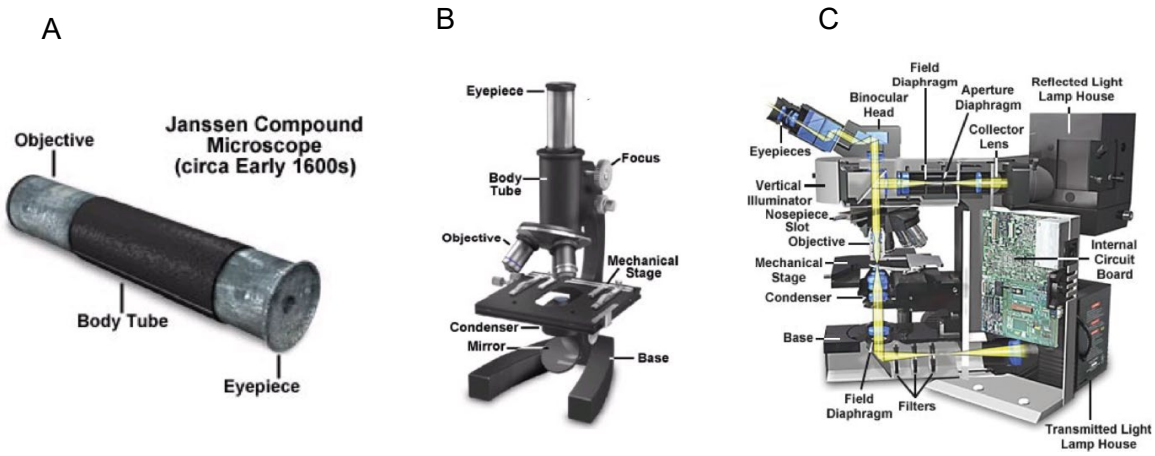

Figure 1: Evolution of microscope compounds

A. *Microscope of Jansen which is basically a magnifying lens;* ***B.*** *Zeiss microscope which displays all the components of a standard microscope;* ***C.*** *Current light microscope.*

Figure 2: Hook microscope and the first observation of cells

A. *Print of Hook microscope with light source in the left and the microscope itself in the right;* ***B.*** *Hook microscope;* ***C.*** *Micrographia, the first book with sketches of microscopic structures; D. The first image of cells in a cork sample taken by Hook in Micrographia.*

concentrates the light into a cone to make the specimen uniformly illuminated. This is called Köhler illumination.

1.2.2. Cell and tissue observation

The invention and the fast improvement of simple microscopes led to the emergence of a whole branch of biology, combining light microscopy and preparation of biological specimens: histology. First empirical during the 17th century because microscopy techniques were rather rudimentary, histology rapidly raised the hypothesis that organs are organized into tissues defined as sets of cells with similar features (Bichat, 1799). Progresses have been made possible thanks to the improvement of fixation and sectioning protocols allowing to get thin enough sections to be observed with a microscope. Later on, the inclusion method, which consists in replacing the water contained in the tissues by paraffin, resin or wax, allowed to embed tissues in rigid blocks, ready to be cut in even thinner sections.

- Unstained specimens

It is however difficult to observe sections under a bright-field microscope without any special adaptations or dyes (Thorn, 2016). Indeed, sections of a few tens of micrometers are almost transparent, with a very low contrast. One possibility to bypass this limitation is to use tissue specific dyes (see below). However, it is possible to increase the contrast of unmarked sections by using the optical properties of the samples.

Dark field microscopy

Dark field microscopy principle is based on the fact that the light transmitted by the sample has two components: the direct light that is not deflected by the sample, and the indirect light that is deflected by the sample. Dark field microscopy allows only the deflected light to be collected. It can therefore be used to observe light-scattering areas, i.e. the contour of opaque objects as well as sudden changes in refractive index. The use of an annular diaphragm condenser allows oblique illumination of the sample and thus only the deflected light to be selected (Fig. 3 -A). However, the highest limitation of this type of microscopy is the light intensity returned by the samples (Macnab, 1976).

Phase contrast microscopy

Thin samples such as cells or tissue sections can be described as phase objects. When light passes through such samples, there is a small variation of light amplitude, high enough to induce a phase variation in the light. Since detectors are only sensitive to variations in intensity, phase variations are transformed into intensity variations. William R. Belknap used for instance contrast phase microscopy to spot chloroplasts (Fig. 3 -B Belknap, 1983).

Polarized light

The polarized light microscope is designed to observe and photograph specimens that are visible mainly due to their optically anisotropic nature. The microscope is equipped with a polarizer, placed in the light path before the specimen, and an analyzer placed in the optical path between the rear opening of the objective and the observation tubes or the camera port. Image contrast results from the interaction of plane polarized light with a birefringent (or double refracted) sample to produce two individual wave components that are each polarized in mutually perpendicular planes. After leaving the sample, the light components become out of phase, but are recombined with constructive and destructive interference as they pass through the analyzer. This recombination creates the final image (Fig. 3 – C). Polarized light allowed the observation of birefringent samples such as muscle tissue from the zebrafish embryo (Smith et al., 2013) or aligned cellulose microfibrils in plant tissues (Green, 1962).

Interferential contrast microscopy

Interferential contrast microscopy uses the principle of light interferometry (Centonze Frohlich, 2008; de Groot, 2015) The concept is to illuminate the sample with two orthogonally polarized beams, which are very slightly offset at the sample level. The principle is based on the detection of the relative phase shift between these two beams, which makes it possible to visualize a phase gradient between the beam that will have passed through the sample and the beam that has not passed through the sample (Fig 3-D).

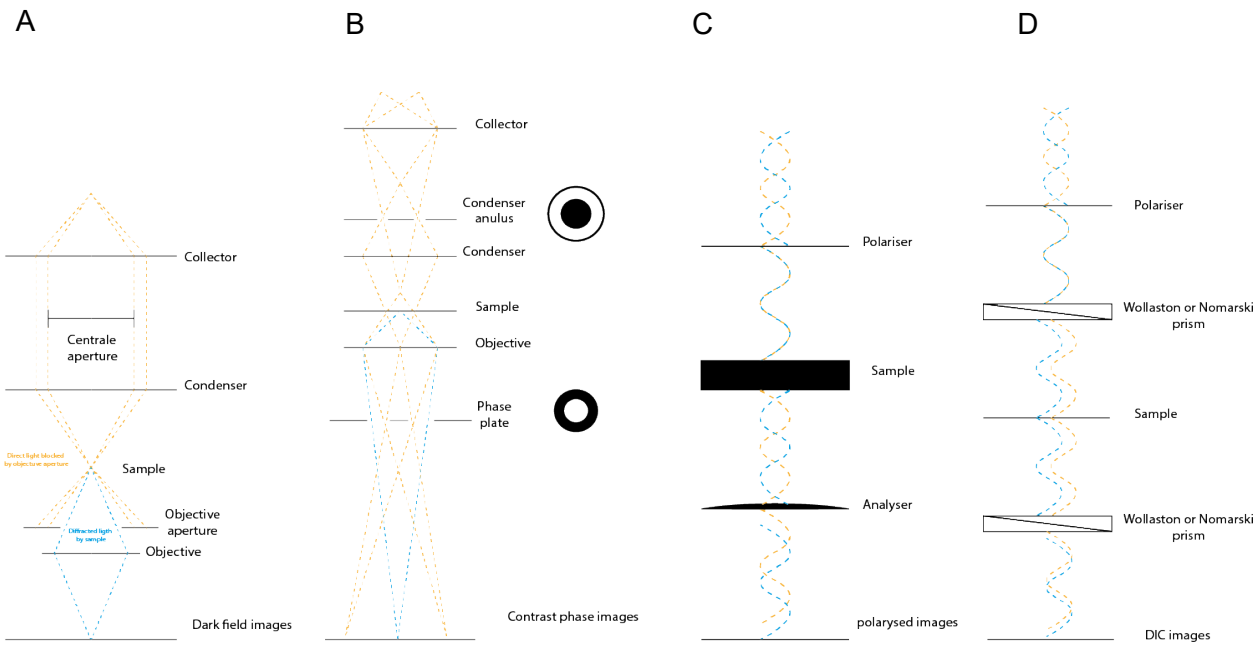

Figure 3: Contrast microscopy

A. *Dark field microscopy, only the light diffracted by the sample is collected;* ***B.*** *Contrast phase microscopy, due to the condenser annulus and the phase plate, the variation of the phase of light is transformed into intensity variation;* ***C.*** *Polarized microscopy, sample is illuminated by polarized light, the difference in term of polarization after passing through the sample is transformed into intensity variation;* ***D.*** *Differential interference contrast microscopy, this microcopy is based on the light interferometry principle. The interference between light, diffracted or not by the sample, allows to produce visible intensity light variation.*

- Stained specimens

To improve observation and make tissues easier to discriminate and characterize, staining protocols have been developed. Many staining can label tissues and cells depending on their components and properties (Titford, 2009). As striking examples of staining protocol, let us cite the Mirande's alum carmine-iodine green in plants (1920). Although not fully specific, carmine and iodine green have affinity for the two major components of the plant extra cellular matrix or cell wall: alum carmine stains cellulose in red and iodine green stains lignin in green. The added value of staining is thus to discriminate tissues which do not necessarily have a different morphological feature. Such protocols are continuously improved to make tissue observations and description more accurate (Mondolot et al., 2001; Parker et al., 1982).

1.2.3. Optical microscope – epifluorescence

- Principle

Fluorescence is the property of a molecule to emit in a specific wavelength (called the emission wavelength) when excited by another specific wavelength (called the excitation wavelength) of higher energy (Fig 4). After absorption with a laser, the molecule goes in a higher electronic state and releases energy when getting back to its initial state. This release of energy can be of different kinds, either vibrations or fluorescence, and thus can be detected.

The microscopes able to detect fluorescence signals are the so-called epifluorescence microscopes. Such microscopes display similar configurations and work in the same way than the bright field optical microscope. Epifluorescence microscopes illuminate samples with light of a specific wavelength, and filter the emitted light to select photons of a particular wavelength (Fig 4) The emitted photons can be observed directly through the binoculars and can be simultaneously imaged and recorded on a CCD (charge-coupled device) camera. However, epifluorescence microscopes poorly discriminate both excitation and emitted wavelength and fluorescence with close wavelength therefore limiting signal discriminations.

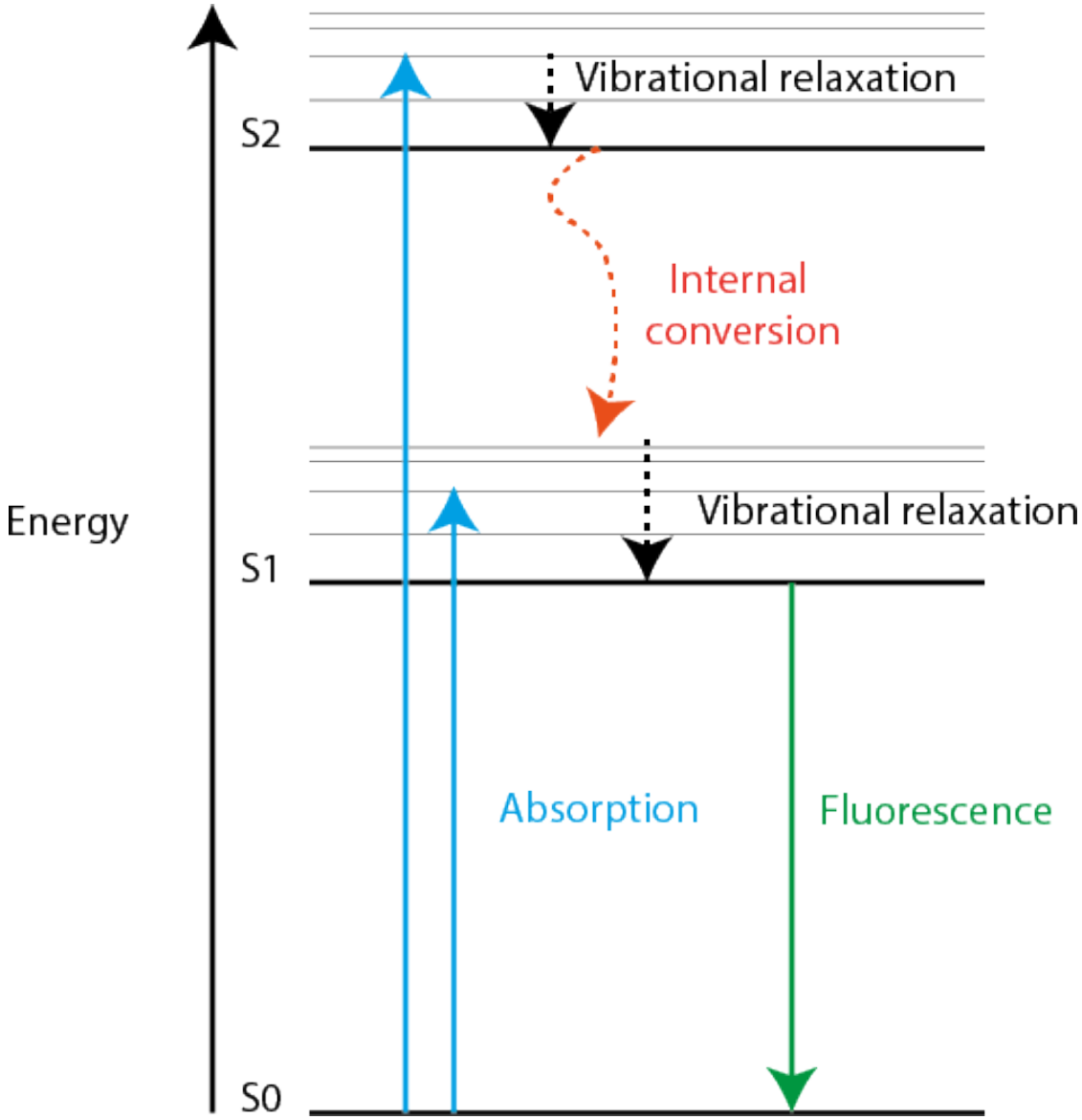

Figure 4: Fluorescence - Jablonski diagram

When a fluorescent protein at a basal energy state (S0) is excited, by light for instance, its energy state moves to higher level of energy (S1, S2). This corresponds to the absorption phase. The protein first comes back to a stable quantic stage – it is the vibrational relaxation - then it reaches a lower quantic stage down to the basal one – it is the internal conversion. During the relaxation phase, from high to basal steady state, a part of the energy is transformed into photons that can be observed by fluorescent microscopy.

- Fluorescence Dyes

Since the 1990s, many fluorescent dyes have been developed to discriminate specific tissues or subcellular components but also to inform on cellular status. For instance, Phalloidin coupled with rhodamine, which fluoresces in red-orange when excited at 552nm, binds actin filaments and is therefore a classic fluorescent dye to mark actin cytoskeleton, for instance in animal cells (Parker et al., 1982). Propidium Iodide (PI) is widely used both in plants and animals, first as a DNA intercalant but also as a cell wall dye, for instance to mark plant cell contours (Johnson et al., 2005). PI fluoresces in red (617nm) when excited at 538nm. Interestingly, being not able to cross plasma membranes, PI can also be used to discriminate between dead and living cells (Ormerod et al., 1993). Other dyes can be used to specifically mark plasma membranes based on the fact that they are made of around 40% lipids. For example, FM4-64, which is a lipophilic dye that binds to fatty acids and cannot enter the cells except if they are injured, is commonly used to image the cellular plasma membrane. Note that FM4-64 can enter the cell by endocytosis, and thus is also a classic marker of inner membrane dynamics (Bolte et al., 2004).

1.2.4. Resolution limits

- Airy spot and Point Spread Function

Optical microscopes all display spatial resolution limitations. The spatial resolution is the minimal distance separating two points that can be distinguished with the microscope. In light microscopy, the resolution is related to the fact that light diffracts in the microscope. Thus, when a point is observed with an optical microscope (for example a bead smaller than the resolution of the microscope) the image of this point is not a point but a spherical structure called the Airy spot (Fig 5-A). The Airy spot consists of a central disc surrounded by concentric circles around it. The image of samples we get with optical microscopes is therefore not the real image of the object, but an image of the object together with the optical aberrations generated by the microscope. Airy's spot is used to calculate the resolution of the microscope. Indeed, if two points are too close, the two Airy spots corresponding to these points will overlap. It will therefore not be possible to distinguish these two points as two distinct objects. Several criteria have been theorized to calculate whether two spots can be separated. For instance, Rayleigh's criterion which states that two spots can be just separated if the first ring of the Airy spot corresponds to the maximum of the second (Fig 5-B).

A

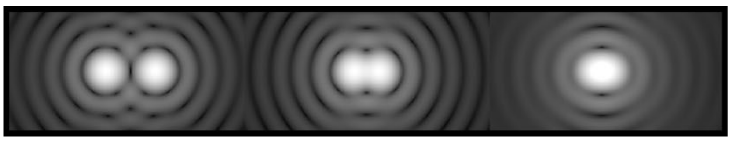

B

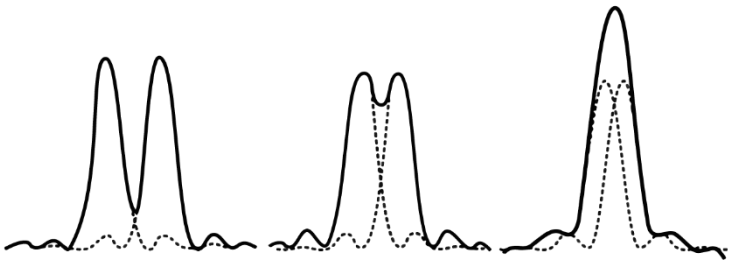

C

$$d = \frac{\lambda}{2n \sin\theta} = \frac{\lambda}{2\mathrm{NA}}$$

Figure 5: Limit of resolution

A. *Airy spot, the circumferential shape represents the image of an under resolved spot in a microscope. The three images represent airy spot from 2 spot which can be separated to 2 spots with cannot be separated with the current microscope.* ***B.*** *Graphical representation of airy spot.* ***C.*** *Formula of resolution where θ is the semi angle of the lens, η is the refractive index of the medium and λ the wavelength of emission.*

The resolution of an optical microscope is governed by optic laws and is equal to the illumination wavelength divided by twice the numerical aperture (NA) of the objective used, with the numerical aperture correlating with the refractive index of the medium and the half angle of the objective aperture (Fig 5-C). Typically, at 488 nm, two objects separated by 200 nm will not be distinguished.

All the aberrations produced by both microscopes and observed samples, and that influence the resolution limit, can be evaluated: this is called the Point Spread Function (PSF). The PSF depends on the system parameters and includes optical aberrations that can be listed as follows. Chromatic aberrations correspond to the difference of focal length between all wavelengths, i.e. each wavelength displays its own focal distance. Spherical aberrations correspond to the fact that the rays of light passing through the periphery of the lens and the rays of light passing through the center of the lens focus on different points. Finally, field-curve aberrations correspond to the curved deformation at the periphery of the image. However, the PSF also depends on the lens immersion and sample refractive indexes. When observing a specimen with a microscope, the image is therefore not the real image of the object, but an image of the object altered by all the aberrations brought by the microscope. The PSF can be estimated theoretically (https://svi.nl/NyquistCalculator) but also experimentally by imaging beads smaller than the resolution. PSF obtained experimentally is closer to the real PSF since it takes into account the characteristics of the system. However, in both cases, it remains an estimation.

Thus, there are three ways to increase the resolution in microscopy. The first is to use a medium with a high refractive index, but this is not always possible. For example, clearing solutions display high refractive index to increase the resolution. However, the clearing solutions are highly toxic, corrosive and can thus only be used on fixed samples. The second way is to use objectives with a much larger half angle. In reality, it is not possible to increase the half angle of aperture indefinitely. Indeed, the half angle of aperture is proportional to the size of the lens. The wider the half angle of aperture, the bigger the lens. Increasing the half angle of aperture indefinitely would amount to having very large objectives and therefore fanciful microscope sizes. The third way is to use shorter illumination wavelengths such as in electronic microscopes. The electron beam shows a much smaller wavelength resulting in a much higher resolution. When using laser excitation, a series of fluorescence microscopes have been developed to improve the resolution of optical microscopes.

- Structured Illumination Microscopy (SIM)

SIM microscopy requires a specific illumination using structured light (Fig 6-A). For each plane, several images are produced with different patterns. These different images are then combined to reconstruct of a super-resolution image (Schermelleh et al., 2019). Nine images are required to make two-dimensional images and 15 to make three-dimensional images (Gustafsson et al., 2008; Jacquemet et al., 2020). SIM microscopy can be used for a wide variety of biological samples. This microscopy is compatible with most fluorescent proteins as long as they resist photobleaching and do not blink (Demmerle et al., 2017).

- Stimulated Emission-Depletion (STED)

STED microscopy is based on confocal laser scanning microscopy (see below). In contrast to confocal, a second hollow beam, a donut-shaped STED beam, is superimposed on the classical excitation beam (Fig 6-B, Heine et al., 2017; Hell and Wichmann, 1994; Klar et al., 2000). In the overlap zone between the two lasers, the STED laser produces a depression of the fluorophores before fluorescence, which has the effect of thinning the emission zone. STED microscopy does not require any specific mounting procedure or mounting medium, but a special care in tissue fixation to preserve tissue integrity as much as possible (Blom and Widengren, 2017).

- Single molecule localization microscopy (PALM/STORM)

Photo-Activated Localization Microscopy (PALM) and Stochastic Optical Reconstruction Microscopy (STORM) are the emission of individual fluorophores recorded by a camera (Fig 6-C). Each image is composed of only a few fluorophore spots of about 200 nm wide (von Diezmann et al., 2017). Tens of thousands of images of flashing fluorophores are recorded successively and subsequently merged to produce a super-resolved image (Baddeley and Bewersdorf, 2018; Jimenez et al., 2020). PALM microscopy is performed using photoactivatable/convertible fluorescent proteins (see below live imaging). STORM microscopy uses fluorophores that are integrated in reducing and oxidizing buffer system (ROXS). Both techniques are based on stochastic switching of single-molecule fluorescence signal from a state OFF, i.e. dark, to a state ON, i.e. fluorescent. The positions of only a few of the individual fluorescent molecules are simultaneously recorded.

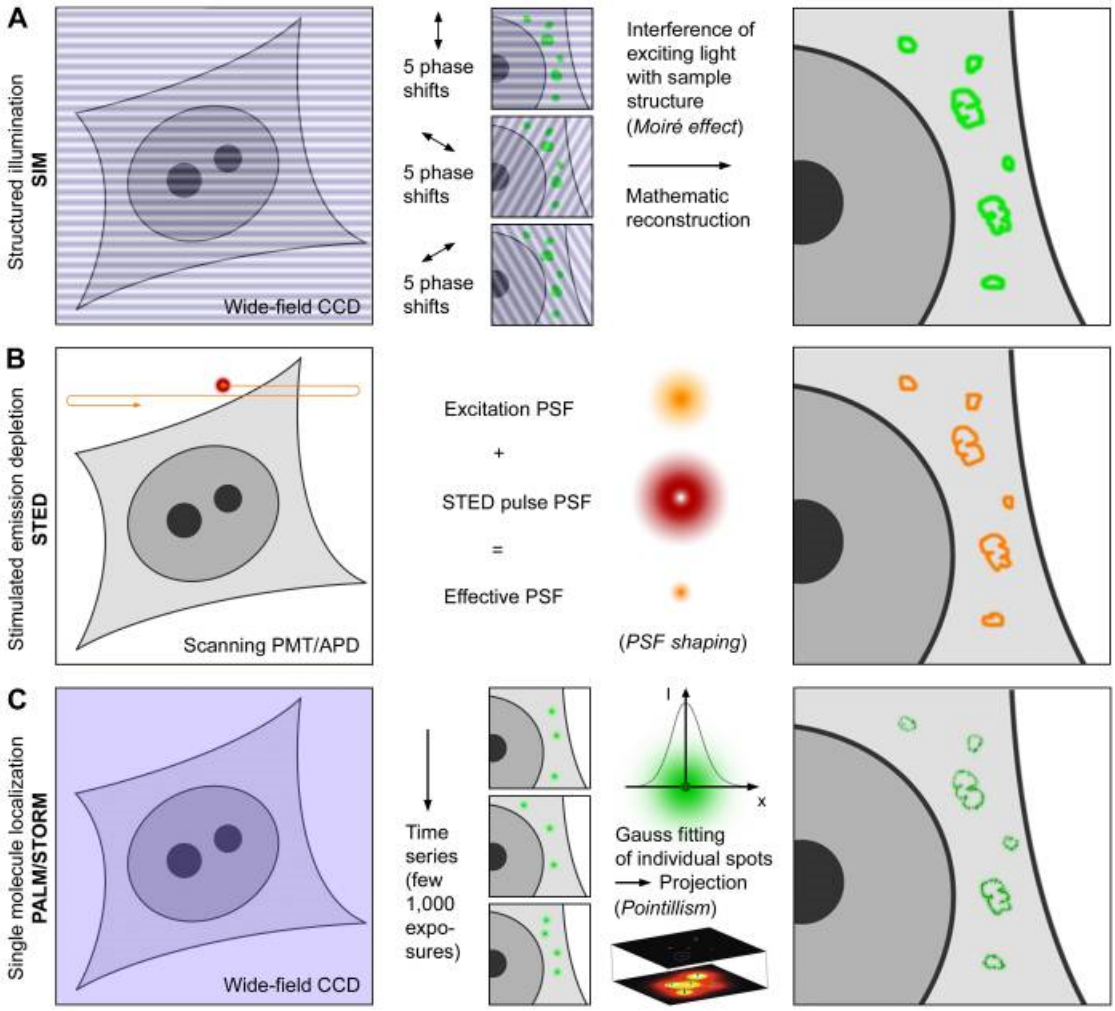

Figure 6: Super resolution microscopies

A. *SIM microscopy, the sample is illuminated with structured light, several images are produced with several kinds of structuration, and a super resolved image is subsequently generated from the mathematical reconstruction of the all the images;* ***B.*** *STED microscopy, two beams are produced, one classical beam (in orange) and one donut- shaped hollow beam (in red). In the two lasers overlapping zone, the STED laser produces a depression of fluorophores before fluorescence which allows the thinning of the emission zone (effective PSF);* ***C.*** *Single molecule localization microscopy (Palm/Storm). In Palm or Storm, a lot of images are taken about blinking flurorophore and the fusion of all of these images results in super resolved images. The blink fluorophore allow to frank airy law. (Schermelleh et al., 2010)*

1.3. Imaging of fixed objects with light microscopy

Beyond the microscope optics, observations also entail sample preparation. From the discovery and characterization of genes, the question was no longer to describe only the organization of tissues and cells, but also to describe how genes are distributed in the nucleus and where mRNA and proteins are expressed and located both at the cell and tissue levels. Molecular biology techniques coupled with histological methods were therefore developed for this purpose.

1.3.1. Gene expression localization

In situ hybridization (ISH) is a technique that consists in synthesizing labelled nucleic acid sequences and to use them to probe their specific target sequences in their native cellular and tissular environment (Gall, 2016; Schwarzacher, 2003). First reported in 1969 to locate repeated DNA sequences in animal cells (Gall and Pardue, 1969) this technique was rapidly adapted to plant tissues (Hutchinson and Lonsdale, 1982). Probes quite rapidly evolved from radioactive to non-radioactive forms, containing modified nucleotides carrying either epitope (biotin) recognized by specific antibodies (avidin) coupled to enzymes or fluorophores, or fluorescent molecules (FISH) (Jiang et al., 1995; Langer-Safer et al., 1982; Rayburn and Gill, 1985). Compared to radioactive and biotinylated probes that give a low spatial resolution (> 1 µm), fluorescent probes, now using a wide range of fluorophores, are rapidly detectable and give signals clear, precise and reliable enough to map single copy genes on chromosomes both in animals and plants (Huber et al., 2018; Langer-Safer et al., 1982; Schwarzacher et al., 1989).

ISH is also a method of choice for *in situ* detection of mRNA in tissues. Since the first use of biotinylated probes showing actin expression in chicken muscle-tissue culture (Singer and Ward, 1982) , the technique has been strongly improved over the years to give more accurate and reliable signals (Levsky, 2003; Volpi and Bridger, 2008). The single-molecule fluorescent ISH (smFISH) technique even allows to evaluate the absolute number of mRNA in single cells (Tutucci et al., 2018). Through multiplexing, the transcriptome of individual cells in tissues is now amenable to analysis (spatial transcriptomics, Ståhl et al., 2016).

1.3.2. Protein localization

Whenever possible, mRNA location must be compared to the corresponding protein. Beyond the fact that the subcellular localization of some proteins regulates their activity the question of knowing whether mRNAs and the resulting proteins accumulate in the same place is of great importance in biology, notably because both mRNAs and proteins can diffuse or be transported across cells and tissues (Itzhak et al., 2016; Jones and Rappoport, 2014; Nimchuk et al., 2011; Plotnikov et al., 2011). The microscopy-based approach to follow subcellular localization of proteins is based on immuno-labelling. If this method provides valuable information on protein localization, it is limited by the availability of specific antibodies, often monoclonal, that can be conjugated either to enzymes that react with a substrate to produce a colored product, or with fluorophore or fluorescent protein (Chen et al., 2018; Evkaikina et al., 2014; Fuchs and Lohmann, 2020; Hansen and Hippenmeyer, 2020). Combining smFISH and immunofluorescence allows to correlate the expression of an mRNA and a protein of interest in single cells (Maekiniemi et al., 2020).

1.4. Live imaging microscopy

1.4.1. Fluorescent proteins

A better understanding and characterization of cellular and molecular processes that control development requires temporal resolution, and thus the observation of living specimens. Such a possibility has become possible thanks to a major breakthrough in molecular biology: the cloning and characterization of fluorescent proteins (Fig 4) that can be observed in vivo (Chalfie et al., 1994; Harper et al., 1999). Isolation and characterization of Fluorescent Protein (FP), including the Green Fluorescent Protein (GFP), excited at a 488nm wavelength (roughly blue light source) to emit at 510nm (green light) brought the opportunity to produce transcriptional and translational reporters fusions that can be stably transformed into transgenic lines (Chalfie et al., 1994). GFP fluorescence can therefore be tracked as a proxy for gene expression and protein location. From the initial engineering of GFP, a large series of fluorescent proteins and several types of fluorescence microscopies have been developed to perform in vivo imaging (Prasher et al., 1992, https://www.fpbase.org/protein/avgfp/).

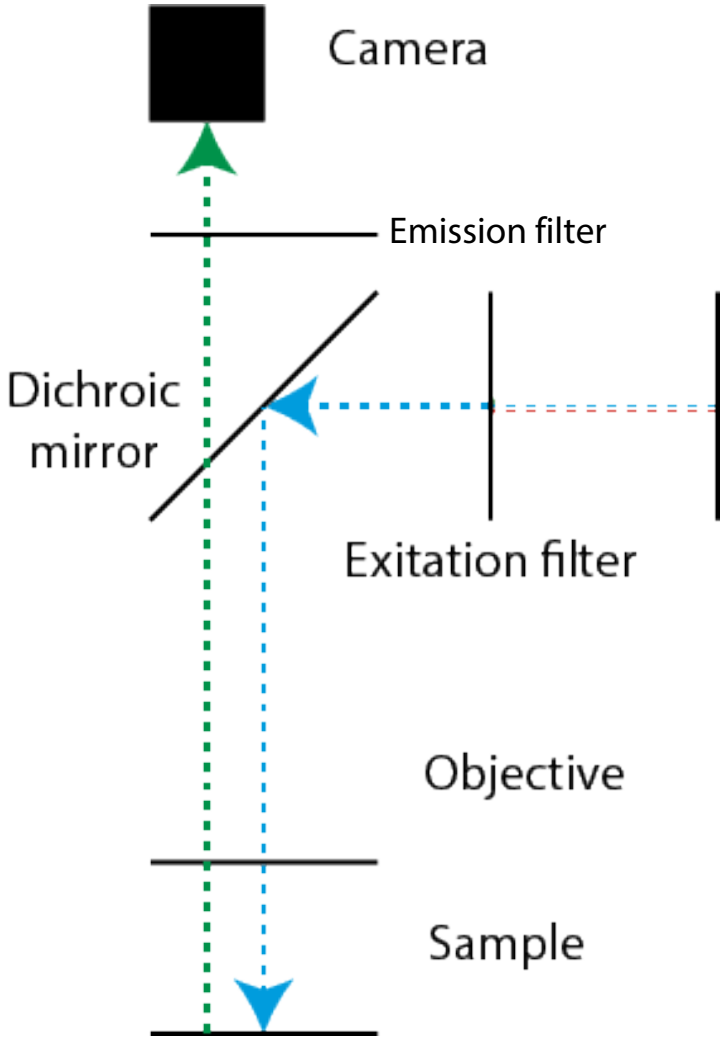

Figure 7: Epi-fluorescence microscope.

The sample is illuminated by light with a specific wavelength. The white light of led is filtered by an emission filter in order to selected the right wavelength (blue here). The fluorescence is collected by the camera. The dichroic mirror allows to separate the illumination (in blue) from the emission (in green) lights.

1.4.2. 2D live imaging

- Epifluorescence

Epifluorescence microscopy, as described above can be used to image fluorescent markers *in vivo* over time. In this case, samples are imaged in a single image, and cameras frame rates allow to follow signals with a very high temporal resolution. The first limitation is obviously the thickness of sample and/or the thickness of signals, i.e. if signals overlay or not. The second limitation is the resolution of epifluorescence microscopes that do not allow fine structures such as vesicles, proteins or cytoskeleton to be tracked (Fig 7).

Coupling high temporal resolution with high 2D resolution therefore became paramount to describe the intracellular structural organization with a nanometric resolution.

- Total Internal Reflection Fluorescent (TIRF) Microscope

TIRF microscopy allows fluorescence to be imaged up to 240nm in depth only. The sample is mounted between slide and lamella. It is illuminated with a characteristic incident angle. Thanks to this angle, the captured fluorescence comes from the evanescent wave of the sample (Fig 8). This allows to generate a very important contrast since all the photons coming from the sample are not captured. Furthermore, the temporal resolution can be high since only a single plane is imaged (Axelrod, 1981).Epifluorescence and TIRF imaging techniques allow high temporal resolution time-lapses but with different spatial resolutions. However, none of them allow three-dimensional imaging while living beings are all, and at whatever scales, 3D structures.

1.4.3. 3D live imaging - Confocal microscopy

Confocal microscopy allows 3D imaging as it allows to discriminate the photons emitted by a specific focal plane of the sample from the photons emitted by rest of the structure which is out of the focal plane. Marvin Minsky patented the confocal microscope in 1957 (Minsky, 1988). The first confocal microscope was commercialized in 1987 by Brad Amos and John White (Amos et al., 1987).

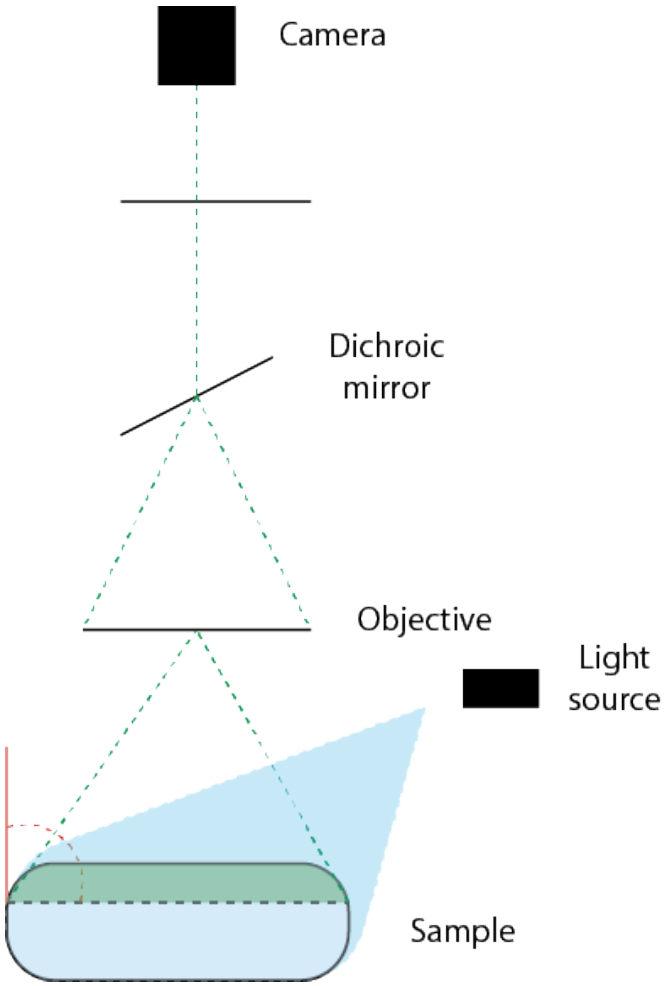

Figure 8: Total Internal Reflection Fluorescence (TIRF) microscopy

The sample is illuminated by a light with a specific angle (in red), due to the Evanescent field only the fluorescence from the 240 first micrometres is collected (in green).

- Confocal laser scanning microscopy

Confocal laser scanning microscopy (CLSM) is currently the most widely used fluorescence microscopy for *in vivo* and/or 3D microscopy. CLSM allows the separation of photons from different focal planes of the sample (Fig 9). To do this, the sample is illuminated by a laser, which excites a fluorescent protein. The emitted photons are recovered by the objective and then the photons emitted at the focus plane of the sample are discriminated from those emitted out of the focus by a pinhole. The pinhole allows to discriminate the photons coming from the part of the sample in focus the photons coming from the part of the sample out of focus (Light and Maverick, 2008; White et al., 1987). Thanks to this trick, only the photon coming from the focus are detected by the PMT. PMT is a photocathode which transform photon in electron signal (Bayguinov et al., 2018). The sample can be moved along the Z axis, to be imaged optical section by optical section, and to ultimately generate the final 3D image. Since PMTs cannot create full image in one time, the sample must be scanned by the laser pixel by pixel, each image corresponding to a matrix of pixels. Such laser scanning technique therefore allows to choose the number of pixels that composes each image, and therefore to have a different pixel size for a given field of view (FOV). It is therefore possible to define an optimal pixel size for a given lens, and depending on the quality and the numerical aperture of the lenses, to produce highly resolved images. CLSM has however several limitations, all related to laser scanning. Depending on microscope settings and on lens properties, time of acquisition (the time to scan the specimen to create the image) can be more or less long, strongly limiting the possibility to get high temporal resolution. It is thus not possible, or at least very difficult, to follow highly dynamics biological processes. Furthermore, for each plane to be scanned, the whole sample is illuminated by the laser (Fig 9). This constant illumination during acquisition time can induce high rates of phototoxicity and photobleaching (decrease of fluorescence). CLSM therefore allows high spatial resolutions to make 3D imaging, but does not allow very high temporal resolutions. Alternative confocal microscopy techniques have been developed to compensate for this limited temporal resolution.

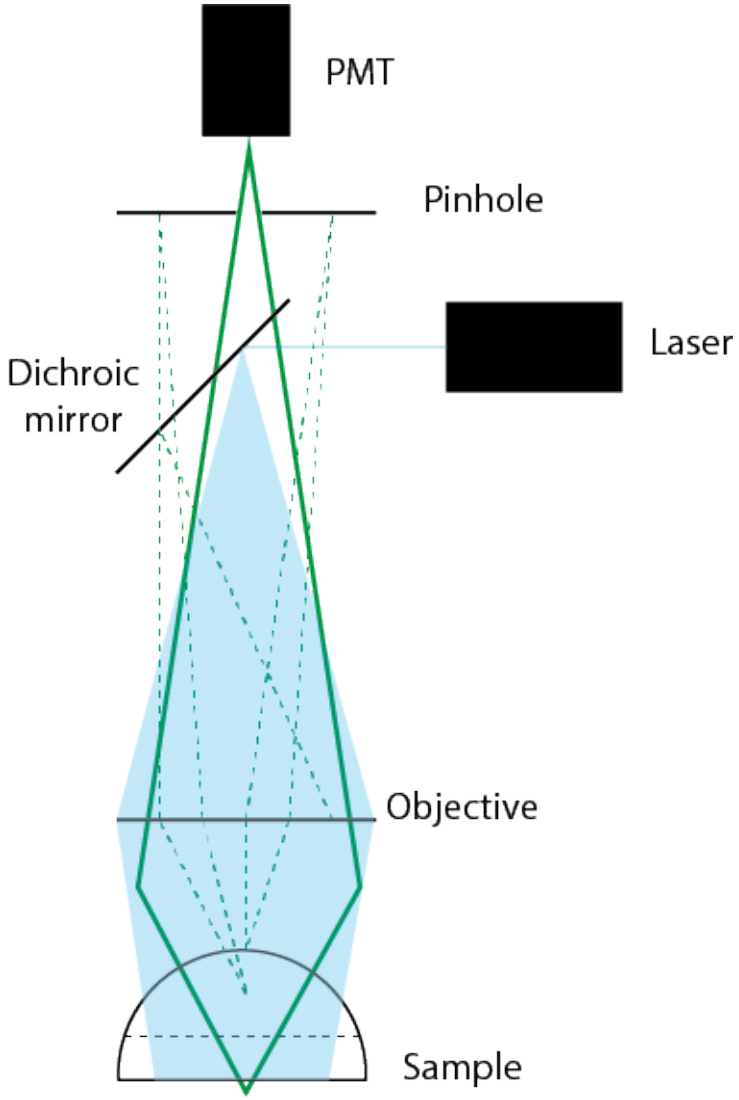

Figure 9: Confocal laser scanning microscopy (CLSM)

The sample is scanned by the laser in all its thickness (blue shape). The fluorescence is produced in all the thickness of the sample (dotted green line). The photons from a specific focal plan are collected through a pinhole (green line) while photons out of the focal plan are stopped (dotted green line).

- Spinning disk

Unlike CLSM, the spinning disk does not use a PMT but a camera. Furthermore, the acquisition is not done by a confocal laser scanning head but by a spinning disk scanning head.

The spinning disk scanning head consists of two coaxially aligned disks with a dichromatic mirror placed in between the two disks (Fig 10). Each disk contains approximately 20,000 pinholes arranged in a series of nested spirals. The upper disc is a glass plate containing Fresnel microlenses on the upper surface that direct and focus light onto perfectly aligned 50 µm pinholes in the lower disc, the Nipkow disk, for transmission to the objective and specimen (Nipkow, 1984).

The excitation light passes through Fresnel microlenses of the first disk before passing through the pinholes of the Nipkow disk and entering the samples. The light emitted from the sample passes back through the confocal pinholes of the Nipkow disc, closer to the microscope port, and is directed *via* a dichromatic beam splitter to lens and the camera (Tanaami et al., 2002).

This specific architecture makes the confocal rotating disk microscopy capable of acquiring thin optical sections from specimens in a similar manner to CLSM, but much faster. Therefore, rotating disk microscopes are capable of imaging, in time, both thin and thick specimens, in 2D and 3D with a high spatial resolution. However, similarly to CLSM, spinning disk microscopy does not allow to image very deep in samples.

All of the microscopy techniques presented above display specific advantages and limitations. Thus, it is essential to choose which advantages and limits are within the scope of the experimental strategy. In other words, the choice of the microscope ultimately depends on the aims of the experiment. Needs can be summarized in three categories: (i) spatial resolution, which corresponds to the capacity of the microscope to separate two points on the specimen, (ii) temporal resolution, which corresponds to the image acquisition time of the microscopes and the frame rate of the camera, and (iii) the volume imaged, which corresponds to the number of slices required during the acquisition of a stack. Unfortunately for microscopists, no microscope combines these three characteristics and it is therefore necessary to choose which type of microscope best suits the experimental needs.

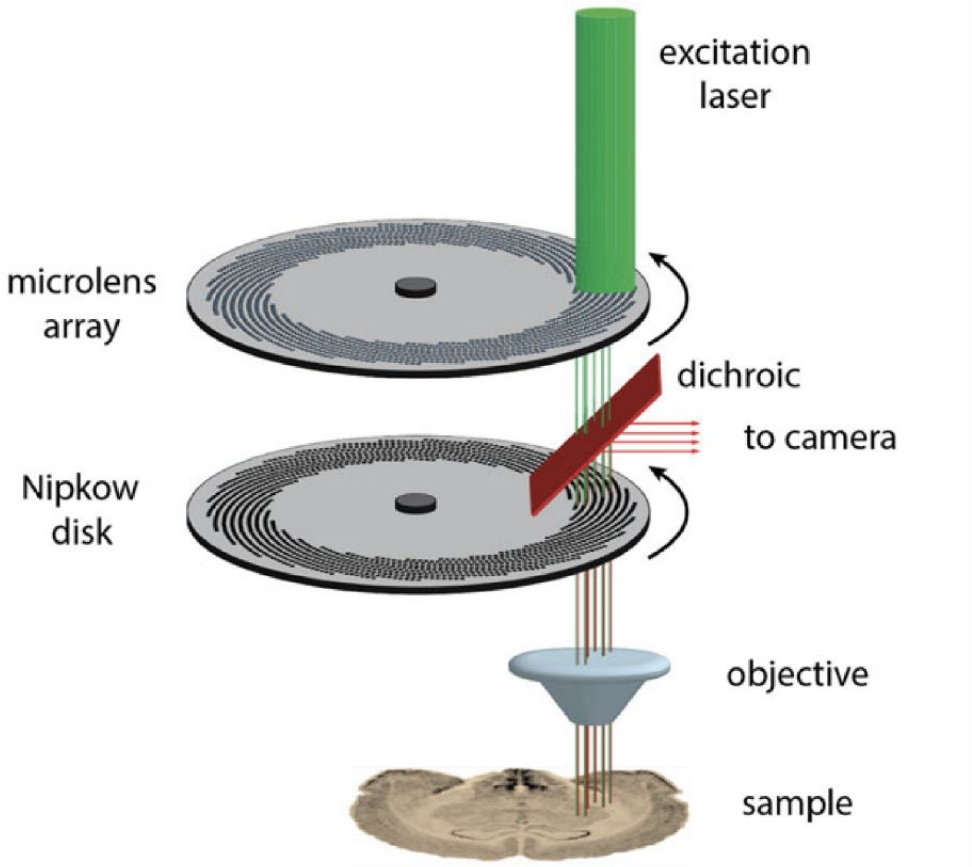

Figure 10: Spinning disk confocal microscopy

Schematic representation of a modern spinning disk confocal microscope. Laser excitation is delivered to the spinning disk unit through a fibre optic light guide, and is projected onto an array of microlenses. The separated beam then passes through a dichroic mirror and the aligned apertures of the spinning disk. Emitted signal passes back through the spinning disk, and is reflected off the dichroic to a CCD or CMOS camera (adapted from Bayguinov et al., 2018*)*

The question then arises as to what type of microscopy to use to generate a large image volume (several hundred slices) with a very high temporal resolution. Combining these two needs makes imaging more complicated.

2. Light Sheet Fluorescent Microscopy (LSFM)

The main feature of light sheet fluorescent microscopy (LSFM) is to combine two distinct light paths (Fig 11). One is the illumination path which creates the light sheet. The second is the fluorescence detection path which is perpendicular to the illumination path (Huisken, 2004).

Although the concept of using a sheet of light to make optical sections had already been reported in the beginning of the 20th century (Fig 11-A, Néculcéa, 1903), the selective plane illumination microscopy (SPIM) appeared in the field of life sciences in 2004 only (Huisken, 2004; Swoger et al., 2014). SPIM microscopy has proven to be a very powerful tool compared to confocal microscopy, especially for biologists imaging development and growth processes in 4D using genetically encoded fluorescent proteins (Prasher et al., 1992; Tsien, 2010). As reported earlier, CLSM displays indeed two main limitations: (i) insufficient penetration of excitation light, and (ii) low image acquisition speed. Spinning disk microscopy strongly improves the second drawback but not the first one. The volume, which can be of a few cubic millimeters, and the opacity of organisms often make high quality imaging of inner tissues difficult to generate. SPIM microscopy has filled this gap.

Various system designs are classified as LSFM (Fig 12). Although different from each other, they all share the same basic characteristics. The instantaneity of the optical sectioning is achieved by illuminating the sample with a light sheet and the fluorescence, generated in the thickness of this light sheet, is imaged with a high-speed camera (Waters and Wittmann, 2014). Specimens, which can be several millimetres thick, can easily be 3D reconstructed by rotating and imaging the samples from different angles (Preibisch et al., 2010; Waters and Wittmann, 2014). Phototoxicity in LSFM has been shown to be low even for long acquisition times or high laser power (Preibisch et al., 2010; Reynaud et al., 2008). Therefore, LSFM is a tool of choice for imaging rapid processes in sensitive samples such as embryos. LSFM has been widely used to image various model systems

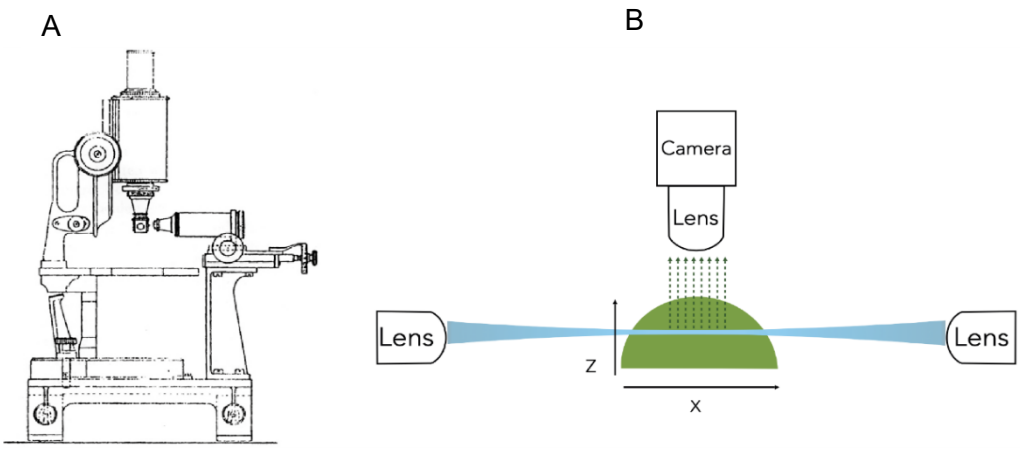

Figure 11: Basics about Light sheet fluorescence microcopy (LSFM)

A. *First apparition of orthogonal illumination in microscopy by Siedentopf and Zsigmondy's (1903). This represents the first conceptual approach of LSFM;* ***B.*** *LSFM principle with two illuminations. Sample (in green) is illuminated in the thickness of the light sheet (in blue). Photons of fluorescence (dotted line) are detected by an observation lens and a camera (sCMOS or CCD). The axial resolution is therefore linked to the thickness of the light sheet and just the part of the sample which is in the light sheet is illuminated.*

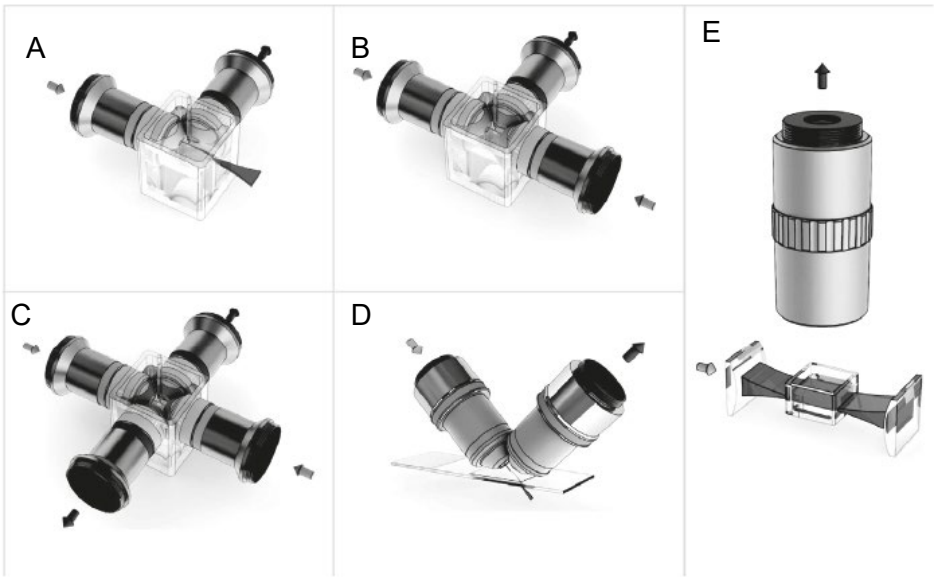

Figure 12: Light sheet fluorescence microcopy implementation

A. *Basic SPIM implementation with one illumination,* ***B.*** *Basic LSFM implementation with two illuminations C. Implementation with two illumination arms and two simultaneous detection units,* ***D.*** *Perpendicular 45° objective configuration (iSPIM) for slide-mounted samples* ***E.*** *Ultramicroscope with two illumination arms. This implementation is more a LSFM macroscope than a microscope. This ultramicroscope is more adapted for big and cleared sample like mouse brain. (adapted from Weber et al., 2014))*

such as zebrafish (arguably the most striking examples of LSFM 3D imaging (Ahrens et al., 2013; Daetwyler et al., 2019; Keller et al., 2008; Scherz et al., 2008; Swoger et al., 2011), fly embryos (Huisken, 2004; Tomer et al., 2012), spheroids (Lazzari et al., 2019; Lorenzo et al., 2011), *Caenorhabditis elegans* (Fickentscher et al., 2018, 2013; Fickentscher and Weiss, 2017), fixed mice embryos (Ichikawa et al., 2013; Wu et al., 2013), and plants (Berthet and Maizel, 2016; Maizel et al., 2011; Ovečka et al., 2015; Sena et al., 2011).

Because it offers the opportunity to address rapid biological phenomena, this technology might challenge some of the results obtained with other microscopy technologies (Ahrens et al., 2013; Krzic et al., 2012; Schmid et al., 2013). However, light sheet microscopy imposes, beyond the illumination itself, careful optimization of sample mounting and the processing of data.

2.1. Illumination

Contrary to single-lens microscopy that requires illumination of the entire specimen volume when imaging a single section, LSFM selectively illuminates the focal plane of the objective. This results in a strong reduction of the delivered energy, each plane being exposed only once during the acquisition procedure (Reynaud et al., 2008).The thickness of the sheet of light, usually of a few micrometers, defines the axial thickness of the illuminated section (Fig 11-B).

In addition, while the same lens is used for both illumination and detection in CSLM, illumination and detection use two different paths in LSFM. As a consequence, while the NA of the lens is the main limiting factor for the resolution in Z in CLSM (and should be as high as possible), the resolution in Z in LSFM only depends on the thickness of the light sheet produced the illumination lens, which are low NA lens. Thus the axial resolution is roughly the same for both high and low detection lens NA in LSFM. While the lateral resolution of LSFM is the same as that of the epifluorescence microscope, the axial resolution is much higher when using low magnification objectives since it only depends on the thickness of the light sheet. LSFM is therefore very useful for imaging large samples using long working distance and low magnification.

The organization of a light sheet microscope is different from more conventional microscopes but comparatively easy to conceptualize. The illumination path is broadly identical to that of epifluorescence microscopes: a detection objective collects light from illuminated focal plane, the fluorescence then passes through a filter and is detected by a camera (Fig 11-B). No dichroic

mirror is needed, as the excitation photons are not in the same path as the emission photons. Moreover, the illumination path, unlike confocal microscopy, generally consists of a coherent light source in the form of a sheet of light.

Similarly, to the other types of microscope, LSFM comes in a wide variety of implementations. Ideally, the microscope is built around the sample. This provides the best image quality and the optimal spatial and temporal resolution for imaging. Depending on the samples of interest, light sheet microscopes can be very different while sharing the same fundamental main components (Fig 12).

2.1.1. Generation of light sheet

There are two different types of light sheets: static light sheets, generated by cylindrical optics (Huisken, 2004), and light sheets generated by fast laser scanning (Keller et al., 2008). Both types of light sheets have advantages and disadvantages. The light sheet generated by laser scanning has more flexibility compared to the sheet of light generated by static light. The thickness of the light sheet generated by laser can be adjusted more easily. In addition, this type of illumination allows to use more particular techniques such as Bessel Beams, structured illumination, 2-photon excitation, and confocal line detection (Fahrbach et al., 2013; Keller et al., 2010; Planchon et al., 2011; Truong et al., 2011; Waters and Wittmann, 2014) . On the other hand, cylindrical optics make the light sheet much easier to generate. In addition, the entire FOV is illuminated at once which decreases the amount of energy applied to the sample and allows faster acquisitions (Fig 13-A).

2.1.2. Light sheet height

The sheet of light should cover the FOV as much as possible. In the case of a sheet of light generated by scanning, this height parameter can be easily adjusted by the scan amplitude. In the case of a static light sheet, this parameter is more difficult to change. The parameter of the optical path needs to be changed in order to modify the thickness of static Gaussian light sheet (Fig 13-A-B).

2.1.3. Light sheet thickness

The thickness of the sheet of light defines the resolution of the optical cross section and thus the axial resolution. The spread of the light sheet along the FOV is proportional to the thickness of the light sheet. The thinner the light sheet, the smaller the area containing this thin part. Conversely, the thicker the light sheet, the wider the area containing the thin part of the light sheet. A thin sheet of light will therefore be used for small FOVs, while a thicker sheet of light will be used for large FOVs. For example, a 1µm thick sheet of light will be used for a 60µm FOV, while a 6µm thick sheet of light will be used for a 600 µm FOV (Fig 11-B and Fig 13-A).

2.1.4. Position of the waist

Once the sheet of light is generated, it must be aligned with the focal plane of the detection lens. The waist must be found and then the sheet of light must be translated along the illumination axis so that the thinnest part of the sheet of light, the waist, is at the center of the FOV (Fig 13-D).

2.1.5. Focus

The sheet of light should illuminate the focal plane of the detection lens. The detection lens being fixed, the light sheet must be moved along the z-axis to match the focus of the detection lens. Fluorescent beads mixed with agarose are generally used to find the focal plane (Fig 13-E).

2.1.6. Tilted light sheet

The last step is to check that the sheet of light overlaps with the focal plane along the entire FOV. This step requires specific accessories such as a grid that can be moved along the illumination axis while remaining in the focal plane (Fig 13-F).

2.2. Detection

In LSFM, optical sections being uniformly generated by the light sheet, pinholes are not necessary to discriminate the illuminated focus plane and images are recorded in a single exposure. Each

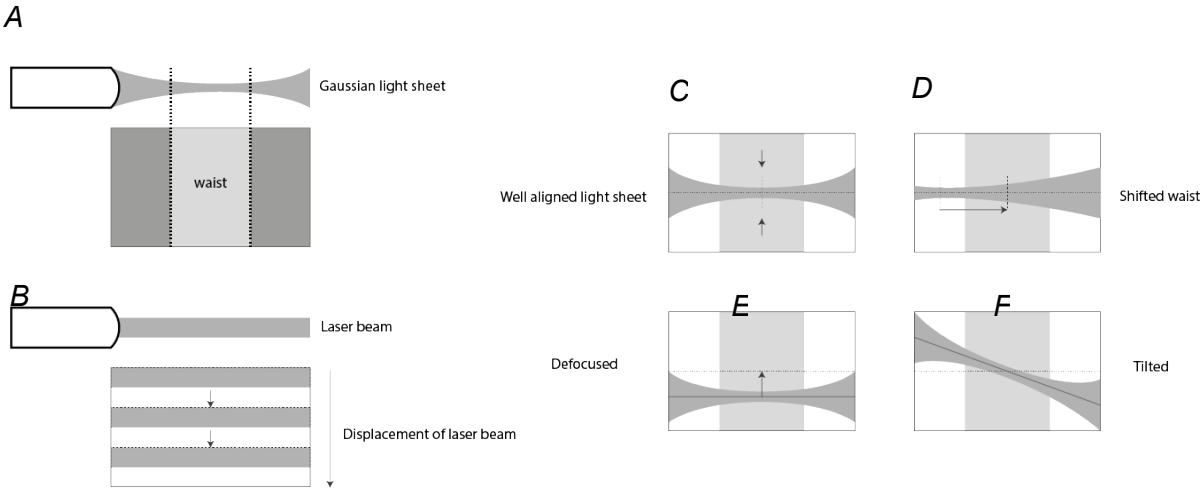

Figure 13: Light sheet setting

A. *Generation of the light sheet with cylindrical optics;* ***B.*** *Generation of the light sheet with laser scanning.* ***C-D-E-F.*** *Once generated, the light sheet is aligned to the focus of the observation lens (horizontal dotted lines) and the waist is moved to fit the Region Of Interest (ROI) of the sample (vertical grey area). Arrows represent how that sheet or the sample need to be moved. (adapted from Weber et al., 2014))*

pixel collects photons during the entire exposure time. Simultaneous recording of all pixels is very efficient and allows to keep the overall excitation intensity at a low level. The use of fast and sensitive cameras can generate large sets of images, faster than with any other techniques, with a high signal-to-noise ratio and minimal phototoxicity, i.e. with little to no impact on samples.

The opportunity to image relatively large samples with high spatial and temporal resolutions might generate very large amounts of data. More than with other microscopies, imaging parameters such as light sheet thickness, Z-pitch and axial resolution, exposure time, region of interest according to the FOV, laser power, camera frame rate, time lapse duration, number of angles for multi-view acquisition, need to be carefully optimized to reach the right balance between image quality and data size. For example, the thinner the light sheet, the better the axial resolution, and the number of sections needs to be high enough to fully image the sample.

The opportunity to rotate the sample gives an important advantage when samples are too thick to be imaged from one side. Multiview reconstructions strongly improve axial resolution by adding overlapping information from several images taken at different angles (Krzic et al., 2012; Preibisch et al., 2010; Schmid et al., 2013). However, optimizing the number of angles to properly image the sample is similarly necessary to avoid overproduction of data to process.

2.3. Use of LSFM

2.3.1. Orientation of the specimen

To generate two perpendicular light paths, LSFM are usually arranged horizontally with the specimen placed at the intersection of the illumination and detection objectives (Waters and Wittmann, 2014). The specimen is therefore mounted vertically in the microscope allowing its easy rotation and orientation. This specific organization allows multi-angle imaging (Fig 12-A-E).

Light sheet microscope is commonly used to image fixed and clarified (Huisken, 2004; Swoger et al., 2011). Nevertheless, due to its considerably reduced phototoxicity, its high acquisition speed and its sample orientation flexibility, it can be used in a relevant way to image living organisms such as cell colonies, tissues, whole animals or plants (Ichikawa et al., 2013; Maizel et al., 2011). Such samples require specific environmental conditions. Light sheet microscopes display the

advantage to be usually equipped with cuvettes in which the samples are immersed. It is thus rather easy to control the imaging conditions in order to follow living samples. All objectives and light paths are usually corrected to be effective at the refractive index of water. If not, this may cause absorption, scattering, and refraction of light, that all limit the penetration of the light sheet as well as its widening and alteration. This can then blur the images (out of focus) or cause scratches to appear on them. To improve the quality of the images, a second illumination arm can be implemented. This additional arm illuminates the sample in the same way as the first arm but from the opposite direction (Fig 12-B, Waters and Wittmann, 2014). The two sheets of light generated by the two illumination arms are aligned on the same plane, and then on the focal plane of the detection lens. These two illumination arms can be controlled separately so that they can be switched on alternatively or simultaneously. The parts of the samples corresponding to each illumination arm can then be assembled either directly by the hardware or in post-processing to generate an image of equal quality over the majority of the FOV. In addition, both illumination arms can be equipped with additional optics to rotate the sheet of light around the center of the FOV to generate more efficient illumination and make shadows to disappear (multidirectional, mSPIM, (Fig 12, Waters and Wittmann, 2014). Double illumination can also improve overall fluorescence excitation of fixed and clarified samples (Dodt et al., 2007; Ermolayev et al., 2009; Waters and Wittmann, 2014). For such samples, it is common to have vertical detection where it is therefore possible to image the samples from above (Fig 12-E). However, some samples, such as live embryos, may be opaque and impossible to image their full depth in a single view. To solve these problems, multi-angle acquisition can be used: the sample is rotated between each acquisition in order to merge all the images from each angle afterwards. This makes possible, on the one hand, to improve the image by adding additional data acquired from different angles and, on the other hand, to be able to merge overlapping data to have isotropic resolution (Fig 12-C, Swoger et al., 2014, 2007). To facilitate multi-angle imaging, in the case of horizontally organized microscopes, a second detector arm can be added (Fig 12-C). This allows the sample to be imaged simultaneously from the front and back. The main advantage is that the slices of each camera are de facto aligned. This can enable real-time image fusion (Krzic et al., 2012; Schmid et al., 2013). If rotation of the sample is not necessary or if the sample cannot be oriented, different types of illuminations can be implemented (e.g., iSPIM, Fig 12, Wu et al., 2013).

2.3.2. Mounting of samples

The mounting of samples is a crucial step when doing microscopy. The peculiar organization of light sheet microscopes requires specific sample preparation that is regularly different from what can be done in so-called conventional microscopes. Sample mounting depends on the nature of the specimen. For cell imaging, the mounting is quite similar to that in confocal microscope. The other kinds of sample imaging are generally done inside a tank meaning that the standard slide-coverslip assembly is not usable. Moreover, in the case of *in vivo* imaging, the samples must be mounted in cylindrical holders to be correctly oriented. The hole is filled with solid medium with enough nutriment for *in vivo* imaging. To make specimen mounting more flexible, different mounting strategies have been developed to address different biological questions (Kaufmann et al., 2012). Fixed samples and more especially of cleared samples are thus immersed in clearing medium suitable for observation. Clearing medium have the same refractive index than the cleared sample. Other, although rarer, techniques, such as ultramicroscopy allow the sample to be illuminated from outside the vessel and observed in the same arrangement as in a straight microscope or macroscopy (Fig 12-E, Dodt et al., 2007).

2.3.3. Some examples of LSFM imaging in animals

- **Drosophila**

The LSFM has been used to image Drosophila embryos *in toto* (Swoger et al., 2007). The implementation of specific protocols on open source systems has made possible to advance embryo imaging at the LSFM rapidly (Ejsmont et al., 2009). For instance, this allowed the tracking of gene expressions over time during Drosophila development. It also made possible to set up functional imaging of the nervous system of Drosophila embryos or cytoplasmic calcium flows (Lemon et al., 2015). The improved resolution of the light sheet devices allows the tracking of protein localization (Chen et al., 2014) and it also allows the monitoring of cell lines during development, which has provided quantitative data on gastrulation in 4D (Chhetri et al., 2015).

- **Caenorhabditis elegans**

Light sheet microscopy was used for mesoscopic imaging of the nematode (Rieckher et al., 2015). It was thus made possible to image the development of the nematode from the early stages to the

adult stage (Wu et al., 2011). In addition, the spatial dynamics of nuclei could be quantified as well as the dynamics of the developing membranes (Gao et al., 2012).

- **Zebra fish**

Larger vertebrate models have been imaged, such as Zebrafish. For instance, the development and function of the heart were detailed as well as the development of the nervous system (Arnaout et al., 2007; Mickoleit et al., 2014). Studies have been able to describe the development of the vascular system in the brain, the intestines and the eye (Alvers et al., 2014; Icha et al., 2016). On the other hand, rapid imaging has been set up to monitor calcium flow in the nervous system (Tomer et al., 2015).

2.3.4. Some examples of LSFM imaging in plants

In the last 10 years, LSFM has also reached the plant development community and, several studies, mostly in *Arabidopsis thaliana*, have been carried out using this microscopy (Berthet and Maizel, 2016; Vyplelová et al., 2017). The environmental conditions for *in vitro* imaging of *Arabidopsis* strongly differ from those for imaging animal models. Light, temperature, nutrient availability are obviously parameters to be taken into account. In contrast to most animal model systems, plants can grow at room temperature, in air and they only need water, salt and light. Yet, gravity is an important parameter to take into account when imaging plants because gravitropism affects the rate and direction of plant growth. The architecture of the inverted microscope is not adapted to plant imaging because it is difficult to mount the samples according to gravity. It is therefore impossible to follow the gravitational growth of plant organs. This is actually why certain teams working on roots have developed vertical confocal microscopes (von Wangenheim et al., 2017).

The horizontal architecture of the LSFM, like openSpim for example, is much more adapted to plant sample mounting and, even more to roots imaging. This allows the aerial organs to grow in the air while the roots develop in the medium (Fig 14-A, Ovečka et al., 2015). The injection of fresh liquid medium by a pump system and lighting of the leaves helps to maintain plants in a proper physiological state. It is an excellent method to study seed germination, seeds can be easily mounted in solidified agar-based media suitable for imaging. This facility mimics natural seed germination conditions. LSFM can be widely applied to reveal cell organization and developmental

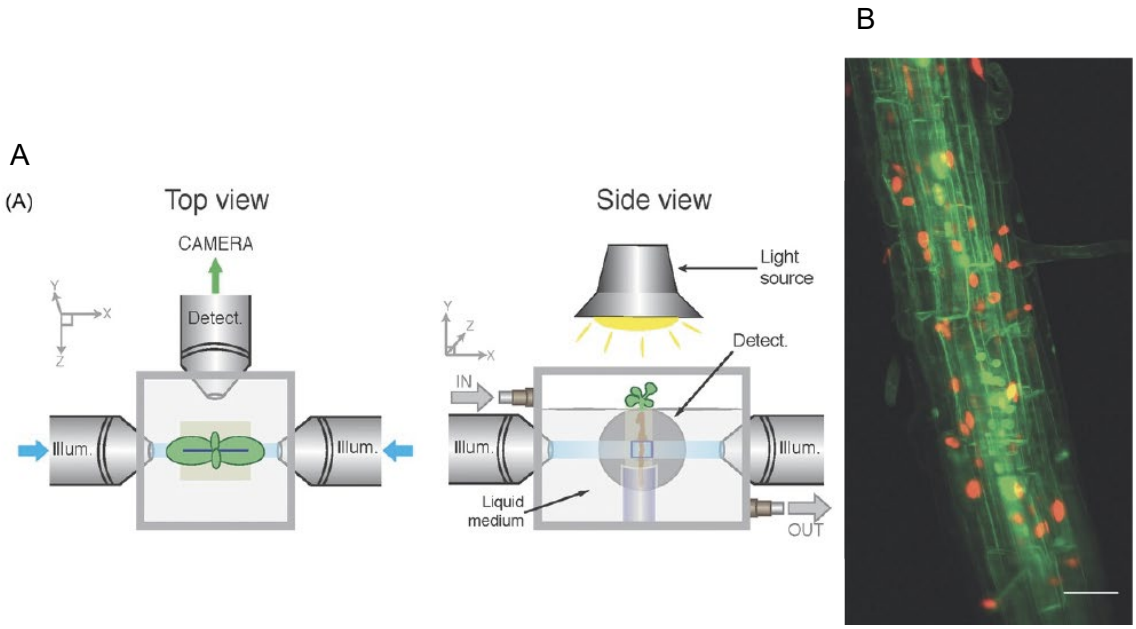

Figure 14: Light sheet fluorescence microcopy for root imaging

A. *Typical mounting for root imaging. A tank (grey square and rectangle) is filled with water, and the roots of seedlings directly grow in a capillary filled with medium. Observations can follow the gravitropism of plant growth;* ***B.*** *Example of a maximum-intensity projection of a stack acquired with a FSFM showed in A. Root of a 7-day-old Arabidopsis plant ubiquitously expressing a plasma membrane marker fused to GFP (Wave131Y, green), a nuclear marker (H2B-RFP, red) as well as a lateral root specific nuclear maker fused to GFP (green) (von Wangenheim et al., 2017). Scale bar is 50 µm.*

processes in primary and lateral roots as well as in the aerial parts of plants, such as hypocotyls, cotyledons, leaves and flowers (Fig 14-A-B, Ovečka et al., 2018).

- LSFM and root imaging

LSFM makes it much easier to image rapid root growth than other types of microscopy. Indeed the fast acquisition time of this microscopy allows it to follow the roots *in toto* over time (Maizel et al., 2011). It thus allows to quantify the long-term growth of primary roots, from germinating seed to root elongation in the adult plant in real time (Lucas et al., 2013). For instance, mitotic activity, growth rates and endosomal movement were quantified during lateral root formation (Fig 14-C, Delevoye et al., 2016). 4D imaging has made it possible to highlight the asynchronous development of the different layers of cells making up the lateral root. In addition, the LSFM could effectively record more rapid aspects of root growth, such as calcium oscillations or intermittent root hair growth. This also applies to specific molecular regulators. For instance, Smékalová et al. described the subcellular localization of the MPK6 kinase using LSFM.

- LSFM and aerial organs

When compared to roots, very few studies have been conducted to monitor plant aerial organ development using the LSFM technology. Some studies have shown that it was possible to image cotyledons, hypocotyls and sepals but only qualitatively (Ovečka et al., 2018). Moreover in the majority of the LSFM systems currently available, it was shown that aerial sample mounting could be difficult to set up (Ristova and Barbez, 2018). More recently, Valuchova et al. described flower germline differentiation in Arabidopsis using LSFM (Valuchova et al., 2020). This study showed the potential of LSFM to image large airborne organs and to monitor subcellular processes over time. Furthermore, the multi-angle reconstruction allowed to highlight the internal organization of this thick tissue. It should be however noticed that the samples were all embedded in agarose for imaging (Valuchova et al., 2020). Building on these pioneering data, one of the primary goals of my PhD was to set-up a robust LSFM-based protocol to image aerial organs, without embedding (see main objectives). In parallel, and to take advantage of the different imaging techniques described above, I developed a research project with two scientific questions: (i) in plant developmental biology, with a focus on meristem and floral determinacy, and (ii) in cell biology, with a focus on microtubule dynamics in relation to cell shape.

3. Developmental biology

Developmental biology is the study of all the processes leading to the building of a whole organism from a single zygote cell. These processes involve geometry, mechanics and biochemistry. All interact with each other to define the final shape, size and structural characteristics of organisms. Developmental biology can be addressed at various scales: molecular, cellular, tissular, organ and body scales. Because plant cells do not migrate, and because cell death is almost absent in very young plant tissues (except for vasculature differentiation), multicellular morphogenesis is much easier to analyze and formalize in plants than in animals.

The data reported in the following sections are mainly from the *Arabidopsis thaliana* model plant (Koornneef and Meinke, 2010; Van Norman and Benfey, 2009). A series of advantages make *Arabidopsis thaliana*, a small eudicot of the *Brassicaceae* family, of particular use: small and fully sequenced genome, small size, short life cycle, robust and easy transformation protocol, and last, but not least, large scientific community.

3.1. Indeterminate and adaptable development in plants

3.1.1. Basics on plant growth

Unlike animals, plants show the striking particularity to produce new organs throughout their lifespan (Fig 15-A). Indeed, embryogenesis in plants does not lead to the establishment of a reduced version of the adult organism, with most organs already present. Thus the seedling only contributes to a really minor part of the adult shape: plant development is largely post-embryonic and the adult body plan results from a continuous production of new organs. This ability to grow over a very long period of time allows plants to adapt their morphogenesis and architecture to their environment.

Establishment of the adult architecture results from the maintenance of populations of pluripotent stem cells that can self-renew and produce differentiated cells that ultimately produce new organs in the form of roots, leaves, stem and flowers (Fig 15-A-B). These stem cells are located in primary meristems. Two kinds of meristems allow the plant to grow in polar directions throughout its lifespan. The root apical meristem (RAM), located at the root tip, generates the underground part of the plant,

i.e. the root system, whereas the shoot apical meristem (SAM), located at the plant apex, produces all aerial organs, i.e. the stems, leaves and flowers (Fig 15-F). Thus, meristems accomplish two functions: they continuously generate new cells to form new organs, but also to self-maintain.

The aerial part of the plant can be divided into iterated modules, or phytomers, which are regularly produced by the SAM. Each phytomer contains a leaf, an axillary meristem at the base of the leaf, and a subtending internode. There are two phases during plant development: a vegetative phase, during which the SAM initiates axillary (vegetative) meristems and leaves, and a reproductive phase, during which the SAM shifts identity to become an inflorescence meristem (IM) that produces flower meristem (FM) and leaves called bracts. Some plants, including *Arabidopsis thaliana*, do not initiate bracts (or form the so-called cryptic bracts, since mutants, such as *puchi*, can make them re-appear (Karim et al., 2009) FMs in turn generate the flowers, i.e. a set of 4 floral organs: sepals, petals, and reproductive organs: stamens and carpels (Fig 15-E-G).

SAMs and IMs only differ by the identity of the organs they generate. Both are located at the apex of the plant stem and both are maintained throughout the life of the plant. Conversely, FMs allow the placement of a set number and type of floral organs. Once this number of organs is reached, the FM becomes inactive. FMs are thus determinate (Fig 15-F).

3.1.2. The SAM, an organized tissue

The cellular organization of the SAM is very ordered. It is composed of three distinct layers of cells. Layer L1 constitutes the epidermis of the meristem. Layer L2 is the sub-epidermal layer. L1 and L2 display a stereotypical organization with cells that divide only in an anticlinal manner. Layer L3, deeper down, corresponds to the body of the meristem. The cell organization is less stereotyped there, with cells dividing along less ordered axes. The floral meristems are organized similarly to the SAM (Bowman and Eshed, 2000; Jenik and Irish, 2000; D. Reinhardt et al., 2003; Satina et al., 1940; Satina and Blakeslee, 1941).

In addition to this organization in layers, meristems also display a radial organization which has different functions in the meristem (Bowman and Eshed, 2000; Laufs et al., 1998; D. Reinhardt et al., 2003). The central zone (CZ) is located at the center of the meristem and includes cells of L1 and L2 and very few of L3 (Fig 16-B). This zone contains the undifferentiated stem cells which display the lowest rate of cell proliferation. After division, the cells are pushed into a zone outside the central

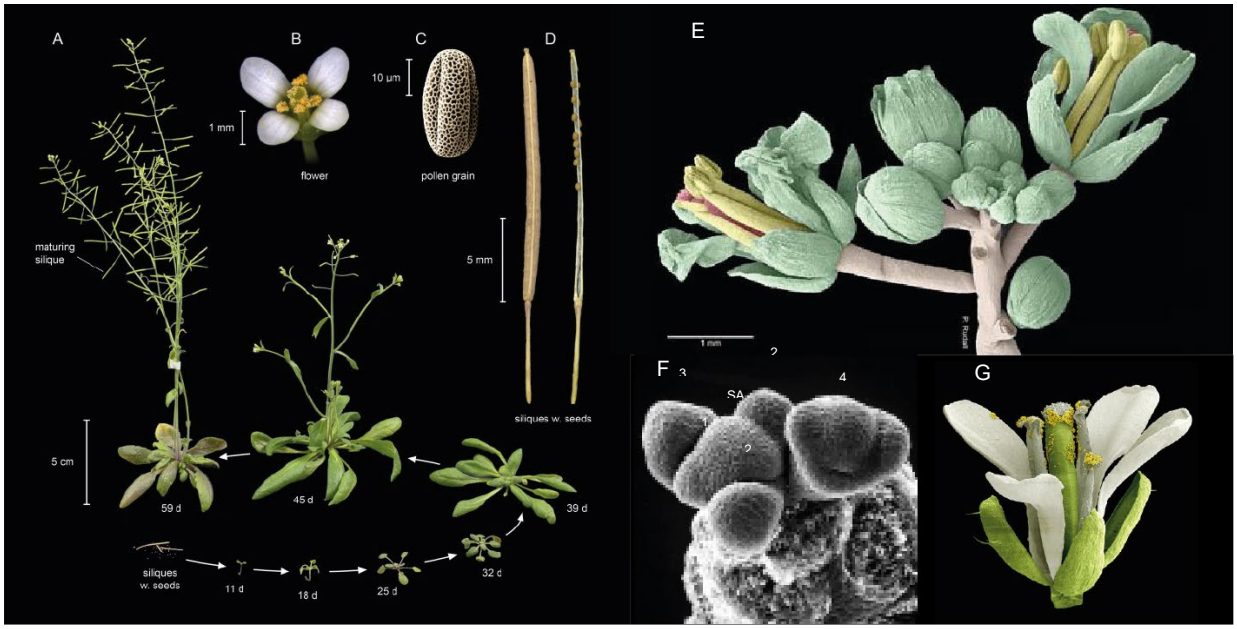

Figure 15: Life cycle of Arabidopsis thaliana

A. *Global life cycle of A. thaliana starting from the seeds to plant with mature silique. The cycle can be dividing in two part. The firts one is the vegetative stage where the plant only produces leaves. The second is the reproductive stage where the plant produces stems and flowers;* ***B.*** *Typical Arabidopsis thaliana flower;* ***C.*** *One pollen grain;* ***D.*** *Mature silique with seeds inside;* ***E.*** *Apex with flowers at various stages of development observed in scanning electron microscope. False colorization shows the stem in gray, petals and sepals in green, stamens in yellow and carpels in red;* ***F.*** *Dissected apex observed in scanning electron microscope with the shoot apical meristem (SAM) at the center and flower meristems at different stages at the periphery (stages are written on flower mersitems);* ***G.*** *Typical A.thaliana flower observed in scanning electron microscope. False colorization shows the sepals in green, the petals in white, the stamens in gray and yellow and the carpels in green (Krämer, 2015))*

zone, which is called the peripheral zone (PZ). It is in this area that the cells become competent to form lateral organs initiating from primordia (Fig 16-B). PZ cells display the highest rate of cell proliferation, particularly in nascent primordia. Immediately below the central zone, a pool of cells, which will be called the organizing center (OC), participates in the activation and maintenance of the stem cells (Laux, 2003; Laux et al., 1996; Mayer et al., 1998). This organization in zones matches the two main functions of the SAM: self-maintenance (CZ and OC) and organogenesis (PZ).

3.1.3. Iterative production of lateral organs

The SAM sequentially produces lateral organs (leaves and axillary meristems or bracts and FM) with a stereotyped and predictable pattern. The resulting spatial position of organs is called phyllotaxis.

Like most angiosperms, *Arabidopsis thaliana* displays a spiral phyllotaxis and the angle between two consecutive primordia is around 137.5 degrees on average (Kuhlemeier, 2007; Kuhlemeier and Reinhardt, 2001). The local accumulation of the plant hormone auxin in the PZ induces primordia initiation (Heisler et al., 2005; Didier Reinhardt et al., 2003; Reinhardt et al., 2000; Vernoux et al., 2000). Furthermore, because this local accumulation of auxin involves an active and polar transport of auxin towards the emerging primordium, this is also accompanied by a depletion of auxin around organs, generating inhibitory fields that prevent primordia formation in the vicinity of newly formed organs. Such inhibitory fields largely explains the phyllotactic patterns (de Reuille et al., 2006; Jonsson et al., 2006; Didier Reinhardt et al., 2003; Smith et al., 2006). In addition to spatial positioning, the temporal sequence of organ initiation, called the plastochrone, also contributes to the robustness of phyllotaxis. Recently, cytokinin signalling has been shown to contribute to plastochrone definition and thus to the spatio-temporal sequence of organ initiation (Besnard et al., 2014).

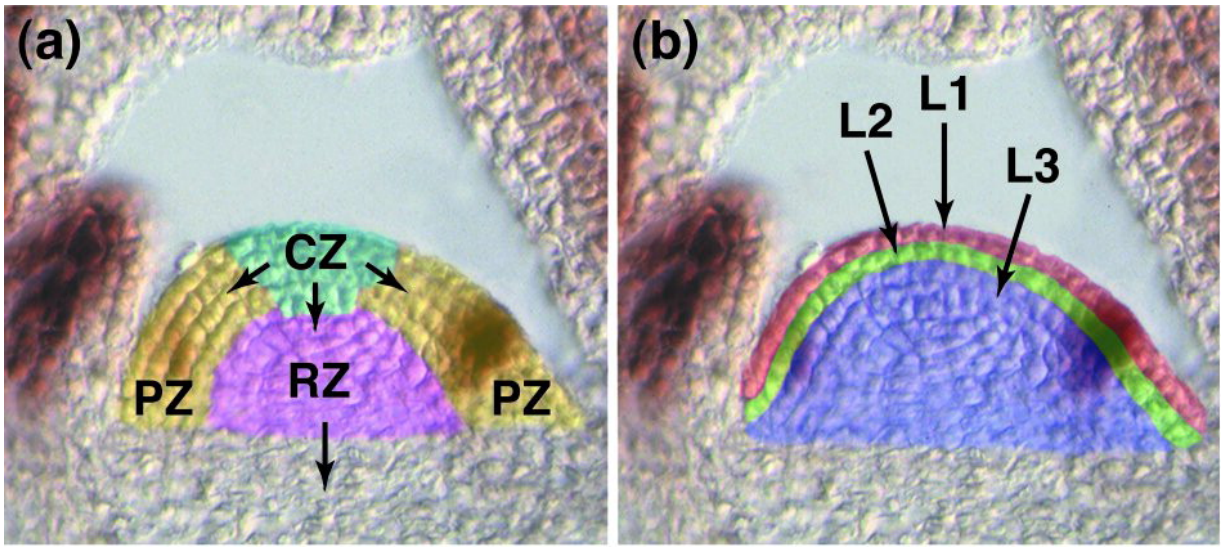

Figure 16: Spatial organization of SAM

A. *The SAM is organized in different circular zones. Cells in green represent the central zone (CZ) these cells are surrounded by cells of the peripheral zone (PZ) in yellow (Bowman and Eshed, 2000). CZ contains the stem cells which maintain the integrity of the SAM. The PZ produces the lateral organs. Cells in violet correspond to the rib zone (RZ);* ***B.*** *The SAM is also organized in layers. The epidermal layer (L1) the sub-epidermal layer (L2) are collectively referred to as the tunica. Cells interior to the L2 form the corpus (L3).*

3.2. Molecular control of stem cell maintenance at the Shoot Apical Meristem (SAM)

The SAM can be divided in different sub regions, based on morphology and division rates. This organization is also marked by distinct genetic regulators. Here I focus on the genetic bases of stem cell maintenance at the SAM.

3.2.1. The CLAVATA/CORYNE/RPK2 pathways restrict the size of the stem cell population

A first series of mutants causing a similar phenotype - both larger and higher SAMs - have been isolated from the 1990s. Genes involved are mainly (i) the genes of the *CLAVATA* (*CLV*) family, made of three members: *CLV1*, *CLV2* and *CLV3*, (ii) *CORYNE* (*CRN*) and, (iii) *RECEPTOR-LIKE PROTEIN KINASE 2* (*RPK2*) (Clark et al., 1995, 1993; Kayes and Clark, 1998; Kinoshita et al., 2010; Muller et al., 2008).

- CLV1, *CLV2, CLV3, CRN* and *RPK2* are in the same genetic pathway

CLV1 encodes a receptor-like kinase (RLK), with extracellular leucine-rich repeats (LRRs), a single transmembrane domain, and an intracellular serine threonine kinase domain, and is specifically expressed in the L3 at the center of the SAM and FM (Clark et al., 1997). *CLV2* encodes another LRR receptor-like protein (RLP), similar to *CLV1*, but it lacks an intracellular kinase domain and is ubiquitously expressed (Clark et al., 1997). Interestingly, *CRN* encodes a protein with an intracellular kinase domain and a transmembrane domain, but lacking the LRR extracellular domain ((Muller et al., 2008). CRN was thus proposed to associate with CLV2 to rebuild a complete and functional RLK (Bleckmann et al., 2010; Muller et al., 2008). *CLV2* and *CRN* are expressed ubiquitously. In fact, the *crn* and *clv2* phenotypes are not restricted to an enlargement of the meristems (Jeong et al., 1999; Muller et al., 2008). *CLV3* is specifically expressed in the L1, L2, and a few L3 cells of the CZ (Fletcher et al., 1999). *CLV3* encodes 96-amino-acid peptide subsequently cleaved into a 12-13-amino-acid peptide then arabinosylated and secreted to localize to the apoplast (Clark et al., 1995; Fletcher et al., 1999; Kondo et al., 2006; Lenhard and Laux, 2003; Ohyama et al., 2009; Rojo et al.,

2002). CLV3 moves laterally and downwards in the SAM to directly bind CLV1 (Lenhard and Laux, 2003; Ohyama et al., 2009). Such binding triggers the signalling pathway through the recruitment of phosphatase and Rho GTPase (Trotochaud et al., 1999).

Although not formally demonstrated, it is now admitted that CLV3 signals through the wo distinct complexes, one formed by two CLV1 receptors and one formed by two CLV2 receptors and two CRN kinases, to activate the CLV-mediated signaling pathway (Muller et al., 2008). More recently, CLV3, was shown to signal in parallel through another receptor-like kinase, RPK2 (Kinoshita et al., 2010).

- The CLV/CRN/RPK2 pathways restrict the size of the central zone

CLV3 mRNA expression domain is laterally expanded in *clv*, *crn* and *rpk2* mutants (Fletcher et al., 1999; Kinoshita et al., 2010; Muller et al., 2008). *CLV3* mRNA expression being restricted to stem cells in the CZ, it has been hypothesized that enlargement of its expression domain in *clv/crn/rpk2* mutants could be an indirect effect of an enlargement of the CZ. Consistent with this hypothesis, the rate of cell proliferation within *clv* mutant SAMs does not increase while moving away from the center of the meristem contrary to what happens in the wild type when passing from the CZ to the PZ (Laufs et al., 1998). But this hypothesis was fully confirmed by the use of inducible *CLV3* RNAi lines also expressing a *pCLV3::GFP* reporter gene (Reddy and Meyerowitz, 2005) . The data showed that disrupting the CLV signaling pathway causes an enlargement of the CZ which precedes that of the whole SAM. Cells from the PZ start expressing the *pCLV::GFP* reporter gene, showing that their identity shifts towards CZ cell identity.

Thus, CLV/CRN/RPK2 act in the same developmental pathways to restrict the size of the CZ by preventing cells from the surrounding PZ to behave as CZ stem cells.

3.2.2. *WUSHEL* (*WUS*) promotes stem cell maintenance

Plants mutant for the *WUSHEL* (*WUS*) gene exhibit a phenotype roughly opposite to that of the *clv/crn/rpk2* mutants (Laux et al., 1996). *wus* mutant SAMs indeed exhibit small, aberrant, flat, apex that initiate a limited number of leaf primordia and axillary meristems. Axillary meristems eventually develop at the base of the leaves and produce a few primordia before stopping. While functioning, these SAMs and axillary meristems look normal, but quickly become flat as their cells differentiate. This “stop and go” growth pattern is maintained after bolting and results in highly branched plants. *wus* meristem are deficient and fail to self-maintain (Laux et al., 1996).Thus *WUS* is necessary for SAM maintenance, but it is not required for SAM initiation (Fig. 17).

WUS encodes a nuclear homeodomain transcription factor that defines a new family of homeodomain genes, the WUS-homeobox (WOX) family conserved during evolution (Costanzo et al., 2014; Mayer et al., 1998; van der Graaff et al., 2009; Wu et al., 2019). *WUS* is specifically expressed in the center of the SAM and FM, in a domain, referred to as the organizing center (OC), located immediately underneath the CZ (Baurle and Laux, 2005; Mayer et al., 1998). The lack of SAM maintenance in *wus* mutant plants thus results from the failure to specify stem cells, which are required to repopulate the PZ, whose cells are regularly incorporated in developing organ primordia.

3.2.3. CLV/WUS loop maintains stem cell homeostasis

The SAM experiences a balance between indeterminate growth at its center coupled with a production of lateral organs at its periphery. The maintenance of a stem cell niche in the CZ, which size is constant, is regulated by a feedback loop between CLAVATA3 (in the CZ) and WUSHEL (originating from the OC, which size is also constant) (Brand et al., 2000; Schoof et al., 2000). A series of experimental data illustrate this molecular relationship. First, *clv wus* double mutant plants are similar to *wus* single mutants showing that *WUS* is necessary for the enlargement of the CZ in *clv* mutant meristems. Indeed, *WUS* mRNA expression pattern is enlarged in *clv* mutants (Schoof et al., 2000). Enlargement of the *WUS* expression domain is thus sufficient to cause defects similar to that of *clv* mutants (Schoof et al., 2000). And conversely, *CLV3* over-expressing lines phenocopy *wus* mutant plants (Brand et al., 2000).

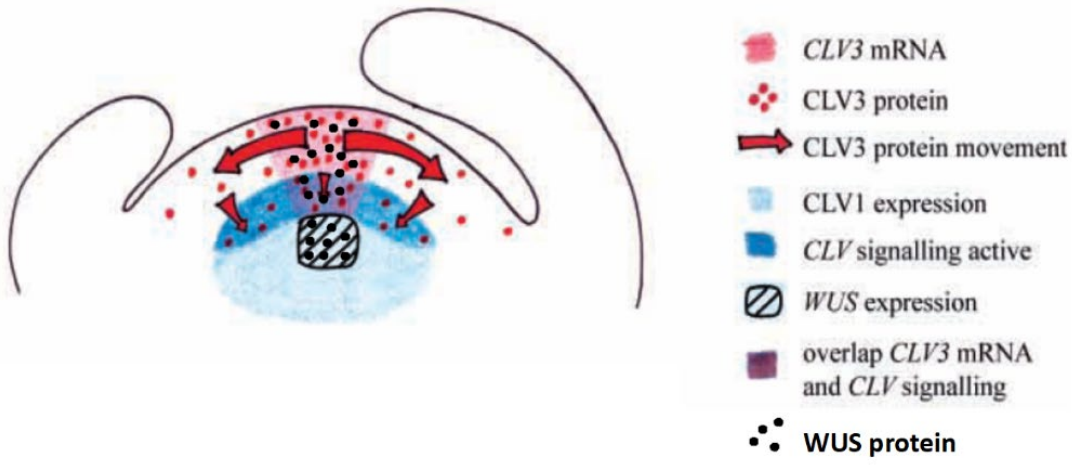

Figure 17: Spatial regulation of the CLV/WUS regulatory loop

CLV3 is expressed in the central zone (red area). The CLV3 protein then moves laterally and downwards in the shoot apical meristem. CLV 3 peptide interactes with CLV1 receptor kinase. This pathway restricts the expression of WUS to the organizing center (blach hatched area). The WUS protein (black point) moves upwards to trigger a CS identity to the CZ cells and to directly induce CLV3 expression.(Lenhard and Laux, 2003)

Interestingly, *WUS* expression domain and stem cell domain expressing *CLV3* do not coincide within the SAM nor the FM, suggesting a non-cell-autonomous function of WUS. WUS protein indeed moves upwards to the CZ through cell-cell symplastic channels called plasmodesmata (Daum et al., 2014; Yadav et al., 2011). In the CZ, WUS, on the one hand, induces a stem cell identity to those cells and, on the other hand, induce *CLV3* expression by directly binding to the *CLV3* regulatory sequences as monomers (Perales et al., 2016; Yadav et al., 2011).

However, *CLV3* expression is not only controlled by WUS, but also by SHOOTMERISTEMLESS (STM). *stm* mutant plants do not develop functional SAM (Barton and Poethig, 1993)(Fig. 18). *STM* encodes a Homeo-Domain Transcription Factor specifically expressed in the SAM (Long et al., 1996; Long and Barton, 1998). Previous data indicated that *STM* promotes stem cell identity by positively regulating *WUS* and also contributing to the full expression level of *CLV3* independently of *WUS* (Clark et al., 1996; Endrizzi et al., 1996; Gallois et al., 2002; Lenhard et al., 2002). It was very recently shown that STM indeed binds the CLV3 regulatory sequences but also interacts directly with WUS (Su et al., 2020). Such an interaction facilitates WUS binding to the *CLV3* promoter to sufficiently induce *CLV3* expression. In turn, as reported above, CLV3, as a secreted glycopeptide, diffuses to bind CLV1 and trigger the CLV signaling pathway. This activation results in the restriction of *WUS* expression through a quite poorly deciphered pathway that includes *POLTERGEIST* and *POLTERGEIST-LIKE1* genes, two phosphatases 2C able to activate *WUS* transcription (Song et al., 2006; Song and Clark, 2005; Yu et al., 2003, 2003, 2000).

Interestingly, the dynamic response to a change in *CLV* signaling is extremely quick. Induction of a strong increase in *CLV3* level is followed within 3 hours by a strong decrease in *WUS* and *CLV3* endogenous mRNAs (Muller et al., 2006). Two models have been proposed to explain why CLV3 does not display a long range spread and never enters the OC, which would result in a constitutive down-regulation of WUS expression. The first one proposes that the diffusion of CLV3 is limited by binding to its receptor CLV1(Lenhard and Laux, 2003) (sequestration theory) while the second one proposes that CLV3 diffuses broadly, but triggers CLV1 trafficking to the lytic vacuoles thus downregulating the amount of plasma membrane-localized CLV1 and therefore buffering the CLV3 signaling(Nimchuk et al., 2011). Furthermore, WUS itself negatively regulates *CLV1* expression in the OC (Busch et al., 2010).

Two major questions remain: Why *is CLV3* induced only in the CZ while the WUS protein is present both in the CZ and OC? Why does the WUS protein only move upwards? It was first reported that WUS binds *CLV3* regulatory elements in the OC only as homodimers thus resulting in the inhibition

of *CLV3* expression (Perales et al., 2016). More recent data suggest that the HAIRY MERISTEM (HAM) family proteins could also be involved in this regulation. *HAM* genes encode GRAS-domain transcription factors (Engstrom et al., 2011; Stuurman et al., 2002; Tian et al., 2004) that are expressed in the basal part of the SAM (Engstrom et al., 2011; Zhou et al., 2018, 2015) (L3). Expression of *HAM* genes thus overlap *WUS* expression and are complementary to *CLV3* expression along the apico-basal axis. Functional characterization of HAM proteins showed that HAM physically interacts with WUS and prevents the activation of CLV3 expression by WUS in the OC (Zhou et al., 2018, 2015). Accordingly, in the absence of the HAM family activity, the CLV3 expression expands into the lower part of the SAM. Thus, WUS' interaction with HAM prevents *CLV3* expression in the OC while its interaction with STM facilitates *CLV3* expression in the CZ. Interestingly, a number of data suggest that HAM interaction WUS may also inhibit WUS movement in all directions, although no formal proof for this has been reported so far.

3.2.4. Other regulators of *WUS* expression

- Repressors

The CLV pathway has a central role in controlling *WUS* expression. However, several other factors have been reported to control stem cell maintenance and/or to restrict OC size, i.e. *WUS* expression domain. These regulators seem to act through *CLV* independent pathways. Here is a non-exhaustive list of additional regulators identified so far.

HANABA TARANU (*HAN*). HAN encodes a GATA transcription factor, and is expressed (among other places) in the center of the meristems. *han* mutants exhibit smaller, flatter SAMs than wild-type plants, with an enlarged, but often diffuse expression of *WUS* (Zhao et al., 2004)

ULTRAPETALA1 (ULT1) and *ULTRAPETALA2* (*ULT2*). *ULT1* and *ULT2* encode putative SAND-domain transcriptional regulators (Carles et al., 2005). *ult1* displays an enlarged SAM similar to that of *clv* mutants, associated with an enlargement of *WUS*, *CLV1* and *CLV3* expression domains, suggesting that ULT1, like the CLV pathway, acts to restrict the size of the OC (Carles et al., 2004; Fletcher, 2001; Monfared et al., 2013).

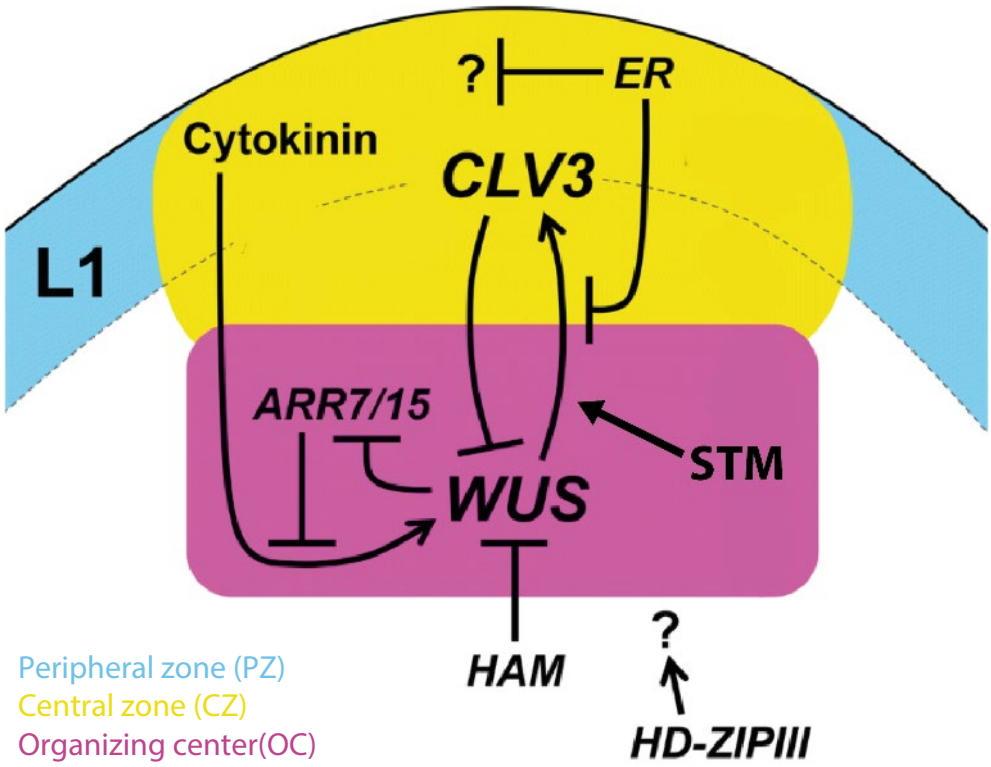

Figure 18: Key regulator of stem cells.

Pathways involved in intercellular communication between tissue layers in the SAM. Yellow indicates the central zone composed of stem cells expressing CLV3. Magenta indicates the organizing center defined by WUS expression. Light blue shows the epidermal L1 layer. Please see main text for further details about each of the factors and pathways. (Adapted from Uchida and Torii, 2019)

Three members of the class III of homeodomain leucine zipper (HD-ZIP III) family of transcription factors, *PHABULOSA* (*PHB*), *PHAVOLUTA* (*PHV*) and *CORONA* (*CNA*), are collectively required to restrict SAM size (Green et al., 2005; Prigge et al., 2005; Williams et al., 2005). Although SAM developmental defects observed in various mutant backgrounds were shown to be due to an increase in *WUS* expression both quantitatively and spatially, suggesting that *PHB*, *PHV* and *CNA* act to restrict the size of the OC (Williams et al., 2005, 2005), more recent data reported that these HD-ZIP III genes allow stem cell recovery even in *wus* mutant background (Huang et al., 2015; Lee and Clark, 2015; Mandel et al., 2016). Similar conclusions were raised with the ERECTA (ER) LRR-RLK, a regulator of many aspects of plant development including meristem size (Mandel et al., 2014; Shpak, 2013). Indeed, recent data reported that the ER genes regulate meristem development in a *WUS*- and *CLV*-independent pathways and through very different mechanisms (Kimura et al., 2018; Mandel et al., 2016). Nevertheless, it was even more recently reported that ER signaling might also directly restrict both CLV3 and WUS expression in the SAM (Zhang et al., 2021). This illustrates the complexity of stem cell regulatory networks and highlights a WUS-dependent and a WUS-independent pathway.

- Activators

STIMPY/WOX9 (*STIP*) is required for SAM growth and positively regulates *WUS* expression in the OC (Wu et al., 2005). Interestingly, *stip* mutant phenotype can be fully rescued by adding sucrose, thus illustrating how nutrients can influence meristematic activity, a research area which is still largely understudied in plant developmental biology (Landrein et al., 2018).

APETALA2 (*AP2*), which encodes a transcription factor required for normal flower development (Jofuku et al., 1994), was also shown to promote stem cell identity by positively regulating *WUS*, either independently of the CLV pathway (Huang et al., 2017; Zhao et al., 2007) or by inhibiting CLV signaling (Wurschum et al., 2006).

Mutations in *SPLAYED* (*SYD*) cause a premature termination of the SAM associated with a strong reduction of *WUS*. *SYD* encodes a chromatin-remodeling ATPase that directly binds to the proximal

promoter region of *WUS*, and likely maintains the chromatin in an accessible state, thus facilitating *WUS* transcription to take place (Kwon et al., 2005).

Finally, the hormone cytokinins have also been shown to be essential for modulating the expression of *WUS* in the OC and thereby the specification of stem cell fate (Chickarmane et al., 2012; Gordon et al., 2009). The Cytokinin regulatory network is quite complex in SAM. The current model proposes that active cytokinin molecules are produced in the L1 and move downwards to promote primary cytokinin responses in the OC resulting in the induction of *WUS* expression (Gruel et al., 2016; Snipes et al., 2018; Zuercher et al., 2013). Interestingly, activation of *WUS* expression by cytokinin correlates with modifications of chromatin marks (Wang et al., 2017). In turn, WUS promotes stem cell fate by increasing cytokinin response within the OC through the repression *ARABIDOPSIS RESPONSE REGULATORS (ARRs)* (Leibfried et al., 2005)*(Fig.18)*. Interestingly, cytokinin was also shown to mediate stem cell activation and homeostasis in response to a number of external signals such as light intensity, sugar or nitrate availability (Carabelli et al., 2007; Landrein et al., 2018; Pfeiffer et al., 2016; Yoshida et al., 2011). However, these cytokinin signaling pathways act in parallel to the TARGET OF RAPAMYCIN (TOR) kinase pathway (Pfeiffer et al., 2016).

WUS expression and stem cell homeostasis are therefore regulated through multiple signals, genes and pathways that all together robustly maintain and confine the stem cell niche before flowers are produced.

3.3. From SAM to flower meristems (FM) and flowers

3.3.1. FM identity versus SAM identity

Flowers develop from floral meristems (FM) produced on the flank of an inflorescence meristem (IM or reproductive SAM, Fig 15-F). FM identity is promoted by the expression throughout the FM of a set of transcription factors referred to as FM identity genes, the most important being *LEAFY* (*LFY*, (Parcy et al., 2002, 1998; Weigel et al., 1992), and *APETALA1* (*AP1*, (Mandel and Yanofsky, 1995). The FM differs from the SAM in three ways: (i) the identity of the organs they produce, (ii) the

phyllotaxis with which these organs are initiated and (iii) the lifespan of the stem cell population in their center.

In *Arabidopsis* the FM produces 4 different types of floral organs: 4 sepals and 4 petals, which are sterile and collectively referred to as perianth, and 6 stamens and 2 carpels, the male and female reproductive organs of the flower, respectively (Fig 15-E-G). The two carpels congenitally fuse during their development to produce the gynœcium. These organs are organized on four concentric rings, or whorls. Thus phyllotaxis is not spiral, but verticillate. Finally, whereas the SAM keeps producing new organs throughout the life of the plant, stem cell maintenance is disrupted in the center of the FM once all floral organs have been initiated. Therefore, contrary to that of the SAM, the FM growth pattern is determinate.

The morphological developmental process of the FMs has been much studied over the last thirty years (Smyth et al, 1990). In *Arabidopsis*, FM development has been divided into 20 stages, starting from the emergence of the FM at the flank of the IM, still fused with it and corresponding to only a small, inconspicuous outgrowth (stage 1), up to seed dispersal (stage 20). FIGURE 19 illustrates some of the FM developmental stages.

Floral meristem has an organization close to the SAM an organizing center and a central area containing the stem cells. In the same way as for the SAM the *CLV-WUS* loop maintains a pool of stem cells during the whole flower morphogenesis.

3.3.2. The ABCE model: specification of floral organs identity

Flower development is stereotypical, i.e. organs develop on successive whorls that consistently show the same identity sequence: sepals, petals, stamen and carpels that produce the gynoecium; The number and shape of each type of organ are furthermore identical in all individuals of a given species (note that stamens are dimorphic in Arabidopsis thaliana). Based on that observation, a series of mutations causing homeotic transformations of floral organs have been isolated. Four classes of genes, expressed in specific but overlapping FM domains, have been shown to specify in combination the identity of the all four newly developed types of organs. This resulted in the so-

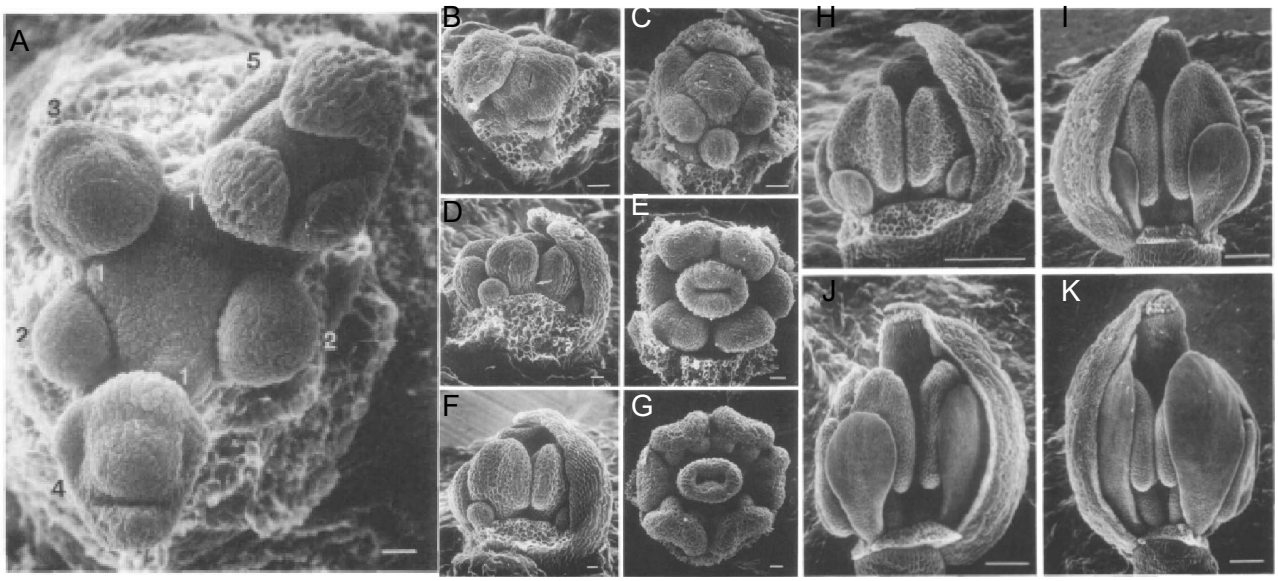

Figure 19: Scanning Electron Micrographs of developing flower mersitems (FM) and flowers of Arabidopsis

A. *Top view of an inflorescence showing the first four stages of FM development;* ***B.*** *FM at stage 5 in which a medial and lateral sepal have been removed;* ***C.*** *Lateral view of a flower bud at stage 6 in which the sepals had fully enclosed the bud;* ***D.*** *Medial view of a flower bud at stage 7 showing that the long stamen primordia are now constricted toward their base;* ***E.*** *Top view of a stage-7 flower bud;* ***F.*** *A flower bud at stage 8 in which the stamen primordia have increased markedly in size, especially in relation to the petal primordia;* ***G.*** *Top view of a stage-8 flower bud in which locules are now clearly visible in the stamens;* ***H.*** *A flower bud at early in stage 9 showing that the petal primordia have become wider toward the top as they start growing rapidly;* ***I.*** *A flower bud in which the petals have just reached the height of the lateral (short) stamens, marking the beginning of stage 10;* ***J.*** *Stigmatic papillae appear on the top of the gynoecium at the start of stage 11;* ***K.*** *Stage 12 is the final stage before the flower opens. It starts when the petals reach the height of the long stamens. (Adapted from Smyth et al., 1990)*

called ABCE model (Bowman et al., 1991; Coen and Meyerowitz, 1991; Ditta et al., 2004; Theissen and Saedler, 2001).

APETALA2 (*AP2*) was assigned to the class A. Mutations in *AP2* cause transformations of sepals into carpelloid leaves, and petals into stamens (Fig 20, Fig 21-B, Fig 22, (Bowman et al., 1991).

AP2 encodes a transcription factor form the AP2 plant-specific protein family which is characterized by the presence of a AP2/ERF DNA-binding domain (Riechmann and Meyerowitz, 1998). *AP2* is expressed in all four types of floral organ (Jofuku et al., 1994). However, its translation is repressed by the miR172 miRNA family in whorls 3 and 4 (Aukerman and Sakai, 2003; Chen, 2004).

APETALA3 (*AP3*) and *PISTILLATA* (*PI*) were assigned to the class B. Flowers mutant for *AP3* and *PI* exhibit the same phenotype: petals are transformed into sepals and stamens into carpels (Bowman et al., 1991). *AP3* and *PI* both encode MADS box transcription factors are mostly expressed in whorls 2 and 3, after a transient extension of *PI* within whorl 4 (Jack et al., 1992; Theissen et al., 2000). MADS stands for MINICHROMOSOME MAINTENANCE 1 (MCM1) from budding yeast, AGAMOUS (AG) from Arabidopsis thaliana, DEFICIENS (DEF) from Antirrhinum majus and SERUM RESPONSE FACTOR (SRF) from humans which all share the ability to bind to the "MADS" domain in gene regulatory sequences (Shore and Sharrocks, 1995). MADS-box proteins bind CArG-boxes, consensus DNA sites whose sequences are CC[A/T]6GG or CTA[A/T]4TAG (Riechmann et al., 1996; Shore and Sharrocks, 1995).

AGAMOUS (*AG*) was assigned to the class A. Mutations in *AG* cause transformation of stamens into petals whereas the fourth whorl is replaced by a new abnormal flower resulting on indeterminate flowers (Fig 20, Fig 21-D, Fig 22, Bowman et al., 1991). *AG* encodes a MADS box transcription factor and is specifically expressed in whorls 3 and 4 (Yanofsky et al., 1990).

Finally, *SEPALLATA1* to *4* (*SEP1* to *4*) were assigned to the class E. Mutations in *SEP1* to *4* revealed that they have a redundant role in specifying floral organ identity (Ditta et al., 2004; Pelaz et al., 2001). *sep123* triple mutant flowers consist only of sepals and *sep1234* quadruple mutant flowers

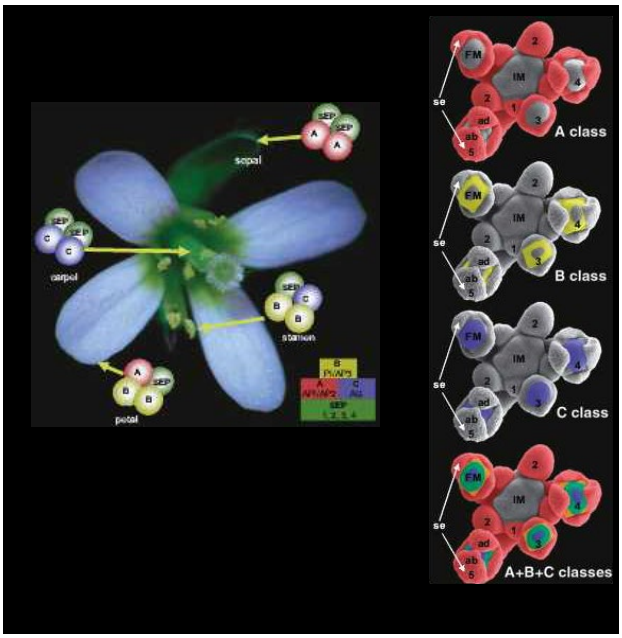

Figure 20: Patterning of ABCE genes

A. *Schematic representation of the interaction of ABC and SEP (class E) proteins in the quartet model for Arabidopsis floral organ identity specification;* ***B.*** *Meristems observed in scanning electron microscopy have been colorized to show expression patterns of A class (red, two outer whorls), B class (yellow, petal and stamen primordia) and C class (blue, two inner whorls) genes. Five flowers at early stages of development are marked 1 to 5 (5 being the oldest). IM: Inflorescence shoot apical meristem, FM: floral meristem, abS: abaxial sepals, adS: adaxial sepals. (Adapted Alvarez-Buylla et al., 2010)*

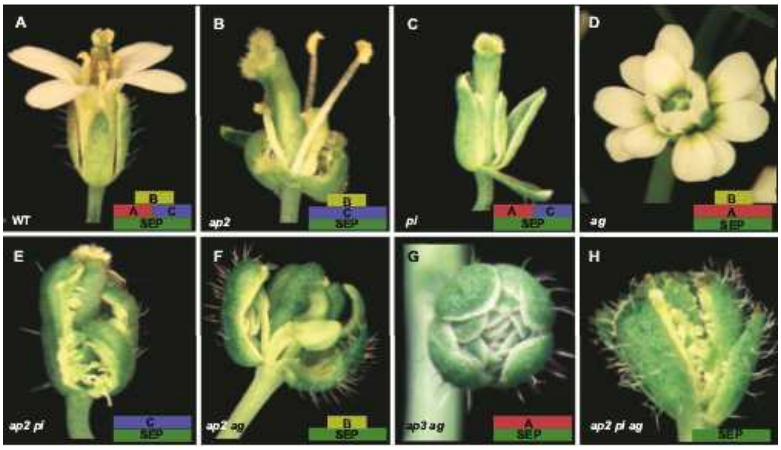

Figure 21: Several mutant for ABC gene

A. *Wild-type (WT) flower;* ***B.*** *Single ap2 mutant flower composed of carpelloid sepals, stamens, stamens and carpels;* ***C.*** *Single pi mutant has flowers composed of sepals, sepals, carpels and carpels;* ***D.*** *ag flower has the stamens transformed into petals and the carpels are replaced by another flower repeating the same pattern;* ***E.*** *ap2 pi double mutant displays flowers composed only of sepalloid carpels;* ***F.*** *ap2 ag flowers have leaf-like organs in the first and fourth whorls and mosaic petal/stamen organs in the second and third whorls;* ***G.*** *The ap3 ag double mutants produce flowers composed of repeated whorls of sepals;* ***H.*** *The ap2 pi ag mutant has leaf-like organs with some residual carpel properties. (Photographs provided by J. Bowman); (Alvarez-Buylla et al., 2010)*

only exhibit leaf-like organs, both being fully indeterminate. *SEP1* to *4* all *AG* encode a MADS box transcription factors with partially overlapping expression patterns in the FM (Krizek and Fletcher, 2005).

Altogether, these data show that floral organ identity relies on the combinatorial action of four classes of genes: A (*AP1* and *AP2*), B (*AP3* and *PI*), C (*AG*) and E (*SEP1-4*), the later acting as scaffolding proteins, necessary for the formation of ABC protein complexes (Fig 20-A,(Immink et al., 2009; Puranik et al., 2014; Theissen et al., 2000). This ABCE model, sometimes called the quartet model is also supported by the fact that A, B, C and E genes are also sufficient to promote floral organ identities: simultaneous ectopic expression of ABCE genes transform leaves into floral organs (Honma and Goto, 2001; Pelaz et al., 2001). The model thus states that the formation of sepals requires the activities of class A and E genes; petals require A, B and E activities; stamens require B, C and E activities; and carpels require C and E activities (Theissen et al., 2000). The model also confers a cadastral function to class A and C genes: class A and C genes repress each other within their functional domains (Fig 20-B, (Drews et al., 1991; Mizukami and Ma, 1992).

This model, based on floral homeotic mutants in *Arabidopsis thaliana* and *Antirrhinum majus* (snapdragon), has been widely used as a framework for understanding floral development and evolution, and was thought to be universal. However, A function, as reported in the model and, contrary to B and C functions, did not appear to be widely conserved in flowering plants (Angenent et al., 2005; Jack, 2004). Recent data refined the A function both in Arabidopsis and Petunia, and showed that A class genes restrict expressions of B and C genes in whorl 1 and 2 rather than promoting whorl 1 and whorl 2 identities *per se* (Krogan et al., 2012; Monniaux and Vandenbussche, 2018; Morel et al., 2017).

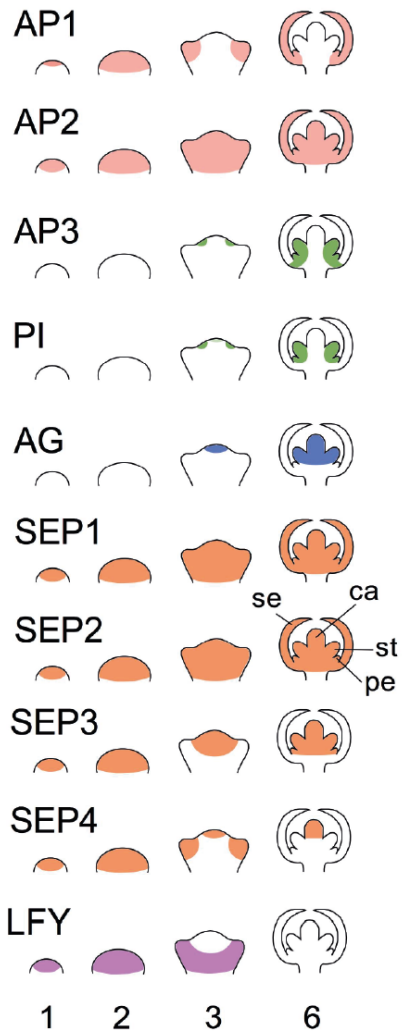

Figure 22: mRNA expression patterns of the Arabidopsis thaliana floral-organ identity genes during two stages of flower development

This figure show the ABC and no ABC gene pattern playing a key role in flower development (Adapted from Alvarez-Buylla et al., 2010)

3.4. FM growth is determinate

3.4.1. The successive steps of FM determinacy

The FM is an axillary meristem, produced at the flank of the IM. During its first stages of development, up to stage 5-6 (Fig 19), the FM thus inherits the potential of indeterminacy from the SAM (Clark et al., 1995, 1993; Endrizzi et al., 1996; Jeong et al., 1999; Laux et al., 1996; Long et al., 1996; Mayer et al., 1998). For instance, the maintenance of stem cells in the center of the flower relies on the same WUS/CLV regulatory loop (Schoof et al., 2000). *WUS* and *CLV1-3* are expressed in a similar way (except that *WUS* is found two cell layers deep instead of three). *WUS* is expressed in FMs from stage 1 onwards and induces CLV3 expression. Its expression peaks at stage 3 to then decreases and becomes undetectable at stage 6, when carpel primordia are initiated and FM terminates (Mayer et al., 1998) Mutations in *WUS* and *CLV3* cause similar phenotypes. *wus* floral development terminates prematurely and exhibits only one organ inside whorl 2, whereas *clv* mutant flowers exhibit more floral organs in each whorl.

However, flowers display a fixed number of whorls and organs per whorl. From stage 6 on in *Arabidopsis*, no additional floral organs are produced by the FM. Carpel primordia fuse to form the gynoecium enclosing the ovules. Stem cells are therefore only transiently maintained within the FM while they are continuously maintained in the SAM: FM are determinate. Several mutants exhibiting loss of floral determinacy phenotype have been isolated so far. They all result in an increase of floral organ number compared to wild-type flowers but may involve distinct processes and refer to different phenotypes.

The first category of phenotypes gathers mutations that affect stem cell homeostasis. In this case, the phenotypes result in the production of extra floral organs on one or several of the first four whorls of the flower. All the phenotypes result from FM enlargement due to the derepression of *WUS* expression. This category includes *clv* mutants (Clark et al., 1995; Kayes and Clark, 1998; Mayer et al., 1998; Schoof et al., 2000), mutants affecting the *CLV* pathway such as *shepherd* (Ishiguro et al., 2002) and *squint* (Prunet et al., 2015), and *ult1* mutant that influences *WUS* expression in CLV-independent pathway (Fletcher, 2001)

The second category of phenotypes gather mutations that affect FM termination. In this case, the phenotypes result in the development of extra organs on whorls produced from the very center of

the FM, in-between the two primary carpels. All the phenotypes result from the maintenance of *WUS* expression beyond stage 6. While the first category of indeterminacy results from spatial alterations of the FM, this second category results from temporal alteration of the FM. The following part addresses the molecular mechanisms that control FM termination.

3.4.2. *AGAMOUS*, a key gene for floral determinacy

AGAMOUS (*AG*) was reported to control stamen and carpels identity. However, mutation in *AG* not only results in homeotic transformation of stamen into petals, but also in a total loss of FM determinacy: new flowers are iteratively produced from the center of the initial flower (Bowman et al., 1991; Yanofsky et al., 1990). Interestingly, these two functions of AG (specifying reproductive organ identities and triggering FM termination) rely on a dose-dependent activity of AG, FM termination requiring the highest level of AG expression (Chuang and Meyerowitz, 2000; Mizukami and Ma, 1995; Sieburth et al., 1995).

Loss of FM termination phenotype results from the maintenance of stem cells beyond stage 6, due the maintenance of *WUS* expression in the OC: *AG* is therefore required to repress *WUS* at the end of flower development (Lenhard et al., 2001; Lohmann et al., 2001). *WUS* is necessary for the loss of FM termination, as *wus ag* double mutant flowers are over-determinate similarly to *wus* flowers (Laux et al., 1996), and is also sufficient to promote an indeterminate growth of the FM as its ectopic expression after stage 6 prolongs FM growth (Lenhard et al., 2001). Interestingly, *AG* expression is directly induced by *WUS*, together with *LFY* (Lenhard et al., 2001; Lohmann et al., 2001; Parcy et al., 1998), making the FM termination controlled by a negative feedback loop similar to the *CLV/WUS* feedback loop that controls stem cell homeostasis in both SAM and FM (Fig 18).

AG expression starts in early stage 3 of flower development with a homogeneous expression pattern in the two central whorls and remains uniformly expressed up to stage 7 in presumed stamens and carpels (Drews et al., 1991; Yanofsky et al., 1990). *WUS* expression starts at stage 1 of flower development and starts slightly decreasing from stage 3 to be totally absent at stage 6 (Mayer et al., 1998). Thus, from stage 3 to 6, *AG* is strongly expressed, in a domain covering the OC where *WUS* is expressed, while *WUS* remains expressed, although slightly decreasing. Two independent regulatory pathways, both involving epigenetic regulations, have been deciphered explaining these expression discrepancies.

3.4.3. AG controls floral determinacy through chromatin modifications

In Eukaryotes, DNA is organized in the form of wrapping around a core octamer of histone proteins made of histones H2A, H2B, H3 and H4. DNA is thus compacted into chromatin, adding a layer of complexity to the regulation of processes that require access to DNA. First identified in *Drosophila*, epigenetic regulation relies on chromatin marks that can either be repressive when deposited by Polycomb repressive complex 2 (PRC2), leading to transcriptional silencing, or activating when deposited by Trithorax Group (TrxG) proteins, leading to transcriptional activation (Hugues et al., 2020; Kassis et al., 2017). These chromatin marks correspond to post-transcriptional modifications (mainely methylations) of histones, the core-proteins of nucleosomes around which DNA is wrapped to form chromatin. Indeed, trimethylation of histone H3 at lysine 27 (H3K27me3) is the diagnostic mark of transcriptional repression. Once trimethylated by PRC2, H3K27m3 is subsequently read by Polycomb repressive complex 1 (PRC1) that silences (through ubiquitination) the targeted locus. PRC2 and PRC1 are part of the Polycomb Group (PcG) proteins. Conversely, trimethylation of histone H3 at lysine 4 and 36 (H3K4me3, H3K36me3) are the main marks of transcriptional activation (Hugues et al., 2020; Kassis et al., 2017).

- AG directly repress WUS expression

A series of experiments showed that AG directly regulates *WUS* expression (Liu et al., 2011). AG directly binds to *WUS* regulatory sequences, and this binding is required for the H3K27me3 enrichment throughout the *WUS* genomic region that participates in its repression. Accordingly, mutations in *CURLY LEAF* (Goodrich et al., 1997), encoding one of the H3K27 methyltransferase subunit of PCR2, results in the delay of floral stem cell termination. However, once bound to the *WUS* locus, AG also recruits TERMINAL FLOWER2/LIKE HETEROCHROMATIN PROTEIN1 (TFL2/LHP1), which is considered as the functional counterpart of PRC1, to *WUS* (Guo et al., 2018; Liu et al., 2011; Turck et al., 2007; Zhang et al., 2007). AG-mediated localization of TFL2/LHP1 at the WUS locus promotes a chromatin loop that blocks the recruitment of RNA polymerase II and therefore the transcription of WUS locus (Guo et al., 2018; Liu et al., 2011). Such a sequence of molecular events would explain why AG does not downregulate *WUS* expression right from stage 3 while it is strongly expressed.

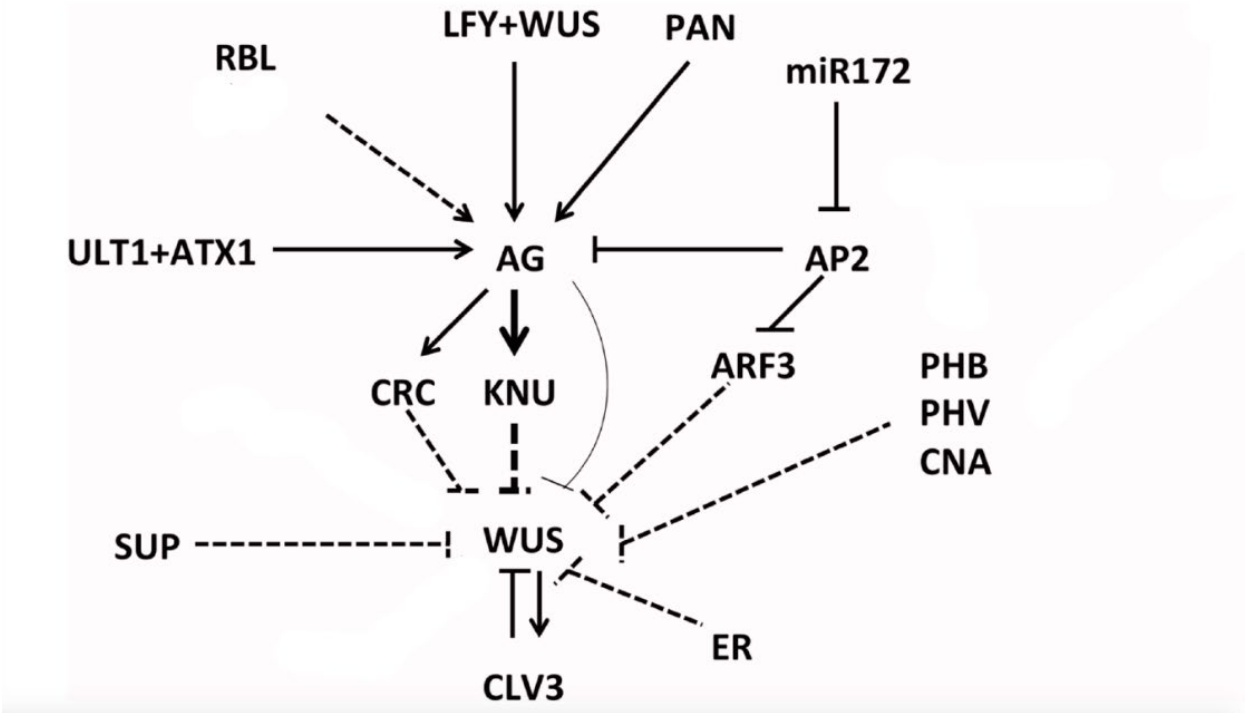

Figure 23: Key regulator of stem cells.

Network of the regulation of stem cell identity gene WUS in direct and indirect way. Lines represent direct regulation and dotted lines indirect regulation

- **Indirect repression of WUS expression by AG**

However, a second pathway was described to also explain such a delay in *WUS* expression turn-off (Fig 23). In this pathway, AG indirectly represses *WUS* expression through the activation of *KNUCKLES* (Bo Sun et al., 2009). *KNU* encodes a C2H2 Zn-finger repressor protein and is expressed in the center of the FM from stage 6 on (Payne et al., 2004; Bo Sun et al., 2009). A mutation in *KNU* results in a mild delay of FM termination due to the maintenance of *WUS* expression (Payne et al., 2004; Bo Sun et al., 2009). AG directly binds the *KNU* locus, thus displacing PRC2 from a wide region of *KNU*: AG and PRC2 compete for *KNU* locus binding thus reducing H3K27m3 and allowing *KNU* expression (Bo Sun et al., 2009; Sun et al., 2014). KNU is subsequently recruited to the *WUS* locus by MINI ZINC FINGER2 to form a complex together with HISTONE DEACETYLASE-like HDA19 and TOPLESS, which in turn inhibits *WUS* expression (Bollier et al., 2018). Furthermore, KNU also directly binds the *WUS* locus to cause eviction of SYD and subsequent recruitment of PRC2 to silence *WUS* expression (Sun et al., 2019).

It however seems that this delay of *WUS* downregulation by the AG/KNU pathway is strengthened by a direct role of AP2 that counteracts AG activity (and not translation) notably on the induction of *KNU* expression: AP2 could serve as a brake in the AG/KNU/WUS loop (Huang et al., 2017).

3.4.4. AG controls floral determinacy through hormonal homeostasis

Hormone signaling plays critical roles during SAM development. For instance, auxin promotes primordium initiation (organ emergence) and cytokinin meristem identity (stem cell fate and absence of differentiation). These two hormones are also essential for proper FM termination and *AG* seems to be strongly involved in their regulation during both early and late stages of FM development (Lee et al., 2019). After FM termination, cytokinin and auxin homeostasis largely influence gynoecium formation.

AG activates the expression of *ETTIN/AUXIN RESPONSE FACTOR 3* (Nemhauser et al., 2000) through GIANT KILLER, a chromatin modifier (Ng et al., 2009). More recently, ETT was shown to directly and indirectly downregulate cytokinin biosynthesis and signaling, thus resulting in the termination of the FM (Zhang et al., 2018). AG therefore promotes FM termination through the regulation of cytokinin homeostasis.

AG also regulates auxin homeostasis. Indeed, at stage 3-4 of flower development (early stage), AG induces *SUPERMAN* expression (Bowman et al., 1992; Breuil-Broyer et al., 2016) that in turn represses the expression of auxin biosynthesis genes *YUCCA 1/4* (*YUC1/4*) (Cheng et al., 2006) locally (Xu et al., 2018). Such a downregulation of auxin distribution possibly prevents over-differentiation at the center of the FM. Later during FM development, at stage 6, when carpel primordia start developing, AG induces *CRABS CLAW* (*CRC)*(Bowman and Smyth, 1999; Gomez-Mena et al., 2005). Both AG and CRC in turn activate *YUC4* expression that promotes auxin biosynthesis and therefore FM termination (Yamaguchi et al., 2018). In parallel, CRC also repress the expression of *TORNADO2* (Cnops et al., 2006), a regulator of auxin homeostasis that contributes to *WUS* expression (Yamaguchi et al., 2017) (Fig.23).

Interestingly, recent data reported that these gene inductions by AG, notably those of *KNU* and *CRC*, absolutely requires the tetramerization of AG and SEP3 (Hugouvieux et al., 2018). Accordingly, a mutation in *SEP3* preventing interactions with other MADS-box-containing proteins but not DNA-binding, specifically triggers FM termination defects.

3.4.5. Regulators of *AG* expression also display floral indeterminacy

Most regulatory sequences controlling *AG* expression are located in its second intron of approximately 3 kb (Deyholos and Sieburth, 2000; Sieburth and Meyerowitz, 1997). For instance, this intronic sequence contains the sequences that bind LEAFY, AP2 or AG itself since AG maintains its own expression (Busch et al., 1999; Deyholos and Sieburth, 2000; Dinh et al., 2012; Moyroud et al., 2011; Yant et al., 2010).

PERIANTHIA (PAN) and *REBELOTE (RBL)*. The bZIP transcription factor PAN was shown to activate AG expression in a putative negative feedback loop (Das et al., 2009; Maier et al., 2009)(Fig.23). Accordingly, *pan* mutants display typical *ag* loss-of-function phenotypes. RBL, which encodes a NOC2 domain-containing protein, was also shown to redundantly influence FM termination although its molecular function in this process remains unclear (de Bossoreille et al., 2018; Prunet et al., 2008).

Trithorax Group genes. Functional characterization of ULT proteins highlighted their roles in regulating *AG* expression(Carles and Fletcher, 2009; Monfared et al., 2013). *ULT1* fulfils the TrxG genetic function by counteracting the PRC2 function and thus reducing the H3K27m3 at the *AG* locus (Carles and Fletcher, 2009). *ULT1 OE* therefore mimics *PRC2* defective mutants. Conversely, mutation in *ULT1* results in the reduction of *AG* expression in the very center of the FM, in a zone including *WUS* expression domain. Such a decrease of *AG* expression allows *WUS* to be expressed beyond stage 6 (Carles et al., 2004; Carles and Fletcher, 2009; Prunet et al., 2008). However, *AG* expression is also positively regulated by *ARABIDOPSIS TRITHORAX1* (*ATX1)*, another TrxG gene from Arabidopsis, although no role of ATX1 on FM determinacy has been reported so far (Alvarez-Venegas et al., 2003).

HUA1, *HUA2*, *HEN* (*HUA ENHANCER*) *2* and *HEN4*. *HUA1* encodes a protein with CCCH zinc fingers RNA binding protein (Cheng et al., 2003; Li et al., 2001), *HUA2* a nuclear protein with an RPR domain (Chen and Meyerowitz, 1999), *HEN2* an RNA helicase (Western et al., 2002) and *HEN4* a putative RNA-binding protein (Cheng et al., 2003; Rodriguez-Cazorla et al., 2015). All these proteins directly or indirectly bind *AG* mRNA playing a critical role on *AG* post-transcriptional regulation, especially splicing. All have been shown to control FM termination through directly regulating *AG* mRNA processing.

APETALA2 (*AP2*) and *miR172* (Fig 22). As discussed above AP2 normally represses *AG* (Drews et al., 1991; Jofuku et al., 1994). Furthermore, *AP2* is transcribed in all four whorls but translated only in the outer two whorls due to a *miR172*-mediated translation inhibition in the inner two whorls (Aukerman and Sakai, 2003; Chen, 2004). Thus, flowers over-expressing a *miR172*-resistent version of *AP2* present a strong loss of FM termination with a lack of *AG* expression in the center of the FM (Zhao et al., 2007). Accordingly, mutations in genes controlling miR metabolisms, such as *DICER-LIKE1* (Jacobsen et al., 1999), HUA ENHANCER1 (Park et al., 2002) or *SQUINT* (Prunet et al., 2015) are often deficient in FM termination.

All these data illustrate how complex and multifactorial the regulation of FM termination is, with many redundancies, suggesting a quite robust regulatory pathway. Thanks to new development in systems biology and imaging, the question of robustness has become a key topic in developmental biology.

4. Developmental plasticity and robustness.

4.1. Transcriptional regulation and variability sustain developmental plasticity and robustness

Developmental robustness is ambivalent: patterns of growth must be reproducible, as body plans are usually comparable within individuals of given species; they also must be plastic to adapt to external and internal changes and fluctuations. In other words, developmental robustness entails a balance between homeostatic mechanisms that ensure that many phenotypes are robust to genetic and environmental variations, and variability promotion to trigger alternative developmental pathways to face genetic and environmental variations. This balance is also a variable, as the ratio between reproducibility and variability promotion can shift as development goes on (Tsugawa et al., 2017).

Among the mechanisms behind developmental variability and robustness, transcription is essential as it can contribute to specific differentiation pathways in various tissues or multiple differentiation pathways from undifferentiated cells or group of cells (Alemu et al., 2014; Mantsoki et al., 2016; Mason et al., 2014; Padovan-Merhar and Raj, 2013; Sprinzak et al., 2010). Besides, the maintenance of stem cells may rely on the relative inefficiency of the transcriptional and translational machinery that maintains the stem cell in an indeterminate state (Momiji and Monk, 2009). Interestingly, variability of gene expression can account for reduced penetrance (Raj et al., 2010).

In plants, the contribution of gene expression variability to plant developmental robustness and plasticity remains poorly documented. Gene expression variability has mainly been assessed during responses to external or internal stimuli (Wang et al., 2011; Waters et al., 2017; Xu et al., 2016) and only more recently as an internal input to support developmental plasticity at tissue level (Meyer et al., 2017).

Although the exact mechanisms behind transcriptional noise remain to be uncovered, relevant molecular factors have been and continue to be identified. For instance, the variability of gene expression in mammals relies on several features of the gene itself spanning from its genomic

structure and regulation to its interacting network (Alemu et al., 2014). RNA polymerase II (Pol II) is obviously a key player in this process as it transcribes all protein-coding genes and many noncoding RNAs throughout eukaryotic genomes and is fundamentally important for most physiological processes (Schier and Taatjes, 2020). Pol II-mediated transcription process starts with the recognition and binding to the TATAA box, a few 30 nucleotides upstream the transcription start site, by the TATA-box Binding Protein (TBP). Binding of TBP is accompanied by the binding of a series of Transcription Factor for RNA Pol II (TFII), altogether forming the PreInitiation Complex (PIC) that subsequently triggers DNA structural changing and Pol II recruitment (Woychik and Hampsey, 2002). The TATA box was shown to be a critical determinant of gene expression noise since mutations in TATA box increase transcriptional noise and genes lacking a TATA box are often associated with lower noise compared to TATA-box containing genes (Blake et al., 2006; Hendy et al., 2017; Hornung et al., 2012; Ravarani et al., 2016). TBP and Mediator complex are essential for this TATA-box-mediated transcriptional variability (Ravarani et al., 2016; Tantale et al., 2016). Once the initiation step is completed RNA PolII is released from the PIC to achieve the elongation and the termination steps (Schier and Taatjes, 2020). Each step of the RNA Pol II transcription cycle is largely regulated by accessory proteins that have a direct impact on Pol II activity. They mediate its response to additional regulatory proteins or modify the chromatin matrix. The Mediator complex is one of these complexes. Conserved among many eukaryotes including plants, the Mediator complex interacts with the PIC to regulate the initiation step but also influences transcription all along the transcriptional cycle (Dolan and Chapple, 2017; Malik et al., 2017; Soutourina, 2018).

The RNA Polymerase II-associated factor 1 Complex (Paf1C) is a second example of a complex interacting with Pol II to control its activity (Mueller and Jaehning, 2002; Shi et al., 1997; Wade et al., 1996). Paf1C interacts either directly with Pol II, especially with its C-terminal domain (CTD), or with some components of the Pol II complex, including the TFII (Amrich et al., 2012; Mueller et al., 2004; Qiu et al., 2012; Xu et al., 2017). Thus, Paf1c plays a key role in the multiple steps of transcription.

Interestingly, mutations in Paf1c subunits increase gene expression noise in yeast (Ansel et al., 2008; Richard and Yvert, 2014). These effects not only rely on the functional interaction with RNA PolII, but also on a larger spectrum of activities (Mueller et al., 2004; Nordick et al., 2008; Penheiter et al., 2005). Interestingly, Paf1C is enriched on active genes (Mayer et al., 2010; Yang et al., 2016) and was shown to control many aspects of development, including for instance cell line specification in both animals and plants (Akanuma et al., 2007; Ding et al., 2009; Fal et al., 2017; Kubota et al., 2014; Langenbacher et al., 2011; Nguyen et al., 2010; Oh et al., 2004; Strikoudis et al., 2016; Takagi

and Ueguchi, 2012; Yu and Michaels, 2010; Zhang et al., 2003). Yet the role of Paf1c in developmental robustness had not been explored specifically, notably in the context of stem cell maintenance. Together with the development of imaging pipelines for developmental biology, this conceptual question is a primary focus of my PhD.

4.2. PolII-associated factor1 complex (Paf1C) influences mRNA accumulation at multiple levels of regulation

4.2.1. Paf1C composition

- Yeast and animals

The proteins of the Paf1 complex were initially discovered in the middle of the 1990s in a search for general transcription factors associated with yeast pol II (Wade et al., 1996). Proteins homologous to the yeast proteins have been found in many eukaryotes making the Paf1C conserved over kingdoms (Tomson and Arndt, 2013). The yeast Paf1C is composed of Paf1, Ctr9, Cdc73, Rtf1 and Leo1 while the complex includes an additional subunit in humans and plants with the WDR61 or SKI8 or VIP3 protein (Kim et al., 2010; Zhang et al., 2003).

Physical interactions within the Paf1C and between the Paf1C and other factors are extremely complex consistent with the large spectrum of Paf1C activities (Jaehning, 2010; Van Oss et al., 2017; Wade et al., 1996).

- Plant

In plants, and especially in *Arabidopsis thaliana*, Paf1C is composed of several subunits that are functionally homologous to those present in yeast and animal cells (Fig. 24). It includes VERNALIZATION INDEPENDENCE (VIP) 3, the homolog of WDR61/SKI8 (Dorcey et al., 2012; Zhang et al., 2003), VIP4, the homolog of Leo (Zhang and van Nocker, 2002), VIP5, the homolog of Rtf1 (Oh et al., 2004), EARLY FLOWER (ELF) 7, the homolog of Paf1 (He et al., 2004), VIP6 (also known as ELF8), the homolog of Ctr9 (He et al., 2004; Oh et al., 2004), and PARAFIBROMINE HOMOLOGICAL PLANT (PHP), the homolog of Cdc73 (He et al., 2004; Jaehning, 2010; Oh et al.,

2008, 2004; Park et al., 2010, 2010; Zhang and van Nocker, 2002). Consistent with the contribution of VIP3, VIP4, VIP5 and VIP6 to a plant Paf1C homologue, these proteins co-immunoprecipitate (Oh et al., 2004) and the corresponding single mutants exhibit comparable growth defects, such as reduced plant size, severely affected fertility and early flowering (Dorcey et al., 2012; Fal et al., 2017; Takagi and Ueguchi, 2012; Zhang et al., 2003).

4.2.2. Paf1C functions

- Transcription elongation and termination and RNA processing

Once bound to the Pol II complex, in the transcription start site vicinity, Paf1C has been shown to facilitate transcription elongation (Costa and Arndt, 2000; Kassis et al., 2017; Pokholok et al., 2002; Rondon et al., 2004; Squazzo et al., 2002). For instance, the human Paf1C was reported to recruit the CDK12 protein that phosphorylates the CTD of Pol II and therefore promotes transcription elongation (Yu et al., 2015).

Paf1C also regulates co- and post-transcriptional RNA processes, including termination, 3′-end processing and stability. Indeed, the poly(A) tail is shorter and an alternative site of polyadenylation is chosen in Paf1C defective mutants (Mueller et al., 2004; Nordick et al., 2008; Penheiter et al., 2005). Moreover, Paf1C stimulates mRNA cleavage and some Paf1C subunits interact directly with several polyadenylation factors (Nordick et al., 2008; Rozenblatt-Rosen et al., 2009). Furthermore, the levels of active Paf1C have been correlated to small nucleolar RNA formation in yeast while mutations in Paf1C members lead to the accumulation of small nuclear RNA transcripts still in yeast (Fig 25, Fischl et al., 2017; Sheldon et al., 2005).

- Chromatin accessibility and modification

In addition to its roles based on direct interactions with Pol II or transcription-associated factors, Paf1C also influences RNA synthesis through modulation of chromatin structure, with consequences on development. Indeed, in vitro studies showed that transcription elongation and efficiency rely at least in part on the chromatin state (Izban and Luse, 1992; Knezetic and Luse, 1986) and several members of the Paf1C influence chromatin remodeling and modification (Zhou et al., 2012).

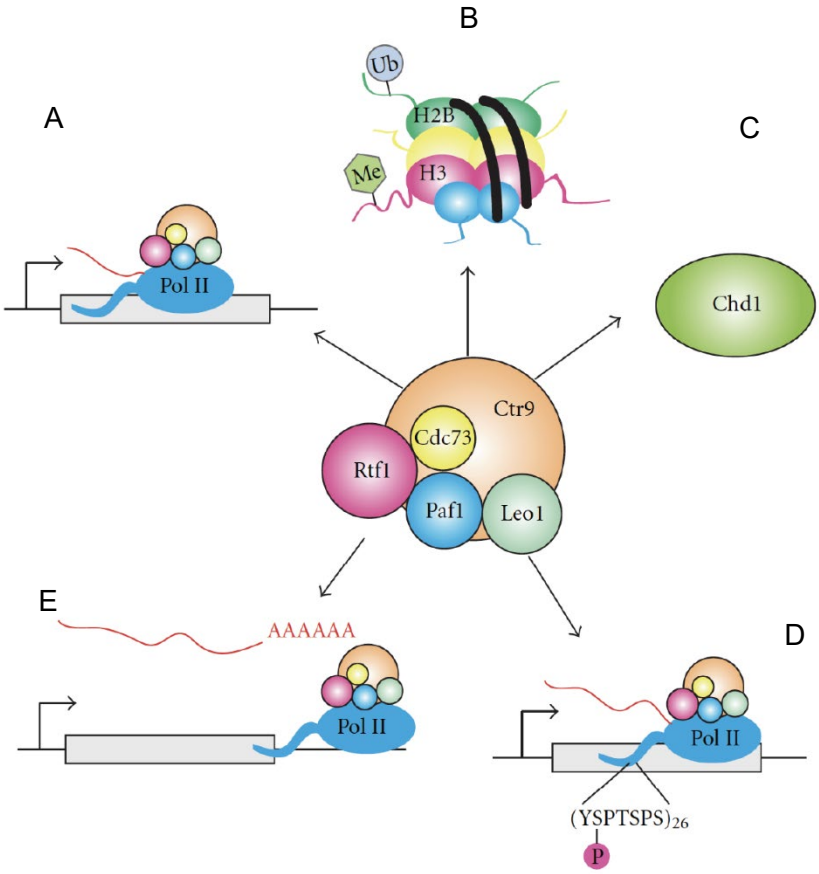

Figure 24: Fonctions of Paf1C

***A.** Paf1C associates with RNA pol II and controls transcription elongation; **B.** Histone regulation and modification by Paf1C; **C.** Paf1C can recruit Chd1 for chromatine remodeling; **D.** Paf1C promotes phosphirylation of the serine 2 of RNA pol II CTD thus promoting transcription elongation; **E.** Paf1C has role in termination of transcription and RNA 3' end of both polydenylated and nonpolyadenylated transcripts. (Crisucci and Arndt, 2011)*

Interestingly, Paf1C directly binds histones and such Paf1C-mediated chromatin remodeling mainly occurs on active genes, i.e. those that are transcribed (Fig 25, Chu et al., 2013; Dermody and Buratowski, 2010).

The Paf1 Complex is required for several types of chromatin modifications. For instance, it promotes the ubiquitination of histone H2B in yeast in humans, which is required for subsequent methylation of histone H3K4 that promotes gene expression and of H3K79 that promotes transcriptional silencing (Kim et al., 2009; Nevan J. Krogan et al., 2003; N. J. Krogan et al., 2003; H. H. Ng et al., 2003, 2003; Huck Hui Ng et al., 2003; Wood et al., 2003; Xiao et al., 2005). In plants, only the impact on H3K4 methylation has been shown (He et al., 2004; Yu and Michaels, 2010)(Fig. 25). However, Paf1C is also required for methylation of histone in yeast, metazoans and plants. This methylation is independent of the H2B methylation pathway. Indeed, Paf1C favours histone H3K36 methylation by the Set2 methyltransferase during transcription elongation (Chu et al., 2007; Jensen et al., 2017; N. J. Krogan et al., 2003; Oh et al., 2008). Conversely, levels of H3K27, a modification important for transcriptional silencing, are higher when Paf1C function is impaired (Chu et al., 2007; Jensen et al., 2017, 2017; N. J. Krogan et al., 2003; Oh et al., 2008). In addition to its role on histone modifications, Paf1C was also reported to promote local histone turnover that also modulate chromatin state (Sadeghi et al., 2015) (Fig. 25).

Altogether, these observations highlight the connections between Paf1C and chromatin structure which likely underlies many of the gene expression changes that arise when Paf1C function is impaired.

4.3. VERNALIZATION INDEPENDENCE 3 (VIP3) in Arabidopsis thaliana

As mentioned above, VIP3 is part of Paf1C. It encodes a protein consisting almost exclusively of repeated Trp-Asp (WD) motifs that physically interacts with VIP4, VIP5 and VIP6, three other members of Paf1C (Oh et al., 2004; Zhang et al., 2003). Interestingly, *VIP3* is also the homolog of the yeast *Superkiller8* (*Ski8*) gene (Zhang et al., 2003). SKI8 is part of the SKI complex which positively regulates exosome activity (Houseley et al., 2006). Indeed, messenger RNAs appear more stable in *vip3/ski8* mutants compared to wild-type plants (Dorcey et al., 2012). Interestingly, human hSki8 as well as VIP3 also associate with Paf1c (Oh et al., 2004; Zhu et al., 2005), which is not the

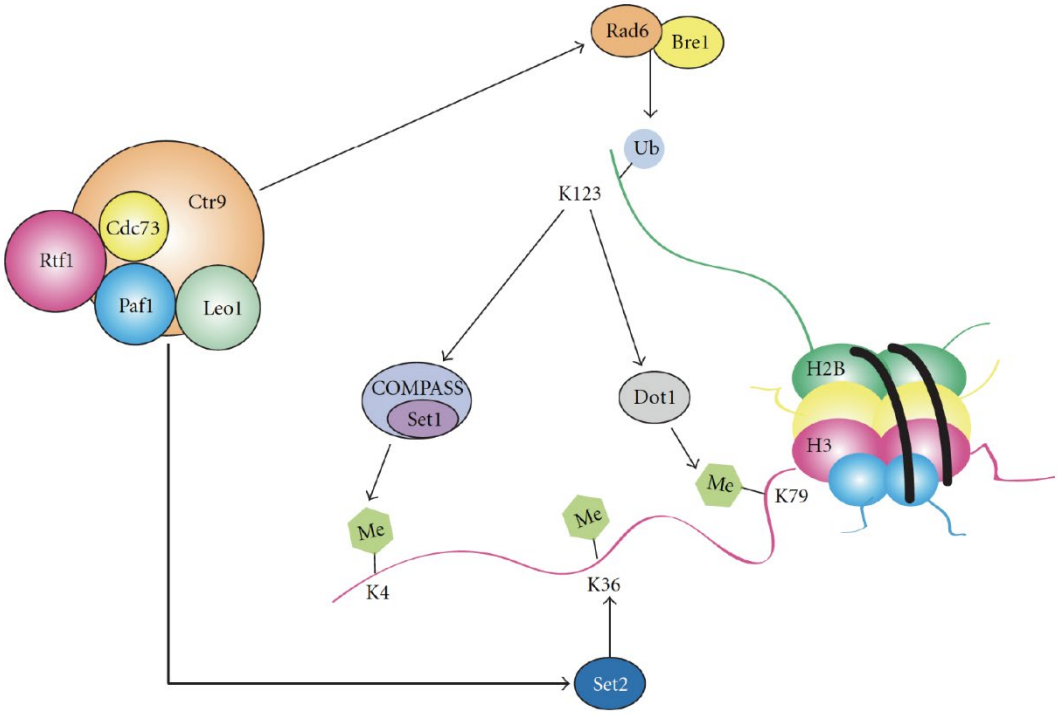

Figure 25: Role of Paf1C in histone mark

The Paf1C promotes histone H2B monoubiquitylation and histone H3 K4, K36, and K79 methylation. In yeast, the ubiquitin conjugating enzyme, Rad6, and the ubiquitin ligase, Bre1, monoubiquitylate H2B K123. H2B monoubiquitylation is a prerequisite for di- and trimethylation of H3 K4 and K79 by the histone methyltransferases Set1 and Dot1, respectively. Histone H3 is methylated on K36 by the methyltransferase Set2. Paf1 and Rtf1 subunits of the Paf1C are required for H2B K123 monoubiquitylation and the downstream di- and trimethylation of H3 K4 and K79. Paf1 and Ctr9 are required for trimethylation of K36 on histone H3. (Crisucci and Arndt, 2011)

case for yeast ScSki8 (Brown et al., 2000; Zhu et al., 2005). VIP3 has been mostly characterized for its role in the Paf1C complex.

VIP3 was initially reported to control flowering time by promoting the expression of *FLOWERING LOCUS C* (*FLC*) an inhibitor of flowering (Michaels et al., 2003; Oh et al., 2004; Zhang et al., 2003). The regulation of Regulation of *FLC* expression is mediated by methylations on histones H3K4, H3K39 and H3K27 (He et al., 2004; Oh et al., 2008; Yu and Michaels, 2010).

Interestingly, VIP3 has also been related to mechanical stress response (Jensen et al., 2017). Indeed, in a forward genetic screen seeking to identify new genes controlling thigmomorphogenesis (the plant response to touch and wind), *vip3* was the only mutation making plants insensitive to repetitive touches. Note that the genetic screen was likely not saturating – other regulators may be found in similar screens in the future. Thigmomorphogenesis relies on multiple genetic targets, including the *TOUCH* genes (Braam and Davis, 1990), and insensitivity to touch in *vip3* was related to defective H3K36 methylation at two *TOUCH* loci (Jensen et al., 2017).

Consistent with the Paf1C functions reported in other models, including developmental controls and cell line specifications, *VIP3* was shown to be required for proper phyllotactic patterns and SAM development (Fal et al., 2017). Such defects coincide with defects of specific gene expression patterns and auxin patterns at the shoot apices. But more interestingly, observations suggested that the robustness of these processes, more than the processes *per se*, was affected in a *vip3* background. Altogether, this provides a key developmental question: can the robustness of stem cell maintenance, and thus flower termination, be maintained when Paf1c-dependent transcription is perturbed?

5. Microtubules

The cytoskeleton is a structure that is essential for the functioning of most living beings. In plants, it is composed of distinct proteins forming the two main types of filaments: actin microfilaments, and microtubules (true intermediate filaments are not present). During my PhD, I conducted a project on microtubule dynamics and cell shape. I will thus only present this microtubular element in more detail.

5.1. Structure

Microtubules were first observed in plant cells by transmission electron microscopy (Ledbetter and Porter, 1963), which relates to the fact that most plant cells exhibit a dense network of cortical microtubules (in contrast to more diffuse and transient microtubule structures in animals). Microtubules are tubes with a diameter of 25 nm (to compare to 10 nm for actin filaments). They are the result of the polymerization of (alpha and beta) tubulin dimers. The wall of the “tube” is therefore made up of protofilaments associated laterally. This structure actually contributes to the high persistence length of microtubules, which in the millimeter range *in vitro* (Gittes et al., 1993). Microtubules are the stiffest fibers of the cytoskeleton (Alberts, 2015). The protofilaments themselves are arranged in an oriented manner within the microtubules. The number of protofilaments required to form a microtubule can vary. *In vitro*, it is described that 8 to 17 protofilaments can form different types of microtubules (Chrétien and Fuller, 2000). Thus, the number of helices may vary (between 2 and 6, Fig 26). This instability in the number of protofilaments and helices induces mechanical stresses within the microtubule and thus allows it to accumulate elastic energy. By far, the most common microtubules *in vivo* are made of 13 protofilaments (Alberts, 2015; Chrétien et al., 1992). Interestingly, some mechanosensory cells in *C. elegans* have been reported to host microtubules with 15 protofilaments, with increased stiffness in relation with their biological functions (Bounoutas et al., 2009). In animals, and because of their high stiffness, microtubules have a large contribution to the mechanical properties to the cells (Durand-Smet et al., 2014; Hyman and Karsenti, 1996). Interestingly, this was also shown in plant cells upon digestion of the cell wall: protoplasts expand upon microtubule depolymerization Durand-Smet et al., 2014)

5.2. Dynamics and self-organization

In vitro, it is possible to study the assembly of the microtubules in controlled conditions. In the presence of GTP, tubulin dimers are capable of forming microtubules. The + end exposing the beta tubulin grows faster than the - end exposing the alpha tubulin.

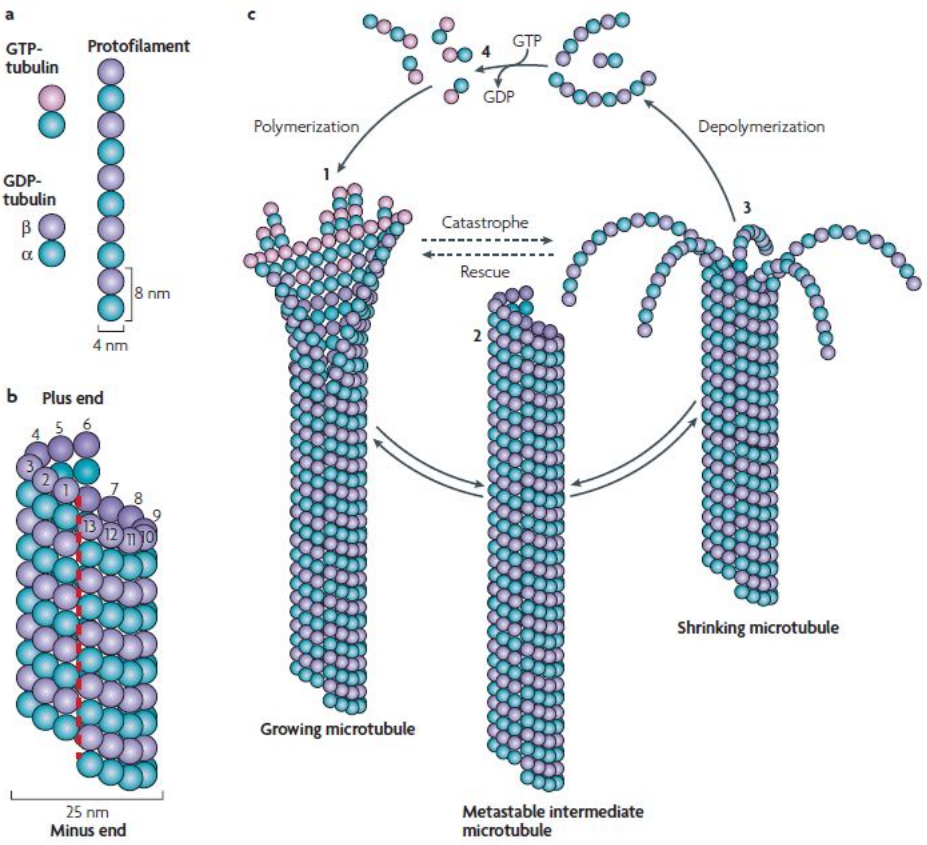

Figure 26: Microtubule structure and dynamics

*Microtubules are composed of stable α/β-tubulin heterodimers that are aligned in a polar head-to-tail fashion to form protofilaments (**A**). The cylindrical and helical microtubule wall typically comprises 13 parallel protofilaments in vivo (**B**). The 12-nm helical pitch in combination with the 8-nm longitudinal repeat between α/β-tubulin subunits along a protofilament generates the lattice seam (red dashed line). Assembly–polymerization and disassembly–depolymerization of microtubules (**C**) is driven by the binding, hydrolysis and exchange of a guanine nucleotide on the β-tubulin monomer (GTP bound to α-tubulin is nonexchangeable and is never hydrolysed). GTP hydrolysis is not required for microtubule assembly per se but is necessary for switching between catastrophe and rescue. Polymerization is typically initiated from a pool of GTP-loaded tubulin subunits (**C-1**). Growing microtubule ends fluctuate between slightly bent and straight protofilament sheets. GTP hydrolysis and release of inorganic phosphate occurs shortly after incorporation and is promoted by burial and locking of the partially exposed nucleotide as a result of the head-to-tail assembly of dimers. It has been postulated that GTP hydrolysis changes the conformation of a protofilament from a slightly curved tubulin-GTP to a more profoundly curved tubulin-GDP structure. This nucleotidedependent conformational model predicts that the curved tubulin-GDP is forced to remain straight when it is part of the microtubule wall. Growing microtubule sheets are thus believed to maintain a 'cap' of tubulin-GTP subunits to stabilize the straight tubulin conformation within the microtubule lattice. Closure of the terminal sheet structure generates a metastable, blunt-ended microtubule intermediate (**C-2**), which might pause, undergo further growth or switch to the depolymerization phase. A shrinking microtubule is characterized by fountain-like arrays of ring and spiral protofilament structures (**C-3**). This conformational change, which is presumably directed by tubulin-GDP, may destabilize lateral contacts between adjacent protofilaments. The polymerization–depolymerization cycle is completed by exchanging GDP of the disassembly products with GTP (**C-4**). (Akhmanova and Steinmetz, 2008)*

The polymerization of the purified microtubules is divided into three phases. The first is a latency phase, where the free subunits are dominant and assemble into short polymers. The second is a growth phase where the polymers elongate by adding subunits. Finally, the third is an equilibrium phase where there is an equal exchange between the pool of free subunits and the creation of polymers (Alberts, 2015). It should be noted that the latency phase was not reported *in vivo*. *In vivo*, nucleation initiation is performed using small polymer fragments stabilized by several proteins, and notably γ-tubulins, to allow stabilization of the negative end of microtubules (Alberts, 2015; Pastuglia and Bouchez, 2007)(Fig. 27).

However, the microtubule + end does not only grow. The microtubules are subjected to a succession of growth phases followed by a depolymerization phase. These phases are called catastrophe and rescue phases. The catastrophe corresponds to the process during which a growing + end stops its polymerization and starts to depolymerize (Fig 26). The protofilaments thus become detached from the tip (Mandelkow and Mandelkow, 1985). Conversely, rescue corresponds to the process during which a microtubule in the depolymerisation phase starts to repolymerize. Microtubules are therefore dynamics structures which constantly polymerize and depolymerize.

Despite this intrinsic dynamics, microtubules can form organized arrays at the cellular scale. Computational modeling has demonstrated that such order is an emerging property of both microtubule dynamics and their behavior when interacting with one another (Dixit and Cyr, 2004). During polymerisation, one microtubule may interact with another in different ways. Either the two microtubules can meet without anything happening, or the meeting induces a catastrophe phenomenon at the level of the incident microtubule, or the incident microtubule will align itself with the second microtubule to form a bundle, in a process called zippering (Dixit and Cyr, 2004; Wasteneys and Ambrose, 2009). Using physical modelling, it has been shown that a network of 20 microtubules can only create an anisotropic network when contacts between microtubules induce catastrophe or bundle formation (Dixit and Cyr, 2004). Subsequently, it was shown that cortical microtubules interact differently depending on their angle of interaction. Indeed, two microtubules will form a bundle if they cross at an angle of less than 40 degrees. Conversely, if the microtubules intersect at an angle greater than 40 degrees, a catastrophe (i.e. rapid depolymerization) will occur (Eren et al., 2012, 2010).

These interactions involve microtubule binding proteins and microtubule regulators, some of which will be detailed below. Note that again this phenomenon is more amenable to analysis in plant cells: cortical microtubules interact in a thin domain of the cell, i.e. almost in a 2D space, thus

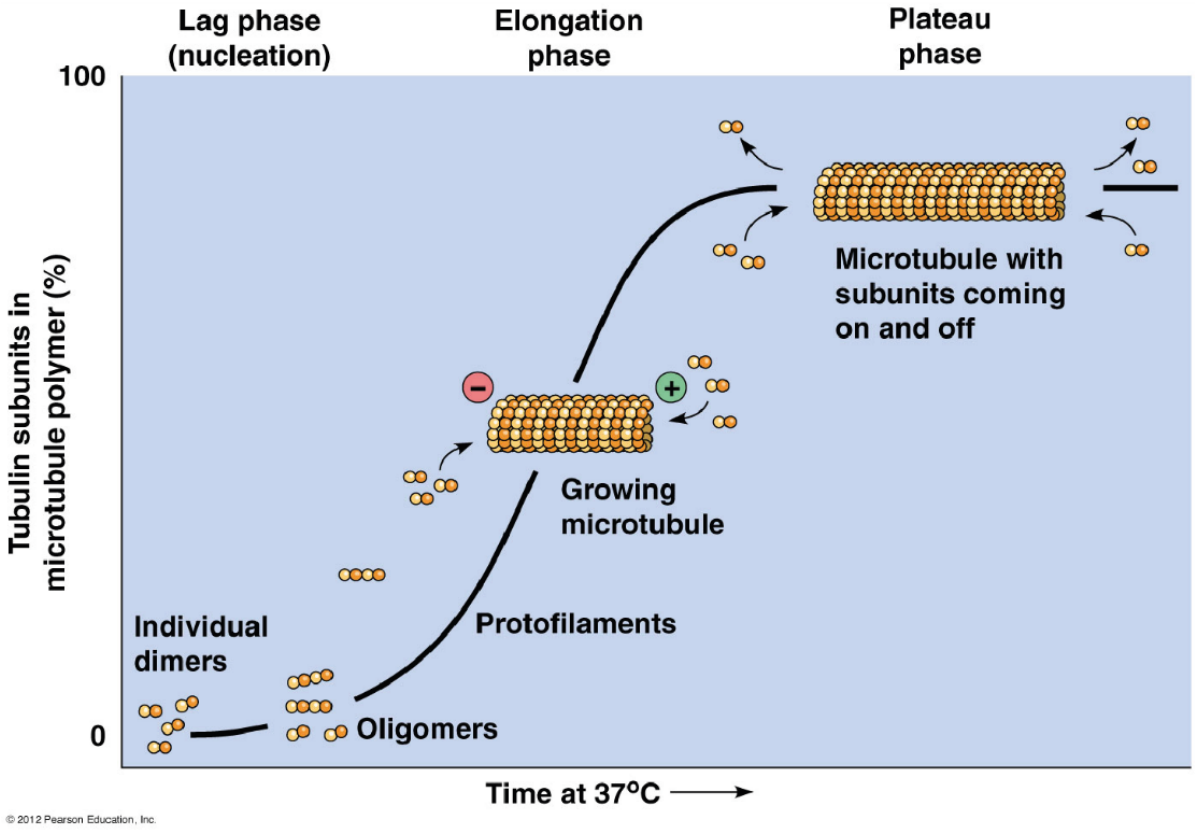

Figure 27: Microtubule polymerization

Microtubule dimers first produce oligomers and then protofilaments: this is the nucleation phase. Then the microtubules polymerize: this is the elongation phase. Finally, the microtubules reach an equilibrium between polymerization and depolymerization at the plateau. Note that the representation here does not capture the exact 3D aspect of the microtubule ends which are splayed, with sheet-like structures at the polymerization end). (adapted from Desai and Mitchison, 1997)

vastly facilitating both the interactions and their analysis (Wasteneys and Ambrose, 2009). Importantly, the balance between intrinsic dynamics and self-organizing properties allow microtubules to rapidly reorganize themselves within the cell.

5.3. Microtubule associated proteins

MAPs are microtubule-associated proteins that bind to the microtubule at different sites, the tip (+), the body of the microtubule and the tip (-). Earlier examples include MAP2 and TAU proteins that bind only to the microtubule body (Kim et al., 1979; Weingarten et al., 1975) or EB1, which binds to the (+) end of growing microtubules and is frequently used in images to track microtubule polymerization trajectories (Chan et al., 2003, Desai and Mitchison, 1997)

Even if we know that MAPs play a role in microtubule dynamics, it is difficult to know whether the difference in dynamics is directly related to MAP activity or to a rearrangement of the microtubule array. Several hypotheses can explain this change in dynamics. Stabilization may be a consequence of the increase in rescue frequency and/or the decrease in catastrophe frequency, these two effects being very often combined with the increase in polymerization rate and/ or the decrease in depolymerization rate. There are a large number of MAPs and these, when over or under-expressed, play a role in the dynamics of the microtubules. Around 200 have been characterized at least to some extent, in plants (Buschmann and Lloyd, 2008). Here we only highlight a few actors.

5.3.1. Polymerization: the role of EB1

EB1 is a protein involved in the promotion of microtubule polymerization. EBI is a protein that binds to the (+) ends of microtubules (Akhmanova and Steinmetz, 2010, 2008; Schuyler and Pellman, 2001; Tirnauer and Bierer, 2000). In plants there are 3 orthologies, EB1 a, EB1 b and EB1 c (Korenbaum, 2002; Mathur et al., 2003). EB1 contains in its N-terminal part a Calponin Homology Domain (CH domain), responsible for its association with microtubules. EB1 allows the recruitment at the (+) end of growing microtubules of a large number of partners. The location of Eb1 allows the regulation of the microtubule network at an architectural level. EB1 increases microtubule dynamics (Coquelle et al., 2009; Rogers et al., 2002; Tirnauer et al., 1999). EB1 accumulates at

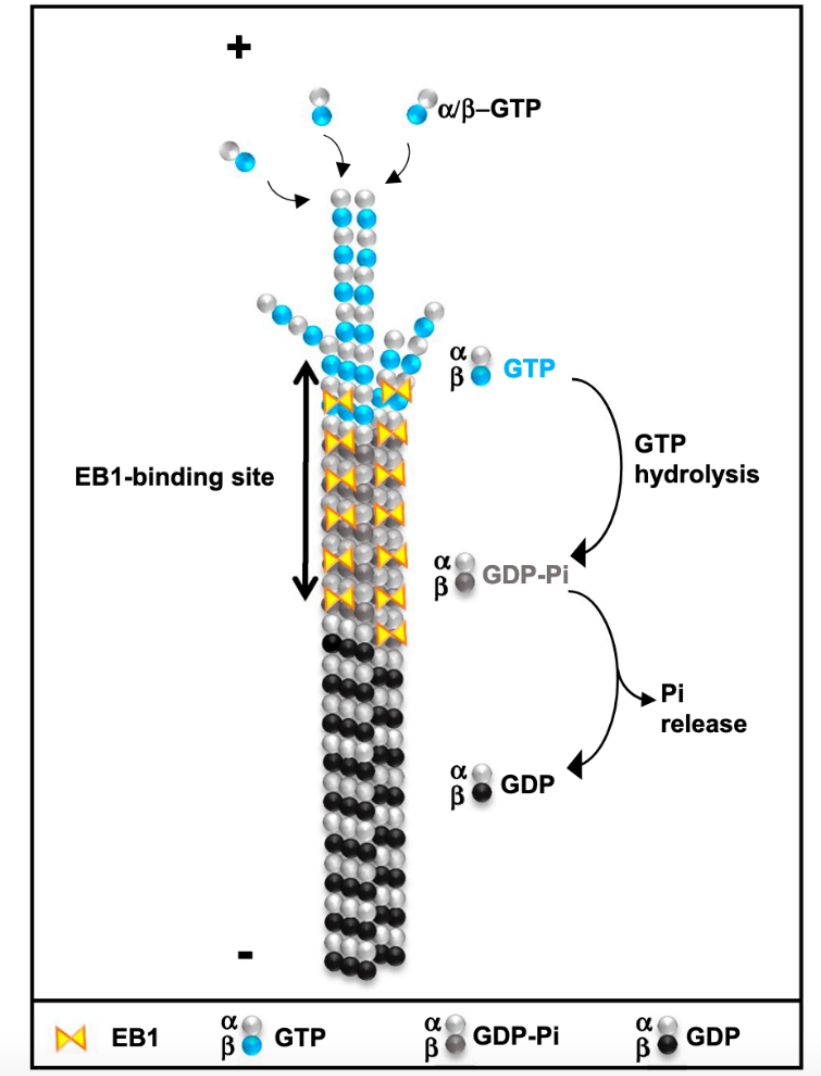

Figure 28: EB1

Nucleotide-dependent EB-binding region at the MT-plus end. MT polymerization is managed by incorporation of GTP-loaded α-/β-tubulin dimers at growing ends. The different nucleotide states of tubulin are presented with the β-tubulin subunit in blue (GTP), grey (GDP-Pi), and black (GDP). Microtubule plus ends undergo two mat-uration steps: GTP hydrolysis and Pi release from GDP-Pi. The EB1-binding site comprises two adjacent tubulin dimers loaded with either GTP-, GDP-Pi, or other intermediate states of GTP hydrolysis. (Nehlig et al., 2017)

the (+) end of the microtubules at the level of the conformational cap of the protofiles (Guesdon et al., 2016). EB1 thus allows the formation of microtubules with 13 protofilaments (Fig 28, des Georges et al., 2008; Maurer et al., 2012; Vitre et al., 2008; Zhang et al., 2015). Recently, EB1 was shown to contribute to microtubule bundling in plants (Molines et al., 2018).

5.3.2. Bundling: the role of MAP65s

One of the key features of certain MAPs is there role in microtubule bundling. This notably relates to the family of MAP65 proteins. Thanks to these proteins, microtubule bundles can be up to 80 times the size of a single microtubule filament (fig 29 – G). This also means that imaging with fluorescent tubulin will mostly these structures than single microtubules. When using MAP4-GFP or related fluorescent markers (e.g. involving the Microtubule Binding Domain of MAP4), only microtubule bundles are observed.

Microtubule bundling obviously change the mechanical properties of microtubules and therefore of the cells. For instance, in plants, it has been shown that the cells surrounding the stomata have a large number of bundles which would enable them to resist the opening and closing of the stomata (DeMichele and Sharpe, 1973; Franks and Farquhar, 2007). Note however, that bundling does not necessarily increase the microtubule network stiffness. In fact, the addition of MAP65-1 to in vitro-growing microtubules under hydrodynamic flow revealed that this protein rather make the microtubule softer. This was proposed to explain how *in vivo*, microtubules exhibit a lower persistence length than pure microtubules (Portran et al., 2013).

Studying the dynamics of the microtubule bundle is a challenging task. Nevertheless, several studies have been carried out on this subject. It would appear that the dynamics of free or bundle-forming microtubules are not significantly different and do not show different rates of polymerization or depolymerization (Shaw and Lucas, 2011). Using SIM microscopy, more recent studies have shown that, although the overall dynamics of free or bundle-forming microtubules are not significantly different, the velocity of the + ends is higher in bundles. Moreover, the polymerisation of all the microtubules within a bundle is synchronized (Komis et al., 2014).

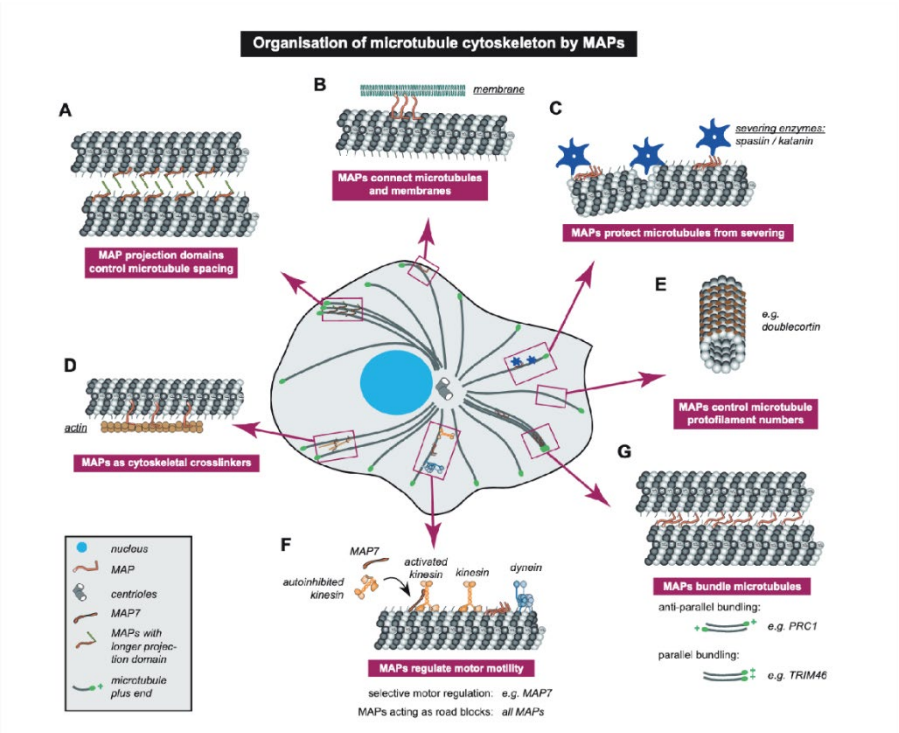

Figure 29: Schematic representation of the different ways MAPs can bind to microtubules

***A.** binding and spacing microtubules with long MAP projection domains; **B.** connecting microtubules to membranes; **C.** protecting microtubules from severing enzymes, and thus, from disassembly; **D.** crosslinking different cytoskeletal elements; **E.** controlling the protofilament numbers of microtubules; **F.** affecting the binding and motility of motor proteins by either forming a complex with the motor, or by occupying the motor path at the microtubule surface; **G.** promoting microtubule bundling, by neutralising acidic tubulin carboxy-terminal tails. (Bodakuntla et al., 2019)*

5.3.3. Catastrophe with kinases and severing with katanin

Microtubule catastrophe can be catalyzed by post-translational modifcations on tubulin, like phosphorylations. For instance, PHS1 is a kinase which promotes the destabilization of cortical microtubules in response to osmotic and saline stresses (Fujita et al., 2013; Naoi and Hashimoto, 2004; Pytela et al., 2010; Walia et al., 2009). PHS1 is inactivated by MAPK kinases (Pytela et al., 2010). NIMA-related kinases, like NEK6, directly phosphorylates tubulins, leading to microtubule depolymerization, with important consequences for plant cell shapes (Takatani et al., 2015).

Microtubule catastrophe also involves more large-scale modifications. The katanin protein allows the depolymerization of microtubules in an ATPasic manner (McNally and Vale, 1993). Consistently, in plants, the overexpression of katanin results in an increase in short microtubules in pavement cells (Stoppin-Mellet et al., 2006). Katanin is capable of cutting microtubules *in vitro* (Burk and Ye, 2002; Stoppin-Mellet et al., 2002). *In vivo*, katanin cuts microtubules at the point of intersection between two microtubules. Two new ends are thus produced. *In vitro* the (+) ends from the body of the microtubules depolymerize rapidly. *In vivo* katatin does not produce the same effect. Katanin will cut the microtubules transverse to the microtubule network. Thus the new ends (+) will polymerize. During a crossing in the presence of Katanin, a new microtubule is created. This allows the cell to reorient its microtubule network longitudinally (Lindeboom et al., 2013). Transverse microtubules are dynamics, so this orientation eventually disappears in favour of a longitudinal orientation (Lindeboom et al., 2013). Microtubule severing in plants appears to depend solely on KTN1, the catalytic p60 subunit of the katanin enzymatic complex (which also comprises different regulatory p80 subunits) (Lindeboom et al., 2013; Wightman et al., 2013; Wightman and Turner, 2007) (Fig.30). Inhibition of katanin leads to a significant reduction in the frequency of microtubule severing, a weakening of cortical microtubule co-alignment and a delay of various cortical microtubule rearrangements. Several Katanin regulators are known. RIC1 is an effector of the GTPase ROP6, which activates KTN1 to promote parallel ordering of the cortical microtubules, notably in pavement cells (Lin et al., 2013). SPR2, a microtubule-associated protein (MAP), accumulates at the microtubule crossover point to prevent separation by KTN1, allowing unordered cortical microtubules to persist in petioles (Wightman et al., 2013). Note however that this is debated as SPR2 was also shown to affect the stability of the microtubule minus ends, with opposite consequences on severing in hypocotyls (Fan et al., 2018).

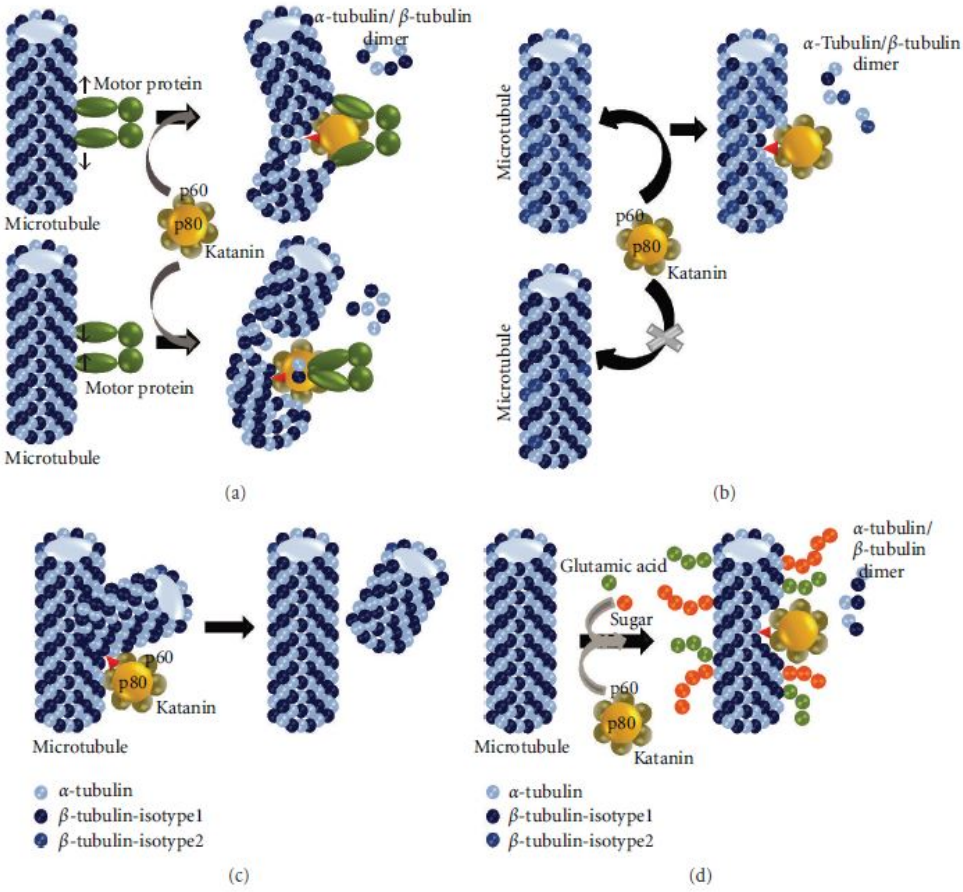

Figure 30: Models of Microtubule severing by Katanin.

A. *Motor proteins bind to microtubules and their movements cause structural bending/deformation (into S or V shape) of microtubules to release tubulins from deformed sites. Katanin binds to these sites and enhances the process of severing;* ***B.*** *Katanin preferentially binds to microtubules which are redundant in specific isotype (isotype2/TBB2) of β-tubulin and catalyzes severing process in these microtubules;* ***C.*** *Katanin binds to branching sites of aberrantly branched microtubule mesh to severe microtubules from branching points;* ***D.*** *Katanin binding and subsequent severing of microtubules is favored when microtubules are post-translationally modified (like poly-glycated, poly-glutamylated). (Ghosh et al., 2012)*

Like the tubulin kinases, katanin, and its regulators, respond to external cues. During the development of cell pavements, the microtubules are ordered locally to limit cell expansion, resulting in indentation. This local ordering of cortical microtubules requires a local accumulation of ROP6 GTPase (Fu et al., 2009), which recruits RIC1 to activate KTN1 (Lin et al., 2013). Light and auxin are used to induce dynamics reorientation of the microtubules in the hypocotyl. Transverse to longitudinal reorientation of cortical microtubules after auxin induction requires ROP6 GTPase RIC1 and KTN1. Similarly, auxin can activate KTN1 through ROP6 and RIC1 to promote reorientation of cortical microtubules. Auxin has been suggested to mediate the signaling of auxin to the ROP6-RIC1-KTN1 pathway (Chen et al., 2001), although this is highly debated because of the questionable role of ABP1 on the one hand, and the possibility that ABP-like proteins may still contribute to this response. The cortical microtubules of hypocotyls reorient when subjected to blue light. Blue light increases the frequency of microtubule severing (Fig 29, Lindeboom et al., 2013).

5.4. Microtubules and Cellulose synthesis

The wall is the extracellular matrix of plant cells. It plays a role in many processes such as growth, differentiation, defense against pathogens or water movement. The cell wall has a different composition depending on the stage of differentiation of the cells. After cell division, the two daughter cells are separated by a structure called the pectin polymer phragmoplast (Cosgrove, 2005). The primary wall is thus a fibrous mesh incorporated into polysaccharides. Like all walled organisms, the primary role of cell walls is to resist to hypo-osmotic stress: cell walls are stiff to prevent the bursting of the protoplast (Wolf et al., 2012). When cells reach a final size and differentiate, different types of secondary cell walls can be deposited depending on the cell types to which they belong (Oda and Fukuda, 2012).

Because of its relation to mechanical stress, the machinery behind the synthesis of the cell wall depends on the perception of mechanical signals. This include the secretory pathway: exocytosis is promoted by membrane tension, and thus when stress increases, secretion of wall matrix components (e.g. pectins, hemicellulose) is predicted to increase too. Another pathway involves the microtubules more directly: cellulose synthesis. Because cellulose microfibrils are thought to be the main load-bearing components in the wall, this is a central focus in plant developmental biology. This involves cortical microtubules (Fig 31).

It has been shown that the orientation of the cellulose microfibrils correlate with the orientation of the cortical microtubule network, making the microtubule organization essential for the direction of cell growth. Indeed, when the microtubule network is disrupted using drugs to depolymerize them, cell growth becomes isotropic (Green, 1962). This shows that in the absence of microtubules, the organization of the wall does not allow the cells to have a particular shape. The correlation between cellulose and microtubules is all the stronger as it has been shown that cellulose synthases move along the microtubules, as imaged by spinning disc confocal microscopy (Paredez, 2006). In addition, both cellulose synthase trajectories and microtubule alignment correlate when microtubules form rotation behaviors in young hypocotyls (Chan et al., 2010). Through the interaction between cortical microtubules and cellulose synthase, it is possible to predict the direction of cell growth. The interaction between cortical microtubules and cellulose synthase involves a large complex, including the linker protein Cellulose synthase interactive protein 1 (CSI1 (Bringmann, 2012; Li et al., 2012; Mei et al., 2012)), which binds both microtubules and cellulose synthase. The cellulose synthase complex includes many other regulatory proteins, and form rosettes of 6 hexamers of cellulose synthase (i.e. 36 cellulose synthase units). It has been proposed that CSI1 contributes to the rotation of the cellulose synthases to help weaving the cellulose microfibrils, although this is still debated (Fig 31, Bringmann, 2012).

Yet, the relationship between the orientation of the microfibrils and the orientation of the microtubule network is not so simple. A rapid disturbance of the microtubule network will not necessarily induce a change in the orientation of the cellulose (Sugimoto et al., 2003). It has also been shown that celluloses synthases do not necessarily interact with microtubules since they can move and along straight lines even in the absence of microtubules (Paredez, 2006). The microtubule network would therefore be more of catalyzer of cellulose reorientation than a necessary guidance mechanism (Chan and Coen, 2020). The microfibrils therefore have the capacity to partially self-organize at the level of the wall. However, the microtubules remain important structures for the organization of the microfibrils because, in addition to helping with their orientation, they are responsible for the length of the cellulose microfibrils, their deposition speed and the insertion of the cellulose microfibrils into the membrane (Gutierrez et al., 2009; Wasteneys, 2004). Consistently, most microtubule regulator mutants displays severe growth and shape phenotypes.

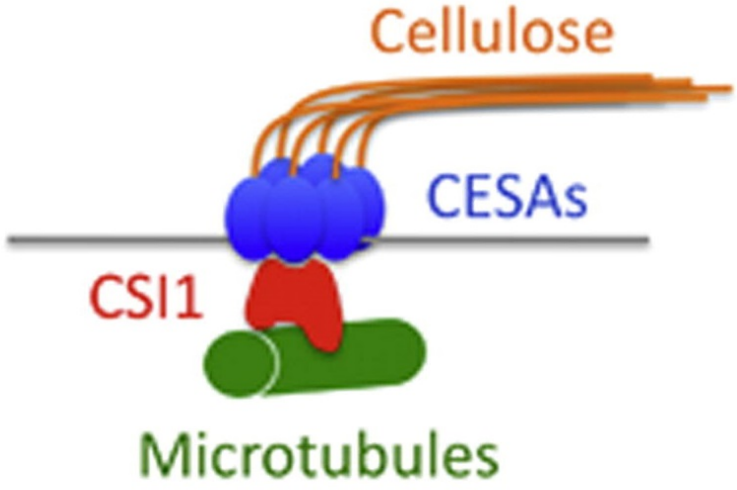

Figure 31: Deposition of cellulose

Microtubules guide the deposition of cellulose in the cell wall through the interaction with CSI1 and the CESAs function. Adapted from Landrein et al., 2013)

5.5. Microtubules and cortical cues

5.5.1 Cortical microtubules and cell shape

Microtubule behavior depends on cell geometry (Williamson, 1990). This conclusion builds on a solid array of experimental and modelling studies (Allard et al., 2010a, 2010b; Ambrose et al., 2011; Besson and Dumais, 2011; Dixit and Cyr, 2004; Eren et al., 2012, 2010; Hawkins and Liu, 2014; Nakamura et al., 2010; Trinh et al., 2021). In particular, microtubules tend to follow the shortest axis of the cell *in vivo*: they are often transverse (Fig 32). This is however not trivial: because of their high persistence length, microtubules should instead align along the flattest part of the cell cortex, and thus align along the long axis of the cell (Mirabet, 2018). Furthermore, microtubules can reorient in short timescales, i.e. without any change in cell geometry. For instance, when a cell is ablated in hypocotyls the microtubules reorient themselves independently of the cell geometry (Verger and Hamant, 2018). Similarly, blue light leads to the reorientation of microtubules in hypocotyl within 10 minutes (Fisher et al., 1996; Lindeboom et al., 2013).

To address these discrepancies, computational modeling has been used to identify possible emerging properties, notably in relation with cell curvature. Different models have been needed to understand and quantify these interactions. In particular, the CLASP protein, which is preferentially located in cell edges, may help microtubules to polymerize while being bent, thus impacting the whle microtubule network organization (Ambrose et al., 2011). This, together with auxin signaling, can recapitulate microtubule behavior and division planes in embryos (Chakrabotty 2018).

5.5.2. A cell cortex under tensile stress

Growth is controlled by two main parameters: turgor pressure and wall extensibility. Turgor pressure is the hydrostatic pressure exerted by the wall on the cell content (Cosgrove, 1993; Peters and Tomos, 1996; Schopfer, 2006). The wall is a visco-elastic structure. As long as the pressure does not exceed the elasticity of the wall, the deformation of the cell is reversible. However, when the pressure becomes greater than the elasticity of the wall, deformation becomes plastic and there is growth of the cell, i.e. an irreversible increase in volume (Boyer, 1988; Cosgrove, 1986, 1987; Matyssek et al., 1988). Turgor pressure is 10 times the atmospheric pressure. The mechanical stress

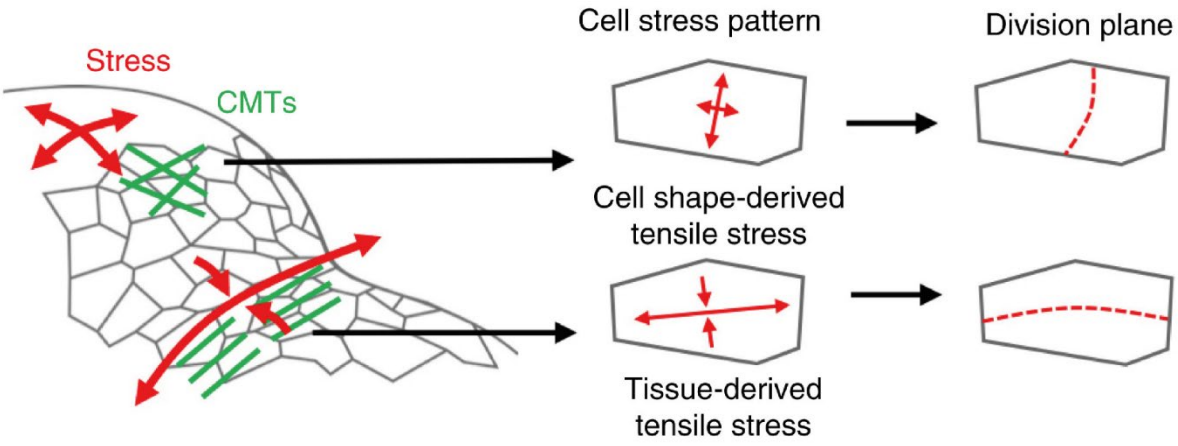

Figure 32: If tissue stress is isotropic (e.g., on top of the SAM), cells divide along the shortest path (Errera's rule), which may also correspond to the cell-derived tensile stress pattern. Regional stress may override cell shape-derived stress, leading to cells dividing along one of the longest paths (e.g., at the organ–meristem boundary). (Adapted from Trinh et al,2021)

applied to the wall is therefore very high, and comes down to tension only, at least in the simplest scenario. Tensile stress is anti-proportional to the thickness of the wall, i.e. the thinner the wall, the greater the tensile stress. The wall properties, both stiffness and mechanical anisotropy, thus modulate growth rate and direction respectively.

The ability of plant cells to resist turgor pressure depends largely on cellulose microfibrils. Cellulose is composed of microfibrils 3 to 5 nm in diameter, which are themselves composed of β1-4 glycans. The rigidity of these microfibrils forces them to have a linear organization in the wall in the form of a parallel network (Cosgrove, 2005). Cellulose is largely responsible for the anisotropy of growth (Green, 1962). Elongating cells have parallel transverse microfibrils which allow them to grow in a directional manner, along the longitudinal axis (Gertel and Green, 1977; Liang et al., 1997; Wei et al., 2006). It seems therefore that cortical microtubules are at the crossroad between cell shape and tensile stress.

5.5.3 Cortical microtubules and tensile stress

In theory, the main direction of tensile stress can modulate the orientation of the microtubules (Wasteneys and Williamson, 1987). This idea can be revisited with new in vitro developments. When microtubules sliding on viscoelastic gel like Polydimethylsiloxane (PDMS) were subjected to tension by stretching the substrate, the randomly moving microtubules aligned themselves along the tension lines. Since the application of tensile stress was transient, the orientation of the microtubules became random shortly after the tension was released. Conversely, microtubules that were put in compression in the same configuration aligned to be orthogonal to the direction of maximum compression (Inoue, 2016). Experiments using optical tweezers have shown that the effect of tension on the microtubules is direct and that the microtubules are able to perceive changes in the magnitude of the force (Franck, 2007; Trushko et al., 2013).

To test this hypothesis in *cellulo*, various mechanical perturbations have been performed on plant protoplasts and plant cells. For instance, cortical microtubules reorient when protoplasts are centrifuged (Wymer et al., 1996). The same thing has been described when protoplasts immersed in agarose are stretched: the microtubule network reorients (Fisher and Cyr, 2000).

Could this be sufficient to explain cortical microtubule orientation in tissues? To test this hypothesis, the pattern of tensile stress in tissues must be calculated. It has long been shown that the epidermal

layer of cells is usually under tension and compresses the internal cells.This hypothesis is correlated with the presence of epidermal cracks in cell-cell adhesion mutants (Verger and Hamant, 2018) or in mutants with extra internal growth and weaker outer epidermis (Asaoka et al., 2021). This is also consistent with the observation that the outer wall of the epidermis in stems is usually thicker than the inner cell wall (Kutschera and Niklas, 2007). This makes it possible to consider plant tissues as pressure vessels, with an epidermis under tension. In a cylindrical organ like a stem, tensile stress is thus predicted to be twice higher along the circumference (Hejnowicz and Sievers, 1995).

Interestingly, such stress pattern match cortical microtubule orientation in elongating cells: the transverse axis of the cell is also the direction of maximal tensile stress. Thus, cortical microtubule orientation may depend on cell geometry, primarily through shape-derived tensile stress pattern (Fig 33). The role of curvature-dependent regulators would modulate this response.

The correlation between stress patterns and cortical microtubule orientations has been observed in several plant tissues (protoplasts , epidermal peels, hypocotyls , shoot apical meristems, cotyledon, leaves, immature seeds, stems, sepals), at different scales, from subcellular to multicellular (Creff et al., 2015; Hamant, 2008; Hervieux, 2016; Jacques et al., 2013; Robinson and Kuhlemeier, 2018; Sampathkumar et al., 2014a; Verger et al., 2018; Wymer et al., 1996).

5.5.4 Cortical microtubules in pavement cells

Pavement cells are the epithelial cells of cotyledon. Cortical microtubules form dense networks in necks (where cells form indentation, when viewed from above) and are largely depleted in lobes (in front of a neck). This behavior relies on the ROP6-RIC1-Katanin pathway previously described (Lin et al., 2013).

Such shape also prescribe stereotypical tensile stress patterns in the outer wall. Interestingly, the direction of tensile stress has been modeled and the orientation of microtubules follows this main direction of stress, at least in young and fast expanding pavement cells (Sampathkumar et al., 2014a). This conclusion was further consolidated with micromechanical perturbations. In particular, the organization of the microtubules could be modified upon compression of the pavement cells: the anisotropy of the microtubules was increased after tissue compression. Cell ablation experiments also induced a reorientation of the microtubules around the ablation, following the predicted tensile stress pattern. Thus, the feedback model that was applied to tissues in previous work could also be

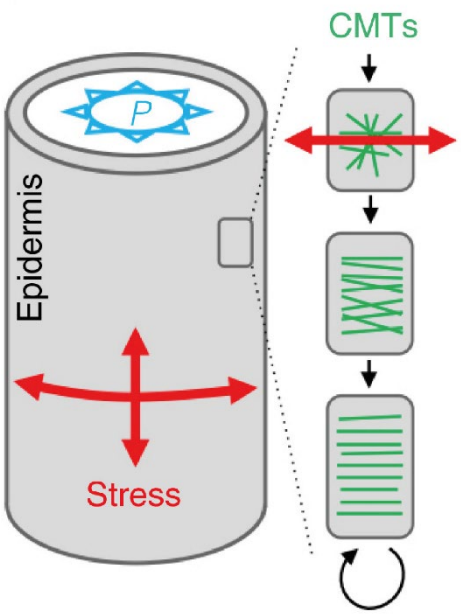

Figure 33: Relation between maximal tensile stress en CMTs alignement

Shape-derived stress pattern in a pressurized cylinder. In principle, the alignment of CMTs with the maximal tensile stress direction would prescribe the direction of cell elongation, thus maintaining both shape and stress pattern. (Adapted from Trinh et al,2021)

applied at the individual cell scale, even in cells with such complex shapes: cortical microtubules align with the stress pattern which will reinforce the cellulose wall at this point and thus change the shape of the cell (Fig 34, Sampathkumar et al., 2014b).

This model is still debated, notably because of the role of anticlinal walls in the final cortical microtubule orientation. Recent modeling work rather confirms that previous model, with a role of anticlinal walls in initiating the stress pattern and microtubule orientation, and stress on the outer wall, maintaining this orientation (Bidhendi et al., 2019). In my PhD, I used pavement cells as model systems to analyze cortical microtubule dynamics with our newly adapted light sheet microscopy for aerial organs. Because both spatial and temporal resolutions were increased, I also developed a quantitative pipeline to analyze the microtubule dynamics in different subcellular regions.

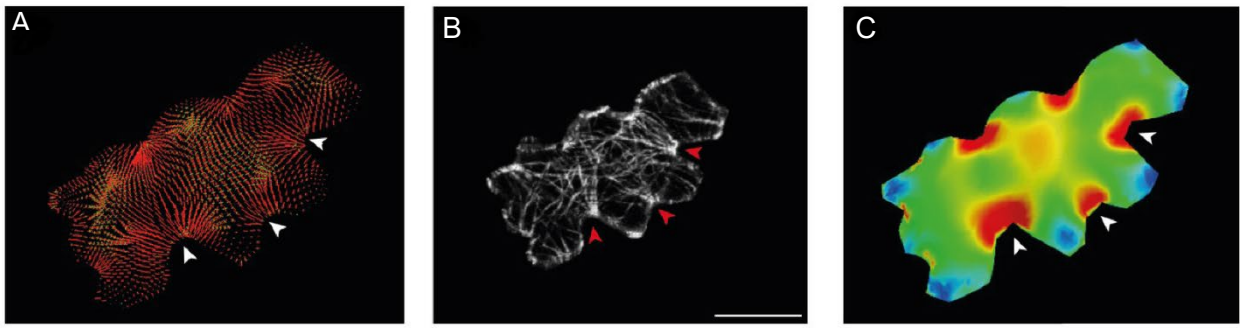

Figure 34: Microtubule patterns correlate with physical stress patterns.

A. *Largest stress direction (red) and second principal stress direction (green) in mechanical models of the pavement cell. White arrowheads indicate regions of convergence of directional tensile stresses in necks of pavement cells;* ***B.*** *Microtubule (YFP-MBD) orientations correlate with the maximal stress direction predicted in the mechanical model;* ***C.*** *Heat map showing the magnitude of stress distribution in the mechanical model. Arrowheads indicate regions of highest stress magnitude in neck regions. Scale bars 20 µm. (adapted from Sampathkumar et al, 2014)*

Main objective of the PhD

I had three goals during my PhD, as reflected by the three parts of the result section.

The first chapter is focused on a developmental question. More specifically, I analyzed the role of VIP3 in flower termination, and the robustness of the associated molecular pathway. To do so, I analyzed *vip3* mutants and contributed to reveal variable indeterminacy defects through wildfield and confocal microscopy. Focusing on specific gene regulator of stem cell maintenance, I relate these phenotypes to the variability of expression pattern of *AGAMOUS* and *WUSHEL*. Altogether this reveals that the biological processes supporting stem cell maintenance are less robust than anticipated.

Yet, confocal microscopy can limit the analysis of developing organs. In the second chapter, I adapted LSFM protocols to image aerial organs of plants. The main goal was to image shoot samples in LSFM without embedding in order to have the same versatility than confocal microscopy. Mounting of samples was validated for different types of aerial organs. The relative advantages and shortcoming of the different microscopy modalities were tested. Once validated that LSFM can produce images of similar or higher quality, I took advantage of LSFM depth of imaging and speed of acquisition to analyze locally the dynamics of microtubules in pavement cell. I could obtain a set of results showing differences of microtubule dynamics depending on subcellular localization in pavement cell and on genotype (*nek6* mutant).

The acquisition of images at high temporal resolution is a necessary condition to the analysis, but not a sufficient one. In the third chapter, I developed several analylitical methods to image a large range of samples for different types of applications. I focused the method on the analysis of sample surfaces from LSFM using MorphoGraphX. After this 2.5D extraction, I used a python library (TimageTK) to segment the images. In the end, this work provides a complete pipeline to acquire and analyze LSFM images from developing shoot organs. Because the three sections are still quite independent, the general discussion is split within the three chapters of the thesis.

Results

6. Paf1c defects challenge the robustness of flower meristem termination in Arabidopsis thaliana

6.1. Abstract

While accumulating evidence suggests that gene regulation is highly stochastic, genetic screens successfully uncovered master developmental regulators, questioning the relationship between transcriptional noise and intrinsic robustness of development. Here we use the Arabidopsis Paf1c mutant vip3, which is impaired in several RNA Pol II-dependent transcriptional processes, to identify developmental modules that are more or less resilient to large-scale genetic perturbations. We find that the control of flower termination is not as robust as classically pictured. In Angiosperms, the floral female organs, called carpels, display determinate growth: their development requires the arrest of stem cell maintenance. In vip3 mutant flowers, carpels displayed a highly variable morphology, with different degrees of indeterminacy defects up to wild-type size inflorescence emerging from carpels. This phenotype was associated with a variable expression of two key regulators of flower termination and stem cell maintenance in flowers, WUSCHEL and AGAMOUS. This phenotype was also highly dependent on growth conditions. Altogether, these results highlight the surprisingly plastic nature of stem cell maintenance in plants, and its Paf1c dependence.

The results and discussion in this section are extracted from a published article, where I appear as co-1st author:

Fal K*, Cortes M*, Liu M, Collaudin S, Das P, Hamant O, Trehin C (2019) Paf1c defects challenge the robustness of flower meristem termination in *Arabidopsis thaliana*. Development. 146(20):dev173377. doi: 10.1242/dev.173377.

The original pdf is also included in the Annex. More specifically, I contributed to figures 34, 35, 36, 37, 38, 39, 40, 43 and 45.

6.2. Results

6.2.1. *vip3* mutants exhibit strong and variable flower indeterminacy

vip3 mutants have previously been reported to display a number of growth defects (Dorcey et al., 2012; Fal et al., 2017; Takagi and Ueguchi, 2012; Zhang et al., 2003). When *vip3* mutants were grown for 3 weeks under short day conditions (21°C), and then transferred to continuous light (16°C), we observed a dramatic loss of floral indeterminacy such that, in some *vip3* plants, a wild-type sized inflorescence would grow out of a carpel (Figs. 35 A,B, Fig. 14, N>30 plants). Whereas this phenotype was observed in both *vip3-1* and *vip3-2* alleles (Fig. 37 - C), in these growth conditions, silique development in the wild type remained entirely unaffected (Fig. 37 – A - C, N>30 plants).

To check whether this phenotype depends on either the temperature or day length shift, we next compared the *vip3-1* phenotype in different growth conditions. Plants grown in similar light conditions but at 21°C in continuous light instead of 16°C displayed a similar phenotype (Fig.40, N=32 plants). We could also see the indeterminacy phenotype when *vip3-1* was constantly grown under short day conditions (Fig. 41 - A, N=9 plants) and under short then long day conditions (Fig. 41 - B, N=22 plants). When grown in long days, the *vip3* mutant was much smaller, with shorter stems, and exhibited a large number of aborted siliques without indeterminacy (Fig. 41- C, N=36 plants). Therefore, floral termination defects in *vip3* only require short day conditions and no other specific growth conditions. Note that, except when plants are grown exclusively under long day conditions resulting in sterile siliques (Fig. 41 - C), the *vip3* mutant was able to produce seeds but with a very low rate (Fig. 42).

The extent of the floral indeterminacy defects in *vip3* depended on growth conditions: the *vip3* phenotype was the most affected in short day and in short day then continuous light

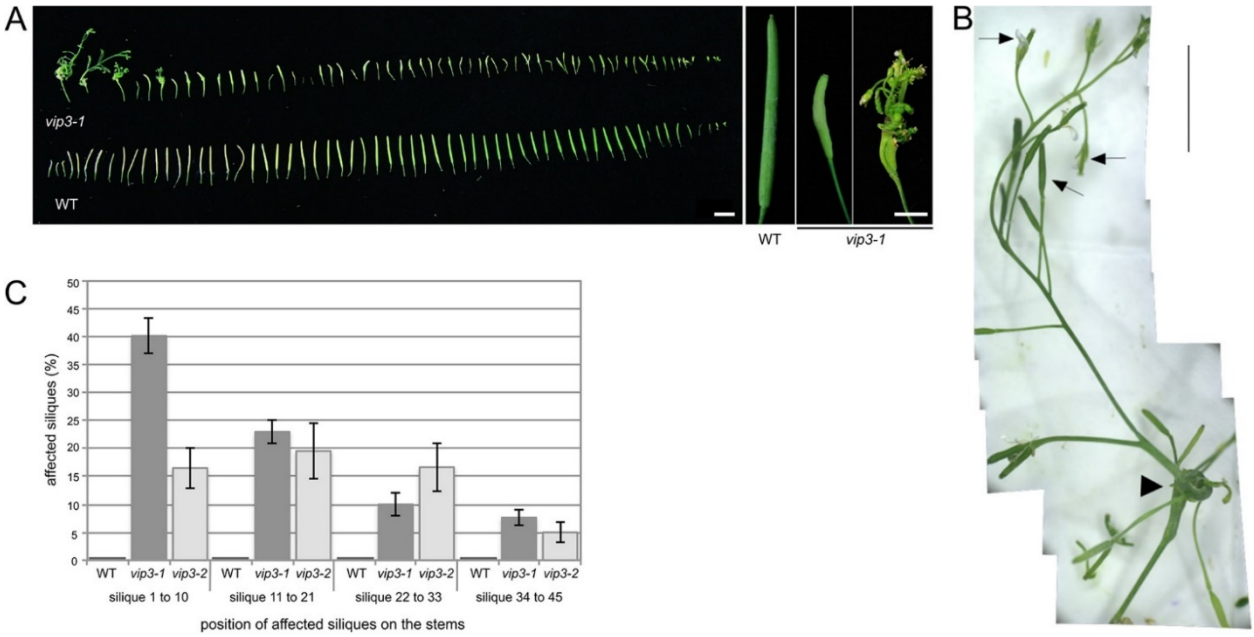

Figure 35: vip3 mutants can exhibit a severe flower indeterminacy phenotype.

A. *Representative phenotype of wild-type and vip3 siliques, from plants grown in short day 21°C then continuous light 16°C conditions (N>30 plants), harvested in a sequence of initiation from the stems of (left panel). Scale bar: 1 cm. Right panel: representative siliques of the wild type and vip3 displaying different degrees of phenotypic defects. Scale bar: 5 mm;* ***B.*** *Representative image of the most severe phenotype in vip3-1 flowers. Arrowhead points at the primary silique; arrows point at secondary carpels. Scale bar: 1 cm;* ***C.*** *Distribution (%) of affected siliques on the stems of the wild type (N=13), vip3-1 (N=60) and vip3-2 (N=20) grown in short day 21°C followed by continuous light 16°C condition (on average, 20% of vip3-1 and 14% of vip3-2 siliques displayed visible indeterminacy defects in these conditions).*

(16°C or 21°C) conditions and appeared to be the closest to a full reversal of floral identity reported in the literature. Note that we observed similar phenotypic defects in *vip6*, a mutant for another component of the Paf1 complex (Fig. 41 - D, N=19 plants). Such data further confirm that flower phenotypes result from defect in the Paf1-C complex and not in the Exome complex involved in mRNA turnover and whom VIP3 is also part of (SKI8) (Dorcey et al., 2012)

Last, the *vip3* indeterminacy phenotype was also highly variable within a single plant (Fig. 36 - A, Fig. 39). In comparison to the wild type, the phenotype ranged from short and bumpy siliques to completely open siliques containing a full inflorescence. With respect to the position of the siliques along the inflorescence stem, we found that early siliques were very often the most affected, although even the last siliques occasionally exhibited a strong phenotype too (Fig. 36 C, Fig. 39 - B).

6.2.2. Supernumerary organs develop from the center of the floral meristem

Except for branching meristem that develop from bract axils in species with a dichasium inflorescence (Claßen-Bockhoff and Bull-Hereñu, 2013) or from sepal axils in *ap1* mutants that lack petals and have sepals displaying bract like features (Irish and Sussex, 1990; Mandel et al., 1992), there are two ways in which flower indeterminacy may occur: either the flower maintains its stems cells after stage 6 (Prunet et al., 2009) (Prunet et al., 2009), or ovules are homeotically converted into carpels (e.g. (Modrusan et al., 1994; Pautot et al., 2001)). In the latter case, one would expect to see multiple carpels growing within a single primary carpel. We never observed such a phenotype in *vip3* mutants, where instead the supernumerary organs all arose from the same stem or at least belonged to the same structure. It is therefore more likely that flower indeterminacy in *vip3* mutants is due to a delay in flower termination. To confirm that hypothesis, we generated longitudinal sections through carpels in both wild-type and *vip3* carpels, and stained the structures with toluidine

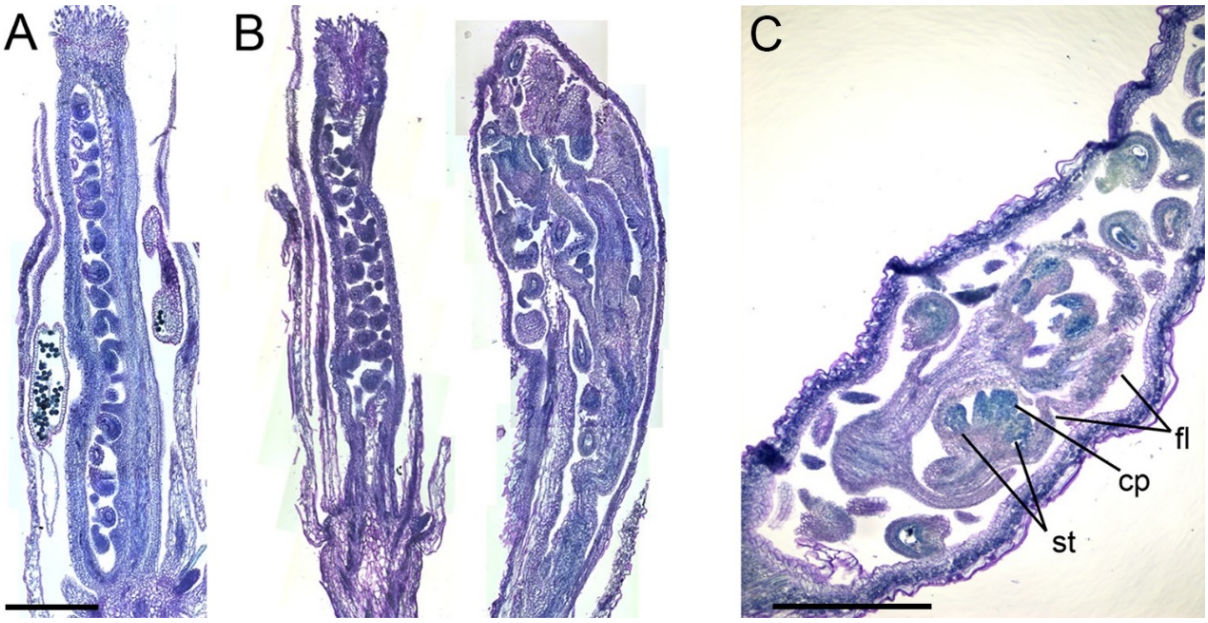

Figure 36: Inflorescence stem and floral organs can be detected in vip3 siliques.

A-C. *Sections in young siliques, stained with toluidine blue. WT; (**A.**) and representative vip3 (**B.**) siliques that illustrate the spectrum of vip3 phenotypes. (**C.**) Section of vip3 silique that demonstrates the presence of floral structures (fl – flower, cp – carpels, st – stamens) inside the silique. Scale bars : 500 µm.*

blue. We observed that supernumerary organs always developed within the primary carpels on a stem emerging from the bottom of the flower (Fig.36, N=44 carpels). We never detected supernumerary organs emerging from ovules. The presence of such long stems within the carpel had not been reported in other indeterminate mutants such as *crc ult*, *crc sqn, crc rbl, pwd, clv1*, or *knu* (Clark et al., 1993; Prunet et al., 2008; B. Sun et al., 2009; Yumul et al., 2013).

6.2.3. RNA-seq analysis of vip3-1 mutant shoot apices reveals genomewide expression defects

Given the strength of the phenotype, we first checked whether specific pathways are affected in *vip3*. To do so, we performed a RNA-seq analysis of the *vip3-1* mutant, using shoot apices (Fig. 43 -A -B, see Material and methods). Note that this material only contained meristems and flowers up to stage 3 (i.e. not fully developed). The fold change for each gene is expressed in the log2 scale (meaning that a factor of e.g. 1 corresponds to a 2-fold change). This analysis revealed defect in *FLC* expression (down-regulation by a factor 4.6, Fig. 43 - C) as already reported (Oh et al., 2008). However, this large-scale analysis did not reveal clear-cut defects in specific flowering pathways, but rather global

defects in the transcriptome, even if we cannot exclude any defects on specific pathways due to statistical and/or detailed annotations limitations. Genes from the same family (e.g. MADS) displayed either reduced (e.g. *AGL31, AGL77)* or enhanced (e.g. *AGL71*) mRNA accumulation in *vip3-1* (Fig. 43 - C). A few putative regulators of *WUS*, such as *ULT2,* exhibited a significant decrease of mRNA accumulation (by a factor 3.1), while *CLV3* mRNA accumulation was higher (by a factor 2.4) in *vip3-1* (Fig. 43 - C). Other putative regulators such as *PHB, ERL1, HAM3, PAN* also show higher mRNA accumulations but with lower rates (by factors 0.6, 0.8, 1 and 1.1, respectively, Fig. 43 - C). Similarly, we also found that hormone signaling pathways were affected, albeit without any clear-cut, specific trend. Yet, expression of genes involved in both auxin and cytokinin pathways seemed to be affected

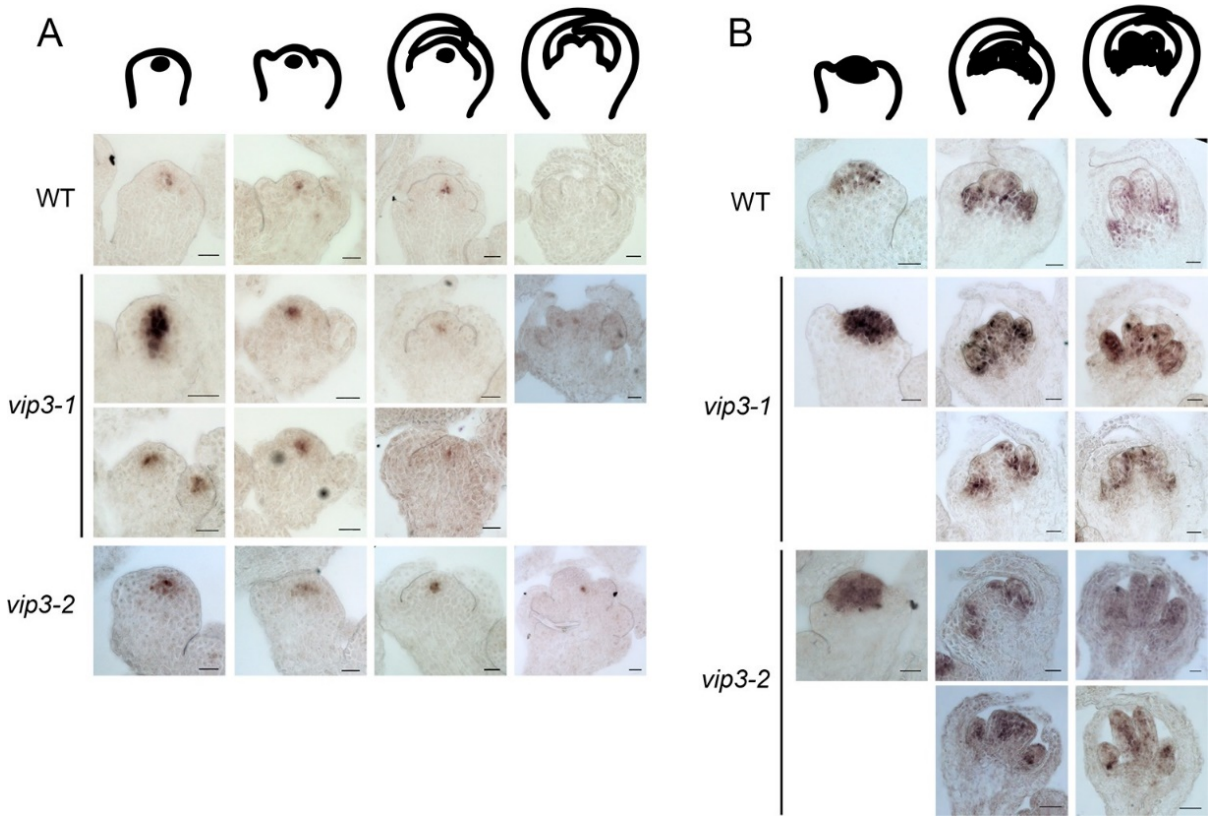

Figure 37: Expression patterns of WUS and AG in vip3 flowers.

*Representative in situ hybridization of WUS (**A**, NWT=34 flowers, Nvip3-1=30 flowers, Nvip3-2=45 flowers) and AG (**B**, NWT=33 flowers, Nvip3-1=35 flowers, Nvip3-2=12 flowers) transcripts in wild-type and vip3 (vip3-1 and vip3-2) flowers at four or three different developmental stages (as represented by schematic*

(Fig. 43 - D). Such data are consistent with previously reported phyllotactic defects in *vip3* (Fal et al., 2017), to recently published data on hormonal control of floral determinacy (Yamaguchi et al., 2018; Zhang et al., 2018) as well as indeterminacy defects reported here. Note that the RNA-seq data obtained previously on *vip3* seedlings also reflected such genomewide alteration, without clear-cut targets (Oh et al., 2008). Altogether, these data are consistent with the hypothesis that the *vip3* mutant would not affect specific pathways, but rather increase transcriptional noise, as assessed in yeast (Ansel et al., 2008). Ideally, single cell RNA-seq analyses would provide quantitative data on transcriptional noise in plants. These results thus call for gene-by-gene analysis of expression patterns of specific regulators of stem cell maintenance and flower termination.

6.2.4. Development of supernumerary organs result from the prolonged maintenance of stem cells in the center of the flower

As our phenotypic analysis suggests that the *vip3* indeterminacy phenotype is caused by a prolonged maintenance of stem cells in flowers, we focused our analysis on the integrator of stem cell maintenance and flower termination, *WUS*. Using *in situ* hybridization, we observed a bright and localized signal in the organizing center of wild-type SAM and young flowers until stage 5 or 6 (Fig. 37 - A, N_{WT}=34 flowers, (Mayer et al., 1998). In *vip3*, we observed flowers with a similar pattern, but some others with more variable patterns. In particular, we could detect *WUS* expression at the center of flowers at a much later stage than in the wild type (Fig. 37- -A, Fig. 43 - B) which is consistent with the indeterminacy phenotype. *WUS* expression domain was also much broader than that of the wild type in certain *vip3* flowers (Fig. 37- A, Fig. 43 , $N_{vip3\text{-}1}$=30 flowers, $N_{vip3\text{-}2}$=45 flowers). To account for this variability in the spatial domain of *WUS* mRNA accumulation in *vip3*, we distinguished different types of patterns: whereas the wild type displayed a single robust pattern, the *vip3* mutant exhibited either a normal *WUS* expression domain (in 51 out of 73 meristems) or a larger and deeper *WUS* expression domain (in 22 out of 73 meristems, Fig. 43 - C). To further confirm these trends, we next analyzed the expression of *WUS* in a line

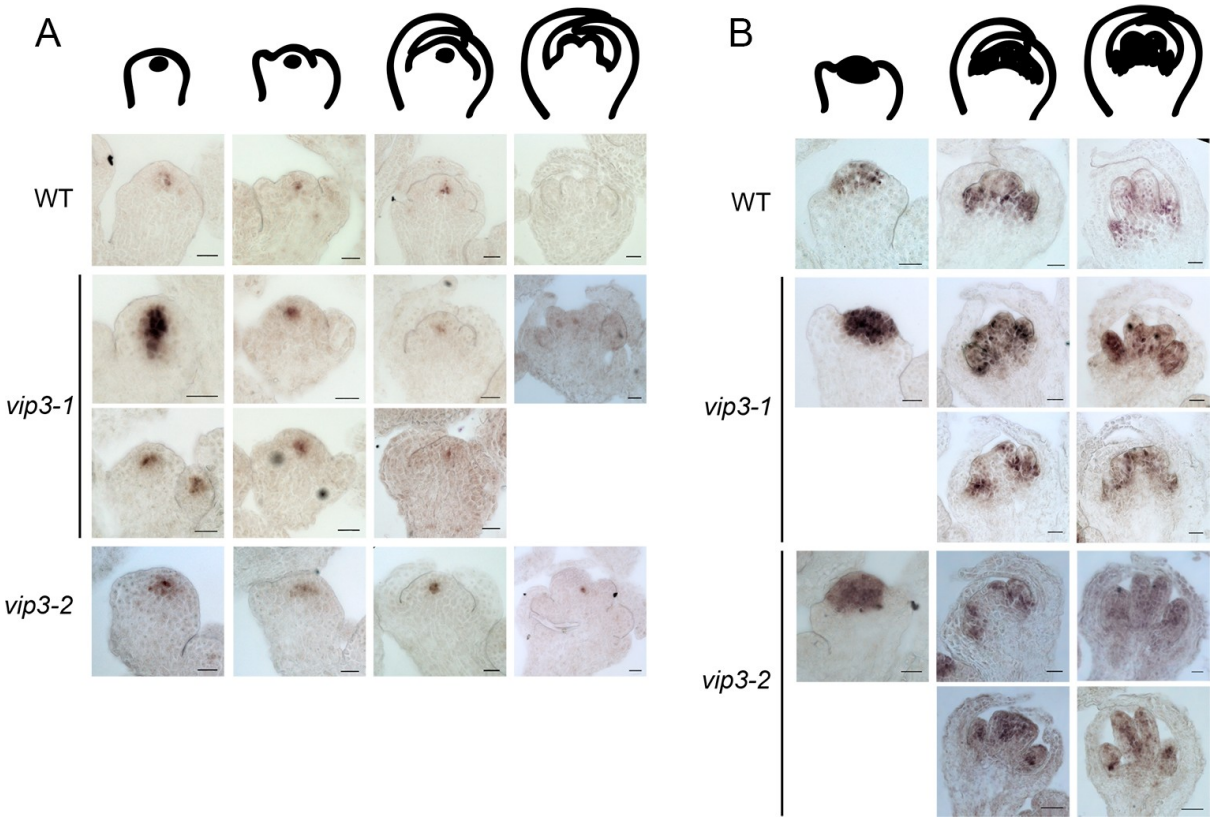

Figure 38: Expression patterns of WUS and AG in vip3 flowers.

*Representative in situ hybridization of WUS (**A**, NWT=34 flowers, Nvip3-1=30 flowers, Nvip3-2=45 flowers) and AG (**B**, NWT=33 flowers, Nvip3-1=35 flowers, Nvip3-2=12 flowers) transcripts in wild-type and vip3 (vip3-1 and vip3-2) flowers at four or three different developmental stages (as represented by schematic*

expressing a fluorescently tagged under the control of *WUS* promoter (*pWUS::3xVENUS-N7* (Pfeiffer et al., 2016)). The fluorescent pattern was wider in both

wild-type and mutant flowers, as compared to our *in situ* hybridization data. Wider *pWUS::GFP* expression domain in the wild type have already been reported (e.g. (Gordon et al., 2009)). Nevertheless, we clearly observed an even wider expression of *WUS* in *vip3* flowers, when compared to wild-type ones (Fig. 38- -A, N_{WT}=94 flowers, $N_{vip3\text{-}1}$=58 flowers). When quantifying the area of *WUS* expression, we found it to be up to twice larger in *vip3* than in the wild type (Fig. 38- B). The coefficient of variation of *WUS* expression area was also significantly increased in *vip3* (Fig. 45 - A). The quantification of the average fluorescence intensity suggested a mild reduction of *WUS* promoter activity in *vip3*, although this might reflect a larger gradient domain (Fig. 38- C). Based on both *in situ* hybridization data and fluorescent reporter lines, *WUS* expression domain appears variable and rather enlarged in *vip3*. As ectopic expression of *WUS* in flowers is also known to generate extra organ in the center of the flower (Lenhard et al., 2001), our data are consistent with the macroscopic indeterminacy phenotype in *vip3*. Note that we could not detect a significant effect of the *vip3* mutation on the *CLV3* spatial expression domain by *in situ* hybridization. Yet, *CLV3* expression seemed to be maintained at later flower stages than in the wild type (in 6 out of 15 flower meristems beyond stage 6, Fig. 46, N_{WT}=10 meristems, 12 flowers, $N_{vip3\text{-}1}$= 9 meristems, 14 flowers, $N_{vip3\text{-}2}$=5 meristems, 5 flowers,). This is consistent with an overall delay in flower termination.

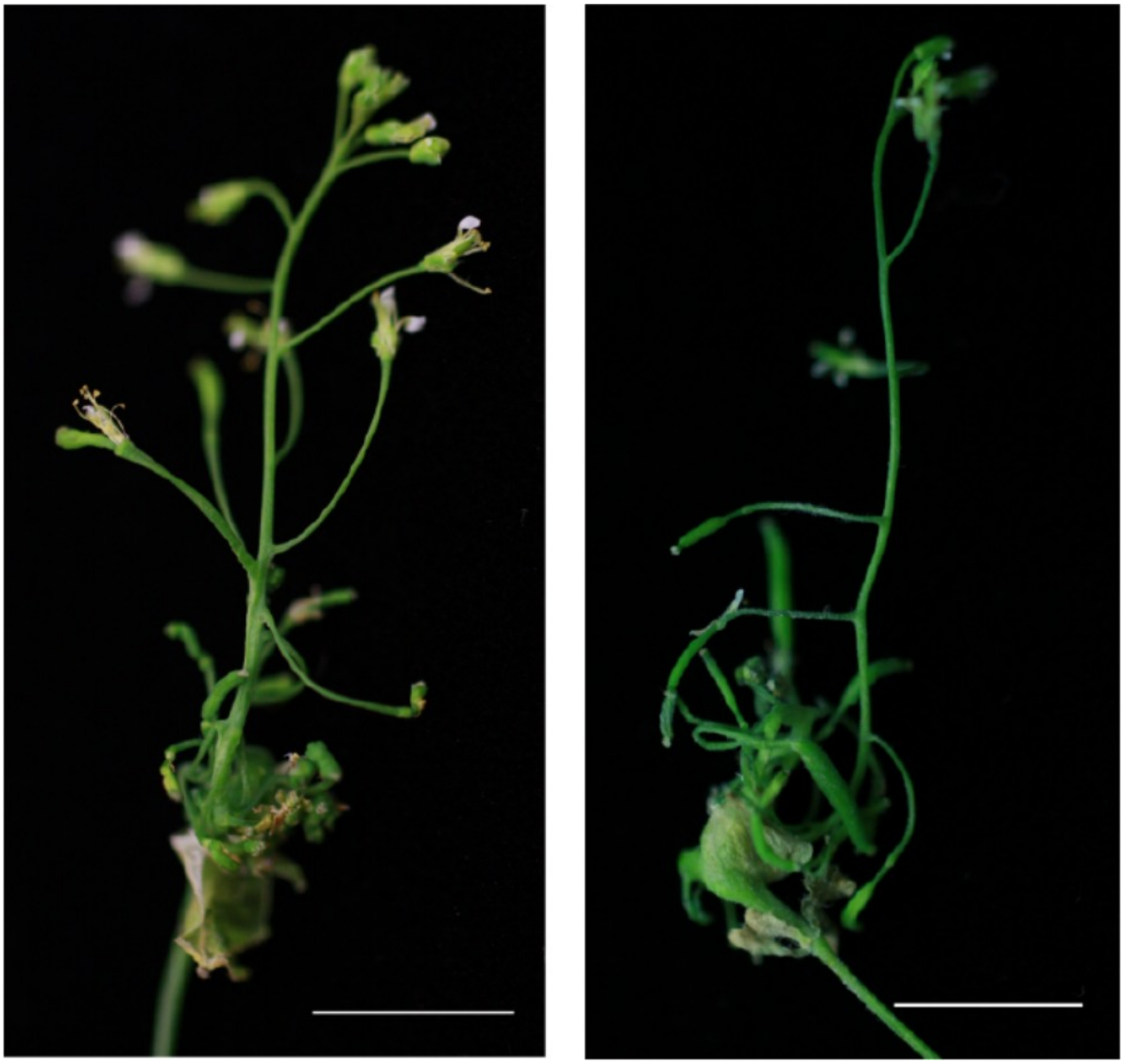

Figure 39: Examples of the most severe indeterminacy phenotypes in vip3-1 siliques.

Representative images of the most severe phenotypes in vip3-1 flowers, displaying an inflorescence stem with siliques and flowers, emerging from a silique. Scale bar: 1 cm.

6.2.5. Mutation in VIP3 results in a lower expression of *AG* in the center of the flower

Given that the *vip3* indeterminacy phenotype is strong and variable, and that it is associated with perturbed stem cell maintenance control, we analyzed the expression of the primary regulator of stem cell arrest in the flower, *AGAMOUS* (*AG*). Analysis of the *AG* mRNA pattern through *in situ* hybridization revealed the expected pattern in the wild type, with strong accumulations in floral whorls 3 and 4, prior to the emergence of stamens and carpels (Fig. 37 - B, N_{WT}=33 flowers). Similar patterns were also observed in certain *vip3* flowers, but *AG* mRNA accumulation appeared much reduced in the center of the whorl 4 in other flowers (Fig. 37- B, $N_{vip3\text{-}1}$=35 flowers, $N_{vip3\text{-}2}$=12 flowers). To further confirm this result, we generated a fluorescently tagged version of AG under its own promoter (*pAG::AG-2xVenus*) and analyzed its expression profile. These data confirmed the results from the *in situ* hybridizations, while also showing a globally reduced level of AG in certain *vip3* flowers (Fig. 38– A - C, N_{WT}=54 flowers, $N_{vip3\text{-}1}$=41 flowers). AG signal intensity was also more variable in *vip3* (Fig. 45 - B). The global area of AG expression was not significantly different in *vip3* and in the wild type, consistent with the observation that the contours were not strongly affected, and that only the center of flower exhibited defects in AG expression (Fig. 38- B). Altogether, these results show that defects in Paf1c-dependent control of transcriptional noise lead to a delay in flower termination, notably through *AG* and *WUS* (Fig. 38- D).

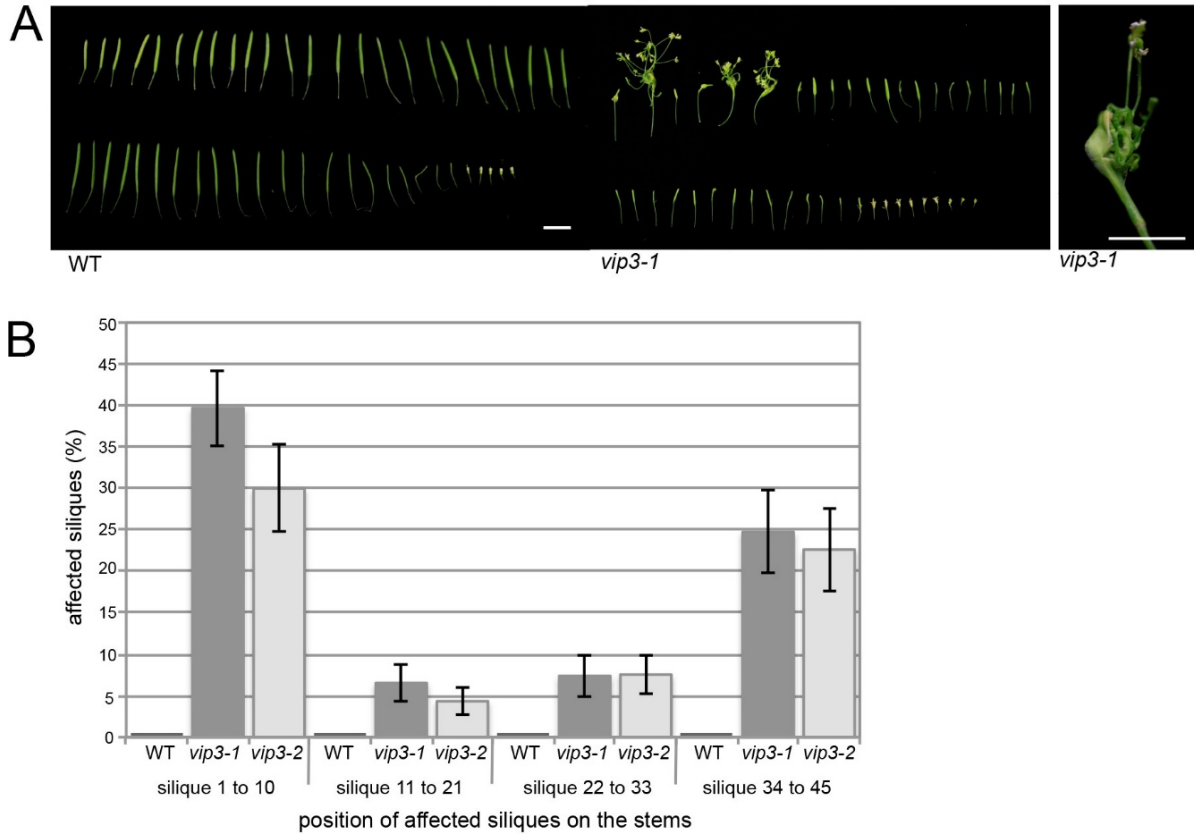

Figure 40: vip3 phenotype in short day then continuous light 21°C.

A. *Phenotype of WT (left panel) and vip3-1 (middle panel) siliques, from plants grown in short day 21°C followed by continuous light 21°C conditions, harvested in a sequence of initiation along the stem. Scale bar : 1 cm. Right panel shows representative silique of the vip3 displaying the indeterminacy phenotype. Scale bar : 5 mm;* ***B.*** *Distribution (%) of affected siliques along the stems of the wild type (N=13), vip3-1 (N=32) and vip3-2 (N=21) grown in short day 21°C followed by continuous light 21°C condition (on average, 19% of vip3-1 and 17% of vip3-2 siliques displayed visible indeterminacy defects in these conditions).*

6.3. Discussion

We have uncovered a strong floral indeterminacy phenotype in *vip3*. Flower development is usually considered to be highly robust in *Arabidopsis thaliana*. Nonetheless, chimeric flowers can be produced at rather low frequency (Hempel and Feldman, 1995). Such flowers result from primordia exhibiting both flowers and paraclades (lateral flowering shoot) features. Here, *vip3* flowers develop normally (in term of identity) but, for a variable proportion, do not stop producing organs beyond stage 6 resulting in short and bumpy siliques up to completely open siliques containing a full inflorescence. Most indeterminacy phenotypes reported so far result in the production of extra floral organs, mostly carpels and stamens, rarely petals except in strong *ag* mutants that reiterate complete flowers (Bowman et al., 1989; Prunet et al., 2008). Thus, in mutants with weaker phenotypes than that of *vip3*, floral meristem identity is never, or extremely rarely, lost. The only cases where a full new inflorescence was reported is in the *clv1-4* flowers where, in rare cases, a new inflorescence with developing flowers emerged from the gynoecium (Clark et al., 1993). Although this is obtained through gain of function, the *pp35S::XAL2* line, in which the MADS box transcription factor XAL2/AGL14 is overexpressed, also displays major indeterminacy defects, resembling that of *vip3* mutants (Pérez-Ruiz et al., 2015). Our results in *vip3* mutants suggest that full reversion may be reachable through a more global perturbation of transcription. This calls for a more systemic investigation of the molecular players behind floral indeterminacy. In fact, these results also question the limits of the reductionist approach: genetic screens for floral indeterminacy did not uncover the *vip3* mutant so far, either because growth conditions were not appropriate, or because variable phenotypes are less likely to be identified and selected.

Early stages of growth in short day conditions appeared essential to trigger the indeterminacy phenotype in *vip3*. This might be consistent with the reported role of the Paf1 complex in the regulation of flowering time and *FLC* expression (Zhang et al., 2003). This also reveals that a rather late phenotype (carpel differentiation) depends on very early

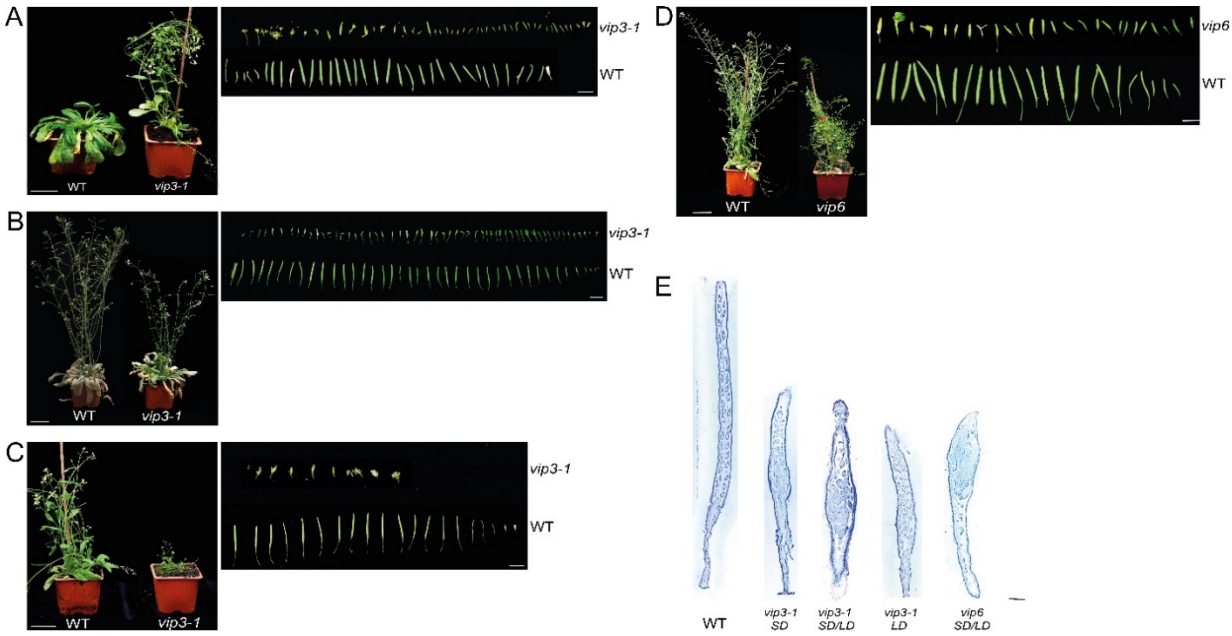

Figure 41: Indeterminacy phenotype in different growth conditions and in different mutants of the Paf1 complex.

A-C. *Phenotypes of WT and vip3-1 mutants grown in short day conditions (**A**, N=9 plants), in short then long day conditions (**B**, N=22 plants), and in long day conditions (**C**, N=22 plants);* ***D.*** *Phenotype of WT and vip6 mutant grown in short day 21°C followed by continuous light 16°C conditions displaying the indeterminacy phenotype (N=19 plants). For each condition, left panels display wild-type and vip adult plants, and right panels the siliques harvested in the order of their initiation along the stem;* ***E.*** *Representative sections in young siliques, stained with toluidine blue, of vip3-1, in each culture condition, and vip6 mutant, displaying the indeterminacy phenotype. Scale bars : 3 cm (**A-D**, left panels); 1 cm (**A-D**, right panels); 500 µm (**E**).*

cues during development. Our findings thus suggest that floral indeterminacy is much more plastic than anticipated, integrating the larger plant status, early on in development. The indeterminacy defects are not detected in long day conditions, but are observed in short day or continuous light conditions. Given that the latter growth conditions enhance meristem size (Hamant et al., 2014), it is possible that a threshold in meristem size is required for the indeterminacy phenotype to exist. In this respect, cytokinins are likely to play a strong integrator role, given their known impact on the regulation of *WUS* expression and meristem size (Landrein et al., 2018; Pfeiffer et al., 2016). Beyond

cytokinins, the larger hormonal network is likely to be involved. For instance, in our RNA-seq analysis, we also find that YUC4, a target of AG and CRC (Yamaguchi et al., 2018), is down-regulated in *vip3-1*. It remains to be shown whether such conclusions apply to other species; data in impatiens may suggest that it is the case (Pouteau et al., 1997).

As *AG* is deregulated in *vip3* mutants, our study also introduces Paf1c as a new player in the flower termination pathway. The use of lines expressing the antisense *AG* RNA reported a range of phenotype spanning from a weak indeterminacy phenotype (normal flower with few extra organs developing inside the primary carpels) to the canonical *ag* phenotype ([sepals-petals-petals]n), each category corresponding to a lower level of endogenous *AG* expression (Mizukami and Ma, 1995). In *vip3*, we observed weaker AG expression in the floral domain that corresponds to the 4th whorl subdomain that develop carpel margins and placenta. The reduced AG level in *vip3* may be consistent with the reported increase in H3K27me3 over the *AG* region in the mutant (see Figure S4 in (Oh et al., 2008)). Our study thus opens the possibility that part of the plasticity in carpel development relies on Paf1c-dependent *AG* expression.

Lastly, our results echo the rising role of incomplete penetrance in developmental plasticity. Incomplete penetrance is intrinsically caused by random fluctuations in gene expression (Raj and van Oudenaarden, 2008). Such variability contribute to cell fate specification in multicellular organisms (Chang et al., 2008). The existence of such variability may lead to incoherencies in gene networks; yet it would also provide a way for the network to become less sensitive to environmental fluctuations. In other words, cells would still retain the ability

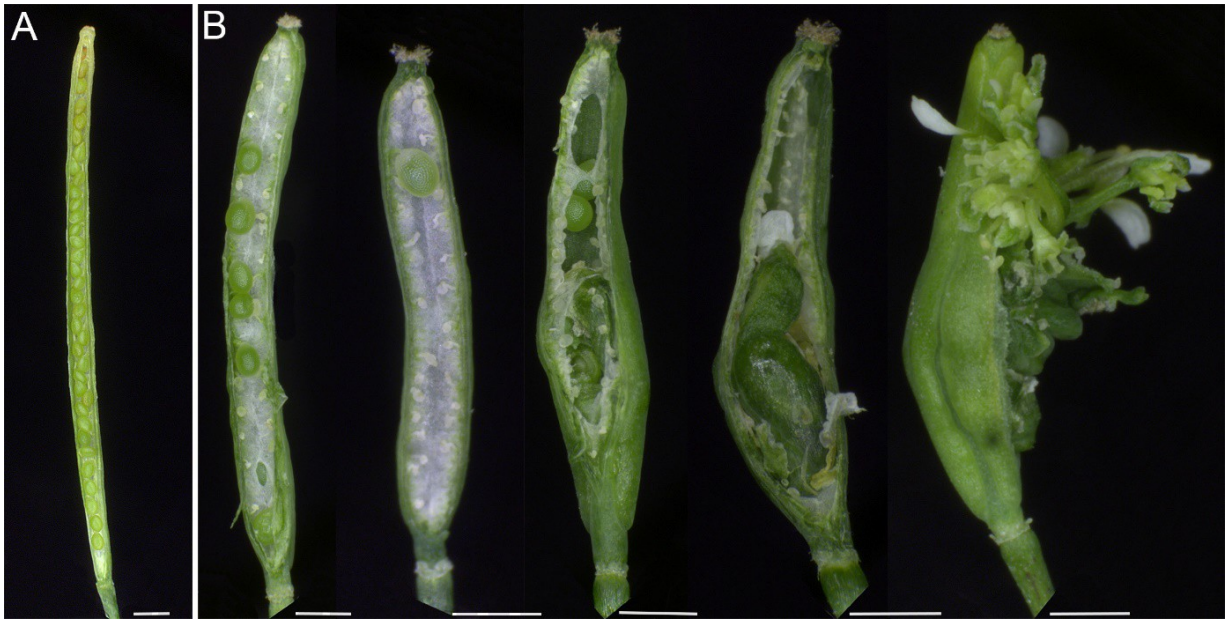

C	Number of ovules per silique		Number of aborted ovules per silique		Number of fertilized ovules per silique	
	WT	vip3-1	WT	vip3-1	WT	vip3-1
Mean	69,4	74,3	2,8	19,7	64,6	6,1
Standard deviation	3,9	18,2	0,9	11	3,7	6,8
Standard error of the mean	0,5	2,1	0,1	1,3	0,4	0,8
% compare to the total number of ovules per silique	-	-	4	26,5	93,1	8,2

Figure 42: Proportion of aborted ovules and seeds in vip3-1.

A-B. *illustrates the range of phenotypes observed in vip3-1 (**B**) compared to Col0 (**A**) (grown in short day and then in continuous light 16°C). vip3-1 displays a strong and highly variable reduction of seed set in siliques showing no indeterminacy. In silique showing indeterminacy no or very few seeds usually develop. Bars = 500 µm;* ***C.*** *Number of aborted ovules and seeds in vip3-1 (N=73 siliques) and WT (N=70 siliques). The standard deviation reflects the variability of the original distribution. The standard error of the mean indicates the precision of estimated means (95% confidence interval).*

to acquire alternative fates, despite the channeling effect of environmental cues (Hart et al., 2014). Interestingly, we find that the *vip3* indeterminacy phenotype occurs when in the wild type, *WUS* expression slowly decreases in flowers. Gene expression fading (in and out) and low levels of gene expression might represent weak points in gene networks, as variability in gene expression (area, intensity, and duration) in such instances may have more pronounced

A

effects. Conversely, the gene regulatory network often promotes clear-cut expression patterns (both in space and time), and this may limit the presence of such weak points. It may appear surprising that a developmental switch as important as the decision to stop or maintain stem cells in a flower would rely on such a robust Boolean control, yet our results in the *vip3* mutant suggests that increased transcriptional noise is sufficient to induce indeterminacy. This calls for an analysis of the adaptive benefits of such a weak control. One may speculate that the number of fruits and seeds could be increased *via* this unusual prolongation of floral stem cell competence, as observed in other species (see e.g. (Tooke et al., 2005).

6.4. Perspectives

6.4.1. Transcription noise but at cell level

AG expression has been evaluated by monitoring the *pAG::AG-2xVENUS* signal within the floral meristem, and suggests that VIP3 dampens transcriptional noise. To check whether this may be consistent with increased transcriptional noise, the RNAseq experiment on wild-type or vip3 apices is not appropriate since values are averaged over the whole tissue. Within the team a "single cell RNAseq" experiment in the *vip3* mutant compared to the wild-type has been launched. This experiment was performed both on cotyledon mesophyll cells and on root cells (for practical reasons). The first analysis aims to measure variations in gene expression from one cell to another. The second analysis aim to compare t-SNE (t-distributed stochastic neighbour embedding;(Denyer et al., 2019; Shulse et al., 2019; Zhang

A

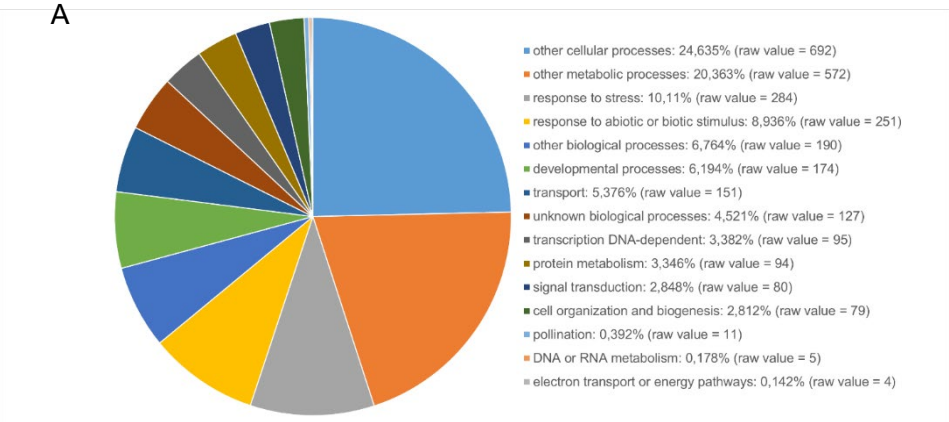

B

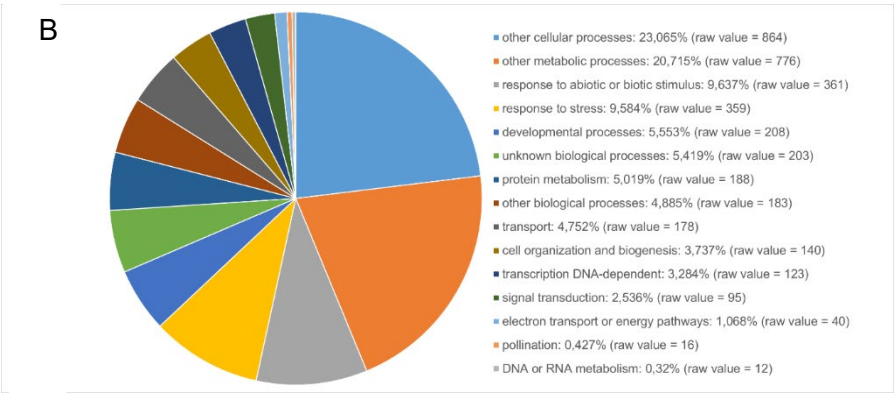

C

	gene_id	gene	log2(fold_change)	p_value
Downregulated	AT1G77080	FLM, FLOWERING LOCUS M / MAF1, MADS AFFECTING FLOWERING 1	-8,89394	5,00E-05
	AT5G65060	FCL3, FLOWERING LOCUS 3 / MAF3, MADS AFFECTING FLOWERING 3	-8,38456	0,0018
	AT5G10140	FLC, FLOWERING LOCUS C	-4,65699	5,00E-05
	AT5G65080	AGL68, AGAMOUS-LIKE 68 / MAF5, MADS AFFECTING FLOWERING 5	-4,15656	5,00E-05
	AT5G65050	AGL31, AGAMOUS-LIKE 31 / MAF2, MADS AFFECTING FLOWERING 2	-3,93607	5,00E-05
	AT5G38740	AGL77, AGAMOUS-LIKE 77	-3,33443	5,00E-05
	AT2G20825	ULT2, ULTRAPETALA2	-3,10298	5,00E-05
	AT5G27580	AGL89, AGAMOUS-LIKE 89	-2,67671	0,00405
	AT4G24540	AGL24, AGAMOUS-LIKE 24	-2,29325	5,00E-05
	AT4G27330	NZZ, NOZZLE / SPL, SPOROCYTELESS	-1,86166	0,00155
	AT5G60440	AGL62, AGAMOUS-LIKE 62	-1,59424	0,00795
	AT5G21150	AGO9, ARGONAUTE 9	-1,2134	5,00E-05
	AT5G57390	AIL5, AINTEGUMENTA-LIKE 5 / CHO1, CHOTTO 1 / EMK, EMBRYOMAKER / PLT5, PLETHORA 5	-0,866008	5,00E-05
	AT2G03060	AGL30, AGAMOUS-LIKE 30	-0,794353	0,001
	AT2G26440	PME12, PECTIN METHYLESTERASE 12	-0,709637	5,00E-05
Upregulated	AT3G20810	JMJ30 / JMJD5, JUMONJI DOMAIN CONTAINING 5	0,505522	0,00085
	AT4G37650	SGR7, SHOOT GRAVITROPISM 7 / SHR, SHORT ROOT	0,507952	0,00035
	AT2G33880	WOX9, WUSCHEL-RELATED HOMEOBOX 9	0,571996	0,00045
	AT2G34710	PHB, PHABULOSA / ATHB-14, ARABIDOPSIS THALIANA HOMEOBOX PROTEIN 14	0,586075	5,00E-05
	AT1G62360	STM, SHOOTMERISTEMLESS	0,589834	0,0001
	AT1G19850	MP, MONOPTEROS / ARF5, AUXIN RESPONSE FACTOR 5	0,608684	0,0019
	AT3G11050	FER2,- FERRITIN 2	0,652661	0,0039
	AT1G69770	CMT3, CHROMOMETHYLASE 3	0,707429	5,00E-05
	AT4G20270	BAM3, BARELY ANY MERISTEM 3	0,779995	5,00E-05
	AT5G62230	ERL1, ERECTA-LIKE 1	0,835578	5,00E-05
	AT5G53950	CUC2, CUP-SHAPED COTYLEDON 2	0,910426	5,00E-05
	AT5G11320	YUC4, YUCCA4	1,05308	5,00E-05
	AT2G45660	SOC1, SUPPRESSOR OF OVEREXPRESSION OF CO 1	1,0598	5,00E-05
	AT4G00150	HAM3, HAIRY MERISTEM 3, ATHAM3, HAIRY MERISTEM 3, HAM3, LOM3, LOST MERISTEMS 3, SCL6-IV	1,08428	5,00E-05
	AT1G68640	PAN; PERIANTHIA, TGA8, TGACG SEQUENCE-SPECIFIC BINDING PROTEIN 8	1,10476	5,00E-05
	AT3G15400	ATA20, ANTHER 20	2,05576	5,00E-05
	AT2G27250	CLV3, CLAVATA3	2,39061	5,00E-05
	AT1G75940	ATA27, BETA GLUCOSIDASE 20, BGLU20	2,50951	5,00E-05
	AT5G51870	AGL71, AGAMOUS-LIKE 71	2,85072	5,00E-05
	AT4G28395	ATA7, ARABIDOPSIS THALIANA ANTHER 7	3,11384	5,00E-05

et al., 2018) to see if the clusters are less well defined for example. At this time, the results have been obtained, but the analysis remains to be conducted, and in fact adapted, to evaluate transcriptional noise level in WT vs. *vip3*. This first attempt may help us to formally demonstrate whether VIP3 controls transcriptional noise globally, as suggested from the analysis of the analogous members in yeast (Ansel et al., 2008).

6.4.1. Vip3 and mechanical stress

vip3 was isolated as being insensitive to mechanical stress (Jensen et al., 2017) This relationship between VIP3 and the response to mechanical stress has only been shown in

one study. Jensen and colleagues showed that even though the *vip3* mutant did not respond to external mechanical stimuli (brushing) the expression of *VIP3* is not significantly altered in 20 days old seedlings brushed for two minutes. This suggests that *VIP3* expression does not respond to mechanical stress. However, further experiments need to be done to better understand the putative relationship between VIP3 and mechanical stress. Quantification of *VIP3* expression rate and protein accumulation under various mechanical stress conditions should be conducted. For instance, it would be relevant to quantify *VIP3* expression by RT-qPCR in plants grown under different mechanical stresses: plants stimulated and unstimulated (brushing), plants grown on different osmolality media, plants under variable illumination conditions. Regarding the expression of *VIP3,* one could determine whether different types of mechanical stress, related to external stimuli, osmolarity or growth rate would influence the expression of VIP3.At the protein level, a VIP3 transcriptional reporter lines would be interesting to generate, to accurately describe the expression pattern of VIP3. Even if the expression of *VIP3* is ubiquitous, it seems to exhibit subtle tissue-dependent expression variations. Significantly, its expression seems to be higher in the layer 1 (L1) and in the boundaries (eFP browser – TAIR – Arabidopsis.org), where mechanical stresses are also higher (Beauzamy et al., 2015; Hamant et al., 2014). This could suggest that VIP3 expression may be controlled by more continuous mechanical stresses (than intermittent touch).

To go even further in the link between VIP3 and the response to the mechanical constraints, the phenotypic study of the mutant should be carried on. For instance, the analysis and quantification of cell growth patterns and responses in response to wall weakening drugs,

D

	gene_id	gene	log2(fold_change)	p_value
Downregulated	AT2G14610	PR1; pathogenesis-related protein 1	-5,18392	5,00E-05
	AT5G59220	HAI1; PP2C protein (Clade A protein phosphatases type 2C)	-1,72227	5,00E-05
	AT4G34760	SAUR-like auxin-responsive protein family	-1,13968	5,00E-05
	AT1G08320	TGA9; bZIP transcription factor family protein	-0,969944	0,00355
	AT1G67710	ARR11; response regulator 11	-0,934393	0,00065
	AT3G23030	IAA2; indole-3-acetic acid inducible 2	-0,884945	0,0009
	AT4G34000	ABF3; abscisic acid responsive elements-binding factor 3	-0,857165	5,00E-05
	AT5G54510	DFL1; Auxin-responsive GH3 family protein	-0,799458	5,00E-05
	AT5G57560	TCH4; Xyloglucan endotransglucosylase/hydrolase family protein	-0,672642	5,00E-05
	AT3G23050	IAA7; indole-3-acetic acid 7	-0,628497	0,00325
	AT1G03430	AHP5; histidine-containing phosphotransfer factor 5	-0,590316	0,0007
	AT4G34750	SAUR-like auxin-responsive protein family	-0,579414	0,00535
Upregulated	AT1G80100	AHP6; histidine phosphotransfer protein 6	0,514231	0,0006
	AT2G22670	IAA8; indoleacetic acid-induced protein 8	0,537947	0,00075
	AT3G63010	GID1B; alpha/beta-Hydrolases superfamily protein	0,572849	0,00025
	AT1G28130	GH3.17; Auxin-responsive GH3 family protein	0,575311	5,00E-05
	AT5G46570	BSK2; BR-signaling kinase 2	0,576718	5,00E-05
	AT1G19850	MP; Transcriptional factor B3 family protein / auxin-responsive factor AUX/IAA-like protein	0,608684	0,0019
	AT1G51950	IAA18; indole-3-acetic acid inducible 18	0,628133	5,00E-05
	AT5G46790	PYL1; PYR1-like 1	0,646811	5,00E-05
	AT2G38120	AUX1; Transmembrane amino acid transporter family protein	0,691917	5,00E-05
	AT2G01570	RGA1; GRAS family transcription factor family protein	0,759926	5,00E-05
	AT1G45249	ABF2; abscisic acid responsive elements-binding factor 2	0,794846	5,00E-05
	AT1G19050	ARR7; response regulator 7	0,811842	5,00E-05
	AT2G38310	PYL4; PYR1-like 4	0,856148	5,00E-05
	AT4G27260	WES1; Auxin-responsive GH3 family protein	0,864813	5,00E-05
	AT1G72450	JAZ6; jasmonate-zim-domain protein 6	0,885443	5,00E-05
	AT1G17380	JAZ5; jasmonate-zim-domain protein 5	0,960683	5,00E-05
	AT4G33950	OST1; Protein kinase superfamily protein	1,02011	5,00E-05
	AT5G13220	JAZ10; jasmonate-zim-domain protein 10	1,03421	5,00E-05
	AT1G19180	JAZ1; jasmonate-zim-domain protein 1	1,04499	5,00E-05
	AT5G11320	YUC4, YUCCA4	1,05308	5,00E-05
	AT2G41310	RR3; response regulator 3	1,11732	5,00E-05
	AT1G77920	TGA7; bZIP transcription factor family protein	1,15091	0,00385
	AT5G17490	RGL3; RGA-like protein 3	1,15216	5,00E-05
	AT3G11410	PP2CA; protein phosphatase 2CA	1,21844	5,00E-05
	AT4G14550	IAA14; indole-3-acetic acid inducible 14	1,31153	0,0009
	AT1G04250	AXR3; AUX/IAA transcriptional regulator family protein	1,58048	0,0001
	AT3G21510	AHP1; histidine-containing phosphotransmitter 1	1,80767	0,00015
	AT1G77690	LAX3; like AUX1 3	2,1705	5,00E-05
	AT4G00880	SAUR-like auxin-responsive protein family	2,62316	5,00E-05
	AT5G13380	Auxin-responsive GH3 family protein	3,54665	5,00E-05
	AT2G46690	SAUR-like auxin-responsive protein family	3,63345	5,00E-05

Figure 43: Differential gene expression in vip3-1 vs. wild-type shoot apices.

A,B. *Gene ontology analysis: categories of genes involved in biological processes that are up-regulated (**A**) and down-regulated (**B**) in vip3-1.* ***C,D.*** *Short list of genes involved in flowering and flower development (**C**) and signaling (**D**) pathways that are misexpressed in vip3-1. Genes that are down-regulated are highlighted in blue, and those that are up-regulated are highlighted in orange.*

such as isoxaben, would inform on the role of VIP3 within the mechanical feedback loop (Hamant, 2008; Heisler, 2010; Hervieux, 2016)).

Interestingly, the mechanical features of the *vip3* mutant are currently under study in the team (Duy-Chi Trinh, pers. com.). In particular, sepals which present a strong phenotype of curvature defect and cotyledons are used for this description, and they appear softer than the wild type, based on AFM measurement and cell deformations after osmotic shocks. To go further, the composition (FT-IR,(Mouille et al., 2003)) and the anatomy (Transmission Electron Microscopy) of the walls will be analyzed. It is possible that *vip3* exhibits a reduced response to touch because it is already under high tensile stress (if walls are softer). This also raises the question as to why general defects in a transcriptional regulator would lead to such a response. Arguably, this could be consistent with a defect in the synthesis and secretion of wall components.

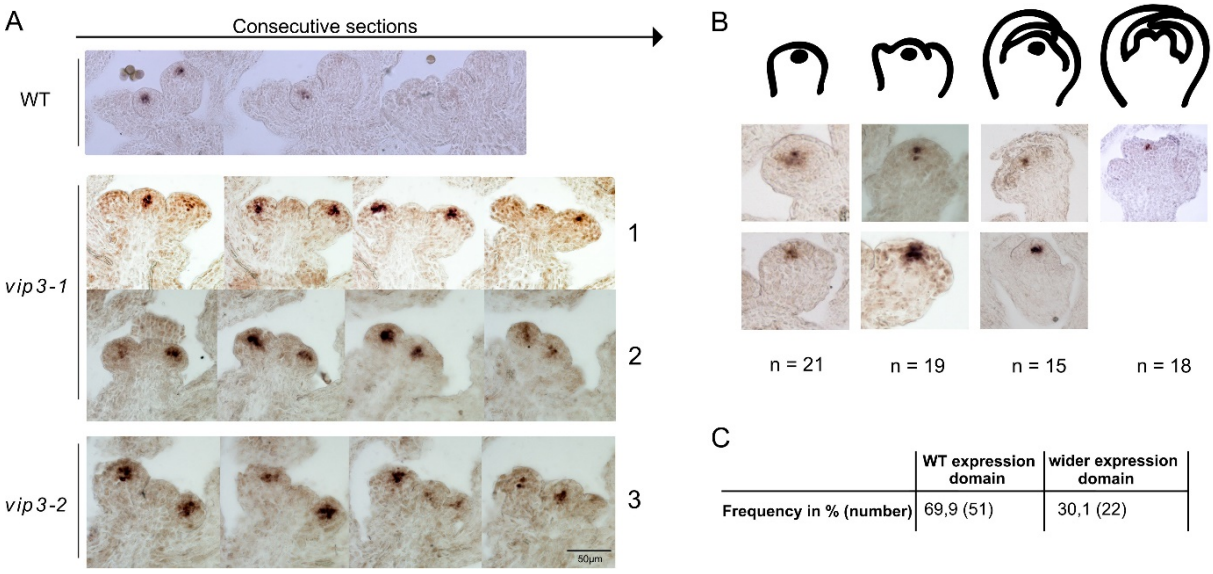

	WT expression domain	wider expression domain
Frequency in % (number)	69,9 (51)	30,1 (22)

Figure 44: Expression patterns of WUS in vip3 flowers.

A, B. *In situ hybridization of WUS transcripts in wild-type (**A**, upper panel) and vip3-1 (**A**, lower panel and **B**).*
A. *Consecutive sections on WT and 3 independent vip3 (1-2: vip3-1; 3: vip3-2) apices showing an expansion of WUS expression domain in vip3-1 floral meristems, when compared to wild type;* ***B.*** *Representative patterns of WUS expression domain in vip3-1 flower buds at four different developmental stages (as represented by schematic drawings). Plants were grown in short day then continuous light 16°C conditions (as in Fig. 1). Scale bar: 50 µm;* ***C.*** *Number of flower meristems displaying a wild-type WUS expression domain and an enlarged WUS expression domain in vip3-1.*

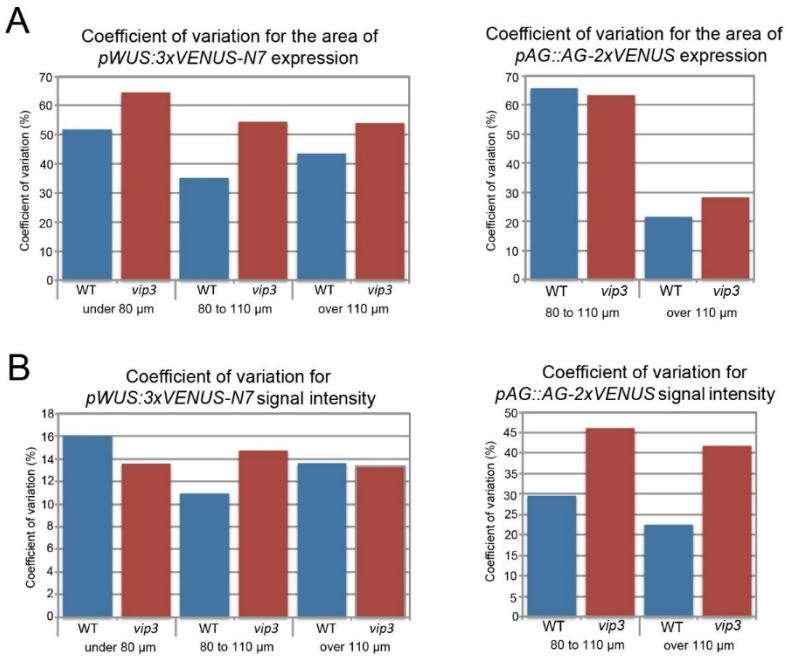

Figure 45: Coefficient of variation for WUS and AG expression area and average intensity in vip3 flowers

A. *Histograms displaying the coefficients of variation (%) for the area of pWUS::3xVENUS-N7 (left) and pAG::AG-2xVENUS (right) expression in wild-type and vip3-1 flowers;* ***B.*** *Histograms displaying the coefficients of variation for the average fluorescence signal intensity of pWUS::3xVENUS-N7 (left) and pAG::AG-2xVENUS (right) expression in wild-type and vip3-1 flowers.*

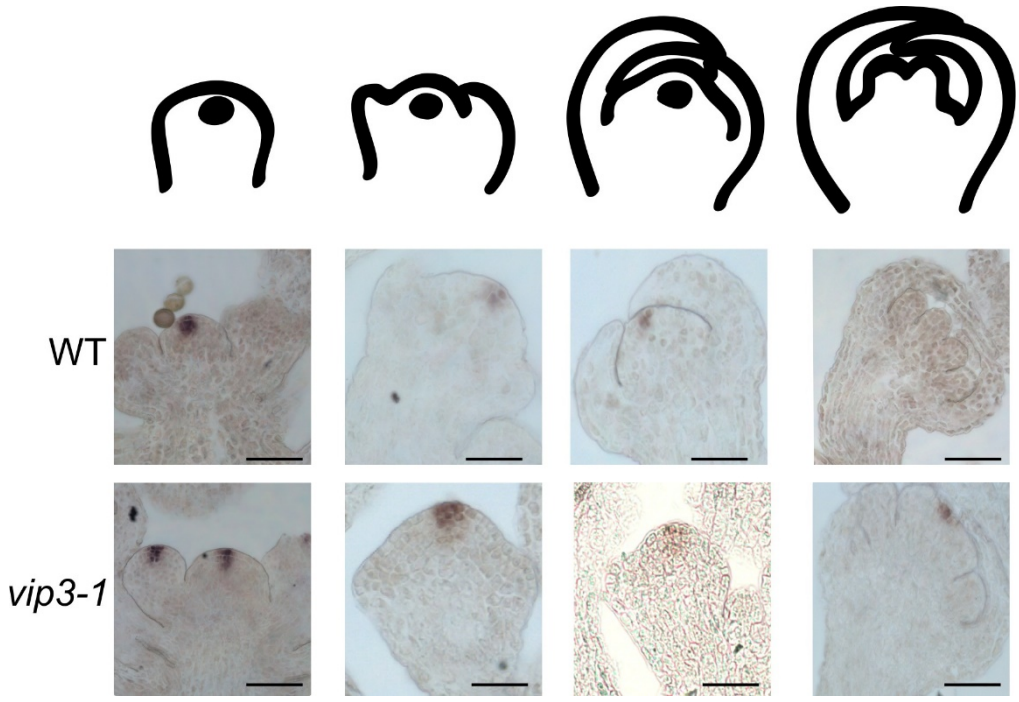

Figure 46: Expression patterns of CLV3 in vip3-1 flowers

*In situ hybridization of CLV3 transcripts in wild-type (**A**) and vip3-1 (**B**). Plants were grown in short day then continuous light 16°C conditions (as in Figure 1). Scale bar = 50 µm.*

7. Imaging and quantification of cortical microtubule dynamics in plant aerial organs using the Alpha3 light sheet microscope

7.1. The technical assets of Alpha3 allows imaging of large aerial organs over time at high spatial resolution

7.1.1. Alpha3 microscope description

Our goal was to develop a Light Sheet Fluorescent Microscopy (LSFM) procedure that would enable the imaging of signals in large plant aerial organs, over 2-3 days or more, similarly to the existing procedures in confocal microscopy (Prunet et al., 2016a; Prunet and Duncan, 2020). Such a goal requires (i) a mounting chamber large enough to receive plant aerial organs, (ii) the use of long-distance objectives and (iii) to keep the samples un-embedded, which is critical for imaging plant shoot tissues *in vivo*.

Figure 47-A shows how the PhaseView Alpha3 light sheet microscope design. The set up consist of two illumination arms which can be installed on an upright stand microscope, in our case, the Olympus statif BX43F . This organization with an upright stand is quite original. A large chamber (W = 21mm; L = 70mm; H = 25mm; Vol = 15mL), can be filled with water or any other liquid medium, and is set between the two excitation objectives (Fig.47 C and D, Fig. 48). This chamber is large enough to host large samples and can even be used for mounting several samples simultaneously (Fig. 47). This set-up is perfectly adapted to our technical constraints and biological question, and was the original rationale for the decision to collaborate with Phaseview on this project.

To further improve sample mountings, a specific holder that can be fixed to the Alpha 3 rotation module was developed (Fig. 47 - D, Fig. 48). More specifically, I developed this holder to easily and properly put the sample in the microscope and allow *in vivo* imaging. The design of the holder was developed in collaboration with an engineer at the mechanical

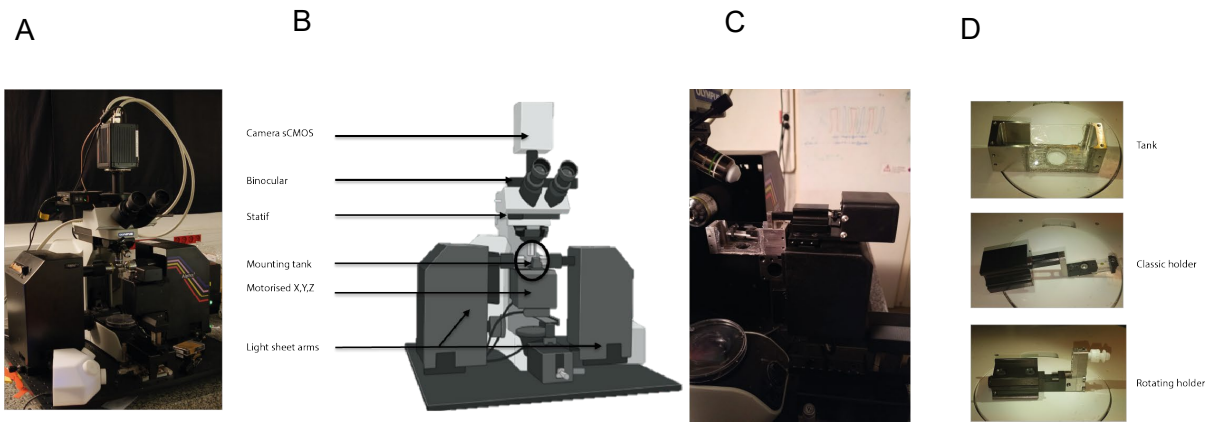

Figure 47 Alpha3 first up right stand LSFM

A. *Alpha3 LSFM produced by PhaseView, Dual illumination light sheet microscope;* ***B.*** *Organization of Alpha3 LSFM, the microscope is composed by two illumination arms, one stand motorized in X,Y,Z, a camera sCMOS;* ***C.*** *Mounting system of Alpha3 microscope, the tank is filled with water, the sample is mounted in a holder motorized in X,Y,Z, ;* ***D.*** *Top – picture of the tank which can be filled with liquid medium, Middle – picture of the basic holder for top view imaging, Bottom – picture of the holder with motorized rotation module, the sample can be oriented automatically in the microscope.*

workshop of ENS de Lyon (Olivier Razebassia). The holder is big enough for the mounting of several samples, while being filled with water or liquid medium. It must adapt to the rotating module of Alpha 3 LSFM in order to be used for all the Alpha3 applications. I work with Olivier Razebassia for the shape and the dimension of the holder and the holder was made by Olivier himself. This holder is a rectangular container (W = 5 mm; L = 10 mm; H = 2 mm; Vol = 0,1 mL) that can be filled with plant culture medium (agarose, MS medium, ACM, etc) thus enabling specimen growth over time.

This set-up does not require samples to be embedded like in the open top SPIMs, but instead allows to image living samples immersed in water. In addition, the double illumination allows to better image thick and opaque tissues (Fig. 47, 48). The sheet of light is set up at the focal plane of the imaging objective and the waist of the light sheet is centered on the region of interest. This protocol is therefore very close to the ones we use when imaging our samples with an upright confocal microscope, and thus allows the live imaging of our suite of aerial plant model systems. The acquisition is done with a Hamamatsu Orca Flash camera 4 C13440 of 2048 by 2048 pixels. The frame rate of the camera is about 100 frames per second which can theoretically allow to image fast biological processes. The Alpha3 LSFM generates images of 2048px by 2048px in 16bit. These settings allow acquisition with a high temporal resolution compared to CSLM (see below).

In contrast to other commercial or Open source LSFM the Alpha3 LSFM architecture is close to an upright confocal microscope. This architecture is quite unique for a commercial LSFM and this organization is more adapted to aerial plant imaging. For instance, the plant gravitropism can be respected during imaging and the overall conditions of imaging can be close to physiological ones.

7.1.2 Organ mounting and imaging

A series of aerial organs (cotyledons, hypocotyls, dissected meristems, and sepals) have been mounted to evaluate the set-up. Each of these organs were mounted in the Alpha 3 quite similarly. The global idea was to directly put the sample on solid agar medium with as little handling as possible and without any embedding.

Cotyledons were imaged either as dissected organs from 7 days-old seedlings or still attached to the seedlings (Fig. 48 - D). They were mounted on the holder filled beforehand with 2%agarose for short time imaging or with MS agar medium for long time imaging. Dissected cotyledons were laid as flat as possible on the agarose taking care not to wound the cells and, glued to the medium with droplets of low melting point agarose not to burn the samples (Fig. 48 -A-B-C). The mounting of dissected cotyledons is easier and work really fine for short time imaging. The mounting of whole seedling is closer to physiological conditions and more suitable for long time imaging. However, they are more difficult to image (even more with mutants with curved cotyledons).

Hypocotyls were mounted in the same way as cotyledons, although they are easier to mount since they are cylindrical structures (Fig. 48 -D). Similarly, to cotyledons, two kinds of mounting can be done: with or without cotyledons. Depending on mutants, cotyledons can make the mounting and illumination of hypocotyls difficult and in such cases, they must be removed. Indeed, the cotyledons can be in the way of the light sheet and therefore interrupt the illumination of hypocotyls. For instance, it is the case for the *p35S::GFP-MBD* line which displays twisted leaves in adult plants and over curved cotyledons in early developmental stages. Unlike cotyledons, the two illumination arms can be used to get a better illumination (more in depth and less scattering).

Sepals were mounted in two different ways depending on imaging protocols and experimental goals. For short time-lapse imaging, sepals were mounted like cotyledons. They were dissected from the flower, laid down flat on medium and glued with droplets of low melting point agarose. For long time-lapse imaging, sepals were not dissected but observed directly on flower, dissected from the apex and laid on the medium (Fig. 48 E - F).

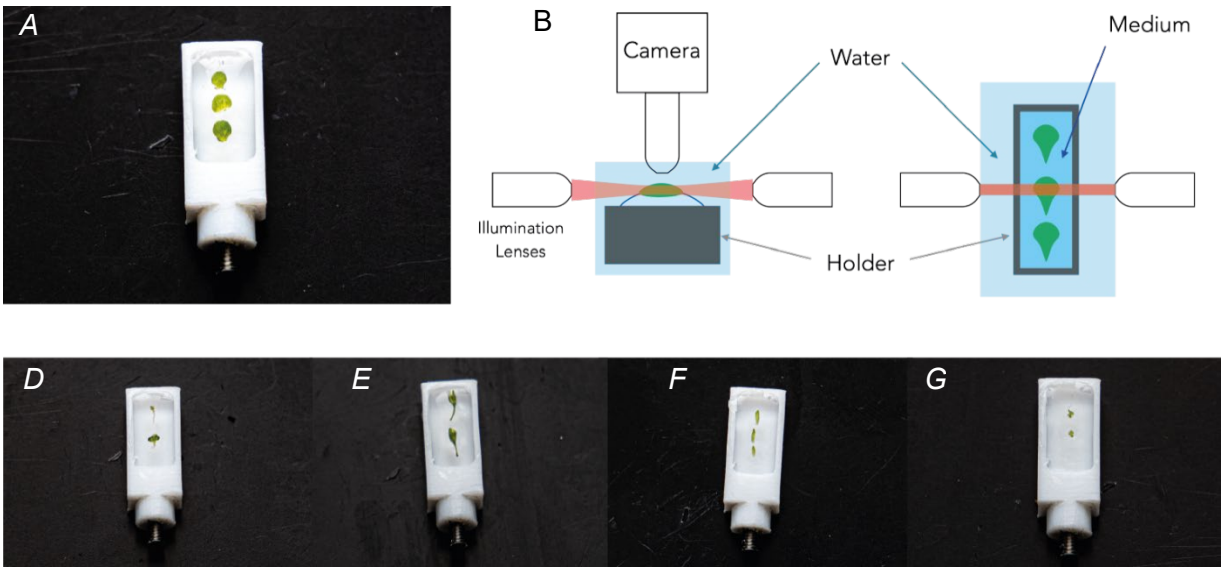

Figure 48: Sample mounting. Alpha 3 LSFM, an easy way to mount in vivo samples

A. *Mounting of cotyledons. Cotyledons are dissected from seedlings, laid down on medium and glued to the medium with a droplet of agarose low melting;* ***B.*** *Scheme showing the side view of cotyledon mounting;* ***C.*** *Scheme showing the top view of cotyledon mounting;* ***D.*** *Hypocotyl mounting, cotyledons are removed from the top of seedlings and hypocotyls are picked into the medium;* ***E.*** *Sepal mounting when sepals are imaged directly on flowers, flower bud are picked into the medium;* ***F.*** *Sepal mounting when sepals are dissected from flower buds, once removed from the flower buds, sepals are laid on the medium;* ***G.*** *Apex mounting, apex are dissected and picked into medium similarly to mounting for up right confocal imaging.*

Finally, for dissected shoot apex, the mounting protocol was similar to the upright confocal microscope mounting protocol (Prunet et al., 2016b; Prunet and Duncan, 2020). Apices were cut from the stem and the biggest flowers removed from the apex to uncover the SAM and the youngest FMs. The dissection was performed in water with the apex planted in 2% agarose. The high concentration of the medium allows to immobilize the specimen properly and the water allows to keep the meristems hydrated. Then the apex can be mounted in the Alpha3 microscope in the same way as for an upright confocal microscope (Stanislas et al., 2017)

After sample mounting, the holder is attached to the diving platform of the Alpha3 rotation module, and the whole device is immersed in water (Fig. 47 – C, Fig 48 - B). This configuration is really favorable since it allows (i) to perform live imaging, and (ii) to compare confocal and LSFM imaging performances in similar mounting conditions.

It should be noted that even if the use of the specifically developed holder is to be preferred (even more for long term imaging), the commercial holder supplied with the microscope also works (Fig. 47- D). That holder does not allow to fix the sample as well as the specific holder. But, when imaging single shoot apices for a short time, it can be useful and allow to mount all the tested organ. Note however, that the sample is not as tightly fixed, there may be more vibration and the sample may tend to move more (especially in Z) during a time lapse experiment of several minutes for example.

Samples were all imaged with an Olympus LUMPlanFL N 40x/0.8NA ∞/0/FN26.5 water immersion lens.

The easiness of sample mounting in Alspha3 opens new opportunities for plant imaging, especially when working with fragile samples or weak signals that require strong and/or long illuminations like in animal embryos for instance (Swoger et al., 2014). Indeed, the energy applied to the samples is much lower than in CSLM and, depending of the setting, induces a photobleaching between 3 and 100 times less important than CSLM (Huisken and Stainier, 2009).

7.1.3 Alpha3 LSFM produces sharper and more contrasted image than Leica SP8 CLSM

The aim of this part was to compare the technical differences and the properties between images taken with the Alpha 3 fluorescent light sheet microscope (LSFM) and images taken with a confocal laser scanning microscope (CLSM), here the Leica SP8, with and without the resonant scanner. The resonant scanner (RS) can be added to the SP8 microscope to increase the speed of acquisition. The resonant scanner device is composed of the two y-scanning mirrors (standard non-resonance) in combination with a resonant galvanometric scanner for the x-direction. This organization allows to scan samples with a higher frame rate, thus increasing the CSLM acquisition speed and reducing the amount of photobleaching.

I therefore compared these 3 kinds of device: Alpha3 LSFM, Leica SP8 CLSM with RS on and Leica SP8 CLSM with RS off (Fig. 49). For this purpose, I imaged dissected meristems expressing the *p35S::LTI6b-GFP* reporter line (which marks plasma membranes) with both SP8 (RS on and RS off) and Alpha3 (Fig. 49 - A). To be able to compare the images provided by both microscopes, the same flower bud was imaged in all the following. Even if some parameters do not exist in both microscopy modalities, I tried to image cells in as conditions that were as identical as possible. SP8 CLSM with RS off was set up with optimal size of pixel (3428 x 3428) with 2% laser and a frame averaging of 4. SP8 CLSM with RS on was set up with maximal size of pixel for this mode (1024 x 1024) with 2% laser and au frame averaging of 8. All the images produced with SP8 were acquired with Leica HCX APO L U-V-I 40x/0.8NA water immersion lens. Signal was analyzed in the same cells (same membranes and same slices).

The intensity profiles on the same positions were measured on each image and show that the image obtained with the Alpha 3 displays a much higher contrast than the images obtained with the SP8 RS on or off: 0-90 grey levels, 7-220 grey levels and 2628-8000 grey levels for the Alpha 3, the SP8 RS off and the SP8 RS on, respectively (Fig. 49 - B). Moreover, the profiles show that the Alpha 3 provides images with a much less noisy signal than the SP8 images, and this is even more obvious with the resonant scanner mode

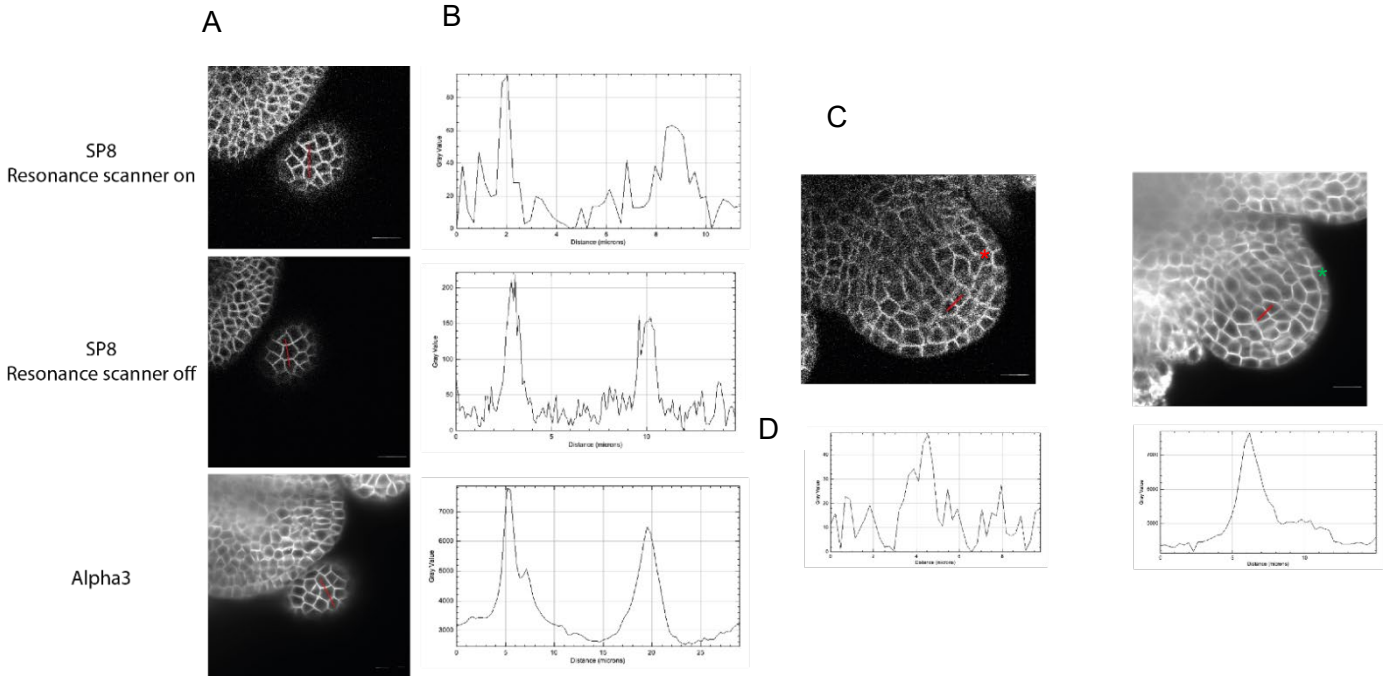

Figure 49 : Alpha3 LSFM produces less noisy and more contrasted images compared to the SP8 CSLM

A. *Optical section of a shoot apex expressing the p35S:: LTi6b-GFP reporter line, imaged in SP8 CSLM with the resonance scanner (RS) on (top),in SP8 CSLM with the RS off (middle) and in Alpha3 LSFM;* ***B.*** *Plot analysis assessing signal properties along the L1 of the FM emerging on the flank of the shoot apex (red lines in A). The Alpha 3 images are more contrasted and less noisy than the SP8 images. This is due to 16 bit images compared to SP8 with 8bit images;* ***C.*** *Approximately the same optical section of a FM expressing the p35S:: LTi6b-GFP reporter line imaged in SP8 CSLM RS (left) on and in Alpha3 LSFM (right);* ***D.*** *Plot analysis assessing signal properties of FM images showed in* ***C*** *The membrane is LSFM (green star) is more define in the boundary compared to confocal images (red star). (scale = 5um)*

(Fig. 49 - B). The peaks corresponding to the membrane signals are higher and sharper on the profiles obtained with the Alpha3 compared to the profiles obtained with the Sp8, in both modalities. A better detection of membrane signals should make segmentation easier, for example (see below). Indeed, less noise will facilitate the detection of local minima of intensity and allow to avoid over segmentation in watershed segmentation in 2D or 3D. Globally, compared to CLSM, Alpha 3 LSFM produce shaper and more contrasted image than Sp8 (with both modality) and images with more resolution (in pixel) compared to SP8 with RS on.

The first noteworthy difference between the Alpha 3 and the conventional SP8 confocal microscope is the number of pixels per image. This number is fixed in the Alpha 3 LSFM because of the use of a camera (Hamamatsu Orca Flash 4) and is of 2048 by 2048 pixels per image. Conversely, the confocal scanner allows to have a virtually unlimited number of pixels and therefore to choose the pixel size. So, the SP8 CLSM images can display a lower size of pixels and, so, higher number of pixels per image, and provide the optimal image resolution (in pixel) for a given objective. For the objective I used, the Nyquist rate is about 0,076 µm, so the size of pixel must be very low to have all the resolution of our lens.

However, the resonant scanning mode, which allows faster imaging, limits the number of pixels per image to 1024 by 1024 pixels. For this amount of pixel, the Nyquist rate is 0.227 µm which is rather far from the optimal Nyquist and the resolution of the lens.

Therefore, for the same objective, the pixels in Alpha 3 images are twice smaller than in SP8 RS on (1024 vs 20148), or, images obtained with the Sp8 RS on correspond to images of the Alpha 3 but with a binning of 2 pixels. The Alpha 3 propose a higher resolution than the Sp8 with RS on. Moreover, the Nyquist rate, which is 0.162 µm, corresponds to the size of pixel given by the microscope, which is 0.1625 µm. The resolution fully corresponds to the resolution of the Alpha 3 microscope.

Sp8 with RS off is not subject to the same limitation of pixel number and the resolution is optimal, equal or higher than the Alpha 3 resolution for a given objective depending on images.

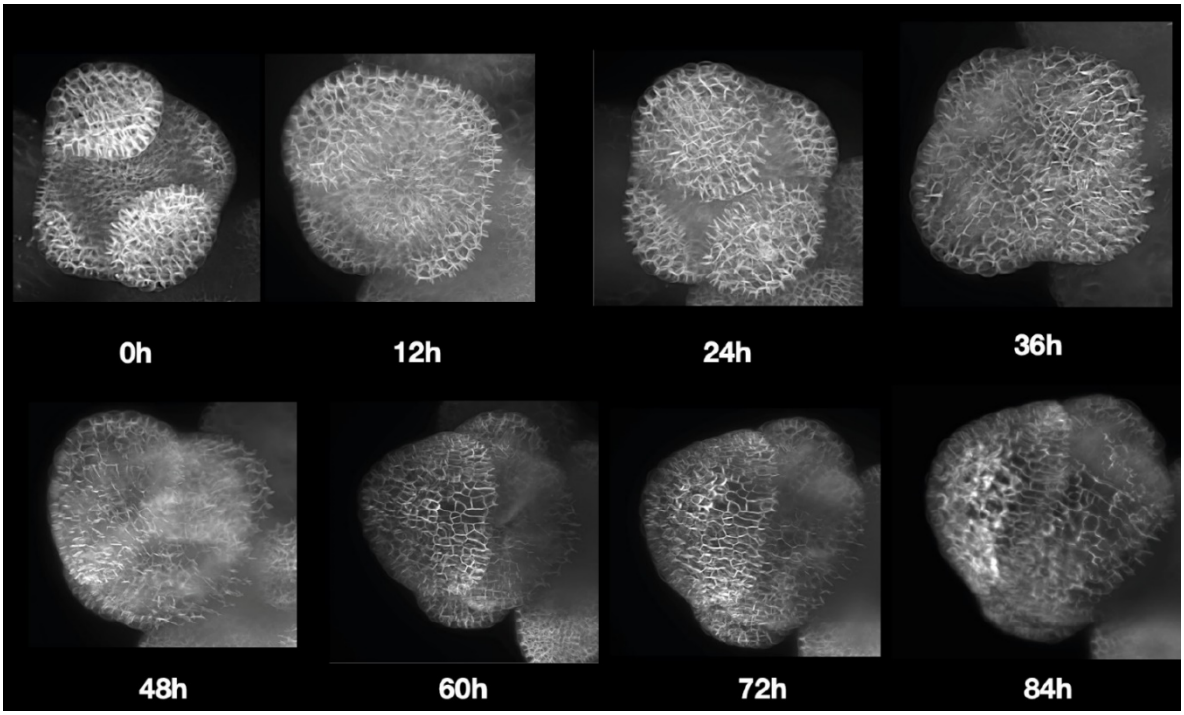

Figure 50: Imaging of flower bud growth during 84h

The flower bud development was followed on a shoot apex from a plant expressing the p35S::LTi6b-GFP reporter line. Shoot apex was prepared as shown in Figure 47 and grown into the tank of the Alpha3 for 84 hours. The tank was filled with ACM liquid medium, changed every 24h.

A second difference in terms of pure image is about the bit depth. Indeed, the Alpha 3 LSFM generates 16 bit images while the SP8 CSLM generates 8 or 12 bit images. 256 grey level for 8 bits, 4096 for 12 bits versus 65536 for 16 bits images. Obviously, an image taken with proper exposure (covering all possible contrast) presents a higher contrast on 16 bits images compared to 8 bits images. This difference in bit depth allows the Alpha 3 to produce images with a higher contrast than the confocal SP8

7.1.4. Alpha3 LSFM enables deeper imaging in samples than SP8 CLSM

As reported in the introduction section, LSFM should allow to image deeper in tissue compared to CLSM. To evaluate this advantage, stage 2 flower buds expressing the *p35S::LTI6b-GFP* reporter line were imaged both with Alpha3 and SP8 microscopes (Fig. 49 - C). With the SP8 conventional CLSM, images show a strong reduction of a structured signal from 12.5 micrometers deep. At this depth, membrane signals start being very noisy in the image obtained with the SP8 CSLM while remaining strongly contrasted on the images obtained with the Alpha3 LSFM (Fig. 49 - D). The intensity plots show one major peak and several attenuated peaks of only twice lower intensity on the image obtained with the Sp8 CSLM while the peak corresponding to the same membrane signal is clear and unique. So, the cell will be more easily segmented at this depth with Alpha 3, when compared to SP8.

Moreover, the membrane signal is almost totally lost in the boundary zone on SP8 images (FIG 49 – C - D). Conversely, the same zone on the Alpha 3 image shows a much more structured signal (Fig. 49 - C). Noise is much less present, and in terms of contrast, it is much easier to distinguish the whole plasma membrane. Moreover, at the periphery of the FM, cell contours are still distinguishable.

This ability of the Alpha3 LSFM to image more easily in depth can be really interesting in the case of gene expression or shape analyses in depth. This open the possibility to image part of aerial organs which cannot be imaged in CLSM.

7.1.5. Alpha3 LSFM enables long-time imaging like SP8 CLSM

Since the mounting procedure does not require the specimen to be embedded, the Alpha3 system offers the possibility to image aerial organ development over long time. This possibility was evaluated by imaging FM development over 84h. This was done on dissected apex following two kinds of procedures.

The first procedure consisted in imaging the same FM every 12h from an apex put in ACM medium and immerged in the tank filled with water (Fig. 47 - 48). Between each observation the apex was put back in the growth chamber. This kind of imaging is easy to set up in the Alpha3 LSFM and similar to the procedure used with CSLM (Prunet et al., 2016a; Prunet and Duncan, 2020). Furthermore, FM grows in proper growth conditions and FM growth dynamics observed during the time lapse is consistent with growth dynamics reported to date (Alvarez-Buylla et al., 2010; Bowman et al., 1989; Roeder and Yanofsky, 2006; Smyth et al., 1990). A second implementation of long-time imaging was tested in the Alpha3 LSFM. In this procedure, the dissected apex was put in ACM medium, immerged in the tank filled with ACM and imaged every hour during 24h. The ACM need to be changed every 12h ideally to avoid contaminations. For longer experiment a microfluidic device needs to be implemented in addition to a lighting system, to keep the samples in conditions close to those of growth chambers.

7.1.6. LSFM requires a data management plan

- An important computer need

During my thesis, I was able to show that the images produced by Alpha3 can be quantified, and that they gave the same results as confocal microscopy (Fig. 59). Nevertheless, several drawbacks can happen regarding the analyses and quantifications of images. First, the amount of data produced by Alpha3 is considerable. Indeed, since the imaging is fast and can go deep into the samples, the generated stacks regularly contain a large number of slices. This large number of slices coupled with the fact that each image is 2048 pixels by

2048 pixels encoded on 16 bits, the amount of data generated is very important. It is not uncommon to make stacks of more than 10 Gb. The data of a timelapse thus becomes colossal. A timelapse of more than 1 Tb of data can be very complicated to process. It is therefore necessary to have the appropriate extensive computer equipment to analyze this amount of data and this limitation may be one of the most important one in LSFM imaging as in medical diagnostic imaging (Aiello et al., 2019). Even though hard disk storage capacities have considerably increased over the last years with prices reducing as such and it is now easy for a user to get a hard disk of about 10 Tb and, even though more and more institutes such as the ENS de Lyon are equipped with work station and calculation servers to quantify raw data, a better definition of experimental procedures is a prerequisite that can substantially reduce the amount of data, as well as a pre-emptive selection of dataset (Kharat and Singhal, 2017).

An additional limitation for users is the knowledge in computer science (ssh, python, ...). In the case of a user with little knowledge of image analysis, the use of commercial software like Imaris or Arivis can be a solution even if it induces a much higher cost (https://imaris.oxinst.com/, https://www.arivis.com/).

- **A different data management approach**

The amount of data also changes the way they must be processed. In some cases, for long timelapse data for example, the analysis parameters can only be chosen on a small portion of the data and even in some cases on down sampled data. The chosen parameters are subsequently applied to the raw data. This way to analyze the image induce a back and forth between the choice of parameter and the real analysis. So the parameter need to be chosen with caution and the strategy for the analysis need to be clarified upstream of the acquisition.

Even though the data generated by Alpha3 can be quantified, the nature of the signal itself is sometimes an issue to analyze the images. Indeed, several softwares, such as MorphographX or TimageTK have been developed for confocal image analyses (Barbier de Reuille et al., 2015). Some parameters, inherent to these programs, can therefore cause

troubles, such as automatic Gaussian blur for instance. These parameters are not in adequacy with the low noise signal of the Alpha3 images. It is therefore necessary to sometimes customize the code of selected libraries to solve such issues.

- **Deconvolution a help for improving the signal?**

As described in this section, it can be difficult to easily handle LSFM images, especially when working with signal projections. Optical aberrations are difficult to correct because they are often more intense than the signal of interest in terms of gray levels. One possibility is to derive the images before doing maximum intensity projections. This solution is relevant only when the signal is not a linear signal close to the limit of the microscope resolution. The deconvolution with the experimental PSF can be used because it removes some of the aberrations. However, it can also generate artifacts on linear structures making the local analysis of the dynamics or orientation of these structures unreliable. Conversely for less structured signals, such as nuclei or membranes, or for global analyses of linear structure orientation, PSF deconvolution is a good solution.

Running the deconvolution LSFM is not as easy as with CSLM. The PSF calculation has indeed to be non-linear on the XY axis to match the variation of the light sheet thickness along those axes. In addition, a differential PSF on the Z-axis is required for opaque samples to reduce scattering inside the sample. Unfortunately, the implementations of differential PSF in Z axis is note trivial so I did not address these constraints.

7.2. Alpha3 LSFM enables fast cortical microtubule imaging

7.2.1. Imaging cortical microtubules with Alpha3 LSFM

All the LSFM advantages reported above prompted us to use the Alpha3 LSFM to image cortical microtubules (CMT) over very short time scales. For this purpose, I imaged CMT on cotyledons using the *p35S::GFP-MBD* line. I chose the cotyledons first because cotyledons are easily accessible and, second because their epidermal cells, the pavement cells, display particular shape and are quite well documented regarding their cytoskeletal patterns (Sapala et al., 2019).

Usually, microtubule imaging provides two kinds of information depending on the type of microscopes used. Either the goal is to analyze global CMTs patterns, and microtubule are imaged with a CLSM to get an average alignment of microtubules with high spatial resolution (Hamant et al., 2008). In this case, CMTs are imaged over the entire periclinal surface of the cells. This might necessitate a high number of slices, depending on the curvature of the cell, and therefore a time of acquisition that do not allow the monitoring of microtubule dynamics (Fig. 51). Alternatively, the goal is to follow CMTs polymerization/ depolymerization, and microtubules are often imaged with spinning disk CLSM or TIRF to follow microtubules with high spatial resolution and high temporal resolution (Grigoriev and Akhmanova, 2010; Movsisyan and Pardo, 2019; Prezel et al., 2017). Such imaging allows to monitor the dynamics of CMTs but not over the entire surface of the cells, due to the curvature. In our experiment we show thanks to LSFM we can investigate the dynamics of microtubules at subcellular resolution in pavement cells.

Pavements cells were imaged in a time-lapse of 10 minutes with a time step of 30 seconds. The duration of 10 minutes, which is fairly short, seemed to be optimal to analyse the “basal” dynamics of microtubules without taking into account microtubules reorientation due to biological responses such as cell division. I was able to image microtubule dynamics every 30 seconds which is quite a fast acquisition considering the volume to be imaged.

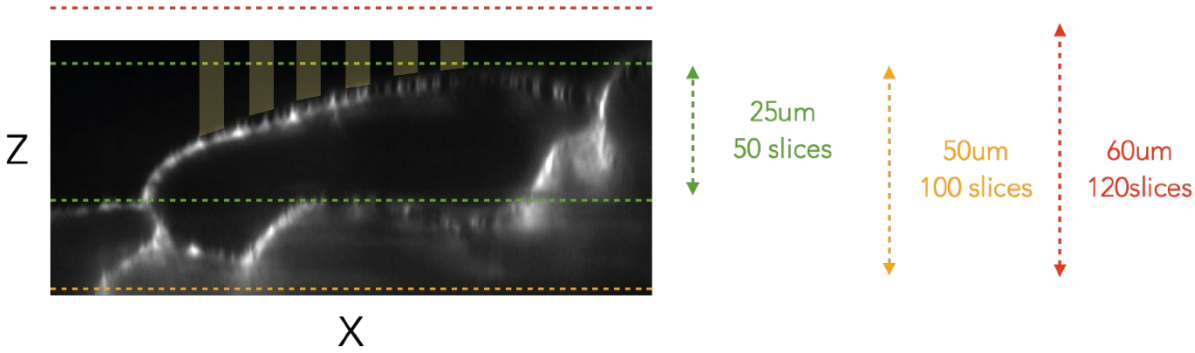

Figure 51: Alpha3 LSFM allow to image entire cell volume with high temporal resolution

The green line represent area of the out CMTs of one pavement cells which is about 25 um so about 50 slices with a Z step of 0.5 um. The orange line represent all the volume of pavement cells which is about 50 um so about 100 slices with a Z step of 0.5 um. The red line represents all the volume of the stack in order to not lost the sample if it move up during imaging. This volume is about 60 um so about 120 slices with a Z step of 0.5 um. The yellow box (box is 30px x 30px) represent the depth of CMTs signal at different point of the cell. This volume can be image in about 30 sec in Alpha 3 LSFM which is fast.

Indeed, each stack contained 120 to 150 slices covering 60 to 75 microns in the z axis and allowing to image all the CMTs of the first layer of cells (Fig. 51). These acquisitions results in 20 stacks of 120 to 150 slices for each cell. Such an acquisition was not possible with the SP8 with the RS which images 7 times slower, even with optimal acquisition parameters and without binning. This factor is even at 60x with the SP8 without the RS.

The specific illumination pathway of LSFM allows fast imaging but also induces signal artefacts. Indeed, as the light sheet illuminates a thick and opaque sample, a diffuse signal originating from the diffraction of the light sheet is produced inside of the tissue: the deeper the position of the light sheet in the sample, the stronger the diffracted signal. Moreover, if the sample and the structures to be imaged are curved (and this was my case with CMTs in pavement cells) thus requiring many Z slices, the diffuse signal due to light sheet diffraction is even higher since, in each Z slice, one part of the structure (CMT) are in focus (in the light sheet) and one part is out of focus (outside of the light sheet but in the diffracted area). The intensity of the diffraction signal in our samples was too high, sometimes higher than CMT signal itself, to get highly contrasted images of CMTs after a projection of the maximum intensity (see Fig. 52 A - B - C). Some parts of image in panel A show regions with really blurred MTs (top left of the cell). For other cells like in panel B a half of the signal was lost in the maximum intensity projection. In the panel C the signal of microtubule was completely lost in the projection. In all these cases it was not possible to monitor the dynamics of microtubules over time and even more with high temporal resolution.

7.2.2. A pipeline to extract the epidermal cortical microtubule signal from stacks

Since the quality of projections was not high enough for quantitative analysis of MT dynamics, I developed, together with Corentin Mollier from the Biophysics group at the RDP, ENS de Lyon, a pipeline which specifically extracts CMTs signal and performs selective Z projections. Note that the conceptual part of the pipeline was developed by myself but Corentin Mollier actually coded the script in python 3. The goal of this pipeline was to improve the quality of the CMTs signal and can presented as follow.

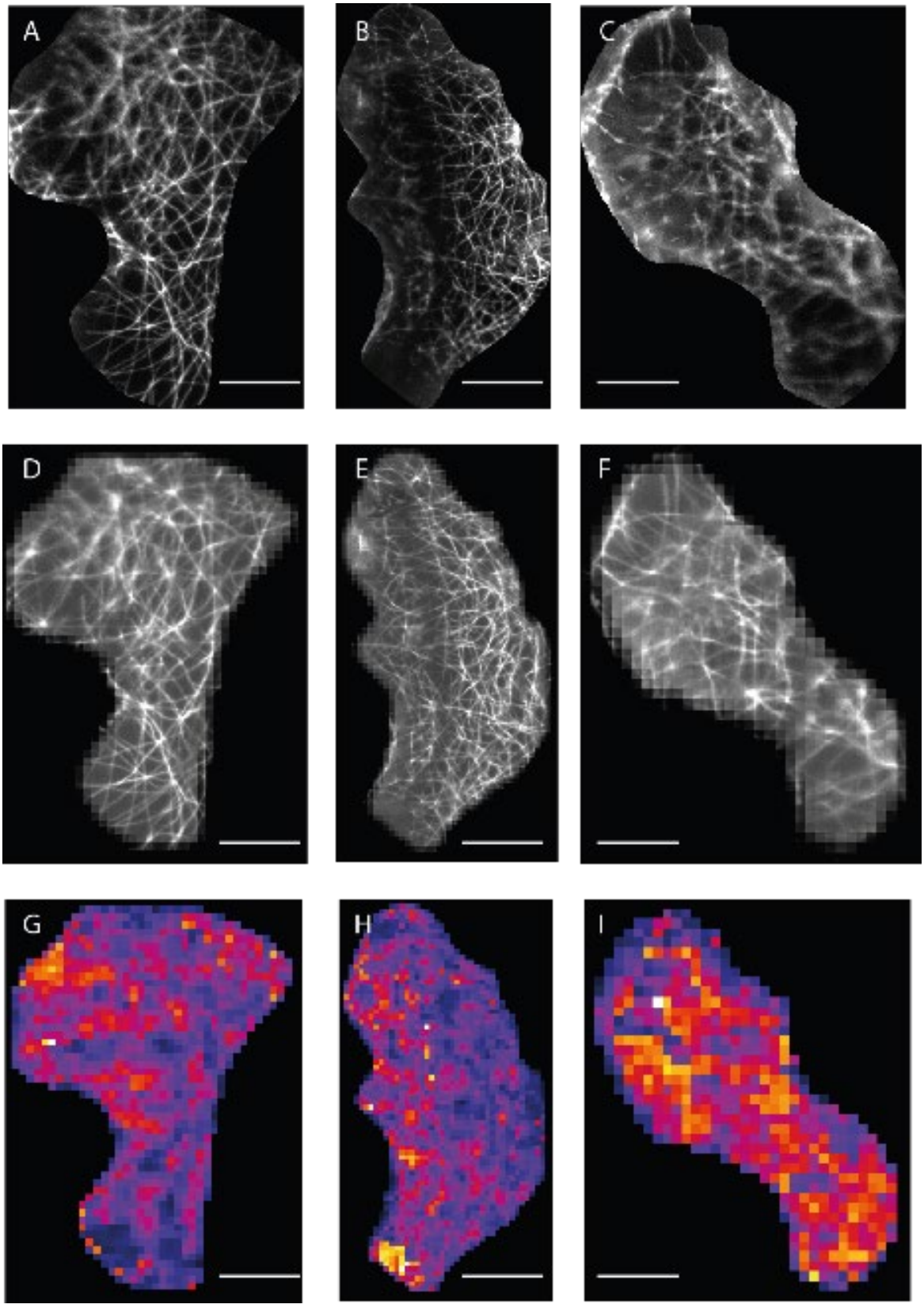

Figure 52: Representative images illustrating the outputs of the two pipelines.

A-B-C. *Maximum intensity projection of three examples of pavement cells imaged in Alpha3 LSFM. D-E-F. Z projections resulting from the pipeline based on local contrast gradient (Figure 52 A to E).* ***G-H-I.*** *Local map of microtubule orientation dynamics resulting from the pipeline based on ImageJ and the Wasserstein distance (Figure 52 F to H).*

The organization of each stack is quite stereotypical and can be subdivided in 4 parts along the z axis (Fig. 53 - C). The first part corresponds to slices that displays no signal: slices in this part are outside of the sample (black slices). The second part (dark grey slices) corresponds to slices that display the diffraction signal: slices in this part are just above and below the CMTs signal. The last part of the stack contains slices with the CMTs signal (Fig.53 - C). With this subdivision, each part displays specific optical parameters among which the local contrast is the most relevant to discriminate slices bearing CMT signals. Indeed, slices without signal, outside of the sample, display very low local contrast. Slices with diffraction signal, whatever its intensity, display a homogenous signal with therefore a low local contrast. Conversely, slices with CMT signal display a structured signal with a high intensity and a low background. Thus, the local contrast of slices containing CMT is higher than the one measured on all other slices (Fig.53 - D).

However, as pavement cells are neither flat nor perfectly orthogonal to the optical axis, the slice with the best CMT signal is not always in the same position in different regions of the stack. Thus, to detect locally the CMTs signal and calculate a projection in an specific manner in different parts of the sample, the stack was subdivided into patches of 30 pixels by 30 pixels (5 µm) that overlap by 20 pixels to increase the resolution of the analysis (Fig. 51 and 53 - C). Algorithmically, the script subdivided the raw stack in patches and saved all the patches in a folder using the scikit-image/skimage python library. Then, for each patches, we measured the local contrast using the local contrast function of scikit-image/skimage python library.

In each patch, the slice with the highest local contrast was selected, and a projection of the mean intensity along Z was made with the n+1 and n-1 slices surrounding the selected slice (Fig. 53- E). This projection was made by the mean projection function of scikit-image/skimage.

In this way it was possible to have a selective Z-projection which strongly enhances the projection of microtubules. If we compare the signal of CMTs between Maximum intensity

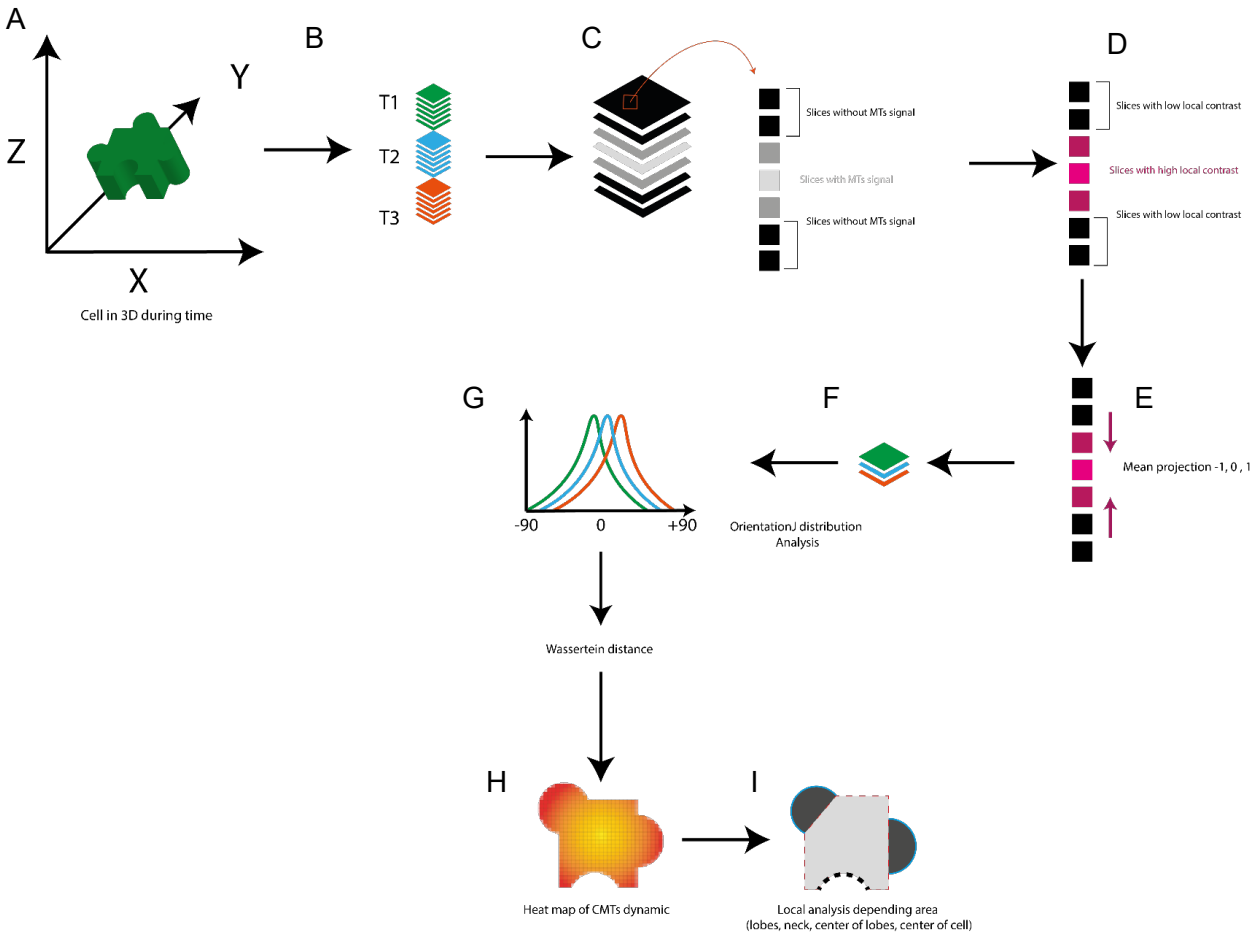

Figure 53: Pipeline for quantitative analysis of microtubules orientation dynamics.

A. *Schematic representation of a 3D pavement cell imaged in LSFM;* ***B.*** *Schematic representation of one stack imaged 3 times during the time lapse (green, blue and red represent the three time points);* ***C.*** *Each stack of each time point is subdivided into patches of 30px (5µm) per 30px patches with 20 px overlapping from one crop to the next. Slices with microtubule signals are labelled in grey;* ***D.*** *Local contrast gradients are evaluated for each slice of each patches. Slices in purple display high local gradients and correspond to slices with microtubule signals;* ***E.*** *Mean projections are done on slices with the highest gradients, adding one slice above and one slice below,* ***F.*** *Mean projection of each patch are concatenated to create a new stack recapitulating the time lapse;* ***G.*** *Orientations of microtubules are analyzed for each time point projection by OrientationJ to retrieve the distributions of microtubule orientations. The distributions are colored according to the time point;* ***H.*** *Differences between distributions are quantified by Wasserstein distance. Heat maps are generated where each crop has a color corresponding to distance value reflecting microtubules orientation dynamics;* ***I.*** *Microtubule orientation dynamics is retrieved for each cell subdomain (as described in Figure 54).*

projection and selective Z-projection in the figure 53 we can see that we recover a lot the lost CMTs signal. Indeed, depending on the raw signal, the effect of the pipeline is different. Between panels A and D we can see that the original projection is average and the gain of MTs signal is only low after the pipeline. In contrast, when we compare panels B and E, we can see that the signal of the CMT is recovered in E in the half of the cell whereas it was almost invisible in the Maximum Intensity Projection before processing the pipeline. The pipeline therefore allows to have a better homogeneity of CMT signal after a selective Z projection. Between C and F panels, we can see we recover all the CMT signal we lost during the maximum intensity projection.

7.2.3. A pipeline to analyze CMT dynamics

Once having generated CMT projections of a high enough quality, the aim was to analyze the local dynamics of CMTs. Here I define the microtubule dynamics as the combination of polymerization/depolymerization and reorientation. This is different than that of the literature (rather focused on polymerization/depolymerization and resulting treadmilling events). Yet, it may provide a more integrative signature of microtubule behavior, i.e. also including the emerging properties of their interactions. The following pipeline was also constructed together with Corentin Mollier.

Each patch (subpart of a stack) was processed with the pipeline described above (discard of the diffraction noise to selectively retain the CMT signal that is subsequently projected along Z). The same was done on every stack of every timepoints of the time-lapse. A new

stack was then generated with the projections of patches at each time point of the time-lapse, i.e. a stack of slices displaying the signal of CTMs over time (Fig. 53 -F).

Then, the CMT signal was analyzed to evaluate how it changes over time. As mentioned above, I hypothesized that changing of the CMT distribution might include two types of events: reorientation and polymerization/depolymerization. One way to quantify the

orientation of microtubule is to calculate the distribution of orientations. The concept is to quantify the orientation of signal in a kernel equal of the thickness of the fibrillar structure we want quantify. The kernel moves from row to row and column to column to analyze the whole image. For each displacement, the value of the signal orientation is thus calculated locally over the whole image. The distribution of these orientations corresponds to the number of kernels with a specific orientation between 90° and -90°. Here the size of the kernel, and so, the size of the microtubule appearing in the images produced by Alpha 3 was measured manually. The size of the microtubule was 3 pixels on average which corresponds to 0,49 µm. For our analysis, we used the ImageJ plugin OrientationJ, which allowed to quantify the distribution. I developed a FIJI macro to analyze each patch of each stack automatically. All the quantitative data are saved in a table.

Thus, the distribution of microtubules was analyzed on each patch with OrientationJ distribution (De Vos et al., 2016). Here, OrientationJ analyzed the objects in a kernel that corresponds to the thickness of CMTs (0,4875 µm). By this way, OrientationJ allowed to detect both changing of orientation and appearance or disappearance of MTs. The differences of distributions from one time point to the next, reflecting the dynamics CMTs, was quantified by the Wasserstein distance (Olkin and Pukelsheim, 1982). The Wasserstein distance corresponds to the minimal energy required to switch from one distribution to another. A Wasserstein distance value was assigned to each patch, from one point of the kinetics to the next. These values are the read-out of CMT dynamics in this specific region over time. A map was produced by the concatenation of all the patches and a value of grey level is assigned to each patch depending on the Wasserstein distance value (Fig. 53 - H).

To validate the pipeline, we first used a set of synthetic MT images (i.e. drawn lines). A first set was created with microtubule rotating, with a gradient of rotation from 0.1 to 50 degrees over 90 slices (Fig. 54). Synthetic CMT signals were created with the same thickness as real CMT s signals, i.e. 0,4875 µm. OrientationJ properly analysed the orientation of microtubules (Fig.54). Moreover, the reconstructed map exhibited a gradient of the Wasserstein distance correlating the amplitude of the movement of the synthetic microtubules. A second test was performed on blinking signal, artificial CMT appearing or disappearing, we call it blinking MT with a gradient of frequency from 1/2 to 1/10 over 90

slices to mimic polymerization/de-polymerization processes. 1/2 correspond to CMTs will appear and disappear one slice out of two and 1/10 correspond to CMTs will appear and disappear one slice out of ten. This test allows to simulate the appearance or disappearance of microtubule in one patch over time. Again, the reconstructed map seemed to validate the pipeline with a gradient of the Wasserstein distance correlating the amplitude of the synthetic microtubules blinking (Fig. 54). Thus, the pipeline detects both microtubule movement, from 0.2 degrees onward, and MT appearing or disappearing gradient with frequency of 1/10. The pipeline can therefore quantify CMTs dynamics during time with a high temporal resolution

The two consecutive pipelines were run on selected cotyledon pavement cells. Cell contours were delimited manually to get rid of the strong GFP signal associated to the transverse section of CMT located along the anticlinal face of the cell. Figures 52 G - H - I show representative heat maps of microtubule dynamics obtained from cells displayed on Figures 52 D - E - F.

7.3. Quantitative analysis of microtubule dynamics in pavement cells

Cotyledon pavement cells display a characteristic wavy shape. It has been proposed that this shape can reduce mechanical stress in epidermis cell wall, when growth is isotropic. Indeed, tensile stress in the outer wall can be directly related to the cell radius, meaning that cells would reduce stress either by growing anisotropically, or when growth is isotropic, by forming lobes with narrower local radius than a large isodiametric cell (Sapala et al., 2018) . The jigsaw puzzle shape triggers a mechanical feedback loop: cortical microtubules align along the largest tensile stress direction (which is prescribed by cell shape), this leads to the local mechanical reinforcement of the cell wall, and in the end, the maintenance of cell shape and associated stress pattern (Sampathkumar et al., 2014b). Indeed, CMTs generally guide the cellulose synthase complex, and thus cellulose microfibril orientations in the wall

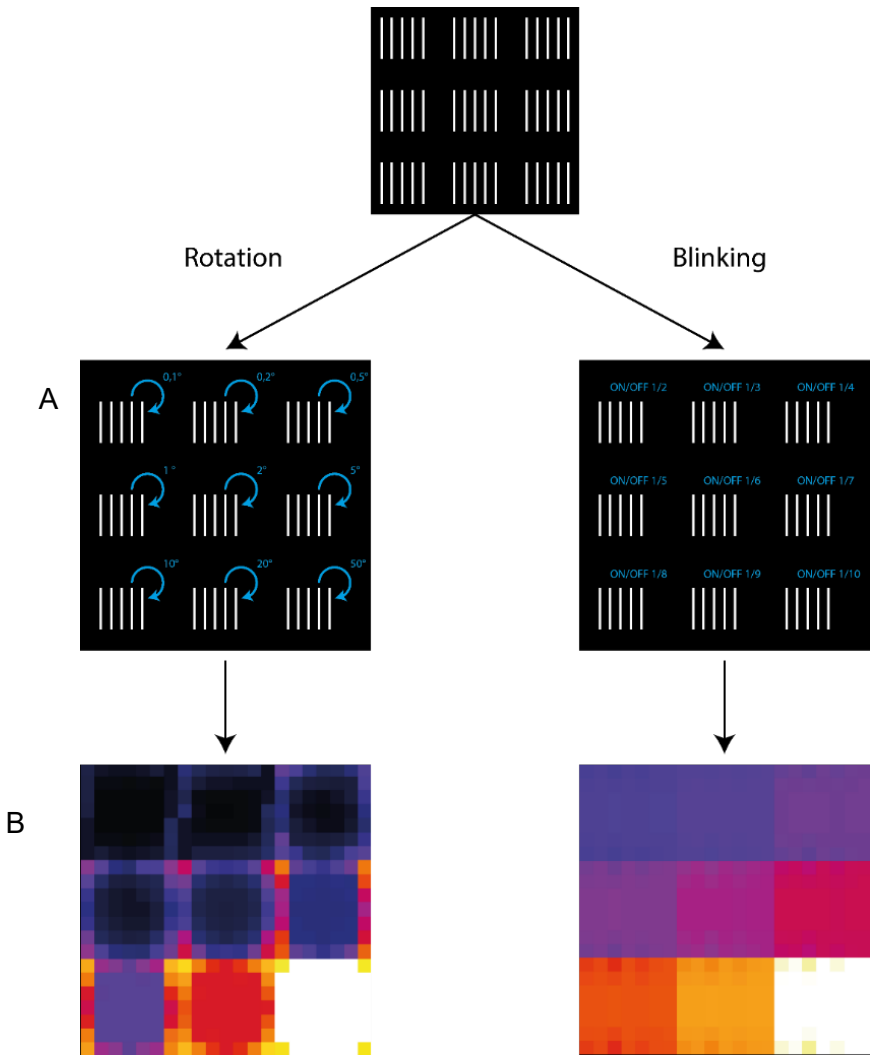

Figure 54: Validation of the pipeline using synthetic banking or rotating microtubules

A. *9 block of synthetic microtubules are produce. Microtubules are animated with a gradient of rotation from 0.1 to 50 degrees over 90 slices for the rotating one. The blinking microtubules are animated with a gradient of blinking from 1/2 to 1/10 over 90 slices ;* ***B.*** *Map of dynamics of microtubules for rotating or blinking microtubules. Results shown that few movement of microtubules can be detect with the pipeline.*

(Gutierrez et al., 2009; Paredez, 2006). Note that cellulose synthesis may also be guided autonomously, i.e. with biases derived from the wall itself (Chan and Coen, 2020). So far, the global pattern of microtubules has been associated with stress, but the local dynamics of cortical microtubules has not been associated to the local pattern of stress, and thus to the local shape descriptors of pavement cells. Are the isotropic CMTs more or less dynamics compared to anisotropic CMTs? Here we used the Alpha3 LSFM to investigate this question.

As discussed above, I generated stacks of 120 to 150 slices (75 µm in depth) every 30sec. The quantitative analysis of microtubules dynamics was performed over a short time lapse of 10 minutes that seems optimal to analyze and quantify the basal dynamics of microtubules, without taking into account important biological phenomena which can induce microtubule reorientation, like cells division for example. Furthermore, this relatively short duration avoids photobleaching. Indeed, even if Alpha3 LSFM induces less photobleaching, with this imaging set up, each slice of 2048 x 2048 pixel is image in 150 milliseconds so for one stack 150 slices the sample is illuminated during 22,5 seconds, which amounts to 75% of the 10 minutes of the timelapse when considering that images are acquired every 30 seconds.

7.3.1. Microtubules appeared more dynamics when imaging with the *pPDF1::mCitrin-MBD* than when imaging with the *pp35S::GFP-MBD*

Using the two pipelines reported above, I first compared the CMT dynamics in cotyledon pavement cells of the *pp35S:: GFP-MBD* and the *pPDF1:: mCitrin-MBD* lines. In *pp35S::GFP-MBD*, the GFP-MBD fusion is expressed in all the cells of all the tissues with a high expected expression level. In fact, this line was selected for its bright signal, notably in the shoot apical meristem (Hamant et al., 2008) In the *pPDF1::mCitrine-MBD*, the mCitrine-MBD fusion is specifically expressed in cells of the layer 1 (Abe et al., 2001), arguably with a comparatively lower expression level. Differences in expression level are not always easy to quantify (Mannerlöf and Tenning, 1997; Peach and Velten, 1991).

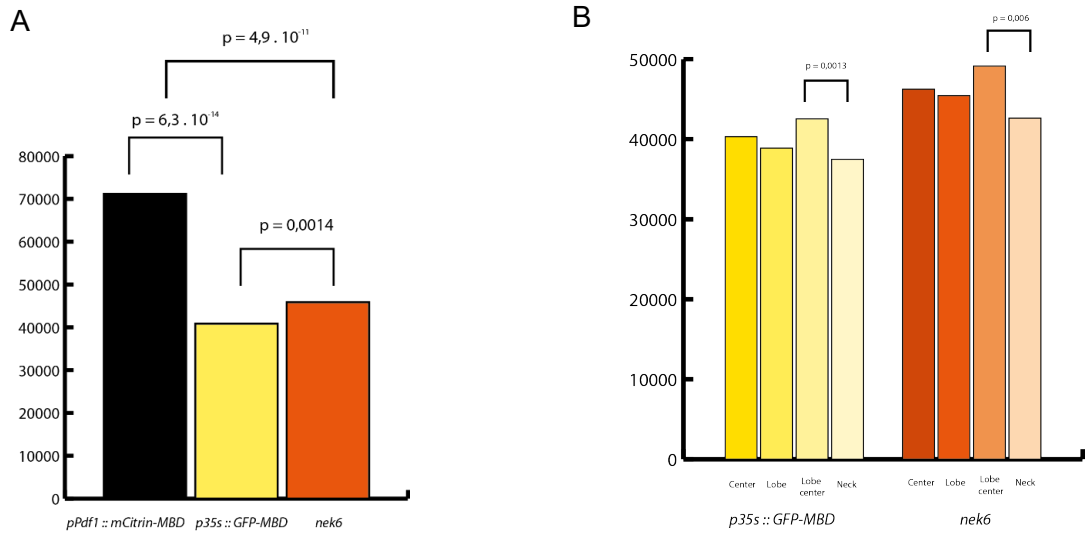

Figure 56 : Quantification of cortical microtubule dynamics in pavement cells

A. *Quantification of CMT dynamics in pPDF:: mCitrin-MBD (n = 16 cells), p35S:: GFP-MBD (n =22 cells) and p35S :: GFP-MBD in nek6 (n=21 cells). Surprisingly, CMT dynamics is higher in pPDF1::mCitrin-MBD than in p35S :: GFP-MBD. CMT dynamics is significantly higher in the nek6 background than in the WT background (p value obtained by Wilkoxon test);* ***B.*** *Quantification CMT dynamics in each pavement cell area of p35S::GFP-MBD and nek6 p35S::GFP-MBD lines. CMT are more dynamics in lobe center and less dynamics in the neck compared to the other area.*

Interestingly, the microtubules appeared to be ca. 57% more dynamics in the pPDF1:: mCitrine-MBD line (calculated Wasserstein distance = 71180) than in the pp35S::GFP-MBD line (calculated Wasserstein distance calculated = 40862, Fig. 56 - A).
Assuming that the pipeline provides a robust enough result, and more than the fluorescent reporter, the choice of the promoter is more likely to be the cause of this difference. The predicted higher expression level under the p35S promoter may be consistent with phenotypes. The p35S::GFP-MBD line indeed displays some macroscopic phenotypes like twisted leaves, which are often associated with stabilized, bundled, cortical microtubules (REF = Celler Wasteneys, cited above). In contrast, the pPDF1:: mCitrin-MBD line does not shows such phenotypes. Note that this is not totally conclusive since the restriction of the expression in the epidermis may be the main reason for the (quasi) absence of phenotypic defects in the pPDF1::mCitrin-MBD line. A systematic comparison should involve the analysis of microtubule dynamics for a given construct, in different lines with different expression levels.

7.3.2. Microtubules appear slightly more dynamics in the *nek6* background

As mentioned above, NEK6 is a kinase that phosphorylates tubulin and leads to the depolymerization of a subset of microtubules (Motose et al., 2011). Based on the analysis of *nek6* mutants, it was proposed that cortical microtubules that best align with tensile stress are preferentially depolymerized (Takatani et al., 2020). Consistently, *nek6* exhibits hyper-aligned microtubules, notably in response to mechanical perturbations. The goal here was to use the *nek6* mutant to check whether our pipeline would be able to detect differences across WT and mutant.

CMT dynamics was evaluated in *nek6* in which the *pp35S::GFP-MBD* construct was introgressed through crossing, and compared to the CMT dynamics calculated in the original *pp35S::GFP-MBD* line. CMTs appears ca. 11 % more dynamics in *nek6* (calculated

Wasserstein distance = 44873) compared to the WT (calculated Wasserstein distance = 40862; Fig. 56 - A). Such a trend was conserved whatever the region of the cell (see below).

This result may be surprising since NEK6 promotes the depolymerisation of a subset of microtubules. One could have expected to see less dynamics microtubules because they are more stable over time. One hypothesis would be that depolymerization is less active in *nek6* but that polymerization is more important. One way to address this hypothesis would be to quantify CMT polymerization rate in *nek6* using the *p35S::GFP- EB1* marker. Alternatively, our result may also reflect the dynamics that our pipeline measures, which also includes microtubule reorientation. Indeed, the *nek6* mutant reorient its microtubules faster than the WT in response to ablation, arguably because microtubules aligned with tensile stress are less depolymerized (Takatani et al., 2020). Thus the higher dynamics observed here in *nek6* may rather reflect its self-organization properties.

7.3.3. CMT dynamics in the various subcellular domains of the pavement cells

Next we evaluated whether the dynamics of CMTs could be different according to the subcellular domains of the pavement cells. To do so, I manually segmented in 2D pavement cell. Then, I defined a series of subcellular regions using PaCeQuant (Möller et al., 2017) (Fig. 55). In particular, PaCeQuant can detect which part of the cell is concave or convex. I developed a FIJI macro which can separate the different regions of the cell.

“Neck” and “lobe” domains were defined as being restricted to the first 5µm within the cell of the neck and lobe areas (Fig. 55). The rest of the lobe (the inner part of the lobe) was considered the “center of lobe”. Finally, the “center of the cell” corresponds to the rest of the cell. The analysis of CMT dynamics in the various areas of the cell was carried out only with the *pp35S::GFP-MBD* line.

Differences between the different subdomains were rather subtly. For instance, there was no statistically significant difference in CMT dynamics between the center of the cell and the

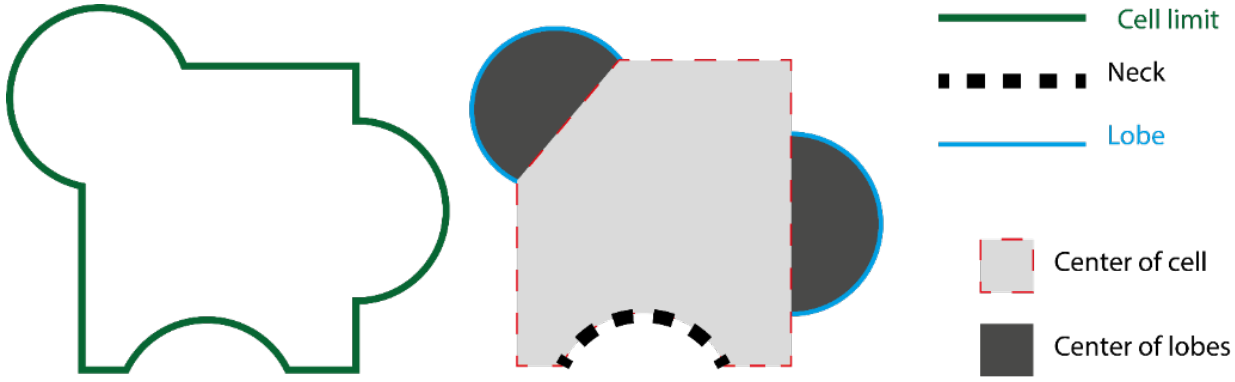

Figure 55: Descriptions of the pavement cell subcellular domains

Cell shape is detected with PaceQuant (green line). Cell is automatically subdivided in several areas. Neck (dotted line) and lobe (solid line) correspond to the first 5µm within the cell, center of lobes correspond to the cell area inside the lobes and the center of the cell corresponds to the rest of the cell.

lobes (Fig. 56). Note that this might result from the fact that, at the center of the cell, as the area analyzed is larger, the behaviors are more averaged. In addition, the center of the cell contains a large number of microtubule bundles. These bundles, much less dynamics, can decrease the average analyzed at the level of the center of the cell. As for the lobes, they are relatively small areas where the number of microtubules is low. This can also impact the analysis. This raises again the question of the CMT density that might trigger a bias on the measurement of CMT measurements. The use of the *pPDF1:: mCitrin-MBD* reporter line, which harbors a higher CMT dynamics possibly due to a lower signal density, would be useful to address these questions.

Despite these shortcomings, some trends could be obtained. The necks displayed the lowest microtubule dynamics (Wasserstein distance = 37498). Conversely, the centers of the lobes exhibited the highest microtubule dynamics (Wasserstein distance = 42544). This represents the highest difference (11,9 %) of CMT dynamics measured in the different regions. Such a difference might be correlated to the fact that, in necks, tensile stress is very directional, a large number of bundle are present, and they keep their orientation for some time. In contrast, inside the lobes (the center of lobe region), tensile stress is predicted to be more isotropic. Consistently, cortical microtubules display no particular orientation and smaller number of bundles. This would explain the observed higher dynamic of CMTs in lobe centers.

7.3.4. CMT dynamics in the various regions of the pavement cells in *nek6*.

Interestingly, the analysis of CMT dynamics in the various areas of *nek6* pavement cells show that CMT are more dynamic in *nek6* than in the WT whatever the region (Fig. 56). This result is consistent with CMT dynamics measured at the cell scale (Fig. 56). In *nek6*, the microtubules would form fewer bundles at the center of the cell, which would explain the increase in the dynamics of the microtubules. Furthermore, when considering variation of CMT dynamics in the various area of pavement cells, a similar trend can be observed in the

nek6 mutant. CMTs seem to be more dynamic in the centers of the lobes than in the necks. It is also possible that the effect of NEK6 on microtubule dynamics is too subtle to generate detectable differences between different regions of the pavement cell. An alternative would be to use a mutant with stronger microtubules and cell shape defects, like katanin mutants.

7.4. Applications for aerial organ imaging with LSFM

7.4.1. 2.5D and surface analysis

MorphoGraphX is one of the most classical image analysis protocols used in plant biology (Barbier de Reuille et al., 2015). This software allows a 2.5D analysis of the surface of the samples. The concept of MorphoGraphX is first to create a 3D volume as close as possible to the shape of the sample. Surface detection can be done either by using a 3D fined edges (Barbier de Reuille et al., 2015). A mesh is then applied to this 3D volume and generates a 2.5D representation of the sample surface. A multidirectional projection is then made on the mesh at a desired depth and a given thickness (Fig. 57). Here we tested whether MorphoGraphX could be used on images obtained with the Alpha3 LSFM.

For this purpose, I used again the *p35S::GFP-MBD and pPDF1::mCitrin-MBD* reporter line. Surface detection turned out to be much more problematic when using the Alpha3 LSFM. As described above, there are some optical aberrations inherent to light sheet microscopy such as a diffraction halo above linear signal like microtubules (Fig. 58 B). As described in the pipeline developed for the analysis of microtubule dynamics, this scattering can be of very strong intensity (see section 7.2). This makes the optimal parameters for surface detection very difficult to set. Thus, depending on the parameters, either the algorithms detect the diffraction as a surface and does not allow the microtubules signal to be properly projected, or fail to detect the surface signal and go inside the sample (Fig. 58).

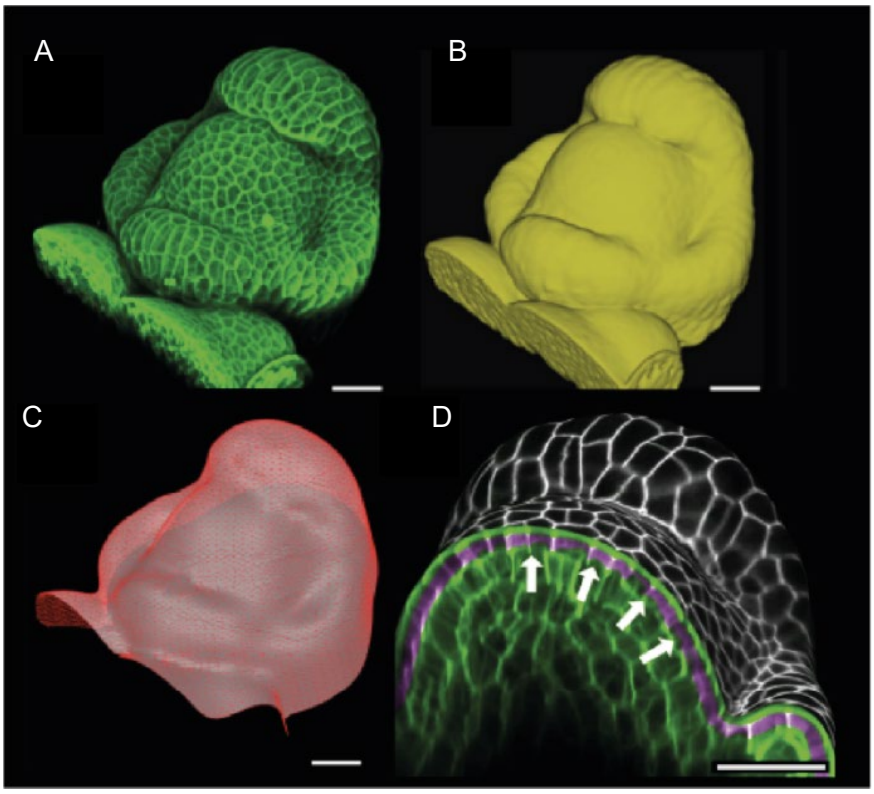

Figure 57 : MorphographX pipeline :

A,B. *After removing noise with 3D filters, the stack (green) is converted into a mask using edge detection (yellow);* ***C.*** *A coarse representation of the surface is extracted with marching cubes, then smoothed and subdivided;* ***D.*** *After subdivision, a thin band of signal representing the epidermal layer (purple) is projected onto the mesh, giving a clear outline of the cells. Note that the projection is perpendicular to the curved surface and its depth is user-defined (in this case, from 2 to 5 µm). Adapted from Barbier de Reuille et al, 2015*

I therefore developed an alternative pipeline to detect the microtubules with MorphoGraphX. The aim of this pipeline was first to remove as much as possible the optical aberrations and second to transform the image of microtubules into an image mimicking the membranes to make the surface easier to detect by the software. The raw images were then deconvolved with Huygens using a measured PSF. This removed much of the halo but unfortunately induced aberrations in the organization of the microtubules. Thus it was not possible to project the signal after deconvolution (Fig. 58).

To completely remove the halo, a substrate background was applied to the deconvolved images. Images resulting from these two filters enable the microtubules to be located more precisely at the surface. Two filters were then applied to transform this signal into a pseudo-membrane signal: a find edges and then a Gaussian blur of 10. This image processing thus allowed to have a uniform surface corresponding to the marking of the microtubules (Fig. 58). This image was used to detect the surface of the signal. The raw image was then used to project the surface signal.

As shown in Figure 59, and with the pipeline described above, the Alpha3 LSFM ultimately allows the same kind of imaging and analysis than CLSM for surface analysis. The added value of LSFM would thus be the speed of acquisition which allow to image either the same type of sample but much faster or be able to image much larger samples in an optimal time (by avoiding sample growth for example). However, this requires image post-processing when the halo issue appears, as illustrated with our pipeline.

In order to characterize more precisely the signal produced by Alpha3 LSFM, and to confirm the relevance of the Alpha3 LSFM, a comparison between the Alpha3 LSFM and the SP8 CSLM was made on a classical experiment of cell ablation. The idea was to fallow the reorientation of microtubules around an ablation. Microtubule orientation was quantified with Fibritool (Burian, 2014) after MorphographX projection as previously explained (Fig. 59). Fibriltool allow to quantify the average orientation and anisotropy of CMT arrays for a given region of interest (like a whole cell surface). The same region was imaged and quantified

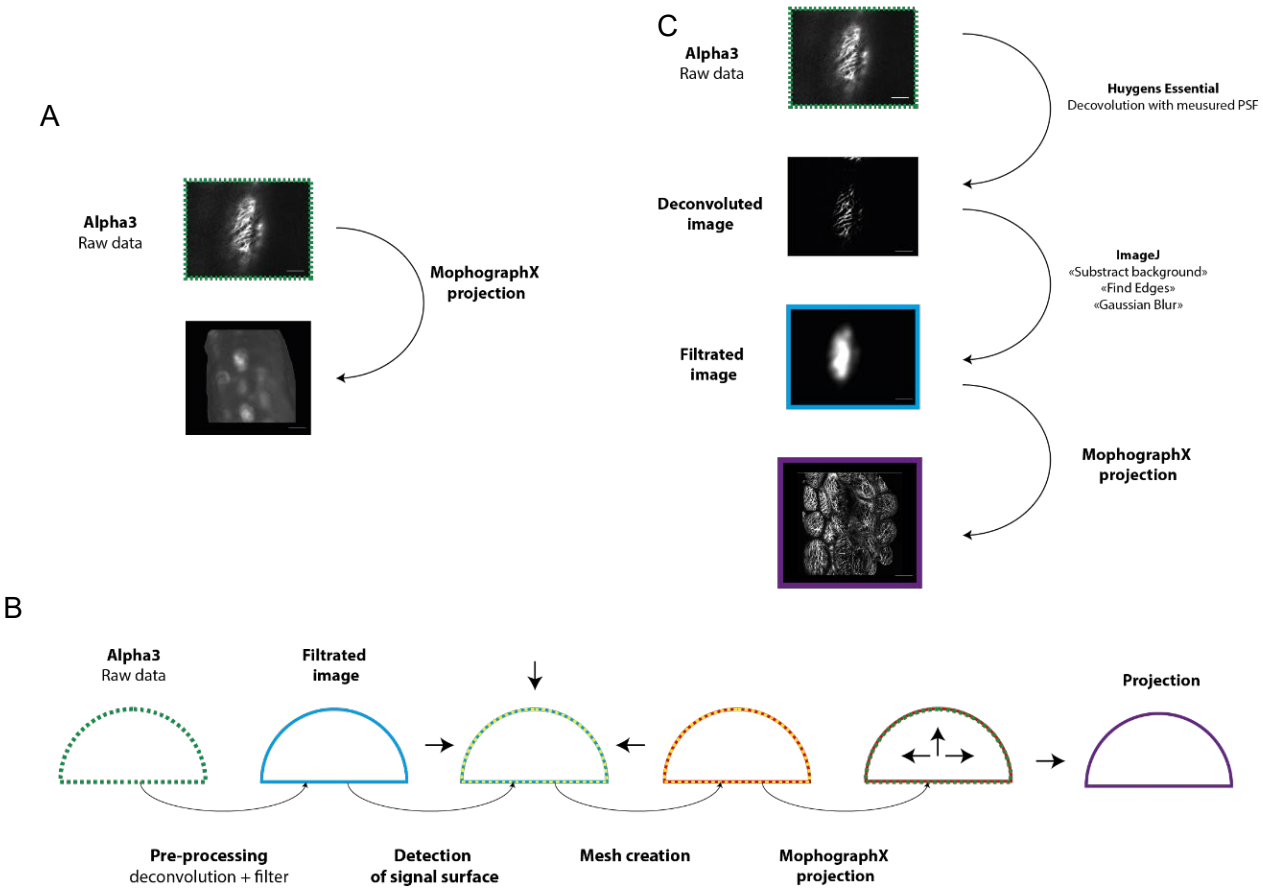

Figure 58: Alpha 3 LSFM for 2,5D analysis, surface analysis

A. *MorphographX analysis pipeline 3D projection of raw stack. Here the signal of microtubule is not detected as the surface. MoprhographX analysis doesn't properly extract the surface of the tissue to project the signal, here the microtubules;* ***B.*** *Pipeline of MorphographX projection with pre -process. Raw data (in green dotted line) is filtered in order to have a membrane like signal (in blue line). The detection of the surface is done of the filtered images (dotted line blue/yellow). The MorphographX mesh is create on this detection of surface (dotted line red/yellow). The raw data is use to make the projection on the mesh;* ***C.*** *Pre-processing of raw data (dotted green line) in order to transform CMTs signal in pseudo membrane labelling. Deconvolution is made on the raw data. A subtract background, 3D filtering finds edges and gaussian blur of 10 (blue line). The detection of surface is done on the filtered image. The projection is done with the raw data (violet line).*
In this specific example, cells in the middle of the sample were ablated.
Images were obtained from hypocotyls expressing pp35S ::GFP-MBD

once in Alpha3 LSFM once with SP8 CSLM RS on. So, the same sample was imaged immediately after ablation and 8h after ablation. Each surface was extracted and analyzed. As shown in Figures 59 - A - B, one could not see any differences between the Alpha3 LSFM and SP8 CSLM, at least qualitatively. Orientation was quantified and compared on 16 different hypocotyls for a total of 112 cells (Fig. 59 C - D). In this experiment, the effect of the ablation seemed rather minor (which may be explained by development age and growth conditions of the hypocotyl, and the presence of tow conflicting stress directions in the hypocotyls, see e.g. (Verger and Hamant, 2018). We could also detect differences in the quantifications of microtubule anisotropy and orientation between SP8 CSLM and Alpha3 LSFM. This will require further testing to further test the robustness of both the imaging protocol, and the microtubule analysis protocol.

7.4.2. 3D segmentation

The ability of the Alpha3 LSFM to image cells more deeply than the SP8 LSCM confocal can be of a great advantage when studying inner cell parameters during development. To test this, I attempted to segment cells of floral meristem, expressing the *pp35S::LTi6b-GFP* reporter line, in three dimensions (Fig. 60 A).

I first used the Python TimagesTK library to segment the cells in 3D (https://github.com/VirtualPlants/timagetk). This library allows to segment in 3D using the watershed technique. The watershed segmentation was done in two steps. First, the detection of local minima theoretically allows to detect the center of the cells. This local minimum is considered as the starting point of the segmentation. The second step consists of the watershed segmentation itself. It turned out that since the library was designed for confocal images, it was not possible to segment the raw cells output from Alpha 3 correctly. Several issues then appeared. The first one was the Gaussian blur stage of the segmentation. As light sheet microscope images are much less noisy than confocal images, the Gaussian blur step usually used upstream of segmentation was counter-productive here. Gaussian blurring made the membranes too diffuse and the pipeline often failed to properly

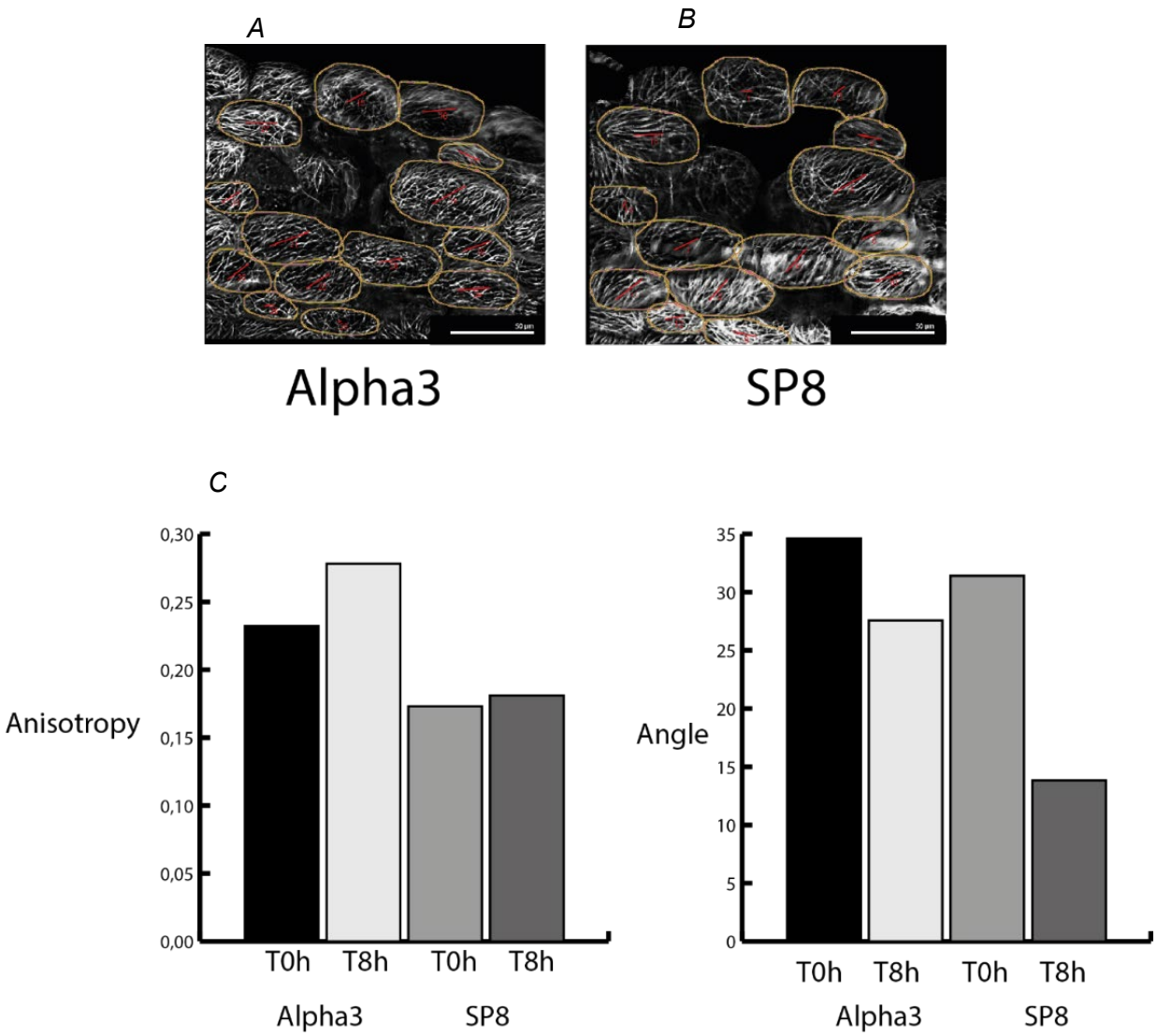

Figure 59: Analysis of microtubule orientation after ablation gives similar results with the Alpha 3 LSFM and the Leica SP8 CLSM

A-B. *Hypocotyl expressing pp35S:: GFP-MBD were imaged using either the Alpha3 LSFM (**A**) or the SP8 CLSM (**B**). MorphographX projection from each sample were generated and cells surrounding the ablation zone (circled in orange) were analyzed for microtubule orientation using Fibritool. Direction and size of the red lines indicate the average direction and the anisotropy of the microtubules;* ***C.*** *Microtubule direction and anisotropy analyzed on same cells imaged either with the Alspha3 or the SP8 microscopes. No significative differences can be detected between Alpha3 and SP8 neither for the anisotropy nor the principal direction (angle). Statistical significance were achieved with T test. n =112 cells from 16 hypocotyls. (Quatification performed with Anais Favre M2 intern in the team)*

detect local minima. The second issue came from the fact that the signal from the outer membranes was much weaker than the signal obtained with a CLSM. As a consequence, the algorithm failed to properly differentiate the background outside of the sample from the first cell layer. It turned out impossible, using the classic parameters of the algorithm, to segment the first layer of cells. The third issue came from the structure of the signal itself. For unknown reasons, it appeared much more complicated to determine the local minima from light sheet images than from confocal images. One hypothesis would be that the low noise together with the low and diffuse membrane signals, even without Gaussian blurring, would prevent to properly detect local minima.

Several tests were conducted to solve these issues. Regarding the first issue, it was easy to remove the Gaussian blur step from the pipeline. I tried to solve the second and third difficulties in a single pipeline. The idea was to bring out the signals of both the external membranes and the membranes that appeared not enough contrasted. For this, I used two different filters. First, I deconvolved the images with the commercial Huygens software using a measured PSF. This allowed (i) to make the membranes sharper, (ii) to increase the contrast between the center of the cells and the membranes and, (iii) to reduce the noise. Next, I used an anisotropic filter to make the membrane signals more intense and to uniformly blur the center of the cells. These two filters only partially solved the problem. They made the inner membranes less diffuse and brought out the external membrane signals, but not enough to detect the local minima. A contour detection step was therefore added to the pipeline before segmentation to artificially separate the inside of the first layer cells from the outside of the sample. Two different algorithms were used: on the one hand, the 3D LSM, which allows to detect the sample topology directly on the 3D stack , and on the other hand, a simple edge detect on each of the slices. From this pipeline, including deconvolution, anisotropic filtering and edge detection, it turned out possible to segment the cells of the first layer as well as the cells further down in the sample. In Figure 60 - A the segmented image contains more than 7000 segmented cells.

A

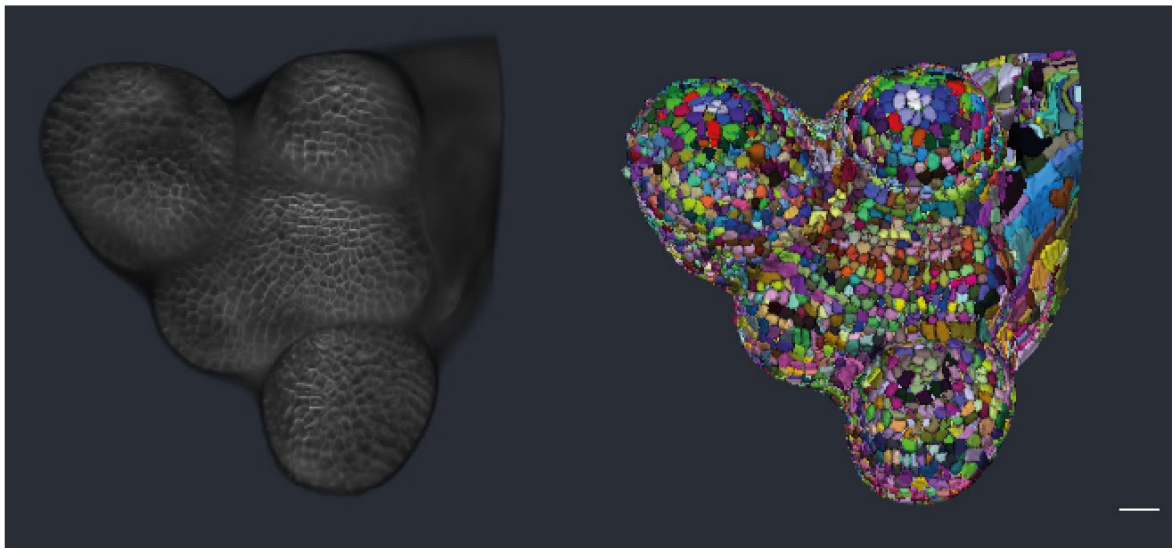

B

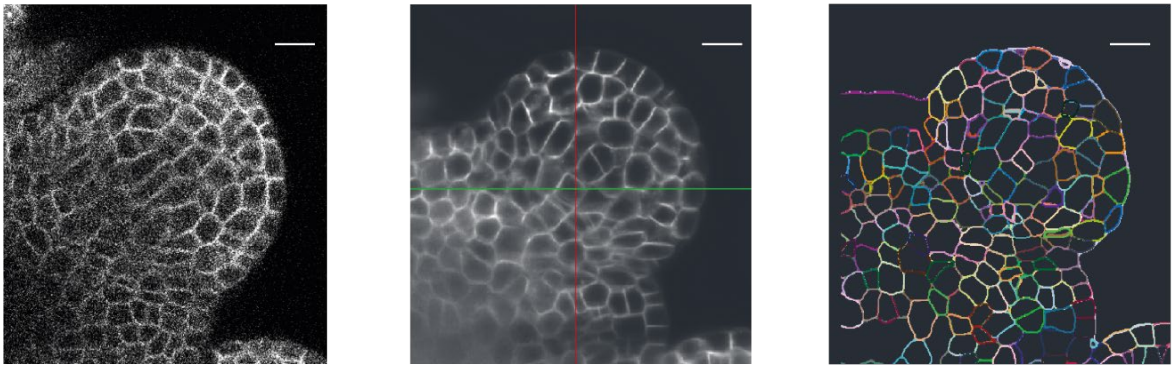

Figure 60: 3D segmentation of Alpha3 LSFM images

A. *Shoot apex expressing the p35S::LTi6b-GFP reporter line imaged with Alpha3 LSFM;* ***B.*** *Segmentation of the stack shown in A by TimageTK python library. More than 7000 cells are segmented;* ***C-D.*** *SP8 CSLM (**C**) and Alpha3 LSFM (**D**) images of a FM imaged 25µm in depth;* ***E.*** *Resulting segmentation of the Alpha3 LSFM image using TimageTK python library. The quality of the SP8 CSLM didn't make segmentation possible.*

Nevertheless, the pipeline should continue to be improved. Indeed, the segmented images display areas with under and over-segmentation errors (Fig. 60 A). The parameters will therefore need to be refined at each steps of the pipeline to stick as close as possible to the signal of the raw images. One possible improvement of this pipeline would be to uncouple the detection part of local minima and the watershed part itself. Indeed, the part of the pipeline allowing to highlight the membranes and to detect the surface could be used only for the detection of local minima. The position of the local minima would subsequently be applied to the raw images to run segmentation steps directly on the raw data. Obviously, the quality of the 3D segmentation would be ultimately checked by comparing the segmentation with a manual segmentation of the same flower bud.

As previously mentionned, the Alpha3 LSFM allows to image signal deeper in tissues. Moreover the large FOV of the Alpha 3 combined the speed of acquisition allow to make stacks of entire dissected apex with a signal quality good enough for segmentation. With the improvement of the protocol and the pipeline of segmentation it could be possible to follow cell shape and cell division during time in inner tissues. However, the segmentation of a high number of cells from large stacks might remain difficult. Indeed, within a large stack, the signal might be different in first slices of the stack compared to the center and the bottom of the stack. The detection of local minima might therefore be very difficult since the detection parameter is fixed. Thus if this parameter is tuned for the top of the signal, the detection might be bad in the center of the sample and *vice versa*. The implementation of a gradient detection of local minima was not possible with the python library we used. Maybe a custom detection will be really relevant for this modality of imaging.

The techniques of segmentation evolve really rapidly and new pipelines, based on neural network, were developed. This kind of pipelines are maybe the level of image analysis we need for segmentation of LSFM Two networks that allow segmentation by deep learning have recently been developed: 3D U-Net (Çiçek et al., 2016) or PlantSeg a plant specific pipeline for volumetric segmentation of plant tissues into cells (Wolny et al., 2020). This kind of analysis maybe will be the answer for 3D segmentation of huge volume and nonlinear signal. By the training of a network with manual and checked segmentation of LSFM images, we would be able to get reliable 3D segmentation. In conclusion of this part I have shown

that images of Alpha3 LSFM can be segmented with some adaptation of classical watershed segmentation.

7.4.3. Neural networks and MTs image enhancement

As reported above, the microtubule signal can be complicated to analyze. The aberrations specific to LSFM can complicate the classical maximum intensity projection. Moreover, if LSFM allows high temporal resolution with high signal intensity, it is much more difficult with weak signal. When signals are low, exposure time would need to be increased. In this case neural network would be the solution to keep a high temporal resolution even with low intensity signals. I thus collaborated with Anurhada Kar, postdoc in the RDP Mosaic team, and we tried to train a neural network in order to rebuild our images.

Neural networks need to be train to learn how to enhance specific types of images. The concept is to have a data set composed of two groups of images. One group of images is be called ground truth. These images are the high-quality images that one would like to get after training the neural network. The second set of images is called low. These images are the images one wants to improve. The two sets of images display exactly the same signal labelling, but one shows a high-quality signal and one a low-quality signal that needs to be improved. The neural network, during the learning process, analyses what transformations of convolution – deconvolution, it must go from a low-quality images to the corresponding ground truth image (Fig. 61).

The difficulty relies in the fact that it is very difficult to have already debugged images for the training data set. Indeed, the images produced by the microscope are already the images with the maximum quality we can have.

In CLSM, the quality of signals can changed by modifying acquisition parameters such as the power of laser and meaning of frames for instance (Weigert et al., 2018). Thus, in CLSM it is possible to generate two set of images for the same FOV but with two different qualities

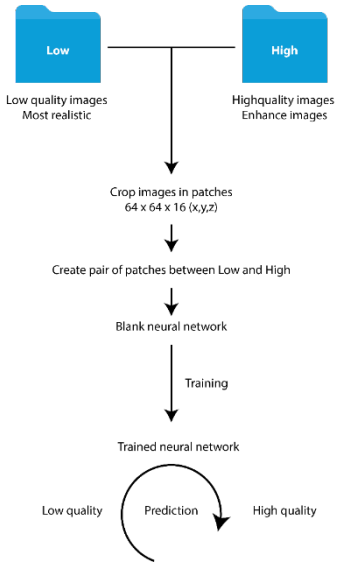

Figure 61: Neural network to enhance signal quality of LSFM images

Pipeline for neural network training. Two sets of images were used: one of a low quality which corresponds to realistic unprocessed images and one of a high quality which corresponds to processed and enhanced images. Images were subdivided into patches of 64x64x16 px. The neural network matches patches of each image to train to properly transform low quality signals into high quality signals. Once trained, the neural network can be used to correctly enhance new images.

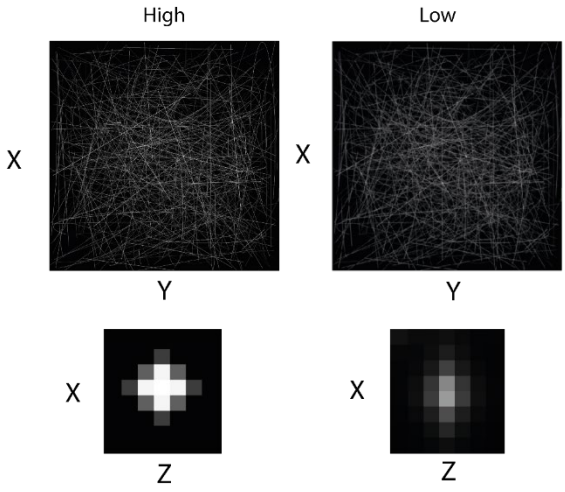

Figure 62: Synthetic CMTs for neural network training

Synthetic images of microtubules created to train the network. Curve and straight lines were created randomly in 3D with parameters similar to that of the true microtubules. High quality synthetic microtubules are perfectly round while low quality synthetic microtubules result from Poisson noise adding and Alpha3 PSF application.

that can used for the training.

In LSFM, there is no imaging parameters equivalent to the CLSM parameters. This makes LSFM easier to use, but for this specific case it is a limitation. It is not possible to have two kinds of signals just by changing imaging parameters. The LSFM give already the best quality of images. To bypass this limitation, I decided to produce synthetic images. The idea was to produce three-dimensional synthetic microtubules with characteristics somewhat similar to those of the microtubules imaged *in vivo*. In order to produce the data set, lines and curves were created randomly in three dimensions using Python libraries. For the ground truth data set, a Gaussian blur was applied to these lines, so that they are not monopixel. Then, pixels below a given value were removed so that the synthetic microtubules were tubular and had a diameter equal to the microtubules *in vivo*. This data set was then duplicated, and a Poisson noise and an experimental PSF was applied on one two datasets. Thus, the low set presented images mimicking both the noise generated by the sCMOS cameras and the aberrations of the microscope (Fig. 62). CSBdeep's 3D denoising neural network was used to improve the microtubules. After training, it allows to have images with a very high signal-to-noise ratio. Unfortunately, after prediction, the previously trained neural network did not allow a correct analysis of the microtubules. Indeed, it should be noted that the denoising works extremely well. Nevertheless, the microtubule signal is disturbed. Indeed, the microtubule signal was partially discontinuous, which does not reflect reality (Fig. 63 A). Moreover, even if in some cases, weak microtubules on the initial image were highlighted after prediction, some microtubules, although strongly present on the initial image, were no longer present on the predicted image. The two signal in green and violet do not fit very well even if violet signal have a better signal-to-noise ratio.

For some cells the prediction seems to be really relevant. In the case of Figure 63 B we can see for the first cell the prediction is quite the same as if a human did it. In panel b for the second cells we can see that the projection create some Mts which are note really present in the raw data. It is therefore impossible to use this trained network for the quantitative analysis of microtubules at the present time.

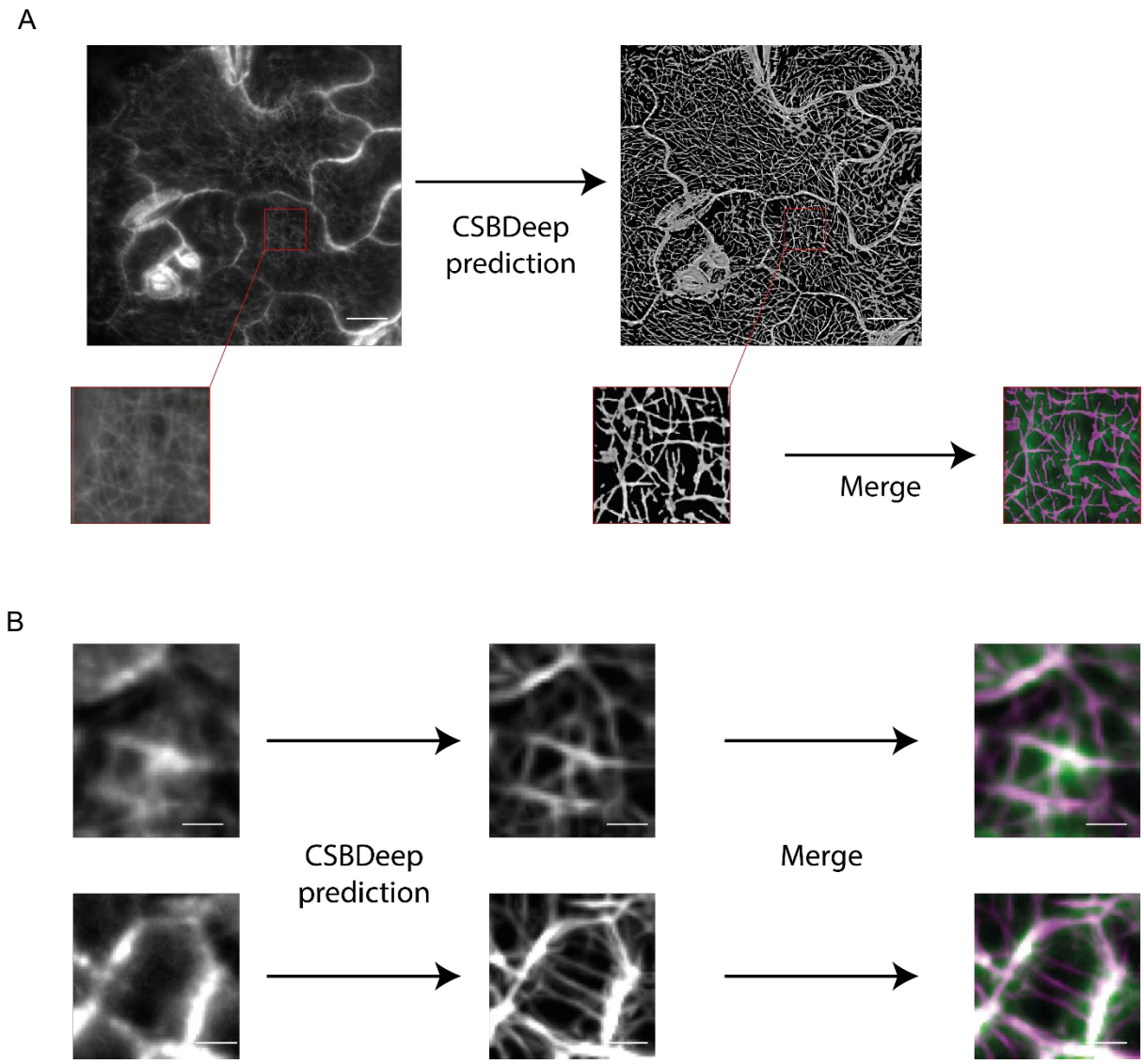

Figure 63: Training from synthetic data doesn't produce reliable microtubule signal enhancement in pavement cells and SAM cells

A. *Maximal intensity projection of CMTs signal in pavement cell (from p35S:: GFP-MBD reporter line) before and after prediction with neural network. In the close up panel and the merge. We can see raw data in green and predicted images in violet. We can see the prediction in not really realistic and doesn't fit really well on the original signal. (scale = 5µm)* ***B.*** *Close-up view of SAM cell (from p35S:: GFP-MBD reporter line) illustrating the non reproductibility of the prediction. Predicted microtubules (in violet) do not match properly with raw data (in green). In the first case the prediction is quite good whereas in the second case the projection is less realistic. (scale = 2.5µm)*

Neural network can actuality be used for several other application in imaging (see several application here https://github.com/HenriquesLab/ZeroCostDL4Mic). Segmentation or neural networks is something more and more done. It is obvious that the LSFM that allows deep membrane imaging coupled with this kind of technology will allow optimal cell segmentation. Work within the team on different neural networks has been able to show the internet of the technique. The PlantSeg neural network published by Wolny and colleagues in 2020 is beginning to be mastered within the team and its use seems adequate for the segmentation of several thousand cells. The implementation of a data set specific to alpha3 would be an important work to implement for the continuation of the work on the microscope.

7.5. Perspectives

7.5.1. Imaging over longer time scales

Alpha3 is a very powerful tool to image sample over long-lasting time lapses. I was able to show that it is possible to set up growth imaging on dissected meristems, and this following two different procedures (Fig. 47 - 48). Interestingly, the imaging chamber is large enough to proceed both classical time lapse imaging, i.e. by putting back the samples into growth chamber between each imaging time point (Barbier de Reuille et al., 2015; Prunet et al., 2016a; Reddy and Meyerowitz, 2005) and time lapse imaging by leaving the samples into the microscope chamber filled with culture medium. This possibility to leave the samples into the chamber coupled to the fact that several samples can be simultaneously mounted is a very promising set up for quantitative imaging over long time lapses.

However, extra implementations are still needed to optimize such long term imaging. To exceed 12 hours of imaging, a light system must be implemented inside the microscope as well as a microfluidic system to renew the medium in the observation chamber. These two implementations have been attempted during my thesis work but were unfortunately unsuccessful. Yet, such a microfluidic system would allow for instance to automatically add drug to the medium and to immediately monitor the effect on samples. Finally, the automatized detection of multiple samples remains probably the most difficult implementation.

Very long time lapses (several days) on dissected meristem, with the sample left in the microscope chamber, are very difficult to manage. Indeed, the meristem grows rapidly upwards. The meristem is thus rapidly out of focus and can even be lost during imaging. A downward movement of the sample might be programmed to compensate for its growth. However, this kind of adjustment is subject to the design of the microscope itself. On commercial systems, without collaboration with the manufacturer, it is very difficult to modify it. An open source system, such as the OpenSPIM, would likely makes such automatic movements easier to program.

Optimization and implementation of the Alpha3 system is definitely a track to follow to improve long time imaging methods to follow samples over longer time lapses with reduced phototoxicity and photobleaching, improved in-depth signal quality and the possibility to track drug effects.

7.5.2. The dynamics of microtubules: a challenge in imaging

- Optimization of imaging parameters

While CSLM are useful and powerful tools to follow cortical microtubule orientation and dynamics parameter over quite long time lapses (for the sake of example: (Hamant et al., 2008; Hervieux et al., 2016; Sampathkumar et al., 2014b; Takatani et al., 2020). Here our goal was rather to test the Alpha3LSFM to follow the behavior of microtubules over relatively short time scales. The acquisition parameters were therefore very important and the trio axial resolution/temporal resolution/spatial resolution was selected as optimal as possible. Thus, the images were taken each 30 seconds. This is already short regarding the number of slices per stack (between 100 and 200). However, one improvement would be to further optimize the acquiring method to reduce the time step as much as possible. The first step would be to use the camera binning to reduce the exposure time. The binning consists in averaging 4 pixels in one. This has the advantage to artificially make the camera much more sensitive. The disadvantage is that the resolution, in terms of pixels, is decreased by two (in

the case of a binning of 2x2). The use of binning would be very interesting when spatial resolution is not too important. It remains to choose what is the best balance between binning and other temporal resolution or maximum spatial resolution and lower temporal resolution. Furthermore, the pipelines have not been tested for these different conditions yet, to check whether the spatial resolution could have an impact on the quantification of the signal. It therefore remains to finish optimizing the pipeline with respect to the optimal spatial resolution.

The other imaging parameter that plays an important role in temporal resolution is the Z-step. Indeed, an optimal balance must be found between axial and temporal resolution. The data on microtubule dynamics reported here were obtained with a Z-step of 0.5µm. However, since *in fine* the analyses are done on projections, it is not necessary to have such a high Z-step resolution. Therefore, a series of trials could be done to optimize the Z-step. A larger Z-step would allow to shorten acquisition time and therefore reduce the time step between two acquisitions. Moreover, the fact that the stacks have fewer slices would make the “local contrast pipeline” more efficient to detect slices with microtubule signals. Indeed, with a Z-step of 1 or 1.5 µm, there would be more microtubules per slice and therefore it would be potentially easier to detect differences in local contrast gradients. It remains to be checked whether there is not too much loss of information with a larger Z-step. By increasing the Z-step from 0.5 to 1 µm, the temporal resolution would increase from 30 to 15 seconds. However, it would also be important to test whether the increase of Z-step would not also increase the probability to get blurry signals on interesting slices, thus reducing the quality of the projection. Preliminary tests with a Z-step of 1.5 µm showed that the amount of information lost is negligible and that the time step can be reduced to around 10 seconds.

- Optimization pipeline parameters

During my PhD, I set up pipeline to detect and analyze microtubule dynamics. In spite of encouraging results and satisfactory positive controls, several additional optimizations would improve the pipeline.

The main challenge of the pipeline is to detect correctly the signal of microtubules and so detected the slices where the signal of microtubule is. In order to improve the detection of signal the same type of pre-processing as the MorphoGraphX analysis can be developed. For MorphoGraphX a pseudo-membrane is generated from the microtubule signal to detect the surface of the signal and then to project the raw data. The work of pre-processing is more difficult than for MorphoGraphX we need to detect what is the constructed signal and what is the diffraction signal (which is the uniform signal). The detection step and then the Z - projection of the signal can thus be separated.

First for the detection step three possibilities of pre-processing are considered here.

1 - A step of deconvolution can be add to the pipeline. The use of deconvolution can be a good choice. Even if, the deconvolution can create artifacts at the level the microtubule signal, the deconvolution removes a part of the diffraction signal. The deconvoluted image can still have diffraction signal and depending of the sample we need to have a detection at the slice. The easiness of deconvolution makes it a good option to improve the pipeline.

2 – An anisotropic filter can be used to highlight the tubular structure and to smooth what is not an interesting solution like for MophoGraphX pipeline. This solution should be able to discriminate the uniform signal (artefactual) from the constructed signal (microtubules). A version of the script is currently under development but the main limitation is the computer power required to filter the entire stacks and also the processing time. This makes the script quite limited and almost unusable for time lapse with a large number of time points.

3 - The use of the neural networks trained in the 7.4.3 section. It has been shown that the aberrations brought by the prediction did not allow to use the new data for local microtubule analysis. Despite this, the network prediction removes all the aberrations induced during imaging. The background noise is removed as well as the set of optical aberrations present below and above the microtubule signal.

The image produced by the three possibilities previously mentioned can be used for the detection of the microtubule signal. The first part of the pipeline where we can detect which slice of a patch have the CMTs can be used on these processed images. Taking the example of neural networks, a prediction of the raw data will be transformed into crop then the detection of the local contrast gradient will be done on these crops and finally the number

of slices detected will be applied to the raw data. Thus, the detection of microtubules can be more precise while exploiting in fine only the raw data.

- Correction of detection

In the pipeline aiming to specifically select slices with microtubule signals and to discard slices with unspecific artefactual signals, the detection of the slices containing the microtubule signal may be sometimes erroneous. To improve this step, a correction script is under development. A height map will be constructed to assign a position number to selected slices (containing microtubule signals) for each crop. In this way, it should be possible to smooth outliers. Indeed, on consecutive patches, i.e. next to each other, the position of slices displaying microtubule signals within the stack should not be very different. So, if one of the positions is aberrant compared to its neighbors, it is replaced by the median position of the other crops, which will be closer to the real position. The final projection should be more reliable. This correction is currently being implemented together with Corentin Mollier.

- Test the pipeline on already published dataset

The relevance and the sensitivity of the two pipelines I developed together with Corentin Mollier have been challenged on a synthetic microtubule data set (Fig. 54). Synthetic artificial microtubules have been created with thickness parameters similar to the ones of real microtubules, and both rotation and blinking have been evaluated with the pipelines. The reconstructed map exhibits a gradient of the Wasserstein distance correlating the amplitude of the movement of the synthetic microtubules, therefore confirming that the pipelines can quantify microtubule dynamics during time with a high temporal resolution (Fig. 55). However, it also seems important to confirm the pipelines on an already published set of data showing microtubule dynamics over time. To do this I will use the data published by

Chan et al, 2007 reporting microtubules movement in AtEB1a–GFP reporter line in hypocoyls (Chan et al., 2007)

7.5.3 Further analysis of microtubule dynamics

- Confirm the difference in dynamics between genotypes

The analysis of microtubule dynamics in *p35S::GFP-MBD* and *pPDF1::mCitrin-MBD* lines shows some differences (Fig. 56). It is unlikely that the fluorescent protein would be responsible for the difference in dynamics. Nevertheless, to check this possibility, the *p35S::mCitrin-MBD* and *pPDF1::GFP-MBD* constructs might be useful. It will be interesting to check whether the nature of the fluorescence could induce some differences in signal quantification.

In order to complete my work and to be able to fully confirm my results, I will image and quantify CMT dynamics in the *nek6* mutant background using the *pPDF1::mCitrin-MBD* reporter line to compare the data with those obtained using the *p35S::GFP-MBD* line (Fig. 56). The cross is ongoing. Other mutants, such as the katanin mutant, may also provide more clearcult differences, and better assess the validity of LSFM.

- Correlation between polymerization and dynamics

To better estimate the importance of the polymerization rate in the dynamics of microtubules, the EB1 reporter line could be used (Tirnauer and Bierer, 2000). This could be performed in the wild-type background, but also in the mutant backgrounds. The crosses of AtEB1a–GFP to *nek6* is under progress.

- **Cotyledon development and microtubule dynamics**

Cotyledon cell shape changes during cotyledon development, switching from an unlobed shape in young stages to a puzzle shape in later development stages. The study of the local dynamics of microtubules during this changing of shape would be relevant. So, it would be interesting to complete the mapping of microtubule dynamics by a local study of microtubule dynamics during lobe and neck formation. A work on cotyledons developing in the dark could be set up as in the dark, cells have no lobes. After being brought to the light they take the shape of a puzzle.

The cells selected for the analysis of microtubule dynamics are in mechanically neutral zones: they are away from the veins, the tip of the cotyledons and the stomata. A data set including cells close to the stomata, at the tip and borders will be produced to quantify if there are differences between these different zones.

The work here on both the LSFM and microtubule dynamics is to be continued in order to have both a finalized and versatile protocol and broad biological data. The optimization of the acquisition and analysis part will allow to extract clean and reproducible data more easily. The increase of data in terms of cotyledon development or anatomical zone of cells will allow to confirm that the dynamics of the microtubules is locally heterogeneous and that it is differential according to the different zones of the cell.

8 MATERIAL AND METHODS

Plant lines

All procedures were performed on plants from the Col-0 ecotype. The pWUS::3xVENUS-N7 reporter lines (Pfeiffer et al., 2016) and T-DNA insertion lines vip3-1 (salk139885) and vip3-2 (salk083364) were used for this study (genotyping primers are listed in Table S1). To generate the pAG::AG-2xVenus line, we used a fragment of genomic AG from Col-0, containing 2655 bp of upstream sequence, the 1061 bp long 5'UTR (which includes intron 1) and 4241 bp from start to stop (which includes the 2999 bp long second intron),

amplified with the pPD381 and pPD413 primers (see Table S1) and transferred with XmaI digestion in BJ36 containing 2xVenus fluorescent reporter. BJ36 with 2xVenus was obtained from pCS2-Venus with pPD441 and pPD442 primers (see Table S1) adding 5xAla at the beginning of Venus and transferred twice in BJ36 through BamHI and XmaI digestion. The pAG::AG-2xVenus obtain fragment was transferred in pART (a kanamycin resistant vector) with XmaI digestion and then transformed in Col-0 plants using Agrobacterium tumefaciens. nek6-1 mutant lines provide from motose et al. 2008 (Motose et al., 2008). Other lines are pp35S::GFP-MBD ,Pdf1::mcitrin-MBD and pp35S::LTI6b-GFP (Cutler et al., 2000)

Growth conditions

In vivo

In “short day” conditions, plants were grown under a 8hr (20°C) / 16hr (15°C) light/dark period. In “long day” conditions, plants were grown under a 16hr (21°C) / 8hr (19°C) light/dark period. In continuous light conditions, plants were grown under continuous light at 16°C or 21°C. In “short day then long day or continuous light conditions”, plants were first grown for 3 weeks in short day conditions and then transferred to long day or continuous light conditions.

In vitro

Seed are sew on on solid custom-made Duchefa ‘Arabidopsis’ medium (DU0742.0025, Duchefa Biochemie). The plant growth in “long day” conditions in phytotron, plants were grown under a 16hr (21°C) / 8hr (19°C) light/dark period. Seedling are image after 7 days of growth.

RNA-seq analysis of vip3 shoot apices

vip3-1 and Col-0 shoot apices (from plants grown in short day 21°C then continuous light 16°C conditions) were dissected, by removing flower older than stage 4. Samples were collected into liquid nitrogen-cooled eppendorf tubes directly after dissection, each tube containing between 30 and 35 apices, 6 samples for each genotype. RNA extraction was performed using the PicoPure RNA Isolation kit Arcturus (ThermoFisher, KIT0204) with an on column DNAase treatment (Qiagen, catalog#79254). After elution, 2 samples were combined together, obtaining the final technical triplicates for each genotype. RNA concentrations in the samples were measured by Bioanalyser (Plant RNA Nano Assay, Agilent Technologies, Chip priming station number 5065- 4401, 16-pin bayonet electrode cartridge order number 5065- 4413) and sent for sequencing. Total RNA libraries preparation, Illumina sequencing and initial data analysis were performed by Fasteris: HiSeq instrument, Basecalling pipeline, HiSeq Control Software HD 3.4.0.38, analysed with Expression_mRNA_tuxedo. Adapter trimming – with Trimmomatic: A flexible read trimming tool for Illumina NGS data (Bolger, A. M., Lohse, M., & Usadel, B., 2014. Trimmomatic: A flexible trimmer for Illumina Sequence Data. Bioinformatics, btu170). Mapping - with BOWTIE 2.0.5 (Langmead et al., 2009), TOPHAT 2.0.6 (http://tophat.cbcb.umd.edu/), SAMTOOLS 1.2 (http://www.htslib.org/). Reference genome - Arabidopsis thaliana Ensembly TAIR10, from iGenome. Expression estimation, normalization and comparison – CUFFLINKS v2.1.1 (http://cufflinks.cbcb.umd.edu/).

Histological sections and in situ hybridization

The in situ hybridization on paraplast–embedded tissues was performed as described in (Vernoux et al., 2011). Shoot apices were sectioned into 8 µm thick slices. The probes for the coding regions of WUS and AG were amplified with specific primers (listed in the Table S1), where the T7 promoter sequence was added to the reverse primer. PCR products were further purified with the QIAquick PCR Purification Kit (QIAGEN Cat No./ID: 28106). In vitro transcription and DIG labeling of the probes were performed with the T7 RNA polymerase (Promega, #P2077) and DIG RNA Labeling Mix (Roche #11277073910). For

histological sections, late flowers (stage15-16) were harvested and paraplast–embedded following the same protocol. After sectioning, paraffin removal and rehydration, the samples were stained with 0.1% toluidine blue solution. Images were acquired using the Zeiss Imager.M2 microscope (20x and 40x objectives) and the Axiocam 503. Results were obtained in triplicates (3 independent rounds of in situ hybridizations, from independently grown plant populations).

Confocal laser scanning microscopy and image analysis

Dissected meristems and plants grown in vitro were imaged with a water dipping lens (x25, NA = 0.8) using a SP8 confocal microscope (Leica, Germany) to generate stack of optical sections with an interval of 0.2 µm between slices. The membranes were stained with FM4-64. Image analysis was performed using the Fiji software (http://fiji.sc/wiki/index.php/Fiji). The fluorescence intensity and size of the fluorescent area were extracted from the maximum projections of the image stacks of each individual flowers using the ROI tool. For smaller flowers, ca. 280 slices were imaged, representing a 56µm-thick stack; for older flowers, ca. 430 slices were imaged representing a 87µm-thick stack. Average diameter of the flowers was calculated by tracing 4 lines between the edges of a flower, crossing in the center with a 45° angle between each 2 of them. The extracted ROI values were further analyzed using Microsoft Excel. Statistical analysis was performed using either Microsoft Excel or R softwares. The two-tailed Student test was performed to compare means of independent biological replicates. Results were obtained in triplicates (3 independent rounds of imaging sessions, from independently grown plant populations).

For the comparison between LSFM and CLSM dissected apex were imaged using the Leica SP8 microscope with 40x (HCX APO, n.a. 0.8) long working distance, water immersion objectives with resonning scanner on. The image is 1024 per 1024 pixel due to technical limitation. Size of the pixel is equal to 0,325 um and the Z step is 0,5 um.

Software and libraries:

TimageTK (REF)

Fibriltool (Burian, 2014)

MorphographX (Barbier de Reuille et al., 2015)

Anisotropic filter (not published)

CSBdeep (Weigert et al., 2018)

Python 3

Time lapse and LSFM

All image are perform in Alpha 3 LSFM with 40x N = 0.8, size of the pixel is 0,1625 um and the Z step is 0,5 um

For the84h time lapse meristems are dissected in water in order to remove all FM older than stage 4. After dissection dissected meristem is stored in phytotron during 24h before imaging.

After each image dissected meristem is put back in the phytotron in a new Petri dishes in order to avoid contamination.

For 12h time lapse meristems are dissected in water in order to remove all FM older than stage 4. After dissection dissected meristem is stored in phytotron during 24h before imaging. The chamber of microscope is file with liquid Duchefa ‘Arabidopsis’ medium. In order to avoid contamination PPM is add to the medium.

Cell ablation

Ablation was performed with needle a less number of cell is ablated. Ablation was performed in 7 days hypocotyl of p35S::GFP-MBD line. Cells were imaged just after ablation and 8h after ablation. Between both imaging sample were put back in phytotron.

9. References

Abe, M., Takahashi, T., Komeda, Y., 2001. Identification of a cis-regulatory element for L1 layer-specific gene expression, which is targeted by an L1-specific homeodomain protein. Plant J. 26, 487–494. https://doi.org/10.1046/j.1365-313x.2001.01047.x

Ahrens, M.B., Orger, M.B., Robson, D.N., Li, J.M., Keller, P.J., 2013. Whole-brain functional imaging at cellular resolution using light-sheet microscopy. Nat. Methods 10, 413–420. https://doi.org/10.1038/nmeth.2434

Aiello, M., Cavaliere, C., D'Albore, A., Salvatore, M., 2019. The Challenges of Diagnostic Imaging in the Era of Big Data. J. Clin. Med. 8, 316. https://doi.org/10.3390/jcm8030316

Akanuma, T., Koshida, S., Kawamura, A., Kishimoto, Y., Takada, S., 2007. Paf1 complex homologues are required for Notch-regulated transcription during somite segmentation. Embo Rep. 8, 858–863. https://doi.org/10.1038/sj.embor.7401045

Akhmanova, A., Steinmetz, M.O., 2010. Microtubule +TIPs at a glance. J. Cell Sci. 123, 3415–3419. https://doi.org/10.1242/jcs.062414

Akhmanova, A., Steinmetz, M.O., 2008. Tracking the ends: a dynamics protein network controls the fate of microtubule tips. Nat. Rev. Mol. Cell Biol. 9, 309–322. https://doi.org/10.1038/nrm2369

Alberts, B., 2015. Molecular biology of the cell, Sixth edition. ed. Garland Science, Taylor and Francis Group, New York, NY.

Alemu, E.Y., Carl, J.W., Corrada Bravo, H., Hannenhalli, S., 2014. Determinants of expression variability. Nucleic Acids Res. 42, 3503–3514. https://doi.org/10.1093/nar/gkt1364

Allard, J.F., Ambrose, J.C., Wasteneys, G.O., Cytrynbaum, E.N., 2010a. A Mechanochemical Model Explains Interactions between Cortical Microtubules in Plants. Biophys. J. 99, 1082–1090. https://doi.org/10.1016/j.bpj.2010.05.037

Allard, J.F., Wasteneys, G.O., Cytrynbaum, E.N., 2010b. Mechanisms of Self-Organization of Cortical Microtubules in Plants Revealed by Computational Simulations. Mol. Biol. Cell 21, 278–286. https://doi.org/10.1091/mbc.e09-07-0579

Alvarez-Buylla, E.R., Benítez, M., Corvera-Poir, A., Chaos Cador, Á., de Folter, S., Gamboa de Buen, A., Garay-Arroyo, A., Jaimes-Miranda, F., Pérez-Ruiz, R.V., Piñeyro-Nelson, A., Sánchez-Corrales, Y.E., 2010. Flower Development, in: The Arabidopsis Book 8.

Alvarez-Venegas, R., Pien, S., Sadder, M., Witmer, X., Grossniklaus, U., Avramova, Z., 2003. ATX-1, an Arabidopsis Homolog of Trithorax, Activates Flower Homeotic Genes. Curr. Biol. 13, 627–637. https://doi.org/10.1016/S0960-9822(03)00243-4

Alvers, A.L., Ryan, S., Scherz, P.J., Huisken, J., Bagnat, M., 2014. Single continuous lumen formation in the zebrafish gut is mediated by smoothened-dependent tissue remodeling. Development 141, 1110–1119. https://doi.org/10.1242/dev.100313

Ambrose, C., Allard, J.F., Cytrynbaum, E.N., Wasteneys, G.O., 2011. A CLASP-modulated cell edge barrier mechanism drives cell-wide cortical microtubule organization in Arabidopsis. Nat. Commun. 2, 430. https://doi.org/10.1038/ncomms1444

Amos, W.B., White, J.G., Fordham, M., 1987. Use of confocal imaging in the study of biological structures. Appl. Opt. 26, 3239. https://doi.org/10.1364/AO.26.003239

Amrich, C.G., Davis, C.P., Rogal, W.P., Shirra, M.K., Heroux, A., Gardner, R.G., Arndt, K.M., VanDemark, A.P., 2012. Cdc73 Subunit of Paf1 Complex Contains C-terminal Ras-like Domain That Promotes Association of Paf1 Complex with Chromatin. J. Biol. Chem. 287, 10863–10875. https://doi.org/10.1074/jbc.M111.325647

Angenent, G.C., Stuurman, J., Snowden, K.C., Koes, R., 2005. Use of Petunia to unravel plant meristem functioning. Trends Plant Sci. 10, 243–250. https://doi.org/10.1016/j.tplants.2005.03.004

Ansel, J., Bottin, H., Rodriguez-Beltran, C., Damon, C., Nagarajan, M., Fehrmann, S., François, J., Yvert, G., 2008. Cell-to-Cell Stochastic Variation in Gene Expression Is a Complex Genetic Trait. PLoS Genet. 4, e1000049. https://doi.org/10.1371/journal.pgen.1000049

Arnaout, R., Ferrer, T., Huisken, J., Spitzer, K., Stainier, D.Y.R., Tristani-Firouzi, M., Chi, N.C., 2007. Zebrafish model for human long QT syndrome. Proc. Natl. Acad. Sci. 104, 11316–11321. https://doi.org/10.1073/pnas.0702724104

Asaoka, M., Ooe, M., Gunji, S., Milani, P., Runel, G., Horiguchi, G., Hamant, O., Sawa, S., Tsukaya, H., Ferjani, A., 2021. Stem integrity in *Arabidopsis thaliana* requires a load-bearing epidermis. Development 148, dev198028. https://doi.org/10.1242/dev.198028

Aukerman, M.J., Sakai, H., 2003. Regulation of flowering time and floral organ identity by a microRNA and its APETALA2-like target genes. Plant Cell 15, 2730–2741. https://doi.org/10.1105/tpc.016238

Axelrod, D., 1981. Cell-substrate contacts illuminated by total internal reflection fluorescence. J. Cell Biol. 89, 141–145. https://doi.org/10.1083/jcb.89.1.141

Baddeley, D., Bewersdorf, J., 2018. Biological Insight from Super-Resolution Microscopy: What We Can Learn from Localization-Based Images. Annu. Rev. Biochem. 87, 965–989. https://doi.org/10.1146/annurev-biochem-060815-014801

Barbier de Reuille, P., Routier-Kierzkowska, A.-L., Kierzkowski, D., Bassel, G.W., Schüpbach, T., Tauriello, G., Bajpai, N., Strauss, S., Weber, A., Kiss, A., Burian, A., Hofhuis, H., Sapala, A., Lipowczan, M., Heimlicher, M.B., Robinson, S., Bayer, E.M., Basler, K., Koumoutsakos, P., Roeder, A.H., Aegerter-Wilmsen, T., Nakayama, N., Tsiantis, M., Hay, A., Kwiatkowska, D., Xenarios, I., Kuhlemeier, C., Smith, R.S., 2015. MorphoGraphX: A platform for quantifying morphogenesis in 4D. eLife 4, e05864. https://doi.org/10.7554/eLife.05864

Barton, M.K., Poethig, R.S., 1993. Formation of the shoot apical meristem in Arabidopsis thaliana: an analysis of development in the wild type and in the shoot meristemless mutant. Development 119, 823–831.

Baurle, I., Laux, T., 2005. Regulation of WUSCHEL transcription in the stem cell niche of the Arabidopsis shoot meristem. Plant Cell 17, 2271–2280. https://doi.org/10.1105/tpc.105.032623

Bayguinov, P.O., Oakley, D.M., Shih, C.-C., Geanon, D.J., Joens, M.S., Fitzpatrick, J.A.J., 2018. Modern Laser Scanning Confocal Microscopy. Curr. Protoc. Cytom. 85, e39. https://doi.org/10.1002/cpcy.39

Beauzamy, L., Louveaux, M., Hamant, O., Boudaoud, A., 2015. Mechanically, the Shoot Apical Meristem of Arabidopsis Behaves like a Shell Inflated by a Pressure of About 1 MPa. Front. Plant Sci. 6. https://doi.org/10.3389/fpls.2015.01038

Belknap, W.R., 1983. Partial Purification of Intact Chloroplasts from *Chlamydomonas reinhardtii*. Plant Physiol. 72, 1130–1132. https://doi.org/10.1104/pp.72.4.1130

Berthet, B., Maizel, A., 2016. Light sheet microscopy and live imaging of plants. J. Microsc. 263, 158–164. https://doi.org/10.1111/jmi.12393

Besnard, F., Refahi, Y., Morin, V., Marteaux, B., Brunoud, G., Chambrier, P., Rozier, F., Mirabet, V., Legrand, J., Lainé, S., Thévenon, E., Farcot, E., Cellier, C., Das, P., Bishopp, A., Dumas, R., Parcy, F., Helariutta, Y., Boudaoud, A., Godin, C., Traas, J., Guédon, Y., Vernoux, T., 2014. Cytokinin signalling inhibitory fields provide robustness to phyllotaxis. Nature 505, 417–421. https://doi.org/10.1038/nature12791

Besson, S., Dumais, J., 2011. Universal rule for the symmetric division of plant cells. Proc. Natl. Acad. Sci. 108, 6294–6299. https://doi.org/10.1073/pnas.1011866108

Bichat, X., 1799. Traité des membranes en général et de diverses membranes en particulier, Richard. ed.

Bidhendi, A.J., Altartouri, B., Gosselin, F.P., Geitmann, A., 2019. Mechanical Stress Initiates and Sustains the Morphogenesis of Wavy Leaf Epidermal Cells. Cell Rep. 28, 1237-1250.e6. https://doi.org/10.1016/j.celrep.2019.07.006

Blake, W.J., Balázsi, G., Kohanski, M.A., Isaacs, F.J., Murphy, K.F., Kuang, Y., Cantor, C.R., Walt, D.R., Collins, J.J., 2006. Phenotypic Consequences of Promoter-Mediated Transcriptional Noise. Mol. Cell 24, 853–865. https://doi.org/10.1016/j.molcel.2006.11.003

Bleckmann, A., Weidtkamp-Peters, S., Seidel, C.A.M., Simon, R., 2010. Stem Cell Signaling in Arabidopsis Requires CRN to Localize CLV2 to the Plasma Membrane. Plant Physiol. 152, 166–176. https://doi.org/10.1104/pp.109.149930

Blom, H., Widengren, J., 2017. Stimulated Emission Depletion Microscopy. Chem. Rev. 117, 7377–7427. https://doi.org/10.1021/acs.chemrev.6b00653

Bollier, N., Sicard, A., Leblond, J., Latrasse, D., Gonzalez, N., Gévaudant, F., Benhamed, M., Raynaud, C., Lenhard, M., Chevalier, C., Hernould, M., Delmas, F., 2018. At-MINI ZINC FINGER2 and Sl-INHIBITOR OF MERISTEM ACTIVITY, a

Conserved Missing Link in the Regulation of Floral Meristem Termination in Arabidopsis and Tomato. Plant Cell 30, 83–100. https://doi.org/10.1105/tpc.17.00653

Bolte, S., Talbot, C., Boutte, Y., Catrice, O., Read, N.D., Satiat-Jeunemaitre, B., 2004. FM-dyes as experimental probes for dissecting vesicle trafficking in living plant cells. J. Microsc. 214, 159–173. https://doi.org/10.1111/j.0022-2720.2004.01348.x

Bounoutas, A., O'Hagan, R., Chalfie, M., 2009. The Multipurpose 15-Protofilament Microtubules in C. elegans Have Specific Roles in Mechanosensation. Curr. Biol. 19, 1362–1367. https://doi.org/10.1016/j.cub.2009.06.036

Bowman, J.L., Eshed, Y., 2000. Formation and maintenance of the shoot apical meristem. Trends Plant Sci. 5, 110–115. https://doi.org/10.1016/S1360-1385(00)01569-7

Bowman, J.L., Sakai, H., Jack, T., Weigel, D., Mayer, U., Meyerowitz, E.M., 1992. SUPERMAN, a regulator of floral homeotic genes in Arabidopsis. Development 114, 599–615.

Bowman, J.L., Smyth, D.R., 1999. CRABS CLAW, a gene that regulates carpel and nectary development in Arabidopsis, encodes a novel protein with zinc finger and helix-loop-helix domains. Development 126, 2387–2396.

Bowman, J.L., Smyth, D.R., Meyerowitz, E.M., 1991. Genetic interactions among floral homeotic genes of Arabidopsis. Development 112, 1–20.

Bowman, J.L., Smyth, D.R., Meyerowitz, E.M., 1989. Genes directing flower development in Arabidopsis. Plant Cell 1, 37–52. https://doi.org/C

Boyer, J.S., 1988. Cell enlargement and growth-induced water potentials. Physiol. Plant. 73, 311–316. https://doi.org/10.1111/j.1399-3054.1988.tb00603.x

Braam, J., Davis, R.W., 1990. Rain-, wind-, and touch-induced expression of calmodulin and calmodulin-related genes in Arabidopsis. Cell 60, 357–364. https://doi.org/10.1016/0092-8674(90)90587-5

Brand, U., Fletcher, J.C., Hobe, M., Meyerowitz, E.M., Simon, R., 2000. Dependence of Stem Cell Fate in Arabidopsis on a Feedback Loop Regulated by CLV3 Activity. Science 289, 617–619. https://doi.org/10.1126/science.289.5479.617

Breuil-Broyer, S., Trehin, C., Morel, P., Boltz, V., Sun, B., Chambrier, P., Ito, T., Negrutiu, I., 2016. Analysis of the Arabidopsis superman allelic series and the interactions with other genes demonstrate developmental robustness and joint specification of male-female boundary, flower meristem termination and carpel compartmentalization. Ann. Bot. 117, 905–923. https://doi.org/10.1093/aob/mcw023

Bringmann, M., 2012. Cracking the elusive alignment hypothesis: the microtubule-cellulose synthase nexus unraveled. Trends Plant Sci 17. https://doi.org/10.1016/j.tplants.2012.06.003

Brown, J.T., Bai, X.X., Johnson, A.W., 2000. The yeast antiviral proteins Ski2p, Ski3p, and Ski8p exist as a complex in vivo. Rna 6, 449–457. https://doi.org/10.1017/S1355838200991787

Burian, A., 2014. FibrilTool, an ImageJ plug-in to quantify fibrillar structures in raw microscopy images 7.

Burk, D.H., Ye, Z.-H., 2002. Alteration of Oriented Deposition of Cellulose Microfibrils by Mutation of a Katanin-Like Microtubule-Severing Protein. Plant Cell 14, 2145–2160. https://doi.org/10.1105/tpc.003947

Busch, M.A., Bomblies, K., Weigel, D., 1999. Activation of a Floral Homeotic Gene in Arabidopsis. Science 285, 585–587. https://doi.org/10.1126/science.285.5427.585

Busch, W., Miotk, A., Ariel, F.D., Zhao, Z., Forner, J., Daum, G., Suzaki, T., Schuster, C., Schultheiss, S.J., Leibfried, A., Haubeiß, S., Ha, N., Chan, R.L., Lohmann, J.U., 2010. Transcriptional Control of a Plant Stem Cell Niche. Dev. Cell 18, 841–853. https://doi.org/10.1016/j.devcel.2010.03.012

Buschmann, H., Lloyd, C.W., 2008. Arabidopsis mutants and the network of microtubule-associated functions. Mol Plant 1, 888–98. https://doi.org/10.1093/mp/ssn060

Carabelli, M., Possenti, M., Sessa, G., Ciolfi, A., Sassi, M., Morelli, G., Ruberti, I., 2007. Canopy shade causes a rapid and transient arrest in leaf development through auxin-induced cytokinin oxidase activity. Genes Dev. 21, 1863–1868. https://doi.org/10.1101/gad.432607

Carles, C.C., Choffnes-Inada, D., Reville, K., Lertpiriyapong, K., Fletcher, J.C., 2005. ULTRAPETALA1 encodes a SAND domain putative transcriptional regulator that controls shoot and floral meristem activity in Arabidopsis. Development 132, 897–911. https://doi.org/10.1242/dev.01642

Carles, C.C., Fletcher, J.C., 2009. The SAND domain protein ULTRAPETALA1 acts as a trithorax group factor to regulate cell fate in plants. Genes Dev. 23, 2723–2728. https://doi.org/10.1101/gad.1812609

Carles, C.C., Lertpiriyapong, K., Reville, K., Fletcher, J.C., 2004. The ULTRAPETALA1 gene functions early in Arabidopsis development to restrict shoot apical meristem activity and acts through WUSCHEL to regulate floral meirstem determinacy. Genetics 167, 1893–1903. https://doi.org/10.1534/genetics.104.028787

Castiglione, F., Pappalardo, F., Bianca, C., Russo, G., Motta, S., 2014. Modeling Biology Spanning Different Scales: An Open Challenge. BioMed Res. Int. 2014, 1–9. https://doi.org/10.1155/2014/902545

Centonze Frohlich, V., 2008. Phase Contrast and Differential Interference Contrast (DIC) Microscopy. J. Vis. Exp. 844. https://doi.org/10.3791/844

Chalfie, M., Tu, Y., Euskirchen, G., Ward, W., Prasher, D., 1994. Green fluorescent protein as a marker for gene expression. Science 263, 802–805. https://doi.org/10.1126/science.8303295

Chan, J., Calder, G., Fox, S., Lloyd, C., 2007. Cortical microtubule arrays undergo rotary movements in Arabidopsis hypocotyl epidermal cells. Nat Cell Biol 9. https://doi.org/10.1038/ncb1533

Chan, J., Calder, G.M., Doonan, J.H., Lloyd, C.W., 2003. EB1 reveals mobile microtubule nucleation sites in Arabidopsis. Nat. Cell Biol. 5, 967–971. https://doi.org/10.1038/ncb1057

Chan, J., Coen, E., 2020. Interaction between Autonomous and Microtubule Guidance Systems Controls Cellulose Synthase Trajectories. Curr. Biol. 30, 941-947.e2. https://doi.org/10.1016/j.cub.2019.12.066

Chan, J., Crowell, E., Eder, M., Calder, G., Bunnewell, S., Findlay, K., Vernhettes, S., Hofte, H., Lloyd, C., 2010. The rotation of cellulose synthase trajectories is microtubule dependent and influences the texture of epidermal cell walls in Arabidopsis hypocotyls. J. Cell Sci. 123, 3490–3495. https://doi.org/10.1242/jcs.074641

Chang, H.H., Hemberg, M., Barahona, M., Ingber, D.E., Huang, S., 2008. Transcriptome-wide noise controls lineage choice in mammalian progenitor cells. Nature 453, 544–547. https://doi.org/10.1038/nature06965

Chen, B.-C., Legant, W.R., Wang, K., Shao, L., Milkie, D.E., Davidson, M.W., Janetopoulos, C., Wu, X.S., Hammer, J.A., Liu, Z., English, B.P., Mimori-Kiyosue, Y., Romero, D.P., Ritter, A.T., Lippincott-Schwartz, J., Fritz-Laylin, L., Mullins, R.D., Mitchell, D.M., Bembenek, J.N., Reymann, A.-C., Böhme, R., Grill, S.W., Wang, J.T., Seydoux, G., Tulu, U.S., Kiehart, D.P., Betzig, E., 2014. Lattice light-sheet microscopy: Imaging molecules to embryos at high spatiotemporal resolution. Science 346, 1257998. https://doi.org/10.1126/science.1257998

Chen, H., Kankel, M.W., Su, S.C., Han, S.W.S., Ofengeim, D., 2018. Exploring the genetics and non-cell autonomous mechanisms underlying ALS/FTLD. Cell Death Differ. 25, 648–662. https://doi.org/10.1038/s41418-018-0060-4

Chen, J.-G., Ullah, H., Young, J.C., Sussman, M.R., Jones, A.M., 2001. ABP1 is required for organized cell elongation and division in Arabidopsis embryogenesis. Genes Dev. 15, 902–911. https://doi.org/10.1101/gad.866201

Chen, X., Meyerowitz, E.M., 1999. HUA1 and HUA2 Are Two Members of the Floral Homeotic AGAMOUS Pathway. Mol. Cell 3, 349–360. https://doi.org/10.1016/S1097-2765(00)80462-1

Chen, X.M., 2004. A microRNA as a translational repressor of APETALA2 in Arabidopsis flower development. Science 303, 2022–2025. https://doi.org/10.1126/science.1088060

Cheng, Y., Dai, X., Zhao, Y., 2006. Auxin biosynthesis by the YUCCA flavin monooxygenases controls the formation of floral organs and vascular tissues in Arabidopsis. Genes Dev. 20, 1790–1799. https://doi.org/10.1101/gad.1415106

Cheng, Y., Kato, N., Wang, W., Li, J., Chen, X., 2003. Two RNA Binding Proteins, HEN4 and HUA1, Act in the Processing of AGAMOUS Pre-mRNA in Arabidopsis thaliana. Dev. Cell 4, 53–66. https://doi.org/10.1016/S1534-5807(02)00399-4

Chhetri, R.K., Amat, F., Wan, Y., Höckendorf, B., Lemon, W.C., Keller, P.J., 2015. Whole-animal functional and developmental imaging with isotropic spatial resolution. Nat. Methods 12, 1171–1178. https://doi.org/10.1038/nmeth.3632

Chickarmane, V.S., Gordon, S.P., Tarr, P.T., Heisler, M.G., Meyerowitz, E.M., 2012. Cytokinin signaling as a positional cue for patterning the apical-basal axis of the growing Arabidopsis shoot meristem. Proc. Natl. Acad. Sci. U. S. A. 109, 4002–4007. https://doi.org/10.1073/pnas.1200636109

Chrétien, D., Fuller, S.D., 2000. Microtubules switch occasionally into unfavorable configurations during elongation. J. Mol. Biol. 298, 663–676. https://doi.org/10.1006/jmbi.2000.3696

Chrétien, D., Metoz, F., Verde, F., Karsenti, E., Wade, R., 1992. Lattice defects in microtubules: protofilament numbers vary within individual microtubules. J. Cell Biol. 117, 1031–1040. https://doi.org/10.1083/jcb.117.5.1031

Chu, X., Qin, X., Xu, H., Li, L., Wang, Z., Li, F., Xie, X., Zhou, H., Shen, Y., Long, J., 2013. Structural insights into Paf1 complex assembly and histone binding. Nucleic Acids Res. 41, 10619–10629. https://doi.org/10.1093/nar/gkt819

Chu, Y., Simic, R., Warner, M.H., Arndt, K.M., Prelich, G., 2007. Regulation of histone modification and cryptic transcription by the Bur1 and Paf1 complexes. Embo J. 26, 4646–4656. https://doi.org/10.1038/sj.emboj.7601887

Chuang, C.F., Meyerowitz, E.M., 2000. Specific and heritable genetic interference by double-stranded RNA in Arabidopsis thaliana. Proc. Natl. Acad. Sci. U. S. A. 97, 4985–4990. https://doi.org/10.1073/pnas.060034297

Çiçek, Ö., Abdulkadir, A., Lienkamp, S.S., Brox, T., Ronneberger, O., 2016. 3D U-Net: Learning Dense Volumetric Segmentation from Sparse Annotation. ArXiv160606650 Cs.

Clark, S.E., Jacobsen, S.E., Levin, J.Z., Meyerowitz, E.M., 1996. The CLAVATA and SHOOT MERISTEMLESS loci competitively regulate meristem activity in Arabidopsis. Development 122, 1567–1575.

Clark, S.E., Running, M.P., Meyerowitz, E.M., 1995. CLAVATA3 is a specific regulator of shoot and floral meristem development affecting the same processes as CLAVATA1. Development 121, 2057–2067.

Clark, S.E., Running, M.P., Meyerowitz, E.M., 1993. CLAVATA1, a regulator of meristem and flower development in Arabidopsis. Development 119, 397–418.

Clark, S.E., Williams, R.W., Meyerowitz, E.M., 1997. The CLAVATA1Gene Encodes a Putative Receptor Kinase That Controls Shoot and Floral Meristem Size in Arabidopsis. Cell 89, 575–585. https://doi.org/10.1016/S0092-8674(00)80239-1

Claßen-Bockhoff, R., Bull-Hereñu, K., 2013. Towards an ontogenetic understanding of inflorescence diversity. Ann. Bot. 112, 1523–1542. https://doi.org/10.1093/aob/mct009

Cnops, G., Neyt, P., Raes, J., Petrarulo, M., Nelissen, H., Malenica, N., Luschnig, C., Tietz, O., Ditengou, F., Palme, K., Azmi, A., Prinsen, E., Van Lijsebettens, M., 2006. The TORNADO1 and TORNADO2 genes function in several patterning processes during early leaf development in Arabidopsis thaliana. Plant Cell 18, 852–866. https://doi.org/10.1105/tpc.105.040568

Coen, E.S., Meyerowitz, E.M., 1991. The war of the whorls: genetic interactions controlling flower development. Nature 353, 31–37. https://doi.org/10.1038/353031a0

Coquelle, F.M., Vitre, B., Arnal, I., 2009. Structural basis of EB1 effects on microtubule dynamics. Biochem. Soc. Trans. 37, 997–1001. https://doi.org/10.1042/BST0370997

Cosgrove, D., 1986. Biophysical Control of Plant Cell Growth. Annu. Rev. Plant Physiol. 37, 377–405. https://doi.org/10.1146/annurev.pp.37.060186.002113

Cosgrove, D.J., 2005. Growth of the plant cell wall. Nat. Rev. Mol. Cell Biol. 6, 850–861. https://doi.org/10.1038/nrm1746

Cosgrove, D.J., 1993. Water Uptake by Growing Cells: An Assessment of the Controlling Roles of Wall Relaxation, Solute Uptake, and Hydraulic Conductance. Int. J. Plant Sci. 154, 10–21. https://doi.org/10.1086/297087

Cosgrove, D.J., 1987. Wall relaxation in growing stems: comparison of four species and assessment of measurement techniques. Planta 171, 266–278. https://doi.org/10.1007/BF00391104

Costa, P.J., Arndt, K.M., 2000. Synthetic Lethal Interactions Suggest a Role for the Saccharomyces cerevisiae Rtf1 Protein in Transcription Elongation. Genetics 156, 535–547.

Costanzo, E., Trehin, C., Vandenbussche, M., 2014. The role of WOX genes in flower development. Ann. Bot. 114, 1545–1553. https://doi.org/10.1093/aob/mcu123

Creff, A., Brocard, L., Ingram, G., 2015. A mechanically sensitive cell layer regulates the physical properties of the Arabidopsis seed coat. Nat Commun 6. https://doi.org/10.1038/ncomms7382

Cutler, S.R., Ehrhardt, D.W., Griffitts, J.S., Somerville, C.R., 2000. Random GFP::cDNA fusions enable visualization of subcellular structures in cells of Arabidopsis at a high frequency. Proc. Natl. Acad. Sci. 97, 3718–3723. https://doi.org/10.1073/pnas.97.7.3718

Daetwyler, S., Günther, U., Modes, C.D., Harrington, K., Huisken, J., 2019. Multi-sample SPIM image acquisition, processing and analysis of vascular growth in zebrafish. Development 146, dev173757. https://doi.org/10.1242/dev.173757

Das, P., Ito, T., Wellmer, F., Vernoux, T., Dedieu, A., Traas, J., Meyerowitz, E.M., 2009. Floral stem cell termination involves the direct regulation of AGAMOUS by PERIANTHIA. Development 136, 1605–1611. https://doi.org/10.1242/dev.035436

Daum, G., Medzihradszky, A., Suzaki, T., Lohmann, J.U., 2014. A mechanistic framework for noncell autonomous stem cell induction in Arabidopsis. Proc. Natl. Acad. Sci. U. S. A. 111, 14619–14624. https://doi.org/10.1073/pnas.1406446111

de Bossoreille, S., Morel, P., Trehin, C., Negrutiu, I., 2018. REBELOTE, a regulator of floral determinacy in Arabidopsis thaliana, interacts with both nucleolar andnucleoplasmic proteins. Febs Open Bio 8, 1636–1648. https://doi.org/10.1002/2211-5463.12504

de Groot, P., 2015. Principles of interference microscopy for the measurement of surface topography. Adv. Opt. Photonics 7, 1. https://doi.org/10.1364/AOP.7.000001

de Reuille, P.B., Bohn-Courseau, I., Ljung, K., Morin, H., Carraro, N., Godin, C., Traas, J., 2006. Computer simulations reveal properties of the cell-cell signaling network at the shoot apex in Arabidopsis. Proc. Natl. Acad. Sci. U. S. A. 103, 1627–1632. https://doi.org/10.1073/pnas.0510130103

De Veylder, L., 2001. Functional Analysis of Cyclin-Dependent Kinase Inhibitors of Arabidopsis. PLANT CELL ONLINE 13, 1653–1668. https://doi.org/10.1105/tpc.13.7.1653

De Vos, W.H., Munck, S., Timmermans, J.-P. (Eds.), 2016. Focus on Bio-Image Informatics, 1st ed. 2016. ed, Advances in Anatomy, Embryology and Cell Biology. Springer International Publishing : Imprint: Springer, Cham. https://doi.org/10.1007/978-3-319-28549-8

Delevoye, C., Heiligenstein, X., Ripoll, L., Gilles-Marsens, F., Dennis, M.K., Linares, R.A., Derman, L., Gokhale, A., Morel, E., Faundez, V., Marks, M.S., Raposo, G., 2016. BLOC-1 Brings Together the Actin and Microtubule Cytoskeletons to Generate Recycling Endosomes. Curr. Biol. 26, 1–13. https://doi.org/10.1016/j.cub.2015.11.020

DeMichele, D.W., Sharpe, P.J.H., 1973. An analysis of the mechanics of guard cell motion. J. Theor. Biol. 41, 77–96. https://doi.org/10.1016/0022-5193(73)90190-2

Demmerle, J., Innocent, C., North, A.J., Ball, G., Müller, M., Miron, E., Matsuda, A., Dobbie, I.M., Markaki, Y., Schermelleh, L., 2017. Strategic and practical guidelines for successful structured illumination microscopy. Nat. Protoc. 12, 988–1010. https://doi.org/10.1038/nprot.2017.019

Denyer, T., Ma, X., Klesen, S., Scacchi, E., Nieselt, K., Timmermans, M.C.P., 2019. Spatiotemporal Developmental Trajectories in the Arabidopsis Root Revealed Using High-Throughput Single-Cell RNA Sequencing. Dev. Cell 48, 840-852.e5. https://doi.org/10.1016/j.devcel.2019.02.022

Dermody, J.L., Buratowski, S., 2010. Leo1 Subunit of the Yeast Paf1 Complex Binds RNA and Contributes to Complex Recruitment. J. Biol. Chem. 285, 33671–33679. https://doi.org/10.1074/jbc.M110.140764

des Georges, A., Katsuki, M., Drummond, D.R., Osei, M., Cross, R.A., Amos, L.A., 2008. Mal3, the Schizosaccharomyces pombe homolog of EB1, changes the microtubule lattice. Nat. Struct. Mol. Biol. 15, 1102–1108. https://doi.org/10.1038/nsmb.1482

Desai, A., Mitchison, T.J., 1997. MICROTUBULE POLYMERIZATION DYNAMICS. Annu. Rev. Cell Dev. Biol. 13, 83–117. https://doi.org/10.1146/annurev.cellbio.13.1.83

Deyholos, M.K., Sieburth, L.E., 2000. Separable whorl-specific expression and negative regulation by enhancer elements within the AGAMOUS second intron. Plant Cell 12, 1799–1810. https://doi.org/10.1105/tpc.12.10.1799

Ding, L., Paszkowski-Rogacz, M., Nitzsche, A., Slabicki, M.M., Heninger, A.-K., Vries, I. de, Kittler, R., Junqueira, M., Shevchenko, A., Schulz, H., Hubner, N., Doss, M.X., Sachinidis, A., Hescheler, J., Iacone, R., Anastassiadis, K., Stewart, A.F., Pisabarro, M.T., Caldarelli, A., Poser, I., Theis, M., Buchholz, F., 2009. A Genome-Scale RNAi Screen for Oct4 Modulators Defines a Role of the Paf1 Complex for Embryonic Stem Cell Identity. Cell Stem Cell 4, 403–415. https://doi.org/10.1016/j.stem.2009.03.009

Dinh, T.T., Girke, T., Liu, X., Yant, L., Schmid, M., Chen, X., 2012. The floral homeotic protein APETALA2 recognizes and acts through an AT-rich sequence element. Development 139, 1978–1986. https://doi.org/10.1242/dev.077073

Ditta, G., Pinyopich, A., Robles, P., Pelaz, S., Yanofsky, M.F., 2004. The SEP4 Gene of Arabidopsis thaliana Functions in Floral Organ and Meristem Identity. Curr. Biol. 14, 1935–1940. https://doi.org/10.1016/j.cub.2004.10.028

Dixit, R., Cyr, R., 2004. The Cortical Microtubule Array: From Dynamics to Organization. Plant Cell 16, 2546–2552. https://doi.org/10.1105/tpc.104.161030

Dodt, H.-U., Leischner, U., Schierloh, A., Jährling, N., Mauch, C.P., Deininger, K., Deussing, J.M., Eder, M., Zieglgänsberger, W., Becker, K., 2007. Ultramicroscopy: three-dimensional visualization of neuronal networks in the whole mouse brain. Nat. Methods 4, 331–336. https://doi.org/10.1038/nmeth1036

Dolan, W.L., Chapple, C., 2017. Conservation and Divergence of Mediator Structure and Function: Insights from Plants. Plant Cell Physiol. 58, 04–21. https://doi.org/10.1093/pcp/pcw176

Dorcey, E., Rodriguez-Villalon, A., Salinas, P., Santuari, L., Pradervand, S., Harshman, K., Hardtke, C.S., 2012. Context-Dependent Dual Role of SKI8 Homologs in mRNA Synthesis and Turnover. PLOS Genet. 8, e1002652. https://doi.org/10.1371/journal.pgen.1002652

Drews, G.N., Bowman, J.L., Meyerowitz, E.M., 1991. Negative regulation of the Arabidopsis homeotic gene AGAMOUS by the APETALA2 product. Cell 65, 991–1002. https://doi.org/10.1016/0092-8674(91)90551-9

Durand-Smet, P., Chastrette, N., Guiroy, A., Richert, A., Berne-Dedieu, A., Szecsi, J., Boudaoud, A., Frachisse, J.-M., Bendahmane, M., Hamant, O., Asnacios, A., 2014. A Comparative Mechanical Analysis of Plant and Animal Cells Reveals Convergence across Kingdoms. Biophys. J. 107, 2237–2244. https://doi.org/10.1016/j.bpj.2014.10.023

Ejsmont, R.K., Sarov, M., Winkler, S., Lipinski, K.A., Tomancak, P., 2009. A toolkit for high-throughput, cross-species gene engineering in Drosophila. Nat. Methods 6, 435–437. https://doi.org/10.1038/nmeth.1334

Endrizzi, K., Moussian, B., Haecker, A., Levin, J.Z., Laux, T., 1996. The SHOOT MERISTEMLESS gene is required for maintenance of undifferentiated cells in Arabidopsis shoot and floral meristems and acts at a different regulatory level than the meristem genes WUSCHEL and ZWILLE. Plant J. 10, 967–979. https://doi.org/10.1046/j.1365-313X.1996.10060967.x

Engstrom, E.M., Andersen, C.M., Gumulak-Smith, J., Hu, J., Orlova, E., Sozzani, R., Bowman, J.L., 2011. Arabidopsis Homologs of the Petunia HAIRY MERISTEM Gene Are Required for Maintenance of Shoot and Root Indeterminacy. Plant Physiol. 155, 735–750. https://doi.org/10.1104/pp.110.168757

Eren, E.C., Dixit, R., Gautam, N., 2010. A Three-Dimensional Computer Simulation Model Reveals the Mechanisms for Self-Organization of Plant Cortical Microtubules into Oblique Arrays. Mol. Biol. Cell 21, 2674–2684. https://doi.org/10.1091/mbc.e10-02-0136

Eren, E.C., Gautam, N., Dixit, R., 2012. Computer simulation and mathematical models of the noncentrosomal plant cortical microtubule cytoskeleton. Cytoskeleton 69, 144–154. https://doi.org/10.1002/cm.21009

Ermolayev, V., Friedrich, M., Nozadze, R., Cathomen, T., Klein, M.A., Harms, G.S., Flechsig, E., 2009. Ultramicroscopy Reveals Axonal Transport Impairments in Cortical Motor Neurons at Prion Disease. Biophys. J. 96, 3390–3398. https://doi.org/10.1016/j.bpj.2009.01.032

Evkaikina, A.I., Romanova, M.A., Voitsekhovskaja, O.V., 2014. Evolutionary aspects of non-cell-autonomous regulation in vascular plants: structural background and models to study. Front. Plant Sci. 5. https://doi.org/10.3389/fpls.2014.00031

Fahrbach, F.O., Gurchenkov, V., Alessandri, K., Nassoy, P., Rohrbach, A., 2013. Self-reconstructing sectioned Bessel beams offer submicron optical sectioning for large fields of view in light-sheet microscopy. Opt. Express 21, 11425. https://doi.org/10.1364/OE.21.011425

Fal, K., Liu, M., Duisembekova, A., Refahi, Y., Haswell, E.S., Hamant, O., 2017. Phyllotactic regularity requires the Paf1 complex in *Arabidopsis*. Development 144, 4428–4436. https://doi.org/10.1242/dev.154369

Fan, Y., Burkart, G.M., Dixit, R., 2018. The Arabidopsis SPIRAL2 Protein Targets and Stabilizes Microtubule Minus Ends. Curr. Biol. 28, 987-994.e3. https://doi.org/10.1016/j.cub.2018.02.014

Fankhauser, G., 1945. Maintenance of normal structure in heteroploid salamander larvae, through compensation of changes in cell size by adjustment of cell number and cell shape. J. Exp. Zool. 100, 445–455. https://doi.org/10.1002/jez.1401000310

Fickentscher, R., Krauss, S.W., Weiss, M., 2018. Anti-correlation of cell volumes and cell-cycle times during the embryogenesis of a simple model organism. New J. Phys. 20, 113001. https://doi.org/10.1088/1367-2630/aaea91

Fickentscher, R., Struntz, P., Weiss, M., 2013. Mechanical Cues in the Early Embryogenesis of Caenorhabditis elegans. Biophys. J. 105, 1805–1811. https://doi.org/10.1016/j.bpj.2013.09.005

Fickentscher, R., Weiss, M., 2017. Physical determinants of asymmetric cell divisions in the early development of Caenorhabditis elegans. Sci. Rep. 7, 9369. https://doi.org/10.1038/s41598-017-09690-4

Fischl, H., Howe, F.S., Furger, A., Mellor, J., 2017. Paf1 Has Distinct Roles in Transcription Elongation and Differential Transcript Fate. Mol. Cell 65, 685-+. https://doi.org/10.1016/j.molcel.2017.01.006

Fisher, D.D., Cyr, R.J., 2000. Mechanical forces in plant growth and development. Gravitational Space Biol. Bull. Publ. Am. Soc. Gravitational Space Biol. 13, 67–73.

Fisher, R.H., Barton, M.K., Cohen, J.D., Cooke, T.J., 1996. Hormonal Studies of fass, an Arabidopsis Mutant That Is Altered in Organ Elongation. Plant Physiol 110, 1109–1121.

Fletcher, J.C., 2001. The ULTRAPETALA gene controls shoot and floral meristem size in Arabidopsis. Development 128, 1323–1333.

Fletcher, J.C., Brand, U., Running, M.P., Simon, R., Meyerowitz, E.M., 1999. Signaling of Cell Fate Decisions by CLAVATA3 in Arabidopsis Shoot Meristems. Science 283, 1911–1914. https://doi.org/10.1126/science.283.5409.1911

Franck, A.D., 2007. Tension applied through the Dam1 complex promotes microtubule elongation providing a direct mechanism for length control in mitosis. Nat Cell Biol 9. https://doi.org/10.1038/ncb1609

Franks, P.J., Farquhar, G.D., 2007. The Mechanical Diversity of Stomata and Its Significance in Gas-Exchange Control. Plant Physiol. 143, 78–87. https://doi.org/10.1104/pp.106.089367

Fu, Y., Xu, T., Zhu, L., Wen, M., Yang, Z., 2009. A ROP GTPase Signaling Pathway Controls Cortical Microtubule Ordering and Cell Expansion in Arabidopsis. Curr. Biol. 19, 1827–1832. https://doi.org/10.1016/j.cub.2009.08.052

Fuchs, M., Lohmann, J.U., 2020. Aiming for the top: non-cell autonomous control of shoot stem cells in Arabidopsis. J. Plant Res. 133, 297–309. https://doi.org/10.1007/s10265-020-01174-3

Fujita, S., Pytela, J., Hotta, T., Kato, T., Hamada, T., Akamatsu, R., Ishida, Y., Kutsuna, N., Hasezawa, S., Nomura, Y., Nakagami, H., Hashimoto, T., 2013. An Atypical Tubulin Kinase Mediates Stress-Induced Microtubule Depolymerization in Arabidopsis. Curr. Biol. 23, 1969–1978. https://doi.org/10.1016/j.cub.2013.08.006

Gall, J.G., 2016. The origin of in situ hybridization – A personal history. Methods 98, 4–9. https://doi.org/10.1016/j.ymeth.2015.11.026

Gall, J.G., Pardue, M.L., 1969. FORMATION AND DETECTION OF RNA-DNA HYBRID MOLECULES IN CYTOLOGICAL PREPARATIONS. Proc. Natl. Acad. Sci. 63, 378–383. https://doi.org/10.1073/pnas.63.2.378

Gallois, J.-L., Woodward, C., Reddy, G.V., Sablowski, R., 2002. Combined SHOOT MERISTEMLESS and WUSCHEL trigger ectopic organogenesis in Arabidopsis. Development 129, 3207–3217.

Gao, L., Shao, L., Higgins, C.D., Poulton, J.S., Peifer, M., Davidson, M.W., Wu, X., Goldstein, B., Betzig, E., 2012. Noninvasive Imaging beyond the Diffraction Limit of 3D Dynamics in Thickly Fluorescent Specimens. Cell 151, 1370–1385. https://doi.org/10.1016/j.cell.2012.10.008

Gayon, J., 2016. From Mendel to epigenetics: History of genetics. C. R. Biol. 339, 225–230. https://doi.org/10.1016/j.crvi.2016.05.009

Gertel, E.T., Green, P.B., 1977. Cell Growth Pattern and Wall Microfibrillar Arrangement: Experiments with *Nitella*. Plant Physiol. 60, 247–254. https://doi.org/10.1104/pp.60.2.247

Gittes, F., Mickey, B., Nettleton, J., Howard, J., 1993. Flexural rigidity of microtubules and actin filaments measured from thermal fluctuations in shape. J. Cell Biol. 120, 923–934. https://doi.org/10.1083/jcb.120.4.923

Gomez-Mena, C., de Folter, S., Costa, M.M.R., Angenent, G.C., Sablowski, R., 2005. Transcriptional program controlled by the floral homeotic gene AGAMOUS during early organogenesis. Development 132, 429–438. https://doi.org/10.1242/dev.01600

Goodrich, J., Puangsomlee, P., Martin, M., Long, D., Meyerowitz, E.M., Coupland, G., 1997. A Polycomb-group gene regulates homeotic gene expression in Arabidopsis. Nature 386, 44–51. https://doi.org/10.1038/386044a0

Gordon, S.P., Chickarmane, V.S., Ohno, C., Meyerowitz, E.M., 2009. Multiple feedback loops through cytokinin signaling control stem cell number within the Arabidopsis shoot meristem. Proc. Natl. Acad. Sci. U. S. A. 106, 16529–16534. https://doi.org/10.1073/pnas.0908122106

Green, K.A., Prigge, M.J., Katzman, R.B., Clark, S.E., 2005. CORONA, a member of the class III homeodomain leucine zipper gene family in arabidopsis, regulates stem cell specification and organogenesis. Plant Cell 17, 691–704. https://doi.org/10.1105/tpc.104.026179

Green, P.B., 1962. Mechanism for Plant Cellular Morphogenesis. Science 138, 1404–1405. https://doi.org/10.1126/science.138.3548.1404

Grigoriev, I., Akhmanova, A., 2010. Microtubule Dynamics at the Cell Cortex Probed by TIRF Microscopy, in: Methods in Cell Biology. Elsevier, pp. 91–109. https://doi.org/10.1016/S0091-679X(10)97006-4

Gruel, J., Landrein, B., Tarr, P., Schuster, C., Refahi, Y., Sampathkumar, A., Hamant, O., Meyerowitz, E.M., Jonsson, H., 2016. An epidermis-driven mechanism positions and scales stem cell niches in plants. Sci. Adv. 2, e1500989. https://doi.org/10.1126/sciadv.1500989

Guesdon, A., Bazile, F., Buey, R.M., Mohan, R., Monier, S., García, R.R., Angevin, M., Heichette, C., Wieneke, R., Tampé, R., Duchesne, L., Akhmanova, A., Steinmetz, M.O., Chrétien, D., 2016. EB1 interacts with outwardly curved and straight regions of the microtubule lattice. Nat. Cell Biol. 18, 1102–1108. https://doi.org/10.1038/ncb3412

Guo, L., Cao, X., Liu, Y., Li, J., Li, Y., Li, D., Zhang, K., Gao, C., Dong, A., Liu, X., 2018. A chromatin loop represses *WUSCHEL* expression in Arabidopsis. Plant J. 94, 1083–1097. https://doi.org/10.1111/tpj.13921

Gustafsson, M.G.L., Shao, L., Carlton, P.M., Wang, C.J.R., Golubovskaya, I.N., Cande, W.Z., Agard, D.A., Sedat, J.W., 2008. Three-Dimensional Resolution Doubling in Wide-Field Fluorescence Microscopy by Structured Illumination. Biophys. J. 94, 4957–4970. https://doi.org/10.1529/biophysj.107.120345

Gutierrez, R., Lindeboom, J.J., Paredez, A.R., Emons, A.M.C., Ehrhardt, D.W., 2009. Arabidopsis cortical microtubules position cellulose synthase delivery to the plasma membrane and interact with cellulose synthase trafficking compartments. Nat. Cell Biol. 11, 797–806. https://doi.org/10.1038/ncb1886

Hamant, O., 2008. Developmental patterning by mechanical signals in Arabidopsis. Science 322. https://doi.org/10.1126/science.1165594

Hamant, O., Das, P., Burian, A., 2014. Time-Lapse Imaging of Developing Meristems Using Confocal Laser Scanning Microscope, in: Žárský, V., Cvrčková, F. (Eds.), Plant Cell Morphogenesis, Methods in Molecular Biology. Humana Press, Totowa, NJ, pp. 111–119. https://doi.org/10.1007/978-1-62703-643-6_9

Hamant, O., Heisler, M.G., Jonsson, H., Krupinski, P., Uyttewaal, M., Bokov, P., Corson, F., Sahlin, P., Boudaoud, A., Meyerowitz, E.M., Couder, Y., Traas, J., 2008. Developmental Patterning by Mechanical Signals in Arabidopsis. Science 322, 1650–1655. https://doi.org/10.1126/science.1165594

Hansen, A.H., Hippenmeyer, S., 2020. Non-Cell-Autonomous Mechanisms in Radial Projection Neuron Migration in the Developing Cerebral Cortex. Front. Cell Dev. Biol. 8, 574382. https://doi.org/10.3389/fcell.2020.574382

Harper, B.K., Mabon, S.A., Leffel, S.M., Halfhill, M.D., Richards, H.A., Moyer, K.A., Stewart, C.N., 1999. Green fluorescent protein as a marker for expression of a second gene in transgenic plants. Nat. Biotechnol. 17, 1125–1129. https://doi.org/10.1038/15114

Hart, Y., Reich-Zeliger, S., Antebi, Y.E., Zaretsky, I., Mayo, A.E., Alon, U., Friedman, N., 2014. Paradoxical Signaling by a Secreted Molecule Leads to Homeostasis of Cell Levels. Cell 158, 1022–1032. https://doi.org/10.1016/j.cell.2014.07.033

Hawkins, C., Liu, Z., 2014. A model for an early role of auxin in Arabidopsis gynoecium morphogenesis. Front. Plant Sci. 5. https://doi.org/10.3389/fpls.2014.00327

He, Y., Doyle, M.R., Amasino, R.M., 2004. PAF1-complex-mediated histone methylation of FLOWERING LOCUS C chromatin is required for the vernalization-responsive, winter-annual habit in Arabidopsis. Genes Dev. 18, 2774–2784. https://doi.org/10.1101/gad.1244504

Heine, J., Reuss, M., Harke, B., D'Este, E., Sahl, S.J., Hell, S.W., 2017. Adaptive-illumination STED nanoscopy. Proc. Natl. Acad. Sci. 114, 9797–9802. https://doi.org/10.1073/pnas.1708304114

Heisler, M.G., 2010. Alignment between PIN1 polarity and microtubule orientation in the shoot apical meristem reveals a tight coupling between morphogenesis and auxin transport. PLoS Biol 8. https://doi.org/10.1371/journal.pbio.1000516

Heisler, M.G., Ohno, C., Das, P., Sieber, P., Reddy, G.V., Long, J.A., Meyerowitz, E.M., 2005. Patterns of Auxin Transport and Gene Expression during Primordium Development Revealed by Live Imaging of the Arabidopsis Inflorescence Meristem. Curr. Biol. 15, 1899–1911. https://doi.org/10.1016/j.cub.2005.09.052

Hejnowicz, Z., Sievers, A., 1995. Tissue stresses in organs of herbaceous plants: II. Determination in three dimensions in the hypocotyl of sunflower. J. Exp. Bot. 46, 1045–1053.

Hell, S.W., Wichmann, J., 1994. Breaking the diffraction resolution limit by stimulated emission: stimulated-emission-depletion fluorescence microscopy. Opt. Lett. 19, 780. https://doi.org/10.1364/OL.19.000780

Hempel, F., Feldman, L., 1995. Specification of Chimeric Flowering Shoots in Wild-Type Arabidopsis. Plant J. 8, 725–731. https://doi.org/10.1046/j.1365-313X.1995.08050725.x

Hendy, O., Campbell, J., Weissman, J.D., Larson, D.R., Singer, D.S., 2017. Differential context-specific impact of individual core promoter elements on transcriptional dynamics. Mol. Biol. Cell 28, 3360–3370. https://doi.org/10.1091/mbc.E17-06-0408

Hervieux, N., 2016. A mechanical feedback restricts sepal growth and shape in arabidopsis. Curr Biol 26. https://doi.org/10.1016/j.cub.2016.03.004

Hervieux, N., Dumond, M., Sapala, A., Routier-Kierzkowska, A.-L., Kierzkowski, D., Roeder, A.H.K., Smith, R.S., Boudaoud, A., Hamant, O., 2016. A Mechanical Feedback Restricts Sepal Growth and Shape in Arabidopsis. Curr. Biol. 26, 1019–1028. https://doi.org/10.1016/j.cub.2016.03.004

Hong, L., Dumond, M., Tsugawa, S., Sapala, A., Routier-Kierzkowska, A.-L., Zhou, Y., Chen, C., Kiss, A., Zhu, M., Hamant, O., Smith, R.S., Komatsuzaki, T., Li, C.-B., Boudaoud, A., Roeder, A.H.K., 2016. Variable Cell Growth Yields Reproducible Organ Development through Spatiotemporal Averaging. Dev. Cell 38, 15–32. https://doi.org/10.1016/j.devcel.2016.06.016

Honma, T., Goto, K., 2001. Complexes of MADS-box proteins are sufficient to convert leaves into floral organs. Nature 409, 525–529. https://doi.org/10.1038/35054083

Hooke, R., 1665. Micrographia.

Hornung, G., Bar-Ziv, R., Rosin, D., Tokuriki, N., Tawfik, D.S., Oren, M., Barkai, N., 2012. Noise-mean relationship in mutated promoters. Genome Res. gr.139378.112. https://doi.org/10.1101/gr.139378.112

Houseley, J., LaCava, J., Tollervey, D., 2006. RNA-quality control by the exosome. Nat. Rev. Mol. Cell Biol. 7, 529–539. https://doi.org/10.1038/nrm1964

Huang, W., Pitorre, D., Poretska, O., Marizzi, C., Winter, N., Poppenberger, B., Sieberer, T., 2015. ALTEREDMERISTEM PROGRAM1 Suppresses Ectopic Stem Cell Niche Formation in the Shoot Apical Meristem in a Largely Cytokinin-Independent Manner. Plant Physiol. 167, 1471-U573. https://doi.org/10.1104/pp.114.254623

Huang, Z., Shi, T., Zheng, B., Yumul, R.E., Liu, X., You, C., Gao, Z., Xiao, L., Chen, X., 2017. APETALA2 antagonizes the transcriptional activity of AGAMOUS in regulating floral stem cells in Arabidopsis thaliana. New Phytol. 215, 1197–1209. https://doi.org/10.1111/nph.14151

Huber, D., Voith von Voithenberg, L., Kaigala, G.V., 2018. Fluorescence in situ hybridization (FISH): History, limitations and what to expect from micro-scale FISH? Micro Nano Eng. 1, 15–24. https://doi.org/10.1016/j.mne.2018.10.006

Hugouvieux, V., Silva, C.S., Jourdain, A., Stigliani, A., Charras, Q., Conn, V., Conn, S.J., Carles, C.C., Parcy, F., Zubieta, C., 2018. Tetramerization of MADS family transcription factors SEPALLATA3 and AGAMOUS is required for floral meristem determinacy in Arabidopsis. Nucleic Acids Res. 46, 4966–4977. https://doi.org/10.1093/nar/gky205

Hugues, A., Jacobs, C.S., Roudier, F., 2020. Mitotic Inheritance of PRC2-Mediated Silencing: Mechanistic Insights and Developmental Perspectives. Front. Plant Sci. 11, 262. https://doi.org/10.3389/fpls.2020.00262

Huisken, J., 2004. Optical Sectioning Deep Inside Live Embryos by Selective Plane Illumination Microscopy. Science 305, 1007–1009. https://doi.org/10.1126/science.1100035

Huisken, J., Stainier, D.Y.R., 2009. Selective plane illumination microscopy techniques in developmental biology. Development 136, 1963–1975. https://doi.org/10.1242/dev.022426

Hutchinson, J., Lonsdale, D.M., 1982. The chromosomal distribution of cloned highly repetitive sequences from hexaploid wheat. Heredity 48, 371–376. https://doi.org/10.1038/hdy.1982.49

Hyman, A.A., Karsenti, E., 1996. Morphogenetic Properties of Microtubules and Mitotic Spindle Assembly. Cell 84, 401–410. https://doi.org/10.1016/S0092-8674(00)81285-4

Icha, J., Schmied, C., Sidhaye, J., Tomancak, P., Preibisch, S., Norden, C., 2016. Using Light Sheet Fluorescence Microscopy to Image Zebrafish Eye Development. J. Vis. Exp. 53966. https://doi.org/10.3791/53966

Ichikawa, T., Nakazato, K., Keller, P.J., Kajiura-Kobayashi, H., Stelzer, E.H.K., Mochizuki, A., Nonaka, S., 2013. Live Imaging of Whole Mouse Embryos during Gastrulation: Migration Analyses of Epiblast and Mesodermal Cells. PLoS ONE 8, e64506. https://doi.org/10.1371/journal.pone.0064506

Immink, R.G.H., Tonaco, I.A.N., de Folter, S., Shchennikova, A., van Dijk, A.D.J., Busscher-Lange, J., Borst, J.W., Angenent, G.C., 2009. SEPALLATA3: the “glue” for MADS box transcription factor complex formation. Genome Biol. 10, R24. https://doi.org/10.1186/gb-2009-10-2-r24

Inoue, D., 2016. Sensing surface mechanical deformation using active probes driven by motor proteins. Nat Commun 7. https://doi.org/10.1038/ncomms12557

Irish, V.F., Sussex, I.M., 1990. Function of the apetala-1 gene during Arabidopsis floral development. Plant Cell 2, 741–753.

Ishiguro, S., Watanabe, Y., Ito, N., Nonaka, H., Takeda, N., Sakai, T., Kanaya, H., Okada, K., 2002. SHEPHERD is the Arabidopsis GRP94 responsible for the formation of functional CLAVATA proteins. Embo J. 21, 898–908. https://doi.org/10.1093/emboj/21.5.898

Itzhak, D.N., Tyanova, S., Cox, J., Borner, G.H., 2016. Global, quantitative and dynamics mapping of protein subcellular localization. eLife 5, e16950. https://doi.org/10.7554/eLife.16950

Izban, M., Luse, D., 1992. The Rna Polymerase-Ii Ternary Complex Cleaves the Nascent Transcript in a 3’-]5’ Direction in the Presence of Elongation Factor-Sii. Genes Dev. 6, 1342–1356. https://doi.org/10.1101/gad.6.7.1342

Jack, T., 2004. Molecular and genetic mechanisms of floral control. Plant Cell 16, S1–S17. https://doi.org/10.1105/tpc.017038

Jack, T., Brockman, L.L., Meyerowitz, E.M., 1992. The homeotic gene APETALA3 of Arabidopsis thaliana encodes a MADS box and is expressed in petals and stamens. Cell 68, 683–697. https://doi.org/10.1016/0092-8674(92)90144-2

Jacobsen, S.E., Running, M.P., Meyerowitz, E.M., 1999. Disruption of an RNA helicase/RNAse III gene in Arabidopsis causes unregulated cell division in floral meristems. Development 126, 5231–5243.

Jacquemet, G., Carisey, A.F., Hamidi, H., Henriques, R., Leterrier, C., 2020. The cell biologist’s guide to super-resolution microscopy. J. Cell Sci. 133, jcs240713. https://doi.org/10.1242/jcs.240713

Jacques, E., Verbelen, J.P., Vissenberg, K., 2013. Mechanical stress in Arabidopsis leaves orients microtubules in a ‘continuous’ supracellular pattern. BMC Plant Biol 13. https://doi.org/10.1186/1471-2229-13-163

Jaehning, J.A., 2010. The Paf1 complex: platform or player in RNA polymerase II transcription? Biochim. Biophys. Acta 1799, 379–388. https://doi.org/10.1016/j.bbagrm.2010.01.001

Jenik, P.D., Irish, V.F., 2000. Regulation of cell proliferation patterns by homeotic genes during Arabidopsis floral development. Development 127, 1267–1276.

Jensen, G.S., Fal, K., Hamant, O., Haswell, E.S., 2017. The RNA Polymerase-Associated Factor 1 Complex Is Required for Plant Touch Responses. J. Exp. Bot. 68, 499–511. https://doi.org/10.1093/jxb/erw439

Jeong, S., Trotochaud, A.E., Clark, S.E., 1999. The Arabidopsis CLAVATA2 gene encodes a receptor-like protein required for the stability of the CLAVATA1 receptor-like kinase. Plant Cell 11, 1925–1933. https://doi.org/10.1105/tpc.11.10.1925

Jiang, J., Gill, B.S., Wang, G.L., Ronald, P.C., Ward, D.C., 1995. Metaphase and interphase fluorescence in situ hybridization mapping of the rice genome with bacterial artificial chromosomes. Proc. Natl. Acad. Sci. 92, 4487–4491. https://doi.org/10.1073/pnas.92.10.4487

Jimenez, A., Friedl, K., Leterrier, C., 2020. About samples, giving examples: Optimized Single Molecule Localization Microscopy. Methods 174, 100–114. https://doi.org/10.1016/j.ymeth.2019.05.008

Jofuku, K.D., Boer, B.G.W. den, Van Montagu, M., Okamuro, J.K., 1994. Control of Arabidopsis Flower and Seed Development by the Homeotic Gene APETALA2. Plant Cell 6, 1211–1225. https://doi.org/10.2307/3869820

Johnson, A.A.T., Hibberd, J.M., Gay, C., Essah, P.A., Haseloff, J., Tester, M., Guiderdoni, E., 2005. Spatial control of transgene expression in rice (Oryza sativa L.) using the GAL4 enhancer trapping system: Spatial control of transgene expression in rice. Plant J. 41, 779–789. https://doi.org/10.1111/j.1365-313X.2005.02339.x

Jones, S., Rappoport, J.Z., 2014. Interdependent epidermal growth factor receptor signalling and trafficking. Int. J. Biochem. Cell Biol. 51, 23–28. https://doi.org/10.1016/j.biocel.2014.03.014

Jonsson, H., Heisler, M.G., Shapiro, B.E., Meyerowitz, E.M., Mjolsness, E., 2006. An auxin-driven polarized transport model for phyllotaxis. Proc. Natl. Acad. Sci. U. S. A. 103, 1633–1638. https://doi.org/10.1073/pnas.0509839103

Karim, M.R., Hirota, A., Kwiatkowska, D., Tasaka, M., Aida, M., 2009. A Role for Arabidopsis PUCHI in Floral Meristem Identity and Bract Suppression. Plant Cell 21, 1360–1372. https://doi.org/10.1105/tpc.109.067025

Kassis, J.A., Kennison, J.A., Tamkun, J.W., 2017. Polycomb and Trithorax Group Genes in Drosophila. Genetics 206, 1699–1725. https://doi.org/10.1534/genetics.115.185116

Kaufmann, A., Mickoleit, M., Weber, M., Huisken, J., 2012. Multilayer mounting enables long-term imaging of zebrafish development in a light sheet microscope. Development 139, 3242–3247. https://doi.org/10.1242/dev.082586

Kayes, J.M., Clark, S.E., 1998. CLAVATA2, a regulator of meristem and organ development in Arabidopsis. Development 125, 3843–3851.

Keller, P.J., Schmidt, A.D., Santella, A., Khairy, K., Bao, Z., Wittbrodt, J., Stelzer, E.H.K., 2010. Fast, high-contrast imaging of animal development with scanned light sheet–based structured-illumination microscopy. Nat. Methods 7, 637–642. https://doi.org/10.1038/nmeth.1476

Keller, P.J., Schmidt, A.D., Wittbrodt, J., Stelzer, E.H.K., 2008. Reconstruction of Zebrafish Early Embryonic Development by Scanned Light Sheet Microscopy. Science 322, 1065–1069. https://doi.org/10.1126/science.1162493

Kharat, A.T., Singhal, S., 2017. A peek into the future of radiology using big data applications. Indian J. Radiol. Imaging 27, 241–248. https://doi.org/10.4103/ijri.IJRI_493_16

Kim, H., Binder, L.I., Rosenbaum, J.L., 1979. The periodic association of MAP2 with brain microtubules in vitro. J. Cell Biol. 80, 266–276. https://doi.org/10.1083/jcb.80.2.266

Kim, J., Guermah, M., McGinty, R.K., Lee, J.-S., Tang, Z., Milne, T.A., Shilatifard, A., Muir, T.W., Roeder, R.G., 2009. RAD6-Mediated Transcription-Coupled H2B Ubiquitylation Directly Stimulates H3K4 Methylation in Human Cells. Cell 137, 459–471. https://doi.org/10.1016/j.cell.2009.02.027

Kim, J., Guermah, M., Roeder, R.G., 2010. The Human PAF1 Complex Acts in Chromatin Transcription Elongation Both Independently and Cooperatively with SII/TFIIS. Cell 140, 491–503. https://doi.org/10.1016/j.cell.2009.12.050

Kimura, Y., Tasaka, M., Torii, K.U., Uchida, N., 2018. ERECTA-family genes coordinate stem cell functions between the epidermal and internal layers of the shoot apical meristem. Development 145, dev156380. https://doi.org/10.1242/dev.156380

Kinoshita, A., Betsuyaku, S., Osakabe, Y., Mizuno, S., Nagawa, S., Stahl, Y., Simon, R., Yamaguchi-Shinozaki, K., Fukuda, H., Sawa, S., 2010. RPK2 is an essential receptor-like kinase that transmits the CLV3 signal in Arabidopsis. Development 137, 4327–4327. https://doi.org/10.1242/dev.061747

Klar, T.A., Jakobs, S., Dyba, M., Egner, A., Hell, S.W., 2000. Fluorescence microscopy with diffraction resolution barrier broken by stimulated emission. Proc. Natl. Acad. Sci. 97, 8206–8210. https://doi.org/10.1073/pnas.97.15.8206

Knezetic, J.A., Luse, D.S., 1986. The presence of nucleosomes on a DNA template prevents initiation by RNA polymerase II in vitro. Cell 45, 95–104. https://doi.org/10.1016/0092-8674(86)90541-6

Komis, G., Mistrik, M., Šamajová, O., Doskočilová, A., Ovečka, M., Illés, P., Bartek, J., Šamaj, J., 2014. Dynamics and Organization of Cortical Microtubules as Revealed by Superresolution Structured Illumination Microscopy. Plant Physiol. 165, 129–148. https://doi.org/10.1104/pp.114.238477

Kondo, T., Sawa, S., Kinoshita, A., Mizuno, S., Kakimoto, T., Fukuda, H., Sakagami, Y., 2006. A Plant Peptide Encoded by CLV3 Identified by in Situ MALDI-TOF MS Analysis. Science 313, 845–848. https://doi.org/10.1126/science.1128439

Koornneef, M., Meinke, D., 2010. The development of Arabidopsis as a model plant. Plant J. 61, 909–921. https://doi.org/10.1111/j.1365-313X.2009.04086.x

Korenbaum, E., 2002. Calponin homology domains at a glance. J. Cell Sci. 115, 3543–3545. https://doi.org/10.1242/jcs.00003

Krizek, B.A., Fletcher, J.C., 2005. Molecular mechanisms of flower development: an armchair guide. Nat. Rev. Genet. 6, 688–698. https://doi.org/10.1038/nrg1675

Krogan, Nevan J., Dover, J., Wood, A., Schneider, J., Heidt, J., Boateng, M.A., Dean, K., Ryan, O.W., Golshani, A., Johnston, M., Greenblatt, J.F., Shilatifard, A., 2003. The Paf1 Complex Is Required for Histone H3 Methylation by COMPASS and Dot1p: Linking Transcriptional Elongation to Histone Methylation. Mol. Cell 11, 721–729. https://doi.org/10.1016/S1097-2765(03)00091-1

Krogan, N. J., Kim, M., Tong, A., Golshani, A., Cagney, G., Canadien, V., Richards, D.P., Beattie, B.K., Emili, A., Boone, C., Shilatifard, A., Buratowski, S., Greenblatt, J., 2003. Methylation of histone H3 by Set2 in Saccharomyces cerevisiae is linked to transcriptional elongation by RNA polymerase II. Mol. Cell. Biol. 23, 4207–4218. https://doi.org/10.1128/MCB.23.12.4207-4218.2003

Krogan, N.T., Hogan, K., Long, J.A., 2012. APETALA2 negatively regulates multiple floral organ identity genes in Arabidopsis by recruiting the co-repressor TOPLESS and the histone deacetylase HDA19. Development 139, 4180–4190. https://doi.org/10.1242/dev.085407

Krzic, U., Gunther, S., Saunders, T.E., Streichan, S.J., Hufnagel, L., 2012. Multiview light-sheet microscope for rapid in toto imaging. Nat. Methods 9, 730–733. https://doi.org/10.1038/nmeth.2064

Kubota, Y., Tsuyama, K., Takabayashi, Y., Haruta, N., Maruyama, R., Iida, N., Sugimoto, A., 2014. The PAF1 complex is involved in embryonic epidermal morphogenesis in Caenorhabditis elegans. Dev. Biol. 391, 43–53. https://doi.org/10.1016/j.ydbio.2014.04.002

Kuhlemeier, C., 2007. Phyllotaxis. Trends Plant Sci. 12, 143–150. https://doi.org/10.1016/j.tplants.2007.03.004

Kuhlemeier, C., Reinhardt, D., 2001. Auxin and phyllotaxis. Trends Plant Sci. 6, 187–189. https://doi.org/10.1016/S1360-1385(01)01894-5

Kutschera, U., Niklas, K.J., 2007. The epidermal-growth-control theory of stem elongation: An old and a new perspective. J. Plant Physiol. 164, 1395–1409. https://doi.org/10.1016/j.jplph.2007.08.002

Kwon, C.S., Chen, C., Wagner, D., 2005. WUSCHEL is a primary target for transcriptional regulation by SPLAYED in dynamics control of stem cell fate in Arabidopsis. Genes Dev. 19, 992–1003. https://doi.org/10.1101/gad.1276305

Landrein, B., Formosa-Jordan, P., Malivert, A., Schuster, C., Melnyk, C.W., Yang, W., Turnbull, C., Meyerowitz, E.M., Locke, J.C.W., Jönsson, H., 2018. Nitrate modulates stem cell dynamics in *Arabidopsis* shoot meristems through cytokinins. Proc. Natl. Acad. Sci. 115, 1382–1387. https://doi.org/10.1073/pnas.1718670115

Langenbacher, A.D., Nguyen, C.T., Cavanaugh, A.M., Huang, J., Lu, F., Chen, J.-N., 2011. The PAF1 complex differentially regulates cardiomyocyte specification. Dev. Biol. 353, 19–28. https://doi.org/10.1016/j.ydbio.2011.02.011

Langer-Safer, P.R., Levine, M., Ward, D.C., 1982. Immunological method for mapping genes on Drosophila polytene chromosomes. Proc. Natl. Acad. Sci. 79, 4381–4385. https://doi.org/10.1073/pnas.79.14.4381

Laufs, P., Grandjean, O., Jonak, C., Kiêu, K., Traas, J., 1998. Cellular Parameters of the Shoot Apical Meristem in Arabidopsis. Plant Cell 10, 1375–1389. https://doi.org/10.1105/tpc.10.8.1375

Laux, T., 2003. The stem cell concept in plants: A matter of debate. Cell 113, 281–283. https://doi.org/10.1016/S0092-8674(03)00312-X

Laux, T., Mayer, K.F., Berger, J., Jurgens, G., 1996. The WUSCHEL gene is required for shoot and floral meristem integrity in Arabidopsis. Development 122, 87–96.

Lazzari, G., Vinciguerra, D., Balasso, A., Nicolas, V., Goudin, N., Garfa-Traore, M., Fehér, A., Dinnyés, A., Nicolas, J., Couvreur, P., Mura, S., 2019. Light sheet fluorescence microscopy versus confocal microscopy: in quest of a suitable tool to assess drug and nanomedicine penetration into multicellular tumor spheroids. Eur. J. Pharm. Biopharm. 142, 195–203. https://doi.org/10.1016/j.ejpb.2019.06.019

Ledbetter, M.C., Porter, K.R., 1963. A “MICROTUBULE” IN PLANT CELL FINE STRUCTURE. J. Cell Biol. 19, 239–250. https://doi.org/10.1083/jcb.19.1.239

Lee, C., Clark, S.E., 2015. A WUSCHEL-Independent Stem Cell Specification Pathway Is Repressed by PHB, PHV and CNA in Arabidopsis. Plos One 10, e0126006. https://doi.org/10.1371/journal.pone.0126006

Lee, Z.H., Hirakawa, T., Yamaguchi, N., Ito, T., 2019. The Roles of Plant Hormones and Their Interactions with Regulatory Genes in Determining Meristem Activity. Int. J. Mol. Sci. 20, 4065. https://doi.org/10.3390/ijms20164065

Leibfried, A., To, J.P.C., Busch, W., Stehling, S., Kehle, A., Demar, M., Kieber, J.J., Lohmann, J.U., 2005. WUSCHEL controls meristem function by direct regulation of cytokinin-inducible response regulators. Nature 438, 1172–1175. https://doi.org/10.1038/nature04270

Lemon, W.C., Pulver, S.R., Höckendorf, B., McDole, K., Branson, K., Freeman, J., Keller, P.J., 2015. Whole-central nervous system functional imaging in larval Drosophila. Nat. Commun. 6, 7924. https://doi.org/10.1038/ncomms8924

Lenhard, M., Bohnert, A., Jürgens, G., Laux, T., 2001. Termination of Stem Cell Maintenance in Arabidopsis Floral Meristems by Interactions between WUSCHEL and AGAMOUS. Cell 105, 805–814. https://doi.org/10.1016/S0092-8674(01)00390-7

Lenhard, M., Jürgens, G., Laux, T., 2002. The WUSCHEL and SHOOTMERISTEMLESS genes fulfil complementary roles in Arabidopsis shoot meristem regulation. Development 129, 3195–3206.

Lenhard, M., Laux, T., 2003. Stem cell homeostasis in the Arabidopsis shoot meristem is regulated by intercellular movement of CLAVATA3 and its sequestration by CLAVATA1. Development 130, 3163–3173. https://doi.org/10.1242/dev.00525

Levsky, J.M., 2003. Fluorescence in situ hybridization: past, present and future. J. Cell Sci. 116, 2833–2838. https://doi.org/10.1242/jcs.00633

Li, J.J., Jia, D.X., Chen, X.M., 2001. HUA1, a regulator of stamen and carpel identities in Arabidopsis, codes for a nuclear RNA binding protein. Plant Cell 13, 2269–2281. https://doi.org/10.1105/tpc.13.10.2269

Li, S., Lei, L., Somerville, C.R., Gu, Y., 2012. Cellulose synthase interactive protein 1 (CSI1) links microtubules and cellulose synthase complexes. Proc. Natl. Acad. Sci. 109, 185–190. https://doi.org/10.1073/pnas.1118560109

Liang, B.M., Sharp, R.E., Baskin, T.I., 1997. Regulation of Growth Anisotropy in Well-Watered and Water-Stressed Maize Roots (I. Spatial Distribution of Longitudinal, Radial, and Tangential Expansion Rates). Plant Physiol. 115, 101–111. https://doi.org/10.1104/pp.115.1.101

Light, V.-J., Maverick, G., 2008. Paradigm shift in laser scanning confocal microscopy: Resonant real time live spectral imaging for cell dynamics. Adv. Biotech.

Lin, D., Cao, L., Zhou, Z., Zhu, L., Ehrhardt, D., Yang, Z., Fu, Y., 2013. Rho GTPase Signaling Activates Microtubule Severing to Promote Microtubule Ordering in Arabidopsis. Curr. Biol. 23, 290–297. https://doi.org/10.1016/j.cub.2013.01.022

Lindeboom, J.J., Nakamura, M., Hibbel, A., Shundyak, K., Gutierrez, R., Ketelaar, T., Emons, A.M.C., Mulder, B.M., Kirik, V., Ehrhardt, D.W., 2013. A Mechanism for Reorientation of Cortical Microtubule Arrays Driven by Microtubule Severing. Science 342, 1245533–1245533. https://doi.org/10.1126/science.1245533

Liu, X., Kim, Y.J., Müller, R., Yumul, R.E., Liu, C., Pan, Y., Cao, X., Goodrich, J., Chen, X., 2011. AGAMOUS Terminates Floral Stem Cell Maintenance in Arabidopsis by Directly Repressing WUSCHEL through Recruitment of Polycomb Group Proteins. Plant Cell 23, 3654–3670. https://doi.org/10.1105/tpc.111.091538

Lohmann, J.U., Hong, R.L., Hobe, M., Busch, M.A., Parcy, F., Simon, R., Weigel, D., 2001. A Molecular Link between Stem Cell Regulation and Floral Patterning in Arabidopsis. Cell 105, 793–803. https://doi.org/10.1016/S0092-8674(01)00384-1

Long, J.A., Barton, M.K., 1998. The development of apical embryonic pattern in Arabidopsis. Development 125, 3027–3035.

Long, J.A., Moan, E.I., Medford, J.I., Barton, M.K., 1996. A member of the KNOTTED class of homeodomain proteins encoded by the STM gene of Arabidopsis. Nature 379, 66–69. https://doi.org/10.1038/379066a0

Lorenzo, C., Frongia, C., Jorand, R., Fehrenbach, J., Weiss, P., Maandhui, A., Gay, G., Ducommun, B., Lobjois, V., 2011. Live cell division dynamics monitoring in 3D large spheroid tumor models using light sheet microscopy. Cell Div. 6, 22. https://doi.org/10.1186/1747-1028-6-22

Lucas, M., Kenobi, K., von Wangenheim, D., Voss, U., Swarup, K., De Smet, I., Van Damme, D., Lawrence, T., Peret, B., Moscardi, E., Barbeau, D., Godin, C., Salt, D., Guyomarc'h, S., Stelzer, E.H.K., Maizel, A., Laplaze, L., Bennett, M.J., 2013. Lateral root morphogenesis is dependent on the mechanical properties of the overlaying tissues. Proc. Natl. Acad. Sci. 110, 5229–5234. https://doi.org/10.1073/pnas.1210807110

Macnab, R.M., 1976. Examination of bacterial flagellation by dark-field microscopy. J. Clin. Microbiol. 4, 258–265.

Maekiniemi, A., Singer, R.H., Tutucci, E., 2020. Single molecule mRNA fluorescent in situ hybridization combined with immunofluorescence in S. cerevisiae: Dataset and quantification. Data Brief 30, 105511. https://doi.org/10.1016/j.dib.2020.105511

Maier, A.T., Stehling-Sun, S., Wollmann, H., Demar, M., Hong, R.L., Haubeiss, S., Weigel, D., Lohmann, J.U., 2009. Dual roles of the bZIP transcription factor PERIANTHIA in the control of floral architecture and homeotic gene expression. Development 136, 1613–1620. https://doi.org/10.1242/dev.033647

Maizel, A., von Wangenheim, D., Federici, F., Haseloff, J., Stelzer, E.H.K., 2011. High-resolution live imaging of plant growth in near physiological bright conditions using light sheet fluorescence microscopy: *Light sheet microscopy of plant growth*. Plant J. 68, 377–385. https://doi.org/10.1111/j.1365-313X.2011.04692.x

Malik, N., Agarwal, P., Tyagi, A., 2017. Emerging functions of multi-protein complex Mediator with special emphasis on plants. Crit. Rev. Biochem. Mol. Biol. 52, 475–502. https://doi.org/10.1080/10409238.2017.1325830

Mandel, M.A., Bowman, J.L., Kempin, S.A., Ma, H., Meyerowitz, E.M., Yanofsky, M.F., 1992. Manipulation of flower structure in transgenic tobacco. Cell 71, 133–43.

Mandel, M.A., Yanofsky, M.F., 1995. A gene triggering flower formation in Arabidopsis. Nature 377, 522–524. https://doi.org/10.1038/377522a0

Mandel, T., Candela, H., Landau, U., Asis, L., Zelinger, E., Carles, C.C., Williams, L.E., 2016. Differential regulation of meristem size, morphology and organization by the ERECTA, CLAVATA and class III HD-ZIP pathways. Development 143, 1612–1622. https://doi.org/10.1242/dev.129973

Mandel, T., Moreau, F., Kutsher, Y., Fletcher, J.C., Carles, C.C., Williams, L.E., 2014. The ERECTA receptor kinase regulates Arabidopsis shoot apical meristem size, phyllotaxy and floral meristem identity. Development 141, 830–841. https://doi.org/10.1242/dev.104687

Mandelkow, E.-M., Mandelkow, E., 1985. Unstained microtubules studied by cryo-electron microscopy. J. Mol. Biol. 181, 123–135. https://doi.org/10.1016/0022-2836(85)90330-4

Mannerlöf, M., Tenning, P., 1997. Variability of gene expression in transgenic tobacco. Euphytica 98, 133–139. https://doi.org/10.1023/A:1003104914242

Mantsoki, A., Devailly, G., Joshi, A., 2016. Gene expression variability in mammalian embryonic stem cells using single cell RNA-seq data. Comput. Biol. Chem., APBC2016 63, 52–61. https://doi.org/10.1016/j.compbiolchem.2016.02.004

Mason, E.A., Mar, J.C., Laslett, A.L., Pera, M.F., Quackenbush, J., Wolvetang, E., Wells, C.A., 2014. Gene Expression Variability as a Unifying Element of the Pluripotency Network. Stem Cell Rep. 3, 365–377. https://doi.org/10.1016/j.stemcr.2014.06.008

Mathur, J., Mathur, N., Kernebeck, B., Srinivas, B.P., Hülskamp, M., 2003. A Novel Localization Pattern for an EB1-like Protein Links Microtubule Dynamics to Endomembrane Organization. Curr. Biol. 13, 1991–1997. https://doi.org/10.1016/j.cub.2003.10.033

Matyssek, R., Maruyama, S., Boyer, J.S., 1988. Rapid Wall Relaxation in Elongating Tissues. Plant Physiol. 86, 1163–1167. https://doi.org/10.1104/pp.86.4.1163

Maurer, S.P., Fourniol, F.J., Bohner, G., Moores, C.A., Surrey, T., 2012. EBs Recognize a Nucleotide-Dependent Structural Cap at Growing Microtubule Ends. Cell 149, 371–382. https://doi.org/10.1016/j.cell.2012.02.049

Mayer, A., Lidschreiber, M., Siebert, M., Leike, K., Soeding, J., Cramer, P., 2010. Uniform transitions of the general RNA polymerase II transcription complex. Nat. Struct. Mol. Biol. 17, 1272-+. https://doi.org/10.1038/nsmb.1903

Mayer, K.F.X., Schoof, H., Haecker, A., Lenhard, M., Jurgens, G., Laux, T., 1998. Role of WUSCHEL in regulating stem cell fate in the Arabidopsis shoot meristem. Cell 95, 805–815. https://doi.org/10.1016/S0092-8674(00)81703-1

McNally, F.J., Vale, R.D., 1993. Identification of katanin, an ATPase that severs and disassembles stable microtubules. Cell 75, 419–429. https://doi.org/10.1016/0092-8674(93)90377-3

Mei, Y., Gao, H.-B., Yuan, M., Xue, H.-W., 2012. The *Arabidopsis* ARCP Protein, CSI1, Which Is Required for Microtubule Stability, Is Necessary for Root and Anther Development. Plant Cell 24, 1066–1080. https://doi.org/10.1105/tpc.111.095059

Meyer, H.M., Teles, J., Formosa-Jordan, P., Refahi, Y., San-Bento, R., Ingram, G., Jönsson, H., Locke, J.C.W., Roeder, A.H.K., 2017. Fluctuations of the transcription factor ATML1 generate the pattern of giant cells in the Arabidopsis sepal. eLife 6. https://doi.org/10.7554/eLife.19131

Michaels, S.D., He, Y.H., Scortecci, K.C., Amasino, R.M., 2003. Attenuation of FLOWERING LOCUS C activity as a mechanism for the evolution of summer-annual flowering behavior in Arabidopsis. Proc. Natl. Acad. Sci. U. S. A. 100, 10102–10107. https://doi.org/10.1073/pnas.1531467100

Mickoleit, M., Schmid, B., Weber, M., Fahrbach, F.O., Hombach, S., Reischauer, S., Huisken, J., 2014. High-resolution reconstruction of the beating zebrafish heart. Nat. Methods 11, 919–922. https://doi.org/10.1038/nmeth.3037

Minsky, M., 1988. Memoir on inventing the confocal scanning microscope: Memoir on Inventing the confocal scanning microscope. Scanning 10, 128–138. https://doi.org/10.1002/sca.4950100403

Mirabet, V., 2018. The self-organization of plant microtubules inside the cell volume yields their cortical localization, stable alignment, and sensitivity to external cues. PLoS Comput Biol 14. https://doi.org/10.1371/journal.pcbi.1006011

Mizukami, Y., Ma, H., 1995. Separation of AG function in floral meristem determinacy from that in reproductive organ identity by expressing antisense AG RNA. Plant Mol. Biol. 28, 767–784. https://doi.org/10.1007/BF00042064

Mizukami, Y., Ma, H., 1992. Ectopic Expression of the Floral Homeotic Gene Agamous in Transgenic Arabidopsis Plants Alters Floral Organ Identity. Cell 71, 119–131. https://doi.org/10.1016/0092-8674(92)90271-D

Modrusan, Z., Reiser, L., Feldmann, K.A., Fischer, R.L., Haughn, G.W., 1994. Homeotic Transformation of Ovules into Carpel-like Structures in Arabidopsis. Plant Cell 6, 333–349.

Molines, A.T., Marion, J., Chabout, S., Besse, L., Dompierre, J.P., Mouille, G., Coquelle, F.M., 2018. EB1 contributes to microtubule bundling and organization, along with root growth, in *Arabidopsis thaliana*. Biol. Open 7, bio030510. https://doi.org/10.1242/bio.030510

Möller, B., Poeschl, Y., Plötner, R., Bürstenbinder, K., 2017. PaCeQuant: A Tool for High-Throughput Quantification of Pavement Cell Shape Characteristics. Plant Physiol. 175, 998–1017. https://doi.org/10.1104/pp.17.00961

Momiji, H., Monk, N.A.M., 2009. Oscillatory Notch-pathway activity in a delay model of neuronal differentiation. Phys. Rev. E 80, 021930. https://doi.org/10.1103/PhysRevE.80.021930

Mondolot, L., Roussel, J.-L., Andary, C., 2001. [No title found]. Histochem. J. 33, 379–385. https://doi.org/10.1023/A:1013798426161

Monfared, M.M., Carles, C.C., Rossignol, P., Pires, H.R., Fletcher, J.C., 2013. The ULT1 and ULT2 trxG Genes Play Overlapping Roles in Arabidopsis Development and Gene Regulation. Mol. Plant 6, 1564–1579. https://doi.org/10.1093/mp/sst041

Monniaux, M., Vandenbussche, M., 2018. How to Evolve a Perianth: A Review of Cadastral Mechanisms for Perianth Identity. Front. Plant Sci. 9. https://doi.org/10.3389/fpls.2018.01573

Morel, P., Heijmans, K., Rozier, F., Zethof, J., Chamot, S., Bento, S.R., Vialette-Guiraud, A., Chambrier, P., Trehin, C., Vandenbussche, M., 2017. Divergence of the Floral A-Function between an Asterid and a Rosid Species. Plant Cell 29, 1605-+. https://doi.org/10.1105/tpc.17.00098

Motose, H., Hamada, T., Yoshimoto, K., Murata, T., Hasebe, M., Watanabe, Y., Hashimoto, T., Sakai, T., Takahashi, T., 2011. NIMA-related kinases 6, 4, and 5 interact with each other to regulate microtubule organization during epidermal cell expansion in Arabidopsis thaliana: Arabidopsis NimA-related kinases. Plant J. 67, 993–1005. https://doi.org/10.1111/j.1365-313X.2011.04652.x

Motose, H., Tominaga, R., Wada, T., Sugiyama, M., Watanabe, Y., 2008. A NIMA-related protein kinase suppresses ectopic outgrowth of epidermal cells through its kinase activity and the association with microtubules. Plant J. 54, 829–844. https://doi.org/10.1111/j.1365-313X.2008.03445.x

Mouille, G., Robin, S., Lecomte, M., Pagant, S., Höfte, H., 2003. Classification and identification of Arabidopsis cell wall mutants using Fourier-Transform InfraRed (FT-IR) microspectroscopy. Plant J. Cell Mol. Biol. 35, 393–404. https://doi.org/10.1046/j.1365-313x.2003.01807.x

Movsisyan, N., Pardo, L.A., 2019. Measurement of Microtubule Dynamics by Spinning Disk Microscopy in Monopolar Mitotic Spindles. J. Vis. Exp. 60478. https://doi.org/10.3791/60478

Moyroud, E., Minguet, E.G., Ott, F., Yant, L., Pose, D., Monniaux, M., Blanchet, S., Bastien, O., Thevenon, E., Weigel, D., Schmid, M., Parcy, F., 2011. Prediction of Regulatory Interactions from Genome Sequences Using a Biophysical Model for the Arabidopsis LEAFY Transcription Factor. Plant Cell 23, 1293–1306. https://doi.org/10.1105/tpc.111.083329

Mueller, C.L., Jaehning, J.A., 2002. Ctr9, Rtf1, and Leo1 are components of the Paf1/RNA polymerase II complex. Mol. Cell. Biol. 22, 1971–1980. https://doi.org/10.1128/MCB.22.7.1971-1980.2002

Mueller, C.L., Porter, S.E., Hoffman, M.G., Jaehning, J.A., 2004. The Paf1 Complex Has Functions Independent of Actively Transcribing RNA Polymerase II. Mol. Cell 14, 447–456. https://doi.org/10.1016/S1097-2765(04)00257-6

Muller, R., Bleckmann, A., Simon, R., 2008. The Receptor Kinase CORYNE of Arabidopsis Transmits the Stem Cell-Limiting Signal CLAVATA3 Independently of CLAVATA1. PLANT CELL 20, 934–946. https://doi.org/10.1105/tpc.107.057547

Muller, R., Borghi, L., Kwiatkowska, D., Laufs, P., Simon, R., 2006. dynamics and compensatory responses of Arabidopsis shoot and floral meristems to CLV3 signaling. Plant Cell 18, 1188–1198. https://doi.org/10.1105/tpc.105.040444

Nakamura, M., Ehrhardt, D.W., Hashimoto, T., 2010. Microtubule and katanin-dependent dynamics of microtubule nucleation complexes in the acentrosomal Arabidopsis cortical array. Nat Cell Biol 12. https://doi.org/10.1038/ncb2110

Naoi, K., Hashimoto, T., 2004. A Semidominant Mutation in an Arabidopsis Mitogen-Activated Protein Kinase Phosphatase-Like Gene Compromises Cortical Microtubule Organization. Plant Cell 16, 1841–1853. https://doi.org/10.1105/tpc.021865

Néculcéa, E., 1903. II. SIEDENTOPF et R. ZSIGMONDY. — Ueber Sichtbarmachung ultramikroskopischer Teilchen, mit besonderer Anwendung auf Goldrubingläser (Méthode permettant de voir les particules ultramicroscopiques et d'en évaluer les dimensions ; application spéciale aux verres rubis à l'or). — Drude's Annalen der Physik, t. X, p. 1-39. J. Phys. Théorique Appliquée 2, 692–702. https://doi.org/10.1051/jphystap:019030020069201

Nehlig, A., Molina, A., Rodrigues-Ferreira, S., Honoré, S., Nahmias, C., 2017. Regulation of end-binding protein EB1 in the control of microtubule dynamics. Cell. Mol. Life Sci. 74, 2381–2393. https://doi.org/10.1007/s00018-017-2476-2

Nemhauser, J.L., Feldman, L.J., Zambryski, P.C., 2000. Auxin and ETTIN in Arabidopsis gynoecium morphogenesis. Development 127, 3877–3888.

Neufeld, T.P., de la Cruz, A.F.A., Johnston, L.A., Edgar, B.A., 1998. Coordination of Growth and Cell Division in the Drosophila Wing. Cell 93, 1183–1193. https://doi.org/10.1016/S0092-8674(00)81462-2

Ng, H. H., Dole, S., Struhl, K., 2003. The Rtf1 component of the Paf1 transcriptional elongation complex is required for ubiquitination of histone H2B. J. Biol. Chem. 278, 33625–33628. https://doi.org/10.1074/jbc.C300270200

Ng, Huck Hui, Robert, F., Young, R.A., Struhl, K., 2003. Targeted Recruitment of Set1 Histone Methylase by Elongating Pol II Provides a Localized Mark and Memory of Recent Transcriptional Activity. Mol. Cell 11, 709–719. https://doi.org/10.1016/S1097-2765(03)00092-3

Ng, K.-H., Yu, H., Ito, T., 2009. AGAMOUS Controls GIANT KILLER, a Multifunctional Chromatin Modifier in Reproductive Organ Patterning and Differentiation. Plos Biol. 7, e1000251. https://doi.org/10.1371/journal.pbio.1000251

Nguyen, C.T., Langenbacher, A., Hsieh, M., Chen, J.-N., 2010. The PAF1 complex component Leo1 is essential for cardiac and neural crest development in zebrafish. Dev. Biol. 341, 167–175. https://doi.org/10.1016/j.ydbio.2010.02.020

Nimchuk, Z.L., Tarr, P.T., Ohno, C., Qu, X., Meyerowitz, E.M., 2011. Plant Stem Cell Signaling Involves Ligand-Dependent Trafficking of the CLAVATA1 Receptor Kinase. Curr. Biol. 21, 345–352. https://doi.org/10.1016/j.cub.2011.01.039

Nipkow, P., 1984. Patentiert im Deutscchen Reiche vom 6. Januar 1884 ab, Patentschrift n°30105, Kaiserliches Patentamt, Ausgegeben den 15. Januar 1885.

Nordick, K., Hoffman, M.G., Betz, J.L., Jaehning, J.A., 2008. Direct interactions between the Paf1 complex and a cleavage and polyadenylation factor are revealed by dissociation of Paf1 from RNA polymerase II. Eukaryot. Cell 7, 1158–1167. https://doi.org/10.1128/EC.00434-07

Oda, Y., Fukuda, H., 2012. Initiation of Cell Wall Pattern by a Rho- and Microtubule-Driven Symmetry Breaking. Science 337, 1333–1336. https://doi.org/10.1126/science.1222597

Oh, S., Park, S., Nocker, S. van, 2008. Genic and Global Functions for Paf1C in Chromatin Modification and Gene Expression in Arabidopsis. PLOS Genet. 4, e1000077. https://doi.org/10.1371/journal.pgen.1000077

Oh, S., Zhang, H., Ludwig, P., Nocker, S. van, 2004. A Mechanism Related to the Yeast Transcriptional Regulator Paf1c Is Required for Expression of the Arabidopsis FLC/MAF MADS Box Gene Family. Plant Cell 16, 2940–2953. https://doi.org/10.1105/tpc.104.026062

Ohyama, K., Shinohara, H., Ogawa-Ohnishi, M., Matsubayashi, Y., 2009. A glycopeptide regulating stem cell fate in Arabidopsis thaliana. Nat. Chem. Biol. 5, 578–580. https://doi.org/10.1038/nchembio.182

Olkin, I., Pukelsheim, F., 1982. The distance between two random vectors with given dispersion matrices. Linear Algebra Its Appl. 48, 257–263. https://doi.org/10.1016/0024-3795(82)90112-4

Ormerod, M.G., Sun, X.-M., Brown, D., Snowden, R.T., Cohen, G.M., 1993. Quantification of Apoptosis and Necrosis by Flow Cytometry. Acta Oncol. 32, 417–424. https://doi.org/10.3109/02841869309093620

Ovečka, M., Vaškebová, L., Komis, G., Luptovčiak, I., Smertenko, A., Šamaj, J., 2015. Preparation of plants for developmental and cellular imaging by light-sheet microscopy. Nat. Protoc. 10, 1234–1247. https://doi.org/10.1038/nprot.2015.081

Ovečka, M., von Wangenheim, D., Tomančák, P., Šamajová, O., Komis, G., Šamaj, J., 2018. Multiscale imaging of plant development by light-sheet fluorescence microscopy. Nat. Plants 4, 639–650. https://doi.org/10.1038/s41477-018-0238-2

Padovan-Merhar, O., Raj, A., 2013. Using variability in gene expression as a tool for studying gene regulation. Wiley Interdiscip. Rev. Syst. Biol. Med. 5, 751–759. https://doi.org/10.1002/wsbm.1243

Parcy, F., Bomblies, K., Weigel, D., 2002. Interaction of LEAFY, AGAMOUS and TERMINAL FLOWER1 in maintaining floral meristem identity in Arabidopsis. Development 129, 2519–2527.

Parcy, F., Nilsson, O., Busch, M.A., Lee, I., Weigel, D., 1998. A genetic framework for floral patterning. Nature 395, 561–566. https://doi.org/10.1038/26903

Paredez, A.R., 2006. Visualization of Cellulose Synthase Demonstrates Functional Association with Microtubules. Science 312, 1491–1495. https://doi.org/10.1126/science.1126551

Park, S., Oh, S., Ek-Ramos, J., van Nocker, S., 2010. PLANT HOMOLOGOUS TO PARAFIBROMIN Is a Component of the PAF1 Complex and Assists in Regulating Expression of Genes within H3K27ME3-Enriched Chromatin. Plant Physiol. 153, 821–831. https://doi.org/10.1104/pp.110.155838

Park, W., Li, J., Song, R., Messing, J., Chen, X., 2002. CARPEL FACTORY, a Dicer Homolog, and HEN1, a Novel Protein, Act in microRNA Metabolism in Arabidopsis thaliana. Curr. Biol. 12, 1484–1495. https://doi.org/10.1016/S0960-9822(02)01017-5

Parker, A.J., Haskins, E.F., Deyrup-Olsen, I., 1982. Toluidine Blue: A Simple, Effective Stain for Plant Tissues. Am. Biol. Teach. 44, 487–489. https://doi.org/10.2307/4447575

Pastuglia, M., Bouchez, D., 2007. Molecular encounters at microtubule ends in the plant cell cortex. Curr. Opin. Plant Biol. 10, 557–563. https://doi.org/10.1016/j.pbi.2007.08.001

Pautot, V., Dockx, J., Hamant, O., Kronenberger, J., Grandjean, O., Jublot, D., Traas, J., 2001. KNAT2 Evidence for a Link between Knotted-like Genes and Carpel Development. Plant Cell 13, 1719–1734. https://doi.org/10.1105/TPC.010184

Payne, T., Johnson, S.D., Koltunow, A.M., 2004. KNUCKLES (KNU) encodes a C2H2 zinc-finger protein that regulates development of basal pattern elements of the Arabidopsis gynoecium. Development 131, 3737–3749. https://doi.org/10.1242/dev.01216

Peach, C., Velten, J., 1991. Transgene expression variability (position effect) of CAT and GUS reporter genes driven by linked divergent T-DNA promoters. Plant Mol. Biol. 17, 49–60. https://doi.org/10.1007/BF00036805

Pelaz, S., Tapia-López, R., Alvarez-Buylla, E.R., Yanofsky, M.F., 2001. Conversion of leaves into petals in Arabidopsis. Curr. Biol. 11, 182–184. https://doi.org/10.1016/S0960-9822(01)00024-0

Penheiter, K.L., Washburn, T.M., Porter, S.E., Hoffman, M.G., Jaehning, J.A., 2005. A Posttranscriptional Role for the Yeast Paf1-RNA Polymerase II Complex Is Revealed by Identification of Primary Targets. Mol. Cell 20, 213–223. https://doi.org/10.1016/j.molcel.2005.08.023

Perales, M., Rodriguez, K., Snipes, S., Yadav, R.K., Diaz-Mendoza, M., Reddy, G.V., 2016. Threshold-dependent transcriptional discrimination underlies stem cell homeostasis. Proc. Natl. Acad. Sci. U. S. A. 113, E6298–E6306. https://doi.org/10.1073/pnas.1607669113

Pérez-Ruiz, R.V., García-Ponce, B., Marsch-Martínez, N., Ugartechea-Chirino, Y., Villajuana-Bonequi, M., de Folter, S., Azpeitia, E., Dávila-Velderrain, J., Cruz-Sánchez, D., Garay-Arroyo, A., Sánchez, M. de la P., Estévez-Palmas, J.M., Álvarez-Buylla, E.R., 2015. XAANTAL2 (AGL14) Is an Important Component of the Complex Gene Regulatory Network that Underlies Arabidopsis Shoot Apical Meristem Transitions. Mol. Plant 8, 796–813. https://doi.org/10.1016/j.molp.2015.01.017

Peters, W.S., Tomos, A.D., 1996. The History of Tissue Tension. Ann. Bot. 77, 657–665. https://doi.org/10.1093/aob/77.6.657

Pfeiffer, A., Janocha, D., Dong, Y., Medzihradszky, A., Schoene, S., Daum, G., Suzaki, T., Forner, J., Longenecker, T., Rempel, E., Schmid, M., Wirtz, M., Hell, R., Lohmann, J.U., 2016. Integration of light and metabolic signals for stem cell activation at the shoot apical meristem. Elife 5, e17023. https://doi.org/10.7554/eLife.17023

Planchon, T.A., Gao, L., Milkie, D.E., Davidson, M.W., Galbraith, J.A., Galbraith, C.G., Betzig, E., 2011. Rapid three-dimensional isotropic imaging of living cells using Bessel beam plane illumination. Nat. Methods 8, 417–423. https://doi.org/10.1038/nmeth.1586

Plotnikov, A., Zehorai, E., Procaccia, S., Seger, R., 2011. The MAPK cascades: Signaling components, nuclear roles and mechanisms of nuclear translocation. Biochim. Biophys. Acta BBA - Mol. Cell Res. 1813, 1619–1633. https://doi.org/10.1016/j.bbamcr.2010.12.012

Pokholok, D.K., Hannett, N.M., Young, R.A., 2002. Exchange of RNA Polymerase II Initiation and Elongation Factors during Gene Expression In Vivo. Mol. Cell 9, 799–809. https://doi.org/10.1016/S1097-2765(02)00502-6

Portran, D., Zoccoler, M., Gaillard, J., Stoppin-Mellet, V., Neumann, E., Arnal, I., Martiel, J.L., Vantard, M., 2013. MAP65/Ase1 promote microtubule flexibility. Mol. Biol. Cell 24, 1964–1973. https://doi.org/10.1091/mbc.e13-03-0141

Pouteau, S., Nicholls, D., Tooke, F., Coen, E., Battey, N., 1997. The induction and maintenance of flowering in Impatiens 9.

Prasher, D.C., Eckenrode, V.K., Ward, W.W., Prendergast, F.G., Cormier, M.J., 1992. Primary structure of the Aequorea victoria green-fluorescent protein. Gene 111, 229–233. https://doi.org/10.1016/0378-1119(92)90691-H

Preibisch, S., Saalfeld, S., Schindelin, J., Tomancak, P., 2010. Software for bead-based registration of selective plane illumination microscopy data. Nat. Methods 7, 418–419. https://doi.org/10.1038/nmeth0610-418

Prezel, E., Stoppin-Mellet, V., Elie, A., Zala, N., Denarier, E., Serre, L., Arnal, I., 2017. TIRF assays for real-time observation of microtubules and actin coassembly: Deciphering tau effects on microtubule/actin interplay, in: Methods in Cell Biology. Elsevier, pp. 199–214. https://doi.org/10.1016/bs.mcb.2017.06.012

Prigge, M.J., Otsuga, D., Alonso, J.M., Ecker, J.R., Drews, G.N., Clark, S.E., 2005. Class III homeodomain-leucine zipper gene family members have overlapping, antagonistic, and distinct roles in Arabidopsis development. Plant Cell 17, 61–76. https://doi.org/10.1105/tpc.104.026161

Prunet, N., Duncan, K., 2020. Imaging flowers: a guide to current microscopy and tomography techniques to study flower development. J. Exp. Bot. 71, 2898–2909. https://doi.org/10.1093/jxb/eraa094

Prunet, N., Jack, T.P., Meyerowitz, E.M., 2016a. Live confocal imaging of Arabidopsis flower buds. Dev. Biol., Plant Development 419, 114–120. https://doi.org/10.1016/j.ydbio.2016.03.018

Prunet, N., Jack, T.P., Meyerowitz, E.M., 2016b. Live confocal imaging of Arabidopsis flower buds. Dev. Biol. 419, 114–120. https://doi.org/10.1016/j.ydbio.2016.03.018

Prunet, N., Morel, P., Champelovier, P., Thierry, A.-M., Negrutiu, I., Jack, T., Trehin, C., 2015. SQUINT promotes stem cell homeostasis and floral meristem termination in Arabidopsis through APETALA2 and CLAVATA signalling. J. Exp. Bot. 66, 6905–6916. https://doi.org/10.1093/jxb/erv394

Prunet, N., Morel, P., Negrutiu, I., Trehin, C., 2009. Time to Stop: Flower Meristem Termination. Plant Physiol. 150, 1764–1772. https://doi.org/10.1104/pp.109.141812

Prunet, N., Morel, P., Thierry, A.-M., Eshed, Y., Bowman, J.L., Negrutiu, I., Trehin, C., 2008. REBELOTE, SQUINT, and ULTRAPETALA1 Function Redundantly in the Temporal Regulation of Floral Meristem Termination in Arabidopsis thaliana. PLANT CELL ONLINE 20, 901–919. https://doi.org/10.1105/tpc.107.053306

Puranik, S., Acajjaoui, S., Conn, S., Costa, L., Conn, V., Vial, A., Marcellin, R., Melzer, R., Brown, E., Hart, D., Theissen, G., Silva, C.S., Parcy, F., Dumas, R., Nanao, M., Zubieta, C., 2014. Structural Basis for the Oligomerization of the MADS Domain Transcription Factor SEPALLATA3 in Arabidopsis. Plant Cell 26, 3603–3615. https://doi.org/10.1105/tpc.114.127910

Pytela, J., Kato, T., Hashimoto, T., 2010. Mitogen-activated protein kinase phosphatase PHS1 is retained in the cytoplasm by nuclear extrusion signal-dependent and independent mechanisms. Planta 231, 1311–1322. https://doi.org/10.1007/s00425-010-1135-8

Qiu, H., Hu, C., Gaur, N.A., Hinnebusch, A.G., 2012. Pol II CTD kinases Bur1 and Kin28 promote Spt5 CTR-independent recruitment of Paf1 complex. Embo J. 31, 3494–3505. https://doi.org/10.1038/emboj.2012.188

Raj, A., Rifkin, S.A., Andersen, E., Oudenaarden, A. van, 2010. Variability in gene expression underlies incomplete penetrance. Nature 463, 913–918. https://doi.org/10.1038/nature08781

Raj, A., van Oudenaarden, A., 2008. Nature, Nurture, or Chance: Stochastic Gene Expression and Its Consequences. Cell 135, 216–226. https://doi.org/10.1016/j.cell.2008.09.050

Ravarani, C.N.J., Chalancon, G., Breker, M., de Groot, N.S., Babu, M.M., 2016. Affinity and competition for TBP are molecular determinants of gene expression noise. Nat. Commun. 7, 10417. https://doi.org/10.1038/ncomms10417

Rayburn, A.L., Gill, B.S., 1985. Use of biotin-labeled probes to map specific DNA sequences on wheat chromosomes. J. Hered. 76, 78–81. https://doi.org/10.1093/oxfordjournals.jhered.a110049

Reddy, G.V., Meyerowitz, E.M., 2005. Stem-Cell Homeostasis and Growth Dynamics Can Be Uncoupled in the Arabidopsis Shoot Apex. Science 310, 663–667. https://doi.org/10.1126/science.1116261

Reinhardt, D., Frenz, M., Mandel, T., Kuhlemeier, C., 2003. Microsurgical and laser ablation analysis of interactions between the zones and layers of the tomato shoot apical meristern. Development 130, 4073–4083. https://doi.org/10.1242/dev.00596

Reinhardt, D., Mandel, T., Kuhlemeier, C., 2000. Auxin regulates the initiation and radial position of plant lateral organs. Plant Cell 12, 507–518. https://doi.org/10.1105/tpc.12.4.507

Reinhardt, Didier, Pesce, E.-R., Stieger, P., Mandel, T., Baltensperger, K., Bennett, M., Traas, J., Friml, J., Kuhlemeier, C., 2003. Regulation of phyllotaxis by polar auxin transport. Nature 426, 255–260. https://doi.org/10.1038/nature02081

Reynaud, E.G., Kržič, U., Greger, K., Stelzer, E.H.K., 2008. Light sheet-based fluorescence microscopy: More dimensions, more photons, and less photodamage. HFSP J. 2, 266–275. https://doi.org/10.2976/1.2974980

Richard, M., Yvert, G., 2014. How does evolution tune biological noise? Front. Genet. 5, 374. https://doi.org/10.3389/fgene.2014.00374

Riechmann, J.L., Meyerowitz, E.M., 1998. The AP2/EREBP family of plant transcription factors. Biol. Chem. 379, 633–646. https://doi.org/10.1515/bchm.1998.379.6.633

Riechmann, J.L., Wang, M.Q., Meyerowitz, E.M., 1996. DNA-binding properties of Arabidopsis MADS domain homeotic proteins APETALA1, APETALA3, PISTILLATA and AGAMOUS. Nucleic Acids Res. 24, 3134–3141. https://doi.org/10.1093/nar/24.16.3134

Rieckher, M., Kyparissidis-Kokkinidis, I., Zacharopoulos, A., Kourmoulakis, G., Tavernarakis, N., Ripoll, J., Zacharakis, G., 2015. A Customized Light Sheet Microscope to Measure Spatio-Temporal Protein Dynamics in Small Model Organisms. PLOS ONE 10, e0127869. https://doi.org/10.1371/journal.pone.0127869

Ristova, D., Barbez, E., 2018. Root Development Methods and Protocols.

Robinson, S., Kuhlemeier, C., 2018. Global compression reorients cortical microtubules in arabidopsis hypocotyl epidermis and promotes growth. Curr Biol 28. https://doi.org/10.1016/j.cub.2018.04.028

Rodriguez-Cazorla, E., Ripoll, J.J., Andujar, A., Bailey, L.J., Martinez-Laborda, A., Yanofsky, M.F., Vera, A., 2015. K-homology Nuclear Ribonucleoproteins Regulate Floral Organ Identity and Determinacy in Arabidopsis. Plos Genet. 11, e1004983. https://doi.org/10.1371/journal.pgen.1004983

Roeder, A.H.K., Yanofsky, M.F., 2006. Fruit development in Arabidopsis. Arab. Book 4, e0075. https://doi.org/10.1199/tab.0075

Rogers, S.L., Rogers, G.C., Sharp, D.J., Vale, R.D., 2002. Drosophila EB1 is important for proper assembly, dynamics, and positioning of the mitotic spindle. J. Cell Biol. 158, 873–884. https://doi.org/10.1083/jcb.200202032

Rojo, E., Sharma, V.K., Kovaleva, V., Raikhel, N.V., Fletcher, J.C., 2002. CLV3 is localized to the extracellular space, where it activates the Arabidopsis CLAVATA stem cell signaling pathway. Plant Cell 14, 969–977. https://doi.org/10.1105/tpc.002196

Rondon, A.G., Gallardo, M., Garcia-Rubio, M., Aguilera, A., 2004. Molecular evidence indicating that the yeast PAF complex is required for transcription elongation. Embo Rep. 5, 47–53. https://doi.org/10.1038/sj.embor.7400045

Rozenblatt-Rosen, O., Nagaike, T., Francis, J.M., Kaneko, S., Glatt, K.A., Hughes, C.M., LaFramboise, T., Manley, J.L., Meyerson, M., 2009. The tumor suppressor Cdc73 functionally associates with CPSF and CstF 3 ' mRNA processing factors. Proc. Natl. Acad. Sci. U. S. A. 106, 755–760. https://doi.org/10.1073/pnas.0812023106

Sadeghi, L., Prasad, P., Ekwall, K., Cohen, A., Svensson, J.P., 2015. The Paf1 complex factors Leo1 and Paf1 promote local histone turnover to modulate chromatin states in fission yeast. EMBO Rep. 16, 1673–1687. https://doi.org/10.15252/embr.201541214

Sampathkumar, A., Krupinski, P., Wightman, R., Milani, P., Berquand, A., Boudaoud, A., Hamant, O., Jönsson, H., Meyerowitz, E.M., 2014a. Subcellular and supracellular mechanical stress prescribes cytoskeleton behavior in Arabidopsis cotyledon pavement cells. eLife 3, e01967. https://doi.org/10.7554/eLife.01967

Sampathkumar, A., Krupinski, P., Wightman, R., Milani, P., Berquand, A., Boudaoud, A., Hamant, O., Jönsson, H., Meyerowitz, E.M., 2014b. Subcellular and supracellular mechanical stress prescribes cytoskeleton behavior in Arabidopsis cotyledon pavement cells. eLife 3, e01967. https://doi.org/10.7554/eLife.01967

Sapala, A., Runions, A., Routier-Kierzkowska, A.-L., Das Gupta, M., Hong, L., Hofhuis, H., Verger, S., Mosca, G., Li, C.-B., Hay, A., Hamant, O., Roeder, A.H., Tsiantis, M., Prusinkiewicz, P., Smith, R.S., 2018. Why plants make puzzle cells, and how their shape emerges. eLife 7, e32794. https://doi.org/10.7554/eLife.32794

Sapala, A., Runions, A., Smith, R.S., 2019. Mechanics, geometry and genetics of epidermal cell shape regulation: different pieces of the same puzzle. Curr. Opin. Plant Biol. 47, 1–8. https://doi.org/10.1016/j.pbi.2018.07.017

Satina, S., Blakeslee, A.F., 1941. Periclinal chimeras in Datura stramonium in relation to development of leaf and flower. Am. J. Bot. 28, 862–871. https://doi.org/10.2307/2436864

Satina, S., Blakeslee, A.F., Avery, A.G., 1940. Demonstration of the three germ layers in the shoot apex of Datura by means of induced polyploidy in periclinal chimeras. Am. J. Bot. 27, 895–905. https://doi.org/10.2307/2436558

Schermelleh, L., Ferrand, A., Huser, T., Eggeling, C., Sauer, M., Biehlmaier, O., Drummen, G.P.C., 2019. Super-resolution microscopy demystified. Nat. Cell Biol. 21, 72–84. https://doi.org/10.1038/s41556-018-0251-8

Scherz, P.J., Huisken, J., Sahai-Hernandez, P., Stainier, D.Y.R., 2008. High-speed imaging of developing heart valves reveals interplay of morphogenesis and function. Development 135, 1179–1187. https://doi.org/10.1242/dev.010694

Schier, A.C., Taatjes, D.J., 2020. Structure and mechanism of the RNA polymerase II transcription machinery. Genes Dev. 34, 465–488. https://doi.org/10.1101/gad.335679.119

Schmid, B., Shah, G., Scherf, N., Weber, M., Thierbach, K., Campos, C.P., Roeder, I., Aanstad, P., Huisken, J., 2013. High-speed panoramic light-sheet microscopy reveals global endodermal cell dynamics. Nat. Commun. 4, 2207. https://doi.org/10.1038/ncomms3207

Schoof, H., Lenhard, M., Haecker, A., Mayer, K.F.X., Jürgens, G., Laux, T., 2000. The Stem Cell Population of Arabidopsis Shoot Meristems Is Maintained by a Regulatory Loop between the CLAVATA and WUSCHEL Genes. Cell 100, 635–644. https://doi.org/10.1016/S0092-8674(00)80700-X

Schopfer, P., 2006. Biomechanics of plant growth. Am. J. Bot. 93, 1415–1425. https://doi.org/10.3732/ajb.93.10.1415

Schuyler, S.C., Pellman, D., 2001. Microtubule "Plus-End-Tracking Proteins." Cell 105, 421–424. https://doi.org/10.1016/S0092-8674(01)00364-6

Schwarzacher, T., 2003. DNA, chromosomes, and in situ hybridization. Genome 46, 953–962. https://doi.org/10.1139/g03-119

Schwarzacher, T., Leitch, A.R., Bennett, M.D., Heslop-Harrison, J.S., 1989. In Situ Localization of Parental Genomes in a Wide Hybrid. Ann. Bot. 64, 315–324. https://doi.org/10.1093/oxfordjournals.aob.a087847

Sena, G., Frentz, Z., Birnbaum, K.D., Leibler, S., 2011. Quantitation of Cellular Dynamics in Growing Arabidopsis Roots with Light Sheet Microscopy. PLoS ONE 6, e21303. https://doi.org/10.1371/journal.pone.0021303

Shaw, S.L., Lucas, J., 2011. Intrabundle microtubule dynamics in the Arabidopsis cortical array. Cytoskeleton 68, 56–67. https://doi.org/10.1002/cm.20495

Sheldon, K.E., Mauger, D.M., Arndt, K.M., 2005. A requirement for the Saccharomyces cerevisiae Paf1 complex in snoRNA 3 ' end formation. Mol. Cell 20, 225–236. https://doi.org/10.1016/j.molcel.2005.08.026

Shi, X.M., Chang, M.P., Wolf, A.J., Chang, C.H., FrazerAbel, A.A., Wade, P.A., Burton, Z.F., Jaehning, J.A., 1997. Cdc73p and Paf1p are found in a novel RNA polymerase II-containing complex distinct from the Srbp-containing holoenzyme. Mol. Cell. Biol. 17, 1160–1169. https://doi.org/10.1128/MCB.17.3.1160

Shore, P., Sharrocks, A.D., 1995. The MADS-box family of transcription factors. Eur. J. Biochem. 229, 1–13. https://doi.org/10.1111/j.1432-1033.1995.tb20430.x

Shpak, E.D., 2013. Diverse Roles of ERECTA Family Genes in Plant Development. J. Integr. Plant Biol. 55, 1238–1250. https://doi.org/10.1111/jipb.12108

Shulse, C.N., Cole, B.J., Ciobanu, D., Lin, J., Yoshinaga, Y., Gouran, M., Turco, G.M., Zhu, Y., O'Malley, R.C., Brady, S.M., Dickel, D.E., 2019. High-Throughput Single-Cell Transcriptome Profiling of Plant Cell Types. Cell Rep. 27, 2241-2247.e4. https://doi.org/10.1016/j.celrep.2019.04.054

Sieburth, L.E., Meyerowitz, E.M., 1997. Molecular dissection of the AGAMOUS control region shows that cis elements for spatial regulation are located intragenically. Plant Cell 9, 355–365. https://doi.org/10.1105/tpc.9.3.355

Sieburth, L.E., Running, M.P., Meyerowitz, E.M., 1995. Genetic separation of third and fourth whorl functions of AGAMOUS. Plant Cell 7, 1249–1258. https://doi.org/10.1105/tpc.7.8.1249

Singer, R.H., Ward, D.C., 1982. Actin gene expression visualized in chicken muscle tissue culture by using in situ hybridization with a biotinated nucleotide analog. Proc. Natl. Acad. Sci. 79, 7331–7335. https://doi.org/10.1073/pnas.79.23.7331

Smith, L.L., Beggs, A.H., Gupta, V.A., 2013. Analysis of Skeletal Muscle Defects in Larval Zebrafish by Birefringence and Touch-evoke Escape Response Assays. J. Vis. Exp. 50925. https://doi.org/10.3791/50925

Smith, R.S., Guyomarc'h, S., Mandel, T., Reinhardt, D., Kuhlemeier, C., Prusinkiewicz, P., 2006. A plausible model of phyllotaxis. Proc. Natl. Acad. Sci. U. S. A. 103, 1301–1306. https://doi.org/10.1073/pnas.0510457103

Smyth, D.R., Bowman, J.L., Meyerowitz, E.M., 1990. Early flower development in Arabidopsis. Plant Cell 2, 755–767. https://doi.org/10.1105/tpc.2.8.755

Snipes, S.A., Rodriguez, K., DeVries, A.E., Miyawaki, K.N., Perales, M., Xie, M., Reddy, G.V., 2018. Cytokinin stabilizes WUSCHEL by acting on the protein domains required for nuclear enrichment and transcription. Plos Genet. 14, e1007351. https://doi.org/10.1371/journal.pgen.1007351

Song, S.-K., Clark, S.E., 2005. POL and related phosphatases are dosage-sensitive regulators of meristem and organ development in Arabidopsis. Dev. Biol. 285, 272–284. https://doi.org/10.1016/j.ydbio.2005.06.020

Song, S.-K., Lee, M.M., Clark, S.E., 2006. POL and PLL1 phosphatases are CLAVATA1 signaling intermediates required for Arabidopsis shoot and floral stem cells. Development 133, 4691–4698. https://doi.org/10.1242/dev.02652

Soutourina, J., 2018. Transcription regulation by the Mediator complex. Nat. Rev. Mol. Cell Biol. 19, 262–274. https://doi.org/10.1038/nrm.2017.115

Sprinzak, D., Lakhanpal, A., LeBon, L., Santat, L.A., Fontes, M.E., Anderson, G.A., Garcia-Ojalvo, J., Elowitz, M.B., 2010. *Cis*-interactions between Notch and Delta generate mutually exclusive signalling states. Nature 465, 86–90. https://doi.org/10.1038/nature08959

Squazzo, S.L., Costa, P.J., Lindstrom, D.L., Kumer, K.E., Simic, R., Jennings, J.L., Link, A.J., Arndt, K.M., Hartzog, G.A., 2002. The Paf1 complex physically and functionally associates with transcription elongation factors in vivo. Embo J. 21, 1764–1774. https://doi.org/10.1093/emboj/21.7.1764

Ståhl, P.L., Salmén, F., Vickovic, S., Lundmark, A., Navarro, J.F., Magnusson, J., Giacomello, S., Asp, M., Westholm, J.O., Huss, M., Mollbrink, A., Linnarsson, S., Codeluppi, S., Borg, Å., Pontén, F., Costea, P.I., Sahlén, P., Mulder, J., Bergmann, O., Lundeberg, J., Frisén, J., 2016. Visualization and analysis of gene expression in tissue sections by spatial transcriptomics. Science 353, 78–82. https://doi.org/10.1126/science.aaf2403

Stanislas, T., Hamant, O., Traas, J., 2017. In-vivo analysis of morphogenesis in plants, in: Methods in Cell Biology. Elsevier, pp. 203–223. https://doi.org/10.1016/bs.mcb.2016.11.008

Stoppin-Mellet, V., Gaillard, J., Vantard, M., 2006. Katanin's severing activity favors bundling of cortical microtubules in plants. Plant J. 46, 1009–1017. https://doi.org/10.1111/j.1365-313X.2006.02761.x

Stoppin-Mellet, V., Gaillard, J., Vantard, M., 2002. Functional evidence for in vitro microtubule severing by the plant katanin homologue. Biochem. J. 365, 337–342. https://doi.org/10.1042/bj20020689

Strikoudis, A., Lazaris, C., Trimarchi, T., Galvao Neto, A.L., Yang, Y., Ntziachristos, P., Rothbart, S., Buckley, S., Dolgalev, I., Stadtfeld, M., Strahl, B.D., Dynlacht, B.D., Tsirigos, A., Aifantis, I., 2016. Regulation of transcriptional elongation in pluripotency and cell differentiation by the PHD-finger protein Phf5a. Nat. Cell Biol. 18, 1127-+. https://doi.org/10.1038/ncb3424

Stuurman, J., Jaggi, F., Kuhlemeier, C., 2002. Shoot meristem maintenance is controlled by a GRAS-gene mediated signal from differentiating cells. Genes Dev. 16, 2213–2218. https://doi.org/10.1101/gad.230702

Su, Y.H., Zhou, C., Li, Y.J., Yu, Y., Tang, L.P., Zhang, W.J., Yao, W.J., Huang, R., Laux, T., Zhang, X.S., 2020. Integration of pluripotency pathways regulates stem cell maintenance in the *Arabidopsis* shoot meristem. Proc. Natl. Acad. Sci. 117, 22561–22571. https://doi.org/10.1073/pnas.2015248117

Sugimoto, K., Himmelspach, R., Williamson, R.E., Wasteneys, G.O., 2003. Mutation or Drug-Dependent Microtubule Disruption Causes Radial Swelling without Altering Parallel Cellulose Microfibril Deposition in Arabidopsis Root Cells. Plant Cell 15, 1414–1429. https://doi.org/10.1105/tpc.011593

Sun, B., Looi, L.-S., Guo, S., He, Z., Gan, E.-S., Huang, J., Xu, Y., Wee, W.-Y., Ito, T., 2014. Timing Mechanism Dependent on Cell Division Is Invoked by Polycomb Eviction in Plant Stem Cells. Science 343, 1248559. https://doi.org/10.1126/science.1248559

Sun, Bo, Xu, Y., Ng, K.-H., Ito, T., 2009. A timing mechanism for stem cell maintenance and differentiation in the Arabidopsis floral meristem. Genes Dev. 23, 1791–1804. https://doi.org/10.1101/gad.1800409

Sun, B., Xu, Y., Ng, K.-H., Ito, T., 2009. A timing mechanism for stem cell maintenance and differentiation in the Arabidopsis floral meristem. Genes Dev. 23, 1791–1804. https://doi.org/10.1101/gad.1800409

Sun, B., Zhou, Y., Cai, J., Shang, E., Yamaguchi, N., Xiao, J., Looi, L.-S., Wee, W.-Y., Gao, X., Wagner, D., Ito, T., 2019. Integration of Transcriptional Repression and Polycomb-Mediated Silencing of *WUSCHEL* in Floral Meristems. Plant Cell 31, 1488–1505. https://doi.org/10.1105/tpc.18.00450

Swoger, J., Muzzopappa, M., López-Schier, H., Sharpe, J., 2011. 4D retrospective lineage tracing using SPIM for zebrafish organogenesis studies. J. Biophotonics 4, 122–134. https://doi.org/10.1002/jbio.201000087

Swoger, J., Pampaloni, F., Stelzer, E.H.K., 2014. Light-Sheet-Based Fluorescence Microscopy for Three-Dimensional Imaging of Biological Samples. Cold Spring Harb. Protoc. 2014, pdb.top080168. https://doi.org/10.1101/pdb.top080168

Swoger, J., Verveer, P., Greger, K., Huisken, J., Stelzer, E.H.K., 2007. Multi-view image fusion improves resolution in three-dimensional microscopy. Opt. Express 15, 8029. https://doi.org/10.1364/OE.15.008029

Takagi, N., Ueguchi, C., 2012. Enhancement of meristem formation by bouquet-1, a mis-sense allele of the VERNALIZATION INDEPENDENCE 3 gene encoding a WD40 repeat protein in Arabidopsis thaliana. Genes Cells 17, 982–993. https://doi.org/10.1111/gtc.12014

Takatani, S., Otani, K., Kanazawa, M., Takahashi, T., Motose, H., 2015. Structure, function, and evolution of plant NIMA-related kinases: implication for phosphorylation-dependent microtubule regulation. J. Plant Res. 128, 875–891. https://doi.org/10.1007/s10265-015-0751-6

Takatani, S., Verger, S., Okamoto, T., Takahashi, T., Hamant, O., Motose, H., 2020. Microtubule Response to Tensile Stress Is Curbed by NEK6 to Buffer Growth Variation in the Arabidopsis Hypocotyl. Curr. Biol. 30, 1491-1503.e2. https://doi.org/10.1016/j.cub.2020.02.024

Tanaami, T., Otsuki, S., Tomosada, N., Kosugi, Y., Shimizu, M., Ishida, H., 2002. High-speed 1-frame/ms scanning confocal microscope with a microlens and Nipkow disks. Appl. Opt. 41, 4704. https://doi.org/10.1364/AO.41.004704

Tantale, K., Mueller, F., Kozulic-Pirher, A., Lesne, A., Victor, J.-M., Robert, M.-C., Capozi, S., Chouaib, R., Backer, V., Mateos-Langerak, J., Darzacq, X., Zimmer, C., Basyuk, E., Bertrand, E., 2016. A single-molecule view of transcription reveals convoys of RNA polymerases and multi-scale bursting. Nat. Commun. 7, 12248. https://doi.org/10.1038/ncomms12248

Theissen, G., Becker, A., Di Rosa, A., Kanno, A., Kim, J.T., Münster, T., Winter, K.-U., Saedler, H., 2000. A short history of MADS-box genes in plants. Plant Mol. Biol. 42, 115–149. https://doi.org/10.1023/A:1006332105728

Theissen, G., Saedler, H., 2001. Plant biology - Floral quartets. Nature 409, 469–471. https://doi.org/10.1038/35054172

Thorn, K., 2016. A quick guide to light microscopy in cell biology. Mol. Biol. Cell 27, 219–222. https://doi.org/10.1091/mbc.e15-02-0088

Tian, C., Wan, P., Sun, S., Li, J., Chen, M., 2004. Genome-Wide Analysis of the GRAS Gene Family in Rice and Arabidopsis. Plant Mol. Biol. 54, 519–532. https://doi.org/10.1023/B:PLAN.0000038256.89809.57

Tirnauer, J.S., Bierer, B.E., 2000. Eb1 Proteins Regulate Microtubule Dynamics, Cell Polarity, and Chromosome Stability. J. Cell Biol. 149, 761–766. https://doi.org/10.1083/jcb.149.4.761

Tirnauer, J.S., O'Toole, E., Berrueta, L., Bierer, B.E., Pellman, D., 1999. Yeast Bim1p Promotes the G1-specific Dynamics of Microtubules. J. Cell Biol. 145, 993–1007. https://doi.org/10.1083/jcb.145.5.993

Titford, M., 2009. Progress in the Development of Microscopical Techniques for Diagnostic Pathology. J. Histotechnol. 32, 9–19. https://doi.org/10.1179/his.2009.32.1.9

Tomer, R., Khairy, K., Amat, F., Keller, P.J., 2012. Quantitative high-speed imaging of entire developing embryos with simultaneous multiview light-sheet microscopy. Nat. Methods 9, 755–763. https://doi.org/10.1038/nmeth.2062

Tomer, R., Lovett-Barron, M., Kauvar, I., Andalman, A., Burns, V.M., Sankaran, S., Grosenick, L., Broxton, M., Yang, S., Deisseroth, K., 2015. SPED Light Sheet Microscopy: Fast Mapping of Biological System Structure and Function. Cell 163, 1796–1806. https://doi.org/10.1016/j.cell.2015.11.061

Tomson, B.N., Arndt, K.M., 2013. The many roles of the conserved eukaryotic Paf1 complex in regulating transcription, histone modifications, and disease states. Biochim. Biophys. Acta 1829, 116–126. https://doi.org/10.1016/j.bbagrm.2012.08.011

Tooke, F., Ordidge, M., Chiurugwi, T., Battey, N., 2005. Mechanisms and function of flower and inflorescence reversion. J. Exp. Bot. 56, 2587–2599. https://doi.org/10.1093/jxb/eri254

Trinh, D.-C., Alonso-Serra, J., Asaoka, M., Colin, L., Cortes, M., Malivert, A., Takatani, S., Zhao, F., Traas, J., Trehin, C., Hamant, O., 2021. How Mechanical Forces Shape Plant Organs. Curr. Biol. 31, R143–R159. https://doi.org/10.1016/j.cub.2020.12.001

Trotochaud, A.E., Hao, T., Wu, G., Yang, Z.B., Clark, S.E., 1999. The CLAVATA1 receptor-like kinase requires CLAVATA3 for its assembly into a signaling complex that includes KAPP and a Rho-related protein. Plant Cell 11, 393–405. https://doi.org/10.1105/tpc.11.3.393

Truong, T.V., Supatto, W., Koos, D.S., Choi, J.M., Fraser, S.E., 2011. Deep and fast live imaging with two-photon scanned light-sheet microscopy. Nat. Methods 8, 757–760. https://doi.org/10.1038/nmeth.1652

Trushko, A., Schäffer, E., Howard, J., 2013. The growth speed of microtubules with XMAP215-coated beads coupled to their ends is increased by tensile force. Proc Natl Acad Sci USA 110. https://doi.org/10.1073/pnas.1218053110

Tsien, R.Y., 2010. Nobel lecture: constructing and exploiting the fluorescent protein paintbox. Integr. Biol. 2, 77–93. https://doi.org/10.1039/b926500g

Tsugawa, S., Hervieux, N., Kierzkowski, D., Routier-Kierzkowska, A.-L., Sapala, A., Hamant, O., Smith, R.S., Roeder, A.H.K., Boudaoud, A., Li, C.-B., 2017. Clones of cells switch from reduction to enhancement of size variability in *Arabidopsis* sepals. Development 144, 4398–4405. https://doi.org/10.1242/dev.153999

Turck, F., Roudier, F., Farrona, S., Martin-Magniette, M.-L., Guillaume, E., Buisine, N., Gagnot, S., Martienssen, R.A., Coupland, G., Colot, V., 2007. Arabidopsis TFL2/LHP1 specifically associates with genes marked by trimethylation of histone H3 lysine 27. Plos Genet. 3, 855–866. https://doi.org/10.1371/journal.pgen.0030086

Tutucci, E., Livingston, N.M., Singer, R.H., Wu, B., 2018. Imaging mRNA In Vivo, from Birth to Death. Annu. Rev. Biophys. 47, 85–106. https://doi.org/10.1146/annurev-biophys-070317-033037

Valuchova, S., Mikulkova, P., Pecinkova, J., Klimova, J., Krumnikl, M., Bainar, P., Heckmann, S., Tomancak, P., Riha, K., 2020. Imaging plant germline differentiation within Arabidopsis flowers by light sheet microscopy. eLife 9, e52546. https://doi.org/10.7554/eLife.52546

van der Graaff, E., Laux, T., Rensing, S.A., 2009. The WUS homeobox-containing (WOX) protein family. Genome Biol. 10, 248. https://doi.org/10.1186/gb-2009-10-12-248

Van Norman, J.M., Benfey, P.N., 2009. Arabidopsis thaliana as a Model Organism in Systems Biology. Wiley Interdiscip. Rev. Syst. Biol. Med. 1, 372–379. https://doi.org/10.1002/wsbm.25

Van Oss, S.B., Cucinotta, C.E., Arndt, K.M., 2017. Emerging Insights into the Roles of the Paf1 Complex in Gene Regulation. Trends Biochem. Sci. 42, 788–798. https://doi.org/10.1016/j.tibs.2017.08.003

Verger, S., Hamant, O., 2018. Plant Physiology: FERONIA Defends the Cell Walls against Corrosion. Curr. Biol. 28, R215–R217. https://doi.org/10.1016/j.cub.2018.01.043

Verger, S., Long, Y., Boudaoud, A., Hamant, O., 2018. tension-adhesion feedback loop in plant epidermis.

Vernoux, T., Kronenberger, J., Grandjean, O., Laufs, P., Traas, J., 2000. PIN-FORMED 1 regulates cell fate at the periphery of the shoot apical meristem. Development 127, 5157–5165.

Vitre, B., Coquelle, F.M., Heichette, C., Garnier, C., Chrétien, D., Arnal, I., 2008. EB1 regulates microtubule dynamics and tubulin sheet closure in vitro. Nat. Cell Biol. 10, 415–421. https://doi.org/10.1038/ncb1703

Volpi, E.V., Bridger, J.M., 2008. FISH glossary: an overview of the fluorescence in situ hybridization technique. BioTechniques 45, 385–409. https://doi.org/10.2144/000112811

von Diezmann, A., Shechtman, Y., Moerner, W.E., 2017. Three-Dimensional Localization of Single Molecules for Super-Resolution Imaging and Single-Particle Tracking. Chem. Rev. 117, 7244–7275. https://doi.org/10.1021/acs.chemrev.6b00629

von Wangenheim, D., Hauschild, R., Fendrych, M., Barone, V., Benková, E., Friml, J., 2017. Live tracking of moving samples in confocal microscopy for vertically grown roots. eLife 6, e26792. https://doi.org/10.7554/eLife.26792

Vyplelová, P., Ovečka, M., Šamaj, J., 2017. Alfalfa Root Growth Rate Correlates with Progression of Microtubules during Mitosis and Cytokinesis as Revealed by Environmental Light-Sheet Microscopy. Front. Plant Sci. 8, 1870. https://doi.org/10.3389/fpls.2017.01870

Wade, P.A., Werel, W., Fentzke, R.C., Thompson, N.E., Leykam, J.F., Burgess, R.R., Jaehning, J.A., Burton, Z.F., 1996. A Novel Collection of Accessory Factors Associated with Yeast RNA Polymerase II. Protein Expr. Purif. 8, 85–90. https://doi.org/10.1006/prep.1996.0077

Walia, A., Lee, J.S., Wasteneys, G., Ellis, B., 2009. Arabidopsis mitogen-activated protein kinase MPK18 mediates cortical microtubule functions in plant cells. Plant J. 59, 565–575. https://doi.org/10.1111/j.1365-313X.2009.03895.x

Wang, J., Liu, D., Guo, X., Yang, W., Wang, X., Zhan, K., Zhang, A., 2011. Variability of Gene Expression After Polyhaploidization in Wheat (Triticum aestivum L.). G3 Genes Genomes Genet. 1, 27–33. https://doi.org/10.1534/g3.111.000091

Wang, J., Tian, C., Zhang, C., Shi, B., Cao, X., Zhang, T.-Q., Zhao, Z., Wang, J.-W., Jiao, Y., 2017. Cytokinin Signaling Activates WUSCHEL Expression during Axillary Meristem Initiation. Plant Cell 29, 1373–1387. https://doi.org/10.1105/tpc.16.00579

Wasteneys, G.O., 2004. Progress in understanding the role of microtubules in plant cells. Curr. Opin. Plant Biol. 7, 651–660. https://doi.org/10.1016/j.pbi.2004.09.008

Wasteneys, G.O., Ambrose, J.C., 2009. Spatial organization of plant cortical microtubules: close encounters of the 2D kind. Trends Cell Biol. 19, 62–71. https://doi.org/10.1016/j.tcb.2008.11.004

WASTENEYS, G.O., WILLIAMSON, R.E., 1987. Microtubule orientation in developing internodal cells of Nitella: a quantitative analysis. Microtubule Orientat. Dev. Internodal Cells Nitella Quant. Anal. 43, 14–22.

Waters, A.J., Makarevitch, I., Noshay, J., Burghardt, L.T., Hirsch, C.N., Hirsch, C.D., Springer, N.M., 2017. Natural variation for gene expression responses to abiotic stress in maize. Plant J. 89, 706–717. https://doi.org/10.1111/tpj.13414

Waters, J.C., Wittmann, T. (Eds.), 2014. Quantitative imaging in cell biology, 1. ed. ed, Methods in cell biology. Elsevier, Acad. Press, Amsterdam.

Wei, C., Lintilhac, L.S., Lintilhac, P.M., 2006. Loss of stability, pH, and the anisotropic extensibility of Chara cell walls. Planta 223, 1058–1067. https://doi.org/10.1007/s00425-005-0152-5

Weigel, D., Alvarez, J., Smyth, D.R., Yanofsky, M.F., Meyerowitz, E.M., 1992. LEAFY controls floral meristem identity in Arabidopsis. Cell 69, 843–859. https://doi.org/10.1016/0092-8674(92)90295-N

Weigert, M., Schmidt, U., Boothe, T., Müller, A., Dibrov, A., Jain, A., Wilhelm, B., Schmidt, D., Broaddus, C., Culley, S., Rocha-Martins, M., Segovia-Miranda, F., Norden, C., Henriques, R., Zerial, M., Solimena, M., Rink, J., Tomancak, P., Royer, L., Jug, F., Myers, E.W., 2018. Content-aware image restoration: pushing the limits of fluorescence microscopy. Nat. Methods 15, 1090–1097. https://doi.org/10.1038/s41592-018-0216-7

Weingarten, M.D., Lockwood, A.H., Hwo, S.Y., Kirschner, M.W., 1975. A protein factor essential for microtubule assembly. Proc. Natl. Acad. Sci. 72, 1858–1862. https://doi.org/10.1073/pnas.72.5.1858

Western, T.L., Cheng, Y., Liu, J., Chen, X., 2002. HUA ENHANCER2, a putative DExH-box RNA helicase, maintains homeotic B and C gene expression in Arabidopsis. Development 129, 1569–1581.

White, J.G., Amos, W.B., Fordham, M., 1987. An evaluation of confocal versus conventional imaging of biological structures by fluorescence light microscopy. J. Cell Biol. 105, 41–48. https://doi.org/10.1083/jcb.105.1.41

Wightman, R., Chomicki, G., Kumar, M., Carr, P., Turner, S.R., 2013. SPIRAL2 Determines Plant Microtubule Organization by Modulating Microtubule Severing. Curr. Biol. 23, 1902–1907. https://doi.org/10.1016/j.cub.2013.07.061

Wightman, R., Turner, S.R., 2007. Severing at sites of microtubule crossover contributes to microtubule alignment in cortical arrays: Microtubule dynamics. Plant J. 52, 742–751. https://doi.org/10.1111/j.1365-313X.2007.03271.x

Williams, L., Grigg, S.P., Xie, M., Christensen, S., Fletcher, J.C., 2005. Regulation of Arabidopsis shoot apical meristem and lateral organ formation by microRNA miR166g and its AtHD-ZIP target genes. Development 132, 3657–3668. https://doi.org/10.1242/dev.01942

Williamson, R., 1990. Alignment of Cortical Microtubules by Anisotropic Wall Stresses. Funct. Plant Biol. 17, 601. https://doi.org/10.1071/PP9900601

Wolf, S., Hématy, K., Höfte, H., 2012. Growth Control and Cell Wall Signaling in Plants. Annu. Rev. Plant Biol. 63, 381–407. https://doi.org/10.1146/annurev-arplant-042811-105449

Wolgan von Goethe, J., 1955. Versuch die Metamorphose der Pflanzen zu erklären.

Wolny, A., Cerrone, L., Vijayan, A., Tofanelli, R., Barro, A.V., Louveaux, M., Wenzl, C., Strauss, S., Wilson-Sánchez, D., Lymbouridou, R., Steigleder, S.S., Pape, C., Bailoni, A., Duran-Nebreda, S., Bassel, G.W., Lohmann, J.U., Tsiantis, M., Hamprecht, F.A., Schneitz, K., Maizel, A., Kreshuk, A., 2020. Accurate and versatile 3D segmentation of plant tissues at cellular resolution. eLife 9, e57613. https://doi.org/10.7554/eLife.57613

Wood, A., Schneider, J., Dover, J., Johnston, M., Shilatifard, A., 2003. The Paf1 complex is essential for histone monoubiquitination by the Rad6-Bre1 complex, which signals for histone methylation by COMPASS and Dot1p. J. Biol. Chem. 278, 34739–34742. https://doi.org/10.1074/jbc.C300269200

Woychik, N.A., Hampsey, M., 2002. The RNA Polymerase II Machinery: Structure Illuminates Function. Cell 108, 453–463. https://doi.org/10.1016/S0092-8674(02)00646-3

Wu, C.-C., Li, F.-W., Kramer, E.M., 2019. Large-scale phylogenomic analysis suggests three ancient superclades of the WUSCHEL-RELATED HOMEOBOX transcription factor family in plants. PLOS ONE 14, e0223521. https://doi.org/10.1371/journal.pone.0223521

Wu, X., Dabi, T., Weigel, D., 2005. Requirement of Homeobox Gene STIMPY/WOX9 for Arabidopsis Meristem Growth and Maintenance. Curr. Biol. 15, 436–440. https://doi.org/10.1016/j.cub.2004.12.079

Wu, Y., Christensen, R., Colón-Ramos, D., Shroff, H., 2013. Advanced optical imaging techniques for neurodevelopment. Curr. Opin. Neurobiol. 23, 1090–1097. https://doi.org/10.1016/j.conb.2013.06.008

Wu, Y., Ghitani, A., Christensen, R., Santella, A., Du, Z., Rondeau, G., Bao, Z., Colon-Ramos, D., Shroff, H., 2011. Inverted selective plane illumination microscopy (iSPIM) enables coupled cell identity lineaging and neurodevelopmental imaging in Caenorhabditis elegans. Proc. Natl. Acad. Sci. 108, 17708–17713. https://doi.org/10.1073/pnas.1108494108

Wurschum, T., Gross-Hardt, R., Laux, T., 2006. APETALA2 regulates the stem cell niche in the Arabidopsis shoot meristem. Plant Cell 18, 295–307. https://doi.org/10.1105/tpc.105.038398

Wymer, C.L., Wymer, S.A., Cosgrove, D.J., Cyr, R.J., 1996. Plant Cell Growth Responds to External Forces and the Response Requires Intact Microtubules. Plant Physiol. 110, 425–430. https://doi.org/10.1104/pp.110.2.425

Xiao, T.J., Kao, C.F., Krogan, N.J., Sun, Z.W., Greenblatt, J.F., Osley, M.A., Strahl, B.D., 2005. Histone H2B ubiquitylation is associated with elongating RNA polymerase II. Mol. Cell. Biol. 25, 637–651. https://doi.org/10.1128/MCB.25.2.637-651.2005

Xu, Q., Zhu, C., Fan, Y., Song, Z., Xing, S., Liu, W., Yan, J., Sang, T., 2016. Population transcriptomics uncovers the regulation of gene expression variation in adaptation to changing environment. Sci. Rep. 6. https://doi.org/10.1038/srep25536

Xu, Y., Bernecky, C., Lee, C.-T., Maier, K.C., Schwalb, B., Tegunov, D., Plitzko, J.M., Urlaub, H., Cramer, P., 2017. Architecture of the RNA polymerase II-Paf1C-TFIIS transcription elongation complex. Nat. Commun. 8, 15741. https://doi.org/10.1038/ncomms15741

Xu, Y., Prunet, N., Gan, E., Wang, Y., Stewart, D., Wellmer, F., Huang, J., Yamaguchi, N., Tatsumi, Y., Kojima, M., Kiba, T., Sakakibara, H., Jack, T.P., Meyerowitz, E.M., Ito, T., 2018. SUPERMAN regulates floral whorl boundaries through control of auxin biosynthesis. EMBO J. 37, e97499. https://doi.org/10.15252/embj.201797499

Yadav, R.K., Perales, M., Gruel, J., Girke, T., Jonsson, H., Reddy, G.V., 2011. WUSCHEL protein movement mediates stem cell homeostasis in the Arabidopsis shoot apex. Genes Dev. 25, 2025–2030. https://doi.org/10.1101/gad.17258511

Yamaguchi, N., Huang, J., Tatsumi, Y., Abe, M., Sugano, S.S., Kojima, M., Takebayashi, Y., Kiba, T., Yokoyama, R., Nishitani, K., Sakakibara, H., Ito, T., 2018. Chromatin-mediated feed-forward auxin biosynthesis in floral meristem determinacy. Nat. Commun. 9, 5290. https://doi.org/10.1038/s41467-018-07763-0

Yamaguchi, N., Huang, J., Xu, Y., Tanoi, K., Ito, T., 2017. Fine-tuning of auxin homeostasis governs the transition from floral stem cell maintenance to gynoecium formation. Nat. Commun. 8, 1125. https://doi.org/10.1038/s41467-017-01252-6

Yang, Y., Li, W., Hoque, M., Hou, L., Shen, S., Tian, B., Dynlacht, B.D., 2016. PAF Complex Plays Novel Subunit-Specific Roles in Alternative Cleavage and Polyadenylation. Plos Genet. 12, e1005794. https://doi.org/10.1371/journal.pgen.1005794

Yanofsky, M.F., Ma, H., Bowman, J.L., Drews, G.N., Feldmann, K.A., Meyerowitz, E.M., 1990. The protein encoded by the Arabidopsis homeotic gene agamous resembles transcription factors. Nature 346, 35. https://doi.org/10.1038/346035a0

Yant, L., Mathieu, J., Dinh, T.T., Ott, F., Lanz, C., Wollmann, H., Chen, X., Schmid, M., 2010. Orchestration of the Floral Transition and Floral Development in Arabidopsis by the Bifunctional Transcription Factor APETALA2. Plant Cell 22, 2156–2170. https://doi.org/10.1105/tpc.110.075606

Yoshida, S., Mandel, T., Kuhlemeier, C., 2011. Stem cell activation by light guides plant organogenesis. Genes Dev. 25, 1439–1450. https://doi.org/10.1101/gad.631211

Yu, L.P., Miller, A.K., Clark, S.E., 2003. POLTERGEIST Encodes a Protein Phosphatase 2C that Regulates CLAVATA Pathways Controlling Stem Cell Identity at Arabidopsis Shoot and Flower Meristems. Curr. Biol. 13, 179–188. https://doi.org/10.1016/S0960-9822(03)00042-3

Yu, L.P., Simon, E.J., Trotochaud, A.E., Clark, S.E., 2000. POLTERGEIST functions to regulate meristem development downstream of the CLAVATA loci. Development 127, 1661–1670.

Yu, M., Yang, W., Ni, T., Tang, Z., Nakadai, T., Zhu, J., Roeder, R.G., 2015. RNA polymerase II-associated factor 1 regulates the release and phosphorylation of paused RNA polymerase II. Science 350, 1383–1386. https://doi.org/10.1126/science.aad2338

Yu, X., Michaels, S.D., 2010. The Arabidopsis Paf1c Complex Component CDC73 Participates in the Modification of FLOWERING LOCUS C Chromatin. Plant Physiol. 153, 1074–1084. https://doi.org/10.1104/pp.110.158386

Yumul, R.E., Kim, Y.J., Liu, X., Wang, R., Ding, J., Xiao, L., Chen, X., 2013. POWERDRESS and Diversified Expression of the MIR172 Gene Family Bolster the Floral Stem Cell Network. PLoS Genet. 9, e1003218. https://doi.org/10.1371/journal.pgen.1003218

Zhang, H., Ransom, C., Ludwig, P., Nocker, S. van, 2003. Genetic Analysis of Early Flowering Mutants in Arabidopsis Defines a Class of Pleiotropic Developmental Regulator Required for Expression of the Flowering-Time Switch Flowering Locus C. Genetics 164, 347–358.

Zhang, H., van Nocker, S., 2002. The VERNALIZATION INDEPENDENCE 4 gene encodes a novel regulator of FLOWERING LOCUS C. Plant J. 31, 663–673. https://doi.org/10.1046/j.1365-313X.2002.01380.x

Zhang, K., Wang, R., Zi, H., Li, Y., Cao, X., Li, D., Guo, L., Tong, J., Pan, Y., Jiao, Y., Liu, R., Xiao, L., Liu, X., 2018. AUXIN RESPONSE FACTOR3 Regulates Floral Meristem Determinacy by Repressing Cytokinin Biosynthesis and Signaling. Plant Cell 30, 324–346. https://doi.org/10.1105/tpc.17.00705

Zhang, L., DeGennaro, D., Lin, G., Chai, J., Shpak, E.D., 2021. ERECTA family signaling constrains *CLAVATA3* and *WUSCHEL* to the center of the shoot apical meristem. Development 148, dev189753. https://doi.org/10.1242/dev.189753

Zhang, R., Alushin, G.M., Brown, A., Nogales, E., 2015. Mechanistic origin of microtubule dynamics instability and its modulation by EB proteins. Cell 162. https://doi.org/10.1016/j.cell.2015.07.012

Zhang, X., Germann, S., Blus, B.J., Khorasanizadeh, S., Gaudin, V., Jacobsen, S.E., 2007. The Arabidopsis LHP1 protein colocalizes with histone H3 Lys27 trimethylation. Nat. Struct. Mol. Biol. 14, 869–871. https://doi.org/10.1038/nsmb1283

Zhao, L., Kim, Y., Dinh, T.T., Chen, X., 2007. miR172 regulates stem cell fate and defines the inner boundary of APETALA3 and PISTILLATA expression domain in Arabidopsis floral meristems. Plant J. 51, 840–849. https://doi.org/10.1111/j.1365-313X.2007.03181.x

Zhao, Y.X., Medrano, L., Ohashi, K., Fletcher, J.C., Yu, H., Sakai, H., Meyerowitz, E.M., 2004. HANABA TARANU is a GATA transcription factor that regulates shoot apical meristem and flower development in Arabidopsis. Plant Cell 16, 2586–2600. https://doi.org/10.1105/tpc.104.024869

Zhou, Q., Li, T., Price, D.H., 2012. RNA Polymerase II Elongation Control. Annu. Rev. Biochem. 81, 119–143. https://doi.org/10.1146/annurev-biochem-052610-095910

Zhou, Y., Liu, X., Engstrom, E.M., Nimchuk, Z.L., Pruneda-Paz, J.L., Tarr, P.T., Yan, A., Kay, S.A., Meyerowitz, E.M., 2015. Control of plant stem cell function by conserved interacting transcriptional regulators. Nature 517, 377-U528. https://doi.org/10.1038/nature13853

Zhou, Y., Yan, A., Han, H., Li, T., Geng, Y., Liu, X., Meyerowitz, E.M., 2018. HAIRY MERISTEM with WUSCHEL confines CLAVATA3 expression to the outer apical meristem layers. Science 361, 502-+. https://doi.org/10.1126/science.aar8638

Zhu, B., Mandal, S.S., Main, A.D., Zheng, Y., Erdjument-Bromage, H., Batra, S.K., Tempst, P., Reinberg, D., 2005. The human PAF complex coordinates transcription with events downstream of RNA synthesis. Genes Dev. 19, 1668–1673. https://doi.org/10.1101/gad.1292105

Zuercher, E., Tavor-Deslex, D., Lituiev, D., Enkerli, K., Tarr, P.T., Mueller, B., 2013. A Robust and Sensitive Synthetic Sensor to Monitor the Transcriptional Output of the Cytokinin Signaling Network in Planta. Plant Physiol. 161, 1066–1075. https://doi.org/10.1104/pp.112.211763